INTERNATIONAL DOCTORAL
SCHOOL OF THE USC

Ismael
Arán Tapia

PhD Thesis

Mathematical modeling of the vestibular system: a path to personalized medicine

Santiago de Compostela, 2024

Doctoral Programme in Materials Science

INTERNATIONAL DOCTORAL SCHOOL OF THE USC

DOCTORAL THESIS

MATHEMATICAL MODELING OF THE VESTIBULAR SYSTEM: A PATH TO PERSONALIZED MEDICINE

Ismael Arán Tapia

Supervisors:

Alberto Pérez Muñuzuri

Andrés Soto Varela

DOCTORAL PROGRAMME IN MATERIALS SCIENCE

SANTIAGO DE COMPOSTELA

2024

"The important thing is not to stop questioning."

Albert Einstein

USC
UNIVERSIDADE
DE SANTIAGO
DE COMPOSTELA

Contents

Preface 7

Abstract 9

Resumen 12

Resumo 15

Motivation 22

Aim and scope 23

1 Introduction 25
- 1.1 Clinical background . . . 25
  - 1.1.1 Vestibular anatomy . . . 26
  - 1.1.2 Vestibular physiology . . . 29
  - 1.1.3 Epley maneuver . . . 31
  - 1.1.4 Head impulse test . . . 32
  - 1.1.5 Magnetic vestibular stimulation . . . 32
- 1.2 Mathematical background . . . 33
  - 1.2.1 Vestibular mathematical modeling . . . 33
  - 1.2.2 Numerical methods . . . 38

2 Methodology 42
- 2.1 Computational geometry . . . 43
- 2.2 Meshing . . . 45
  - 2.2.1 Fluid region . . . 45
  - 2.2.2 Solid region . . . 48
  - 2.2.3 Electromagnetic region . . . 48
- 2.3 Dimensionless numbers . . . 49
  - 2.3.1 Epley maneuver . . . 49
  - 2.3.2 Head impulse test . . . 51
  - 2.3.3 Magnetic vestibular stimulation . . . 51
- 2.4 Equations . . . 51
  - 2.4.1 Epley maneuver . . . 52
  - 2.4.2 Head impulse test . . . 53
  - 2.4.3 Magnetic vestibular stimulation . . . 55
- 2.5 Boundary conditions . . . 57

2.5.1 Fluid and solid regions . . . 57
2.5.2 Electromagnetic region . . . 57
2.6 Coordinate systems . . . 60
2.7 Definition of the rotations . . . 62
2.7.1 Rotation for the Epley maneuver . . . 62
2.7.2 Rotation for the head impulse test . . . 64
2.8 Measurement of the vestibular stimulation . . . 66
2.8.1 Shear strain XY . . . 66
2.8.2 Numerical slow-phase velocity . . . 67
2.8.3 Experimental slow-phase velocity . . . 69
2.9 Clinical study . . . 69

3 Results and discussion **72**
3.1 Epley maneuver . . . 73
3.1.1 Results . . . 74
3.1.1.1 Analysis of the standard Epley maneuver . . . 74
3.1.1.2 Personalization of the Epley maneuver . . . 79
3.1.2 Discussion . . . 83
3.1.2.1 Biophysics behind the Epley maneuver . . . 84
3.1.2.2 Numerical analysis . . . 85
3.1.2.3 Clinical overview . . . 87
3.1.3 Summary . . . 89
3.1.4 Future work . . . 89
3.2 Head impulse test . . . 90
3.2.1 Results . . . 91
3.2.1.1 Qualitative analysis of effect of rotations . . . 91
3.2.1.2 Stimulation response of cristae ampullares . . . 94
3.2.1.3 Mapping the stimuli . . . 95
3.2.1.4 Maximum and minimum directions . . . 101
3.2.1.5 Origin of rotation . . . 107
3.2.2 Discussion . . . 108
3.2.2.1 Biophysical process during the head impulse test . . . 108
3.2.2.2 Interpretation of the stimuli . . . 109
3.2.2.3 Inertial forces and origin of rotation . . . 110
3.2.3 Summary . . . 111
3.2.4 Future work . . . 111
3.3 Magnetic vestibular stimulation . . . 112
3.3.1 Results . . . 113
3.3.1.1 Sensitivity to the boundary conditions . . . 113
3.3.1.2 Biophysical variables in magnetic vestibular stimulation . . . 115
3.3.1.3 Experimental validation of numerical results . . . 119
3.3.1.4 Simulated eye movement responses to head orientations . . . 122
3.3.2 Discussion . . . 124
3.3.2.1 Model robustness . . . 124
3.3.2.2 Biophysics behind magnetic vestibular stimulation . . . 125
3.3.2.3 Numerical prediction of the magnetic vestibular stimulation . . . 127

USC UNIVERSIDADE DE SANTIAGO DE COMPOSTELA

3.3.3 Summary 128
3.3.4 Future work 128

4 Conclusions **130**

Abbreviations **132**

List of figures **133**

List of tables **139**

List of publications **142**

Copyright Permissions **144**

Dissemination of reseach **146**

Funding information **147**

Bibliography **148**

USC UNIVERSIDADE DE SANTIAGO DE COMPOSTELA

Preface

Embarking on a journey to contribute to the scientific community through this thesis is a deeply rewarding and challenging experience. Before delving into this research project, I would like to provide some context regarding the genesis of this work and express my profound gratitude to those who supported me along the way.

From a young age, I have harbored deep curiosity about the world around us, always questioning the reasons behind things. This innate curiosity likely directed my educational path towards physics and mathematics, offering me a unique lens through which to understand the world. The shift in my professional interests towards medical research can be attributed in part to my parents, particularly my father, who instilled in me a fascination with otoneurology.

During my predoctoral stage, I was fortunate to receive guidance and insights from clinical professionals in otoneurology as well as support in the fields of physics and mathematics. This interdisciplinary guidance has enabled me to conduct research on the vestibular system. Thanks to this support, I have been able to comprehend the physiology and pathophysiology of the vestibular system, along with the mathematical tools and physics concepts necessary to complete this doctoral dissertation.

Given the multidisciplinary nature of this research, clarity and conciseness are essential to ensure accessibility to individuals across various fields. Learning to communicate effectively across these diverse domains without compromising rigor is one of the most valuable lessons I will carry forward. Consequently, I have strived to make this research comprehensible and intriguing, regardless of your professional or academic background. I hope to convey the significance and potential impact of this work.

I am deeply grateful for the support of everyone who participated in my journey. Special thanks to my advisors, Alberto Pérez Muñuzuri and Andrés Soto Varela, and Vicente Pérez Muñuzuri, who first believed in me during my early stages as a researcher. Together with my mentors in the United States, Bryan K. Ward and Dale C. Roberts, they have been instrumental in shaping me as a researcher, granting me the freedom to design my own research and develop critical thinking skills. Their mentorship has been invaluable, and, for that, I am immensely thankful.

I would also like to acknowledge my colleagues from the Nonlinear Physics Group. Despite working in different fields, we have shared countless hours in the laboratory, facing the challenges and celebrating the triumphs of our doctoral journey.

To my friends and family, your unwavering encouragement and support have been sources of strength. Your understanding during times when I needed to disconnect and focus on my work, and your warm welcome when I returned, means the world to me. Special mention goes to my parents, Ismael Arán González and Ana Tapia Gil, and my brother, Carlos Arán Tapia. Their unconditional love and support have been with me since birth. Without my father's encouragement, this project would not have been fruitful.

USC UNIVERSIDADE DE SANTIAGO

Finally, I owe a debt of gratitude to my wife Raisa Babaeva. She selflessly set aside her personal and professional pursuits over the years, believing in me, and supporting my doctoral research. Much of the credit belongs to her. I am incredibly fortunate to have such a supportive partner by my side. Special thanks also to our beloved cat, Kiara, whose affectionate interruptions while lying on my keyboard have provided moments of comfort and joy.

I also extend my thanks to all the other researchers I have met during these years, the doctors and patients who are the reason for this study, and the developers of the software and tools that have enormously facilitated my research. This includes acknowledgments to all sources of financing I received during these years, especially to the Xunta de Galicia, which provided me with a salary as a predoctoral researcher.

In summary, I aspire to motivate future researchers to delve into this fascinating field. The intricate workings of the inner ear and their significant impact on our perception of the world are both captivating and enigmatic. The human body, particularly the vestibular system, is a marvel that never ceases to amaze me with its intricacy and beauty.

USC
UNIVERSIDADE DE SANTIAGO DE COMPOSTELA

Abstract

Despite the crucial role of the vestibular system in balance and spatial orientation, current understanding of its mechanisms remains incomplete. This doctoral thesis aims to develop and validate mathematical models of the vestibular system to deepen our understanding of vestibular physiology and improve diagnostic and therapeutic accuracy in the field of otorhinolaryngology. To achieve this, high-performance computing has been utilized, which enables the resolution of numerical methods based on mathematical, physical, and medical foundations. This thesis exemplifies the application of interdisciplinary strategies in personalized medicine and highlights the importance of clinical trials as a method to validate the results obtained through numerical simulations.

Although numerical simulations are widely used in other areas of biomedical research, their application to the vestibular system is relatively novel. Owing to technological advances in recent decades, it has become possible to model vestibular behavior based on mathematical and physical principles. This new approach could enable personalized medicine for the diagnosis and treatment of vestibular disorders. However, the implementation of these mathematical models has certain limitations that this thesis aims to address, such as the lack of clinical data, insufficient quality of medical images, limited knowledge of vestibular physiology, and difficulty in implementing multidisciplinary approaches.

Interdisciplinary collaboration is essential to advance in this field, integrating neuroscience, otorhinolaryngology, physics, and mathematics to create accurate models. The synergy between researchers from different specialties ensures the applicability and usefulness of these models in clinical practice. In this way, an intuitive interface can be provided to physicians, facilitating diagnostic and treatment decisions. Simultaneously, clinical trials can help validate these models, ensuring their effectiveness in real-world situations. This process facilitates the development and adaptation of various populations and pathological conditions.

All these aspects constitute the fundamental basis of this doctoral thesis. The research begins with a rigid model of the membranous labyrinth, addressing the behaviors observed during episodes of vertigo. This initial model specifically aims at individualized treatment of benign paroxysmal positional vertigo using the Epley maneuver. Subsequently, the focus shifts to the vestibular receptors located in the ampullae. Here, the elastic nature of this region of the vestibular system is incorporated to evaluate the response to the head impulse test, thus providing a greater physiological understanding of vestibular function and paving the way for personalized diagnosis of vestibular diseases. Finally, this research delves into the modeling of magnetic vestibular stimulation caused by magnetic resonance imaging machines, adding a magnetohydrodynamic model that allows for controlling the response of the vestibular system based on external fields with the aim of preventing the occurrence of unwanted symptoms. This progressive integration of complexity underscores the potential of mathematical models in personalized vestibular medicine, suggesting promising, cost-effective, and noninvasive

approaches for future clinical applications.

This thesis is divided into four chapters: an introduction to the topic, a methodological description of the simulation and numerical validation method, a presentation and discussion of the obtained results and proposals for future research developments, and finally, the conclusions of the thesis.

The first chapter of this thesis presents a comprehensive introduction to the clinical and mathematical context of the vestibular system. It begins by describing the anatomy and physiology of the vestibular apparatus, including a detailed description of the morphology and function of the different vestibular receptors. Additionally, it addresses benign paroxysmal positional vertigo from a clinical perspective and its treatment using the Epley maneuver, the head impulse test, and magnetic vestibular stimulation. Subsequently, the chapter delves into the mathematical modeling of vestibular function, reviews previous models, and introduces modern numerical methods that enhance the understanding and prediction of vestibular responses. This introduction provides a better understanding of the methods used to perform the simulations employed in this research.

The second chapter of this thesis details the methodology for creating mathematical models and numerical simulations of the problems described in the introduction, as well as their clinical validation. It begins by describing the modeling of human vestibular anatomy using high-resolution imaging techniques, such as micro-computed tomography, to create accurate simulations of the vestibular structures. The meshing process is discussed in detail, emphasizing the importance of mesh quality and density to obtain precise results while balancing the computational cost. The identification of dimensionless numbers is also addressed, along with a description of the fluid, solid, and electromagnetic equations used in the models. A variety of modeling methods have been employed, including fluid-structure interaction, the finite volume method, the finite element method, and Lagrangian particle models, which require significant computational resources on supercomputers. The boundary and initial conditions, coordinate systems, and rotational functions are also defined to ensure that the simulations reflect real conditions. This chapter also details how the analysis of vestibular stimulation generated in the cristae ampullares is conducted and explains how theoretical predictions of nystagmus are compared with experimental data from patients. Finally, a clinical trial conducted at Johns Hopkins University is described, where the experimental and simulation results of vestibular magnetic stimulation caused by the magnetic fields created in MRI machines were compared. This chapter offers a detailed description of the models and criteria used, facilitating an understanding of the results and discussion presented in this thesis.

The third chapter presents the results of the numerical simulations and discusses their theoretical and clinical implications, organized in a structure that progresses in ascending order of complexity. This increased detail in the models allows us to address the challenges presented by each of the problems to be solved in this thesis.

Initially, a rigid model of the membranous labyrinth combined with a Lagrangian particle model was used to simulate the Epley maneuver. This simulation predicts the trajectories of otoconia, analyzing how different head movements affect their repositioning and the time they take to reach their final position. The discussion covers the biophysical mechanisms of the maneuver, the role of different forces, and the potential for personalized modifications based on individual anatomy to improve the treatment outcomes of benign paroxysmal positional vertigo, suggesting future work, such as exploring other treatment maneuvers and clinically evaluating the simulation results.

Subsequently, the focus shifts to the head impulse test using a fluid-structure interaction model that considers the elasticity of the cupulae and their interaction with the endolymph. The simulations provide qualitative and quantitative analyses of endolymph fluid dynamics and stimulation in the cristae ampullares during head rotations. This allowed for the creation of a three-dimensional stimulation map to determine the planes of rotation that caused the maximum and minimum stimulation in each crista ampullaris. The discussion challenges previous hypotheses, showing that the vestibular response is more aligned with the angular acceleration of the head than with the angular velocity. It also emphasizes the importance of considering the orientation of the cupulae for precise and personalized diagnosis, recommending future research to improve the diagnostic accuracy of rotational tests and the design of precise mathematical models.

Finally, a fluid-structure interaction model coupled with a magnetohydrodynamic model is used to study the effect of magnetic fields on the vestibular system. The results highlight the biophysical variables that influence magnetic vestibular stimulation, and the numerical predictions are validated using experimental data. The discussion addresses the robustness of the model and the influence of variables, such as patient age, on stimulation results. It also explores the Lorentz force hypothesis, which explains how the slow-phase velocity of nystagmus varies with head orientation. This analysis concludes with a summary of the essential findings of the study and proposes possible avenues for future research, such as refining the models and exploring new clinical applications of magnetic vestibular stimulation. This includes improving the safety and efficacy of MRI techniques and developing new diagnostic and treatment techniques for vestibular disorders.

The fourth chapter presents the conclusions of this thesis, highlighting the potential of this research in personalized medicine applied to various vestibular disorders. The implications of the developed mathematical models are discussed, showing how personalized simulations could adapt diagnoses and treatments to the individual needs of each patient, thereby improving effectiveness and minimizing risks. This chapter acknowledges the limitations of the current research, including the need for more extensive clinical validation and a deeper understanding of vestibular physiology to ensure the accuracy and clinical utility of these models.

Overall, this study marks a significant advancement in the application of mathematical models and numerical simulations to personalized vestibular medicine, addressing the complexity of vestibular anatomy and physiology. The relevance and effectiveness of these models for future innovations in clinical practice depends on their degree of interdisciplinarity and rigorous clinical validation.

USC
UNIVERSIDADE DE SANTIAGO DE COMPOSTELA

Resumen

A pesar del papel crucial del sistema vestibular en el equilibrio y la orientación espacial, nuestra comprensión actual de sus mecanismos sigue siendo incompleta. Esta tesis doctoral tiene como objetivo desarrollar y validar modelos matemáticos del sistema vestibular que permitan profundizar en la comprensión de la fisiología vestibular y mejorar la precisión diagnóstica y terapéutica en el campo de la otorrinolaringología. Para ello se ha utilizado la computación de alto rendimiento, que permite resolver métodos numéricos basados en fundamentos matemáticos, físicos y médicos. Esta tesis ilustra cómo la aplicación de estrategias interdisciplinarias puede avanzar en la medicina personalizada y subraya la importancia de los ensayos clínicos para validar los resultados obtenidos a través de simulaciones numéricas.

Aunque las simulaciones numéricas se utilizan ampliamente en otras áreas de la investigación biomédica, su aplicación al sistema vestibular es relativamente novedosa. Gracias a los avances tecnológicos de las últimas décadas, ha sido posible modelizar el comportamiento vestibular a partir de fundamentos matemáticos y físicos. Este nuevo enfoque podría permitir aplicar la medicina personalizada en el diagnóstico y tratamiento de los trastornos vestibulares. Sin embargo, la implementación de estos modelos matemáticos tiene ciertas limitaciones que esta tesis pretende abordar, como son la falta de datos clínicos, la insuficiente calidad de las imágenes médicas, el limitado conocimiento de la fisiología vestibular y la dificultad en la implementación de enfoques multidisciplinarios.

La colaboración interdisciplinar es esencial para avanzar en este campo, integrando neurociencia, otorrinolaringología, física y matemáticas para crear modelos precisos. La sinergia entre investigadores de diferentes especialidades asegura la aplicabilidad y utilidad de estos modelos en la práctica clínica. De esta manera, se puede proporcionar al médico una interfaz intuitiva, facilitando las decisiones de diagnóstico y tratamiento. Al mismo tiempo, los ensayos clínicos ayudan a validar estos modelos, garantizando su eficacia en situaciones del mundo real. Este proceso facilita su desarrollo y adaptación a diversas poblaciones y condiciones patológicas.

Todos estos aspectos constituyen la base fundamental de esta tesis doctoral. La investigación comienza con un modelo rígido del laberinto membranoso, que aborda los comportamientos observados durante episodios de vértigo. Este modelo inicial tiene como objetivo específico el tratamiento individualizado del vértigo posicional paroxístico benigno mediante la maniobra de Epley. Posteriormente, el foco se centra en los receptores vestibulares ubicados en las ampollas. Aquí se incorpora la naturaleza elástica de esta región del sistema vestibular para evaluar la respuesta al test de impulso cefálico, proporcionando así un mayor conocimiento fisiológico de la función vestibular y abriendo el camino hacia un diagnóstico personalizado de las enfermedades vestibulares. Finalmente, esta investigación profundiza en la modelización de la estimulación vestibular magnética provocada por máquinas de resonancia magnética, añadiendo un modelo magnetohidrodinámico que permite controlar la respuesta del

sistema vestibular en función de campos externos, con el objetivo de prevenir la aparición de síntomas no deseados. Esta progresiva integración de complejidad subraya el potencial de los modelos matemáticos en la medicina vestibular personalizada, sugiriendo enfoques prometedores, rentables y no invasivos para futuras aplicaciones clínicas.

Esta tesis está dividida en cuatro capítulos: una introducción clínica y matemática, una descripción metodológica del método de simulación y validación numérica, una presentación y discusión de los resultados obtenidos junto a propuestas para futuras investigaciones, y finalmente, las conclusiones de la tesis.

El primer capítulo de esta tesis presenta una introducción completa al contexto clínico y matemático del sistema vestibular. Comienza describiendo la anatomía y fisiología del aparato vestibular, incluyendo una descripción detallada de la morfología y la función de los diferentes receptores vestibulares. Además, aborda desde una perspectiva clínica el vértigo posicional paroxístico benigno y su tratamiento mediante la maniobra de Epley, el test de impulso cefálico y la estimulación vestibular magnética. Posteriormente, el capítulo profundiza en la modelización matemática de la función vestibular, revisando modelos anteriores e introduciendo métodos numéricos modernos que mejoran la comprensión y predicción de las respuestas vestibulares. Esta introducción sirve para comprender mejor los métodos utilizados para realizar las simulaciones que se emplean a lo largo de esta investigación.

El segundo capítulo de esta tesis detalla la metodología para crear los modelos matemáticos y simulaciones numéricas de los problemas descritos en la introducción, así como su validación clínica. Comienza describiendo la modelización de la anatomía vestibular humana utilizando técnicas de imagen de alta resolución, como la tomografía microcomputarizada, para crear simulaciones precisas de las estructuras vestibulares para cada estudio específico. El proceso de mallado se discute en detalle, enfatizando la importancia de la calidad y densidad del mallado para obtener resultados precisos mientras se equilibra el costo computacional. También se aborda la identificación de números adimensionales, junto con una descripción de las ecuaciones de fluidos, sólidos y electromagnéticas utilizadas en los modelos. Se han empleado una variedad de métodos de modelización, incluyendo la interacción fluido-estructura, el método de volúmenes finitos, el método de elementos finitos y modelos de partículas Lagrangianas, que requieren significativos recursos computacionales en supercomputadoras. Las condiciones de contorno e iniciales, los sistemas de coordenadas y las funciones de rotación se definen para asegurar que las simulaciones reflejen condiciones reales. Este capítulo también explica como se realiza el análisis de la estimulación vestibular generada en las crestas ampullares y compara las predicciones teóricas del nistagmo con datos experimentales de pacientes. Finalmente, se detalla un ensayo clínico realizado en la Universidad Johns Hopkins, donde se compararon los resultados experimentales y de simulación de la estimulación vestibular magnética causada por los campos magnéticos creados en las máquinas de resonancia magnética. Este capítulo proporciona una descripción completa de los modelos y criterios utilizados en cada estudio para entender los resultados y discusiones de esta tesis.

El tercer capítulo presenta los resultados de las simulaciones numéricas y discute sus implicaciones teóricas y prácticas, organizándose en una estructura que va en orden ascendente de complejidad. Este aumento en el detalle de los modelos nos permite abordar los desafíos que presentan cada uno de los problemas a resolver en esta tesis.

Inicialmente, se utilizó un modelo rígido del laberinto membranoso combinado con un modelo de partículas Lagrangiano para simular la maniobra de Epley. Esta simulación predice las trayectorias de las otoconias, analizando cómo los diferentes movimientos de la cabeza

USC UNIVERSIDADE

afectan su reposicionamiento y el tiempo que tardan en alcanzar su posición final. La discusión abarca los mecanismos biofísicos de la maniobra, el papel de las diferentes fuerzas y el potencial de modificaciones personalizadas basadas en la anatomía individual para mejorar los resultados del tratamiento del vértigo posicional paroxístico benigno, sugiriendo futuros trabajos como explorar otras maniobras de tratamiento y evaluar clínicamente los resultados de las simulaciones.

A continuación, el foco se desplaza al test de impulso cefálico mediante un modelo de interacción fluido-estructura, que considera la elasticidad de las cúpulas y su interacción con la endolinfa. Las simulaciones proporcionan análisis cualitativos y cuantitativos de la dinámica del fluido endolinfático y la estimulación en las crestas ampullares durante las rotaciones de la cabeza. Esto permitió realizar un mapeado tridimensional de la estimulación para determinar los planos de rotación que provocan estimulación máxima y mínima en cada cresta ampular. La discusión desafía hipótesis previas, mostrando que la respuesta vestibular está más alineada con la aceleración angular de la cabeza que con la velocidad angular. También se enfatiza la importancia de considerar la orientación de las cúpulas para un diagnóstico preciso y personalizado, recomendando investigaciones futuras para mejorar la precisión diagnóstica de las pruebas de rotación y el diseño de modelos matemáticos precisos.

Finalmente, se emplea un modelo de interacción fluido-estructura acoplado con un modelo magnetohidrodinámico para estudiar el efecto de los campos magnéticos en el sistema vestibular. Los resultados destacan las variables biofísicas que influyen en la estimulación vestibular magnética, y se validan las predicciones numéricas con datos experimentales. La discusión aborda la robustez del modelo y la influencia de variables como la edad del paciente en los resultados de la estimulación. También se explora la hipótesis de la fuerza de Lorentz, explicando cómo la velocidad de la fase lenta del nistagmo varía con la orientación de la cabeza. Este análisis culmina con un resumen de los hallazgos esenciales del estudio y propone posibles vías para futuras investigaciones, como refinar los modelos y explorar nuevas aplicaciones clínicas de la estimulación vestibular magnética. Esto incluye mejorar la seguridad y eficacia de las técnicas de resonancia magnética, así como desarrollar nuevas técnicas de diagnóstico y tratamiento para los trastornos vestibulares.

El cuarto capítulo presenta las conclusiones finales de esta tesis, destacando el potencial de esta investigación en la medicina personalizada aplicada a diferentes trastornos vestibulares. Discute las implicaciones de los modelos matemáticos desarrollados, mostrando cómo las simulaciones personalizadas permitirían adaptar los diagnósticos y tratamientos a las necesidades individuales de cada paciente, mejorando su efectividad y minimizando los riesgos. El capítulo reconoce las limitaciones de la investigación actual, incluyendo la necesidad de una validación clínica más extensa y una comprensión más profunda de la fisiología vestibular para asegurar la precisión y utilidad clínica de estos modelos.

En general, esta investigación marca un avance significativo en la aplicación de modelos matemáticos y simulaciones numéricas a la medicina vestibular personalizada, abordando la complejidad de la anatomía y fisiología vestibular. La relevancia y eficacia de estos modelos para futuras innovaciones dentro de la práctica clínica dependerán de su grado de interdisciplinariedad y de una validación clínica rigurosa.

USC
UNIVERSIDADE DE SANTIAGO DE COMPOSTELA

Resumo

A pesar da relevancia do sistema vestibular para o equilibrio e a orientación espacial, hoxe en día non temos unha comprensión completa dos seus mecanismos fisiopatolóxicos. Esta tese doutoral enfócase no desenvolvemento e validación de modelos matemáticos do sistema vestibular para mellorar a precisión diagnóstica e terapéutica no ámbito da otorrinolaringoloxía. A través de simulacións numéricas e técnicas de alto rendemento computacional, esta investigación aborda esta lagoa, ofrecendo novas ferramentas para a personalización do diagnóstico e o tratamento dos trastornos vestibulares. Desta forma, estes modelos non só axudan a comprender mellor a fisioloxía vestibular, senón que tamén permiten simulacións personalizadas que poden prever a eficacia dos tratamentos, optimizando os recursos e a eficiencia dos procedementos clínicos actuais. O traballo ilustra a necesidade de estratexias interdisciplinarias no mundo da medicina personalizada e subliña a importancia de futuras validacións clínicas para integrar estes avances na práctica médica cotiá.

O sistema vestibular, localizado no oído interno, desempeña un rol fundamental para o correcto desenvolvemento da vida. Este sistema foise adaptando ás condicións ambientais cambiantes desde os primeiros vertebrados ata os seres humanos modernos. Porén, a pesar da súa longa viaxe formando parte de nós, non foi ata a chegada dos avances tecnolóxicos nos últimos séculos que se puido comezar a desentrañar os complexos mecanismos detrás da función vestibular. Un destes avances é a aplicación das matemáticas e a física ao mundo da bioloxía, e neste caso a aplicación dos fundamentos matemáticos e físicos para modelar o comportamento do sistema vestibular. Isto trouxo consigo unha nova perspectiva de abordaxe que permitiu descifrar gran parte da fisioloxía e a fisiopatoloxía vestibular. Hoxe en día, coa chegada da computación de alto rendemento, deuse un paso máis adiante que permitiu a creación de simulacións numéricas máis complexas, ofrecendo unha perspectiva máis precisa da fisioloxía vestibular. En comparación cos modelos simplificados que se desenvolveron inicialmente, os investigadores agora poden explorar a anatomía tridimensional do sistema vestibular, acadando unha representación máis realista do seu complexo comportamento biofísico.

Aínda que estas aplicacións se empregan amplamente noutros campos biomédicos, o uso de simulacións numéricas no contexto do sistema vestibular segue sendo relativamente inexplorado, con potencial para responder a preguntas fundamentais e proporcionar novas aplicacións. Unha aplicación prometedora destes avances é a medicina personalizada, un campo emerxente destinado a revolucionar os enfoques terapéuticos e as ferramentas de diagnóstico para optimizar a eficacia e eficiencia para cada paciente. Xa que actualmente, as terapias e os diagnósticos para os trastornos vestibulares non están personalizados, o que pode dificultar a detección de certas patoloxías ou facer ineficaces as terapias necesarias. Un enfoque prometedor para implementar a medicina personalizada na patofisioloxía vestibular é simular as condicións vestibulares de suxeitos individuais. Non obstante, ao comezo deste proxecto de tese, era

evidente a falta de modelos matemáticos centrados neste obxectivo. Esta deficiencia débese probablemente á falta de datos clínicos adecuados, ás técnicas de imaxe médica que permitan unha resolución aceptable da estrutura membranosa do oído interno, ao limitado coñecemento da fisioloxía vestibular e ao enfoque multidisciplinar necesario.

Neste senso, a colaboración interdisciplinaria foi, é e seguirá a ser crucial para o avance deste campo. A integración de coñecementos de neuroloxía, otorrinolaringoloxía, física e matemáticas permitirá o desenvolvemento de modelos máis completos e precisos. Ademais, colaboracións con científicos de índole máis clínica e experimental cos coñecementos científicos máis teóricos pode asegurar que os pés sobre os que se cimenta esta nova área de investigación sexan sólidos, certificando que os modelos desenvolvidos sexan relevantes e útiles na práctica médica diaria.

A forma de abordar esta complexa iteración entre campos tan diversos da ciencia é a través do desenvolvemento de ferramentas de software baseadas nos modelos matemáticos. Estas ferramentas poden proporcionar interfaces intuitivas para que os clínicos aproveiten os resultados de simulacións personalizadas, permitíndolles tomar decisións informadas sobre o diagnóstico ou o tratamento dos pacientes. A integración na práctica clínica destas ferramentas e a súa accesibilidade serán cruciais para a súa adopción xeralizada. Por outro lado, os ensaios clínicos serán un paso fundamental para validar os modelos matemáticos e as simulacións desenvolvidas. A través destes ensaios, poderase avaliar a eficacia dos modelos en situacións reais de diagnóstico e tratamento, proporcionando datos críticos para a súa mellora continua. Os resultados dos ensaios clínicos tamén poden servir para axustar os modelos ás necesidades de diferentes poboacións e condicións clínicas, aumentando así a súa aplicabilidade e impacto.

Estes aspectos constitúen a esencia deste traballo de investigación. Empregando un enfoque multidisciplinar que integra coñecementos en medicina, física e matemáticas, o obxectivo principal desta tese foi desenvolver e validar modelos matemáticos avanzados do sistema vestibular para facilitar a medicina personalizada. Este obxectivo xeral perseguiuse a través da creación e aplicación de simulacións numéricas para mellorar o diagnóstico, o tratamento e a comprensión dos trastornos vestibulares.

Para lograr este obxectivo, esta investigación componse de diferentes modelos matemáticos ordenados nunha estrutura que vai en orde ascendente de complexidade. Este aumento no detalle dos modelos permítenos abordar os desafíos que presentan cada un dos problemas a resolver nesta tese. Deste modo, a investigación comeza cun modelo ríxido do labirinto membranoso, que aborda os comportamentos observados durante episodios de vertixe. Este modelo inicial ten como obxectivo específico o tratamento individualizado da vertixe posicional paroxística benigna mediante a manobra de Epley. Posteriormente, o foco céntrase nos receptores vestibulares situados nas ampollas. Aquí incorpórase a natureza elástica desta rexión do sistema vestibular para avaliar a resposta á proba de impulso cefálico, proporcionando así un maior coñecemento fisiolóxico da función vestibular e abrindo o camiño cara a un diagnóstico personalizado das enfermidades vestibulares. Finalmente, esta investigación profundiza na modelización da estimulación vestibular magnética provocada por máquinas de resonancia magnética, engadindo un modelo magnetohidrodinámico que permite controlar a resposta do sistema vestibular en función de campos externos, co obxectivo de previr a aparición de síntomas non desexados.

Aínda que estes modelos matemáticos poderían ser adaptados para investigar outras enfermidades vestibulares, esta investigación enfócase na súa aplicación para a medicina personalizada do sistema vestibular, ofrecendo un método de baixo custo, non invasivo e

efectivo para futuras aplicacións clínicas. Desta forma, espérase que os resultados desta investigación teñan un impacto significativo tanto na saúde individual dos pacientes como nos sistemas sanitarios a nivel global.

Este documento estrutúrase en catro capítulos que guían ao lector a través dunha análise exhaustiva e detallada deste traballo de investigación sobre o sistema vestibular. O primeiro capítulo ofrece unha introdución ampla ao tema, establecendo o contexto tanto clínico como técnico, e definindo todos os termos e conceptos necesarios para que a tese sexa totalmente autocontida. No segundo capítulo, descríbese a metodoloxía empregada para a realización das simulacións numéricas e a súa validación, facilitando o entendemento de todos os modelos matemáticos desenvolvidos. O terceiro capítulo está dedicado á presentación e discusión dos resultados, permitindo comparar estes achados coa literatura existente e destacar as novas contribucións ao campo. Ademais, tamén se propón un resumo de cada un dos estudos e se suxire un camiño a seguir para futuras investigacións. Finalmente, o cuarto capítulo resume as principais conclusións da investigación, enfatizando as implicacións destes modelos matemáticos. Este fluxo lóxico e coherente no desenvolvemento dos capítulos asegura que cada sección contribúa de maneira significativa ao entendemento desta contribución orixinal e o seu impacto no campo da otorrinolaringoloxía e da medicina personalizada.

Capítulo 1: Introdución

O primeiro capítulo ofrece unha descrición xeral e completa do contexto clínico e matemático necesario para comprender todos os aspectos importantes da investigación realizada.

A primeira parte do capítulo comeza cunha explicación da anatomía vestibular, incluíndo as estructuras do aparato vestibular como o labirinto óseo e membranoso situado no oído interno. Esta última está composta por unha serie de túbulos e sacos que forman unha estrutura pechada con paredes elásticas cheas de fluido endolinfático. Dentro deste labirinto membranoso atópanse os receptores vestibulares, que inclúen a mácula utricular e a mácula sacular. Tamén se atopan as tres crestas ampulares, situadas no interior da cúpula de cada canal semicircular (horizontal, posterior e superior).

A continuación, ofrécese unha visión detallada da fisioloxía do sistema vestibular, explicando como os receptores vestibulares, compostos por células ciliadas, transforman a información mecánica dos movementos en sinais eléctricos que son procesados polo cerebro para coordinar as respostas motoras, como o reflexo vestibulo-ocular e o nistagmo. As máculas están especializadas en detectar aceleracións lineais grazas a pequenos cristais de carbonato cálcico chamados otoconias, mentres que as crestas ampulares detectan aceleracións angulares debido á deflexión das cúpulas elásticas que son sensibles ao movemento do fluído endolinfático. A orientación espacial dos canais semicirculares é crucial neste sentido, xa que a súa disposición en planos ortogonais facilita a división dos movementos angulares da cabeza en tres compoñentes.

Adicionalmente, este capítulo aborda unha descrición clínica dunha das principais desordes vestibulares, como é a vertixe posicional paroxística benigna. Esta desorde é tratada mediante a manobra de Epley, que permite reposicionar as otoconias desprendidas da mácula utricular fóra dos lugares que causan sintomatoloxía. Tamén se describe unha das ferramentas de diagnóstico máis utilizadas, a proba de impulso cefálico, que avalía de forma independente a función dos canais semicirculares. Por outra banda, discútese a estimulación vestibular magnética,

USC UNIVERSIDADE DE SANTIAGO DE COMPOSTELA

xerada pola resposta vestibular ás forzas magnéticas xeradas durante as probas de resonancia magnética.

A segunda parte do capítulo céntrase no modelado matemático do sistema vestibular. Explora os principios biofísicos que rexen a función vestibular e revisa os modelos anteriores empregados para explicar as respostas vestibulares ás rotacións. Estes modelos iniciais, que describían o desprazamento volumétrico da cúpula como unha ecuación diferencial ordinaria de segunda orde, foron refinados ao longo das décadas para incorporar as complexidades adicionais da anatomía e a interacción física entre a endolinfa e o labirinto membranoso.

Esta sección tamén destaca as limitacións dos modelos tradicionais e introduce métodos numéricos máis modernos, enfatizando os seus posibles beneficios no estudo da función vestibular. Estes modelos numéricos permiten explicar a resposta vestibular dun xeito cuantitativo e máis preciso, permitindo predicións que poden ser validadas experimentalmente. Isto facilita simular escenarios complexos que axudan a identificar os principais factores que influencian certas condicións fisiolóxicas e patolóxicas do sistema vestibular. A partir de softwares que utilizan métodos robustos e precisos para a resolución das ecuacións correspondentes, e a súa resolución en supercomputadores, poden acadarse uns resultados novidosos, os cales son empregados nesta tese.

Deste modo, o primeiro capítulo establece unha sólida base teórica e clínica que facilita a comprensión da anatomía e fisioloxía do sistema vestibular, así como a utilidade clínica dos modelos matemáticos desenvolvidos na tese.

Capítulo 2: Metodoloxía

O segundo capítulo describe a metodoloxía necesaria para desenvolver os modelos matemáticos e as simulacións numéricas empregadas nesta investigación, así como os ensaios clínicos realizados que permiten a súa validación.

Comeza cunha descrición da xeometría computacional, detallando como se modelou a anatomía vestibular humana empregando imaxes obtidas por técnicas de alta resolución como a microtomografía computarizada. Desta forma, conséguese determinar con precisión as estruturas vestibulares que serven para resolver as simulacións numéricas de forma individualizada. Seguidamente, profundízase no proceso de mallado, que implica discretizar o dominio computacional en pequenos elementos para facilitar a resolución das simulacións numéricas. A calidade e densidade da malla son cruciais para garantir resultados precisos, e o capítulo describe os esforzos realizados para alcanzar un equilibrio óptimo entre o custo computacional e a precisión en cada un dos modelos deseñados.

A identificación dos números adimensionais proporciona unha visión da física subxacente do sistema, permitindo comparar os efectos relativos de diferentes forzas e variables. Isto axuda a simplificar as complexas ecuacións que rexen o comportamento do sistema vestibular, facilitando a análise e interpretación dos resultados. De esta forma pódense derivar correctamente as ecuacións a partir das leis fundamentais de conservación de masa, momento e enerxía, así como das ecuacións de Maxwell para o comportamento electromagnético. As ecuacións de conservación garanten que as simulacións respecten as leis físicas fundamentais da mecánica clásica e do electromagnetismo, mentres que as ecuacións de Maxwell permiten modelar con precisión os efectos dos campos magnéticos nas estruturas vestibulares. Empregáronse métodos de modelaxe fluído-estructura, métodos de volumes finitos, métodos de elementos finitos e modelos de partículas lagranxianas para resolver as

ecuacións de forma acoplada. Isto requiriu un gran esforzo computacional e a realización das simulacións en supercomputadores.

Descríbense tamén as condicións de contorno e iniciais, os sistemas de coordenadas empregados e, de ser o caso, a definición das funcións de rotación. Todas estas definicións son esenciais para asegurar que as simulacións reflictan as condicións reais atopadas no sistema vestibular humano, permitindo a resolución do problema matemático de forma precisa. Ademais, explícase como se realizou a análise dos resultados a partir da deformación cortante nunha dirección determinada que corresponde coa estimulación das células ciliadas nas crestas ampulares. Desta forma, puido predecirse de forma teórica a velocidade da fase lenta do nistagmo e comparala coas observacións experimentais realizadas nos movementos oculares dos pacientes.

O capítulo conclúe describindo o ensaio clínico levado a cabo na Universidade de Johns Hopkins nos Estados Unidos. Neste ensaio, avaliáronse pacientes en diferentes máquinas de resonancia magnética para comparar as observacións numéricas e experimentais da estimulación vestibular magnética.

En resumo, este capítulo presenta de forma integral todos os modelos e criterios empregados para levar a cabo as simulacións numéricas referentes a esta tese.

Capítulo 3: Resultados e discusión

Este capítulo presenta os resultados das simulacións numéricas e discute as súas implicacións teóricas e clínicas. A través de tres seccións, móstrase a complexidade crecente dos modelos empregados, comezando cun modelo ríxido para a manobra de Epley, despois introducindo elasticidade para estudar a proba de impulso cefálico e, finalmente, implementando o efecto dun campo magnético que axuda a comprender mellor a estimulación vestibular magnética.

A primeira sección utiliza un modelo ríxido do labirinto membranoso xunto cun modelo de partículas lagranxiano para explicar os resultados da manobra de Epley, que inclúen unha análise da manobra estándar e os efectos das posibles variantes en cada un dos pasos da mesma. Grazas aos resultados das simulacións, é posible coñecer o percorrido das otoconias durante a manobra, identificando como diferentes movementos da cabeza poden afectar o reposicionamento destas partículas e canto tempo lles levaría alcanzar a súa posición final.

A discusión dos resultados da manobra de Epley iníciase cunha avaliación dos mecanismos biofísicos detrás da manobra, que permite comprender o rol das diferentes forzas que aparecen durante a mesma e as similitudes con outros estudos previos. A continuación, discútese a análise numérica dos resultados das simulacións, sinalando que as modificacións personalizadas baseadas na anatomía individual do paciente poderían mellorar os resultados do tratamento do BPPV. Por último, realízase unha avaliación dos resultados da simulación dende unha perspectiva clínica. Estas modificacións poderían axudar a predicir as posicións óptimas da cabeza e os tempos de reposo para cada paciente, ofrecendo información valiosa aos clínicos que non pode ser obtida mediante observacións clínicas ou de imaxe.

Esta sección do capítulo conclúe cun resumo dos puntos clave e suxestións para futuros traballos que se poderían ou estánse a realizar. Como, por exemplo, a exploración doutras manobras de tratamento ou a avaliación clínica dos resultados mediante un estudo clínico que está a levarse a cabo na actualidade.

USC DE COMPOSTELA

Dentro da seguinte sección, preténdese entender mellor a proba de impulso cefálico a partir dun modelo fluído-estrutura. Estas simulacións numéricas presentan unha maior complexidade xa que teñen en conta a elasticidade das cúpulas e o seu efecto bidireccional coa endolinfa. Estes resultados inclúen análises cualitativas e cuantitativas dos efectos destas rotacións na dinámica do fluido endolinfático e da estimulación xerada nas crestas ampullares. Grazas á simulación de diferentes direccións de rotación, foi posible determinar os planos de rotación que producen unha estimulación máxima e mínima en cada cresta, xerando así un mapa de estimulación tridimensional. A través deste mapeado completo, determinouse a relación angular entre os máximos, mínimos e as orientacións das estructuras que forman a anatomía vestibular estudada. Finalmente, evalúase o efecto das rotacións cando se cambia a súa orixe.

A discusión explora todos os procesos biofísicos que acontecen durante a proba de impulso cefálico, permitindo a interpretación dos estímulos e o papel das forzas inerciais e a orixe da rotación. Desta forma, determinouse que a resposta do sistema vestibular a esta proba rotacional está máis aliñada coa aceleración angular que coa velocidade angular da cabeza, desafiando as suposicións previas noutros estudos. Isto resalta a importancia de considerar a orientación das cúpulas e non só a dos canais semicirculares nas probas de rotación para proporcionar un diagnóstico máis preciso e personalizado.

Ao final desta sección, proporciónase un resumo dos achados e recomendacións para futuras investigacións co obxectivo de mellorar a precisión diagnóstica das probas rotacionais como a proba de impulso cefálico e o deseño de modelos matemáticos máis precisos. Tamén se discuten certas limitacións actuais ao aplicar este tipo de modelos de simulación na clínica diaria, como pode ser a calidade limitada das imaxes médicas en humanos vivos.

A última sección deste capítulo utiliza un modelo fluído-estrutura similar ao empregado na proba de impulso cefálico, acoplado cun modelo magnetohidrodinámico, para determinar o efecto dos campos magnéticos no sistema vestibular. Os resultados céntranse nas variables biofísicas que inflúen na estimulación vestibular magnética, incluíndo a sensibilidade ás condicións de contorno e a robustez do modelo. Desta forma, puidéronse validar as predicións numéricas con datos experimentais, mostrando como diferentes intensidades e orientacións da cabeza dentro da máquina de resonancia magnética afectan ás respostas de movemento ocular. Confirmando a validación dos resultados, elaborouse unha avaliación das diferentes respostas para diversas orientacións da cabeza.

A discusión comeza describindo a robustez do modelo e como diferentes variables, como a idade do paciente, poden influír nos resultados de estimulación. A continuación, discútense os efectos biofísicos, tanto teóricos como experimentais, os cales respaldan a hipótese da forza de Lorentz. Desta forma, analízase como a resposta da fase lenta do nistagmo varía en función das diferentes orientacións da cabeza, proporcionando unha comprensión da estimulación vestibular magnética que non fora descrita con anterioridade.

Esta sección remata cun resumo dos puntos clave do estudo e suxestións para futuros traballos nesta novedosa forma de estimulación vestibular. A investigación futura pode centrarse en refinar os modelos e explorar novas aplicacións da estimulación vestibular magnética en diferentes contextos clínicos, como mellorar a seguridade e eficacia das técnicas de imaxe por resonancia magnética, así como desenvolver novas técnicas de diagnóstico e tratamento para trastornos vestibulares.

USC
UNIVERSIDADE DE SANTIAGO DE COMPOSTELA

Capítulo 4: Conclusión

O capítulo final resume as conclusións xerais da tese, enfatizando o potencial dos modelos matemáticos deseñados e das simulacións numéricas realizadas para transformar a medicina personalizada nos trastornos vestibulares. Descríbense as implicacións deste tipo de simulacións personalizadas para adaptar as probas e tratamentos ás necesidades individuais de cada paciente, aumentando a súa efectividade e reducindo os riscos.

O capítulo tamén aborda as limitacións da investigación actual, como a necesidade dunha validación clínica máis extensa e unha comprensión máis profunda da fisioloxía vestibular. A validación clínica é esencial para garantir que os modelos desenvolvidos sexan precisos e útiles na práctica clínica.

En definitiva, esta investigación representa un avance significativo no uso de modelos matemáticos e simulacións numéricas na medicina personalizada no campo dos trastornos vestibulares. Ao abordar a complexidade da anatomía e fisioloxía vestibular, e ao desenvolver modelos que permiten a personalización dos tratamentos, esta tese senta as bases para futuras innovacións que poden transformar o diagnóstico e o tratamento destas condicións. A interdisciplinariedade e a validación clínica serán claves para o éxito continuo neste campo, asegurando que os modelos desenvolvidos sexan tanto precisos como útiles na práctica clínica.

USC
UNIVERSIDADE DE SANTIAGO DE COMPOSTELA

Motivation

Understanding the intricacies of the human body and its functions has always been a cornerstone of scientific inquiry. Among these, the vestibular system stands out because of its crucial role in maintaining balance and spatial orientation; however, it remains one of the less understood sensory systems. This thesis seeks to bridge this gap by exploring the vestibular system through mathematical modeling, with the aim of advancing the field of personalized medicine.

The vestibular system, located in the inner ear, is responsible for detecting and relaying information about various types of movements, aiding organisms in maintaining balance and spatial orientation. This ancient sensory system is deeply rooted in the early stages of vertebrate evolution [1]. Over millions of years, the vestibular system has adapted in size and shape to suit changing environmental conditions and habitats, particularly during the transition from aquatic to terrestrial life [2]. This evolutionary journey culminated in the sophisticated sensory apparatus that we know today.

Despite its long history, the vestibular system has not been well understood until recently. The first mention of its existence dates back to ancient Egypt around 1500 B.C.. [3]. However, it was not until advancements in electrophysiology and neuroimaging were made that researchers could better understand the complex interplay between sensory information and neural processing underlying vestibular function [4]. Additional progress has been facilitated by contributions from anatomy, physiology, and neuroscience. In the 20th century, the development of mathematical models by pioneers such as Steinhausen in 1933 marked a significant leap [5]. His work has paved the way for subsequent studies aimed at understanding the vestibular system from a physical perspective, an area of ongoing scientific exploration.

Advancements in high-performance computing have enabled the creation of more complex numerical simulations, offering a more accurate perspective of vestibular physiology. From the initial two-dimensional models, researchers can now explore the three-dimensional anatomy of the vestibular system, striving for a more realistic representation of its complex biophysical behavior. Although such applications have been extensively employed in other biomedical fields, the use of numerical simulations in the context of the vestibular system remains relatively unexplored, with the potential to answer core questions and provide novel applications.

One promising application of these advancements is personalized medicine, a burgeoning field aimed at revolutionizing therapeutic approaches and diagnostic tools tailored to optimize effectiveness and efficiency for individual patients. The main motivation of this thesis is to contribute to the ongoing development of a comprehensive mathematical model that explains the functioning of the vestibular system, with a focus on applications in personalized medicine, as explained in the following sections.

USC
UNIVERSIDADE
DE SANTIAGO
DE COMPOSTELA

Aim and scope

Having described the motivation for this doctoral research, the aim and significance of this study are now presented. This chapter clarifies the structure and objectives of this thesis and outlines how the overarching hypothesis of the research will be tested in the following chapters.

Currently, therapies and diagnoses for vestibular disorders are not personalized, potentially hindering the detection of certain pathologies or rendering the necessary therapies ineffective. A promising approach for implementing personalized medicine for vestibular pathophysiology is to simulate the vestibular conditions of individual subjects. However, at the outset of this thesis project, a lack of mathematical models focusing on this aim was evident. This deficiency is likely due to a lack of appropriate clinical data, insufficient quality of medical images, limited understanding of vestibular physiology, and the multidisciplinary knowledge required in this field.

Employing a multidisciplinary approach that integrates expertise in medicine, physics, and mathematics, the primary aim of this thesis is to develop and validate advanced mathematical models of the vestibular system to facilitate personalized medicine. This overarching goal has been pursued through the creation and application of numerical simulations to improve the diagnosis, treatment, and understanding of vestibular disorders. These simulations are intended to offer a low-cost and noninvasive method for conducting studies and treatments on patients.

To achieve this objective, this research comprises different mathematical models organized in a structure that progresses in ascending order of complexity. The investigation begins with a rigid model of the membranous labyrinth, which addresses the behaviors observed during episodes of vertigo. This initial model specifically aims at the individualized treatment of benign paroxysmal positional vertigo (BPPV) using the Epley maneuver (EM). Subsequently, the focus shifts to the vestibular receptors located in the ampullae. Here, the elastic nature of this region of the vestibular system is incorporated to evaluate the response to the head impulse test (HIT), thus providing a greater physiological understanding of vestibular function and paving the way for personalized diagnosis of vestibular diseases. Finally, this research delves into the modeling of magnetic vestibular stimulation (MVS) caused by magnetic resonance imaging (MRI) machines, adding a magnetohydrodynamic (MHD) model that allows for controlling the response of the vestibular system based on external fields, with the aim of preventing the occurrence of unwanted symptoms.

Although these mathematical models can be adapted to investigate other vestibular disorders, this research focuses on their application in personalized medicine for the vestibular system, paving the way for future clinical applications. Thus, the results of this study are expected to have a significant impact on both the individual health of patients and healthcare systems, shaping the future of vestibular medicine.

USC UNIVERSIDAD DE CANTABRIA

This thesis comprises four chapters. The first chapter provides an introduction to the clinical and mathematical background necessary to understand the context of this research,

situates the current study in the related literature, and establishes the research tools and knowledge required for subsequent chapters. The second chapter describes the methodology followed for designing the mathematical models, detailing how the numerical simulations were designed in the order of increased complexity. The third chapter presents the results, discusses these findings, summarizes how they respond to the aim of this thesis, and outlines future work to continue these research lines. Finally, the fourth chapter offers general conclusions based on the results of this thesis.

USC
UNIVERSIDADE
DE SANTIAGO
DE COMPOSTELA

Chapter 1

Introduction

Part of the text and figures for this chapter are reproduced from the following publications

(I) Arán-Tapia, I.[1,2,3], Soto-Varela, A.[4], Pérez-Muñuzuri, V.[1,3], Santos-Pérez, S.[4], Arán, I.[5], Muñuzuri, A. P.[1,2]. Numerical Simulations of the Epley Maneuver With Clinical Implications.*Ear & Hearing* **45**(4):1033-1044, July/August (2024). ISSN: 0196-0202. DOI: www.doi.org/10.1097/AUD.0000000000001493.

(II) Arán-Tapia, I.[1,2,3], Soto-Varela, A.[4], Pérez-Muñuzuri, V.[1,3], Santos-Pérez, S.[4], Arán, I.[5], Muñuzuri, A. P.[1,2]. Numerical simulations to determine the stimulation of the crista ampullaris during the Head Impulse Test. *Comput Biol Med.* **163**, 107225 (2023). ISSN: 0010-4825. DOI: https://doi.org/10.1016/j.compbiomed.2023.107225.

(III) Arán-Tapia, I.[1,2,3], Pérez-Muñuzuri, V.[1,3], Muñuzuri, A. P.[1,2], Soto-Varela, A.[4], Otero-Millan, J.[6,7], Roberts, D. C.[7], Ward, B. K[8]. The Biophysics of Magnetic Vestibular Stimulation: Clinical Insights from High-Field MRI. Under review in *Communications Medicine* (2024). ISSN: 2730-664X.

[1]Group of Nonlinear Physics, University of Santiago de Compostela, Spain
[2]Galician Center for Mathematical Research and Technology (CITMAga), Spain
[3]Cross-disciplinary Research in Environmental Technologies (CRETUS), Spain
[4]Department of Otorhinolaryngology, Hospital of Santiago de Compostela, Spain
[5]Department of Otorhinolaryngology, Hospital of Pontevedra, Spain
[6]Herbert Wertheim School of Optometry and Vision Science, University of California, USA
[7]Department of Neurology, Johns Hopkins University, USA
[8]Department of Otolaryngology-Head and Neck Surgery, Johns Hopkins University, USA

Before this introductory chapter, we discussed the motivation, aim, and scope of this thesis, emphasizing the design of computational simulations of the vestibular system as the core of this research project. Therefore, it is necessary to establish a comprehensive understanding of the clinical and mathematical background of the vestibular system to provide an appropriate context for this thesis.

1.1 Clinical background

USC UNIVERSIDADE DE SANTIAGO DE COMPOSTELA

Relative to the clinical background, we first delve into the intricate anatomy of the vestibular apparatus and explore its structural components and vestibular receptors.

Subsequently, we examine the physiology of the vestibular system and elucidate its role in maintaining a constant orientation in space and time to preserve balance. Furthermore, clinical descriptions of the different conditions studied in this thesis are provided, including the common vestibular disorder known as benign paroxysmal positional vertigo, the head impulse test as a critical diagnostic tool for vestibular dysfunction, and the emerging field of magnetic vestibular stimulation and its implications for vestibular research and clinical practice.

By offering a comprehensive overview of these clinical aspects, my intention is to provide you with the necessary clinical foundation to effectively comprehend all the subsequent chapters of this thesis.

1.1.1 Vestibular anatomy

The vestibular apparatus resides within the membranous labyrinth of the inner ear [6]. This labyrinth is composed of a series of tubes and sacs forming a closed structure with elastic walls filled with endolymphatic fluid, as depicted in Figures 1.1a and 1.1b, from two different perspectives. Anchored to the bony labyrinth of the temporal bone by bridles, it creates an interstitial space for another fluid called the perilymph. The largest sac in the membranous labyrinth is the utricle, which connects to three semicircular canals: horizontal or lateral, posterior, and superior or anterior. These canals originate and terminate in the utricle, with the superior and posterior canals merging to form the common crus immediately before emptying into the utricle. Each semicircular canal has a dilation called the ampulla, the inside of which contains a gelatinous structure known as the cupula. The cupula extends to the roof and walls of the ampulla, completely separating the endolymph compartments of the semicircular canal and utricle. Although there are other important regions within the membranous labyrinth, such as the saccule, endolymphatic sac, and cochlea, as they were not included in this study, a detailed description may be unnecessary.

The membranous labyrinth anatomical structures separate the endolymphatic and perilymphatic fluids, preserving their distinct ionic environments. Perilymph resembles blood plasma with low potassium and high sodium concentrations, whereas endolymphatic fluid is similar to intracellular fluid with high potassium and low sodium concentrations [7]. Endolymph in the vestibular apparatus originates from perilymph through specialized cells, known as dark cells, which regulate its electrochemical composition through the secretion of potassium ions from the perilymph to the endolymph [8]. This potassium circulation provides endolymph with the role of transducing external forces into fluid motion, resulting in an appropriate stimulus for vestibular receptors. In contrast, perilymph provides structural support and acts as a protective barrier, preventing sound vibrations from interfering with vestibular receptor responses.

There are different vestibular receptors in the inner ear, but they are composed of similar sensory cells known as hair cells. These hair cells consist of a large stereocilium called the kinocilium and a group of smaller stereocilia that move along with it. A schematic representation is shown in Figure 1.2a. Depending on their role and morphology, two types of hair cells exist in the vestibular system: Type I and Type II. All of these are connected to the nervous system by afferent nerve fibers and are surrounded by structural cells called supporting cells.

USC UNIVERSIDADE DE SANTIAGO DE COMPOSTELA

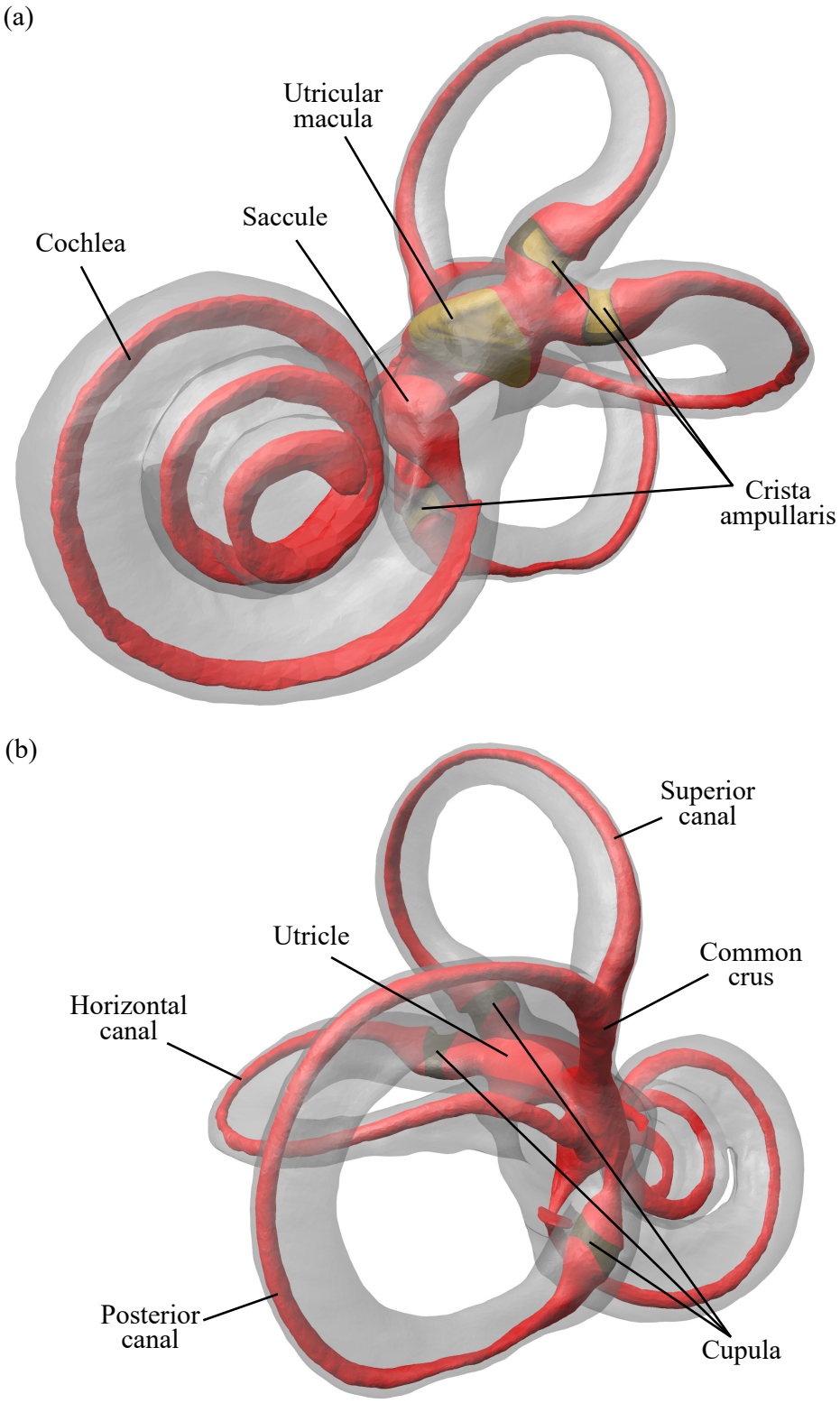

Figure 1.1: An illustration depicting the anatomy of the inner ear in a human specimen. The membranous labyrinth filled with endolymph is depicted in red, whereas the bony labyrinth is shown in gray. The vestibular receptor locations used in this study are highlighted in yellow. (a) Front view. (b) Back view. The three-dimensional model was generated using a high-resolution medical image obtained from the Ariadne Toolbox [9].

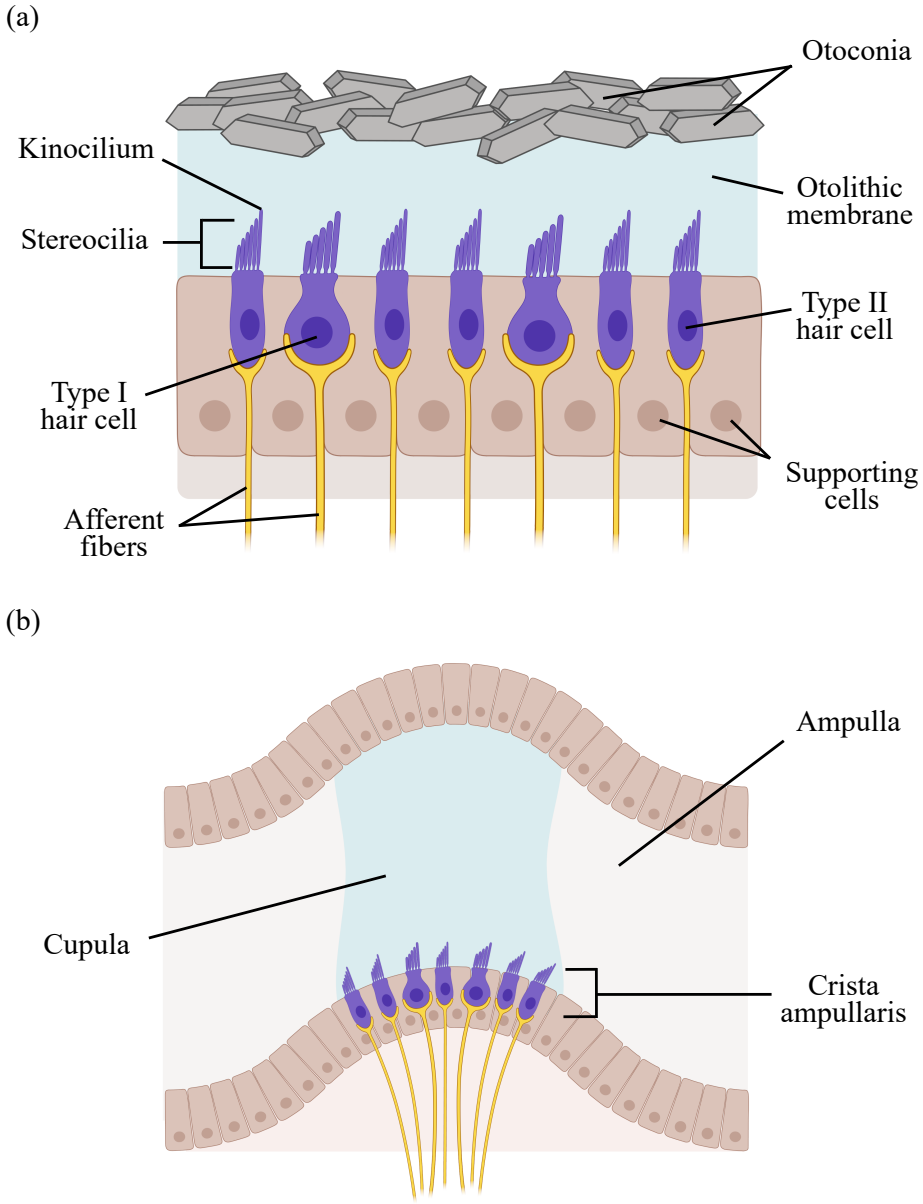

Figure 1.2: Illustrations of the vestibular receptors. (a) Structure of the utricular and saccular macula, including otoconia, and detailed representation of hair cells. (b) Structure of the crista ampullaris and its location in the ampulla. The hair cell types are similar for both types of vestibular receptors. Created with www.biorender.com.

There are two vestibular receptors, the utricular and saccular macula, which share a common structural framework, but they are located at different locations. The saccular macula is located in the anterior part of the saccule, whereas the utriclar macula is located at the bottom of the anterior part of the utricle, as shown in Figure 1.1a. These maculae house sensory hair cells at the bottom, which are covered by a gelatinous layer known as the otolithic membrane, as shown in Figure 1.2a. The otolithic membrane comprises several layers with distinct properties [10], including an upper layer composed of small calcium carbonate crystals called otoconia. These otoconia are embedded in the membrane, forming a denser structure on the roof. Another

vestibular receptor is the crista ampullaris, which is positioned in the inferior part of the cupula of each semicircular canal where hair cells are embedded, as illustrated in Figure 1.2b.

1.1.2 Vestibular physiology

The vestibular system plays a pivotal role in maintaining balance and navigating the environment. This is achieved through the vestibular receptors shown in Figure 1.2, which are specialized structures that detect and transmit sensory signals related to head and body motions. This section explores the physiology of these two vestibular receptors, which is crucial for the diagnosis and treatment of vestibular disorders.

The utricular and saccular maculae are specialized structures that enable the detection of linear acceleration and head position relative to gravity. Specifically, the utricular macula is primarily responsible for detecting horizontal movements, whereas the saccular macula is more sensitive to vertical movements. The function of these structures is facilitated by otoconia, which are denser than the surrounding tissues and fluids. When the head tilts or moves linearly, the otoconia shift, causing the otolithic membrane to move. This motion bends the stereocilia of hair cells, resulting in the generation of an electrical signal that is transmitted to the brain.

The crista ampullaris, another critical vestibular receptor, is located within each semicircular canal and specializes in detecting angular accelerations resulting from rotational head movements. When the head rotates, the inertia of the endolymphatic fluid exerts pressure on the cupula, causing deflection in the hair cells located in the cristae ampullares. Given that this vestibular receptor has been the focus for numerical simulation modeling, its physiology will be explained in more detail.

Similar to hair cells in the macula, sensory cells in the crista have a resting potential that is altered when cilia deflection occurs, thereby modifying their electrical resistance and creating a nervous stimulus. This deflection results in two possibilities: the movement of hair cells towards or away from the kinocilium, which determines whether the response is excitatory or inhibitory. According to Ewald's second law, excitation of any semicircular canal produces a greater response than inhibition. Additionally, the orientation of hair cells within a specific cupula, as shown in Figure 1.2b, remained consistent, but their directional orientation depended on the specific semicircular canal. In the horizontal semicircular canals, the kinocilia are oriented towards the utricle. A deflection of the cupula towards the utricle (utriculipetal) leads to excitation, whereas a deflection towards the semicircular canal results in inhibition. Conversely, in the posterior and superior semicircular canals, excitation occurs when the cupula deflects towards the semicircular canals (utriculifugal), and inhibition occurs when it deflects towards the utricle. This phenomenon is known as Ewald's third law.

Therefore, special attention must be paid to the orientation of the semicircular canals. Ideally, the semicircular canals should lie in orthogonal planes with 90° angles between them. It is also important to consider how these semicircular canal planes are oriented with respect to the space planes. The horizontal canal is inclined 20° to the axial plane (XY), whereas the posterior and superior canals are positioned 45° to the sagittal (XZ) and coronal (YZ) planes. This orientation is mirrored in the other labyrinth, allowing the six semicircular canals to be divided into three canal pair planes: left horizontal and right horizontal canals (LHRH), left anterior and right posterior canals (LARP), and right anterior and left posterior canals (RALP). Figure 1.3 depicts the orientation of these three canal pair planes relative to each other and to the spatial planes. When a semicircular canal is excited during rotation, the canal in the

same plane on the opposite side is inhibited, whereas the other four semicircular canals in the perpendicular planes are not stimulated. This spatial orientation allows the vestibular system to divide angular head movements into three components, facilitating the transmission of nerve impulses corresponding to different planes of space [11].

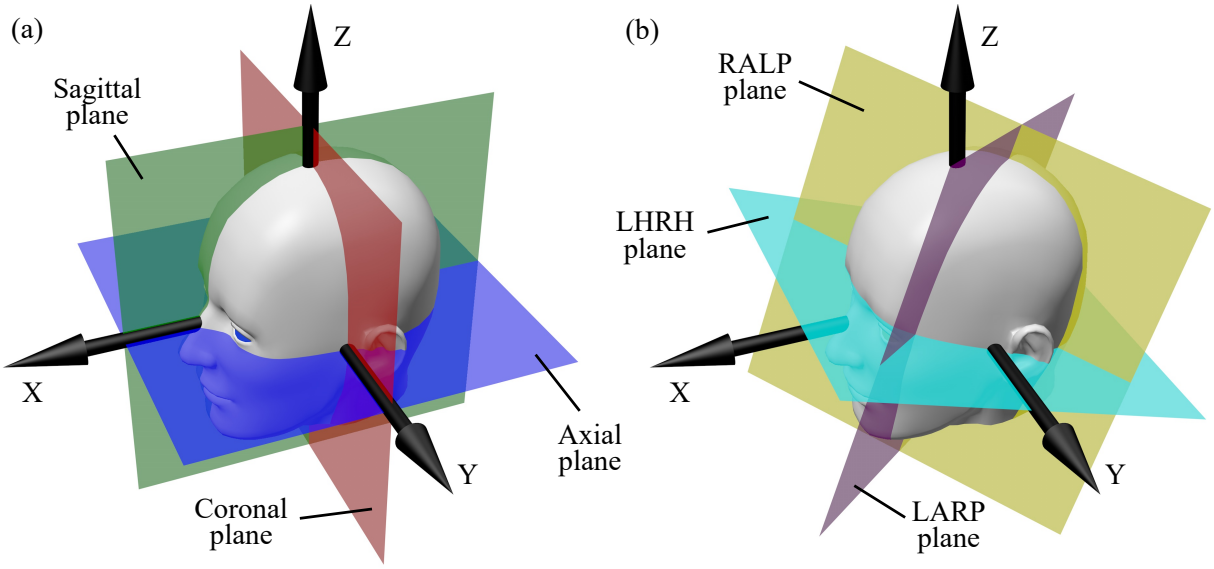

Figure 1.3: Reference orthogonal planes for the head and the orientation of the semicircular canals. (a) The axial, coronal, and sagittal planes were used as references for the orientation of the head. (b) The planes of the left horizontal-right horizontal (LHRH), left anterior-right posterior (LARP), and right anterior-left posterior (RALP) canal pairs encompass the orientations of the six semicircular canals. The LHRH plane is inclined at 20º to the axial plane, while the LARP and RALP planes maintain orthogonality with each other and with the LHRH plane, and are oriented at 45º relative to the coronal and sagittal planes.

Electrical currents generated by hair cells in the cristae ampullares are collected by different afferent terminals and sent to the brain through intricate neurological pathways. The central nervous system can also modulate these signals via efferent fibers that directly connect to hair cells, thereby adjusting the sensitivity and response of the vestibular system [6]. This fine-tuned signaling enables the coordination of eye and head movements through the vestibulo-ocular reflex (VOR), which ensures visual stability during head motion. The VOR compensates for head movements by generating eye movements in the opposite direction while maintaining a steady gaze on a fixed object. For example, during counterclockwise rotation over the LHRH plane, endolymphatic fluid generates utriculipetal and utriculifugal flows in the left and right horizontal semicircular canals, respectively. This process excites hair cells in the left crista ampullaris and inhibits those in the right crista, resulting in a VOR that moves the eyes to the right. A schematic representation of this vestibular activity is shown in Figure 1.4.

Another important type of eye movement is nystagmus, which refers to involuntary rhythmic oscillation of the eyes that can occur under various physiological and pathological conditions. Nystagmus is characterized by a slow phase in one direction, followed by a fast corrective phase in the opposite direction. It can be spontaneous or induced, and its characteristics, such as direction and frequency, provide valuable information for diagnosing vestibular and neurological disorders. Typically, the parameter studied is the slow-phase

velocity (SPV), which is a response function proportional to the head velocity during rotation [12].

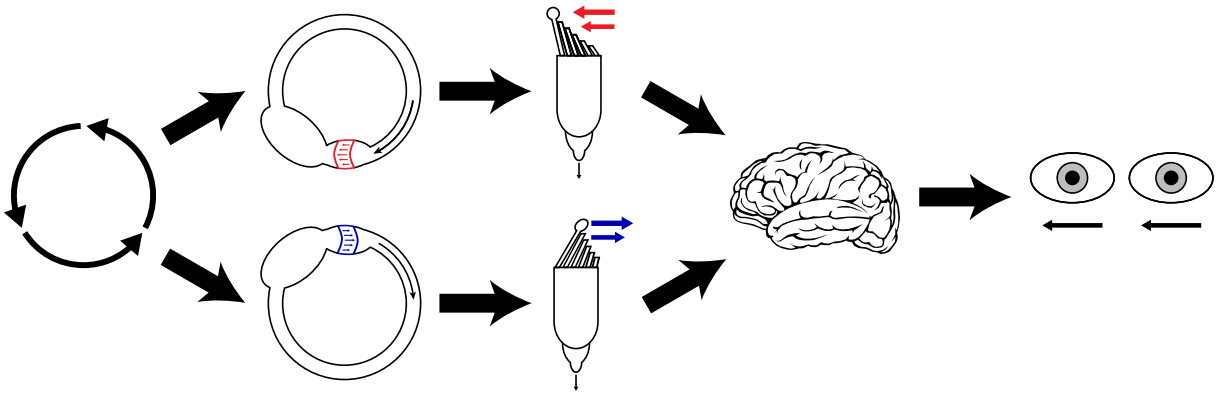

Figure 1.4: Vestibular stimulation scheme for horizontal semicircular canals during a counterclockwise rotation over the left horizontal-right horizontal (LHRH) plane. The endolymphatic fluid moves in the opposite direction of rotation, generating utriculipetal and utriculifugal flows in the left and right horizontal semicircular canals, respectively. This generates excitation in the hair cells located in the left crista ampullaris (red) and inhibition in the hair cells located in the right crista ampullaris (blue). Both of these electric currents are transmitted to the brain, which interprets these signals and generates a response in the extraocular muscles, providing a displacement of the eyes that counteracts the head rotation, known as the vestibulo-ocular reflex (VOR). Brain image collected from www.pixabay.com.

Understanding these physiological processes helps us appreciate how disruptions in the vestibular system can lead to balance disorders and underpin the development of diagnostic and therapeutic strategies. Further mathematical descriptions of these neurological processes and VOR are provided in section 1.2 Mathematical background, enhancing our comprehension of how theoretical models can replicate and predict physiological responses. Now that we have seen the anatomy and physiology of the vestibular system, the clinical aspects of the conditions employed in designing the numerical simulations are introduced.

1.1.3 Epley maneuver

Vertigo is a common and highly incapacitating symptom in the general population [13]. The most frequent cause of vertigo is benign paroxysmal positional vertigo (BPPV) [14], with an estimated prevalence of 10–140 per 100000 and a lifetime prevalence of 2.4 % [15, 16].

BPPV is caused by the displacement of otoconia, which, under normal conditions, are attached to the macula of the utricle, as shown in Figure 1.2a. When otoconia dislodge from their usual location in the utricular macula, they become free in the endolymph of the posterior labyrinth and are prone to enter one of the semicircular canals, most commonly the posterior semicircular canal, followed by the horizontal and superior canals [16]. The possibility of entering one of the semicircular canals depends on the effect of gravity relative to the orientation of the head. Once otoconia are present in the canal, they can either move freely and cause displacement of the endolymph (canalithiasis), or less commonly adhere to the cupula, resulting in cupula deflection in specific head orientations (cupulolithiasis) [17]. Both situations stimulate the hair cells of the cristae ampullares, consequently producing nystagmus and a subjective

sensation of vertigo. Patients with BPPV typically experience recurrent episodes of vertigo that are brief (lasting less than a minute in canalithiasis) and triggered by head movements such as lying down, getting up, rolling over in bed, bending over, or looking up.

The treatment of BPPV primarily involves canalith repositioning procedures (CRP), which involve a series of specific head and body movements performed by a healthcare provider to guide displaced otoconia back to the vestibule, alleviating vertigo symptoms. Among the various maneuvers designed for each canal, the Epley maneuver (EM) is the most commonly used for the posterior semicircular canal [18].

These maneuvers are highly effective in resolving symptoms, although they have a high recurrence rate [19]. Fortunately, this common cause of vertigo can be treated effectively and straightforwardly. However, despite the high effectiveness of these maneuvers, a notable proportion of patients with BPPV, estimated to be approximately 12.5 % of positive diagnoses [20], do not experience symptom resolution with standard treatment. Even after receiving a confirmatory diagnosis and undergoing multiple maneuvers, the symptoms persisted. These patients consume significant healthcare resources, endure prolonged periods of incapacity, and impose a burden on their families. Thus, what initially appears to be a benign and easily treatable condition can evolve into persistent medical, familial, and occupational challenges without a straightforward solution.

1.1.4 Head impulse test

Among the wide variety of clinical tests used to assess vestibular function, the rotational test determines the vestibular response when the head is rotated, allowing for the examination of the VOR during movements similar to those experienced in daily life. Rotational tests were first described by Bárány at the beginning of the 20th century [21], and they remain widely used today, encompassing a variety of tests that diagnose vestibular function at different frequencies ranging from 0.01 to 6 Hz [22].

Currently, the head impulse test (HIT) is the preferred method for rotational testing because it presents several advantages over alternative tests for assessing vestibular function. Rapid head movements in the HIT allow for efficient evaluation of vestibular function without interference from other oculomotor control systems [23]. The availability of camera assistance during the test further enhances its utility, as it allows for precise recording and analysis of ocular movements that cannot be observed with the naked eye. Unlike some tests that may induce discomfort or motion sickness in patients, the HIT is generally well tolerated owing to its brief duration and simplicity, making it a valuable tool for the routine assessment of vestibular function [24].

Owing to the high velocities applied in this test and the specific orientation of these rotations, rotations are typically performed in the canal plane pairs shown in Figure 1.3b. This approach allows for the independent assessment of the function of each semicircular canal, thereby enabling the detection of dysfunction in specific canals. This is in contrast to other rotary tests that simultaneously study both membranous labyrinths.

1.1.5 Magnetic vestibular stimulation

Magnetic resonance imaging (MRI) is the cornerstone of modern clinical diagnostics, with the strength of the magnetic field being a critical determinant of signal clarity and image

resolution. However, the use of high-field MRI systems often leads to reports of dizziness and nystagmus in individuals near these devices, with symptoms worsening as the field strength increases [25, 26, 27].

This phenomenon and its connection to the vestibular system date back to the early 21st century, when nystagmus was observed in darkness inside MRI machines [28]. The underlying mechanism is only partially understood today; however, it has been established as a new method of activating the vestibular system, called magnetic vestibular stimulation (MVS). Prevailing theories suggest that the Lorentz force is responsible for this stimulus, generated by the interaction between the strong static magnetic field of the MRI machine and the ionic currents in the labyrinth, which flow from dark cell regions to hair cell regions to maintain the electrochemical potential balance between both inner ear fluids [29, 30, 31]. The Lorentz force, which is always constant, causes the cupulae to move to a specific position, producing a response equivalent to constant acceleration of the head, resulting in sustained nystagmus. Although the Lorentz effect increases with the strength of the magnetic field, it typically does not cause harmful effects in humans except for temporary dizziness and nausea.

MVS has significant implications for studies of vestibular physiology and adaptation, interpretation of functional MRI studies, and human safety during diagnostic imaging [32]. This technique has potential applications in the study and treatment of vestibular and other neurological disorders, although its development is still at an early stage and requires further exploration. Most clinical studies and theoretical validations have been and continue to be conducted at Johns Hopkins Hospital (Maryland, USA), where I had the opportunity to undertake my doctoral stay and learn about this novel field of research.

1.2 Mathematical background

As explained previously in this chapter, not all aspects of the physiology of the vestibular system can be entirely explained by its mechanics, as the behavior of the hair cells and afferents is sometimes more complex. However, several approximations can be made to describe a direct relationship between cupula displacement relative to the forces occurring in the inner ear and the final stimulus that generates the VOR. Since the displacement of the cupula depends solely on the macromechanical properties, the vestibular function can be studied through mathematical models based on physics, biology, and engineering fundamentals. Therefore, understanding the biophysics underlying the vestibular system elucidates its function and links neurological processes to macromechanical effects.

In this section, we delve into the biophysical principles governing the structure and function of the vestibular apparatus and explore how previous models were generated to explain vestibular function during rotations. Following that, a brief description of more modern mathematical methods and techniques is provided, discussing their potential benefits in studying vestibular function. This foundation enables a better understanding of the following chapter, where the methodology and underlying rationale for the numerical simulations are described.

1.2.1 Vestibular mathematical modeling

USC DE COMPOSTELA

Mathematical models of biological systems provide the ability to explain their functions in a quantitative manner, allowing for predictions that can be validated experimentally. Thus, researchers can investigate the effects of physiological or pathophysiological conditions without

the need for invasive procedures. These models typically start with the simplification of reality, aiming for more complexity and detail as experience and new resolution methods are developed. In the context of the vestibular system and its response to rotation, a common simplification is to consider an individual membranous semicircular canal as a closed, ideal, and rigid ring filled with endolymph.

To explain the behavior of a semicircular canal during eccentric rotations, consider an ideal horizontal semicircular canal rotating relative to its own plane, with angular acceleration in the counterclockwise direction, as shown in Figure 1.5. This canal is equivalent to the left horizontal semicircular canal presented in Figure 1.4, the entire mechanical process during rotation is now described. Initially, when the head is at rest, the endolymph within the semicircular canals remains stationary, exerting no force on the cupula. When the head rotates, the endolymph lags behind due to inertia, causing relative motion between the endolymph and cupula (t1). As a result, the cupula deflects in the opposite direction to the head movement until it reaches a final position where the frictional force between the endolymph and cupula balances the force exerted by the moving endolymph. At this point, a fully developed endolymph vortex with constant velocity is generated in the utricle (t2) [33, 34]. When angular deceleration occurs, the endolymph moves in the opposite direction, altering the vortex direction in the utricle and exerting a force on the cupula in the opposite direction (t3). Once the rotation ceases and the angular acceleration becomes zero, the endolymph continues to move due to inertia, gradually reducing its velocity, and the cupula returns to its resting position (t4).

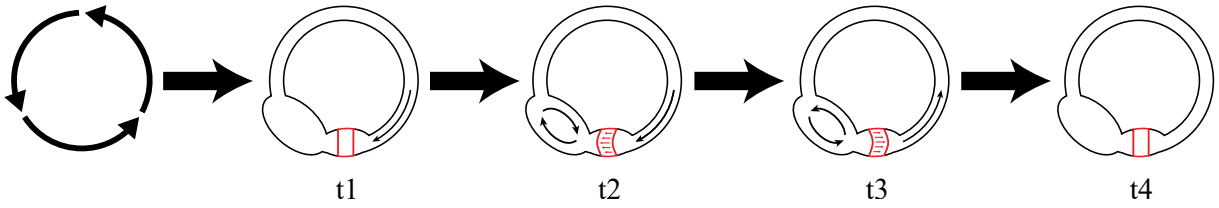

Figure 1.5: Schematic representation of the endolymph and cupula displacements during a counterclockwise rotation. The cupula (red) behaves like an overdamped pendulum, generating both excitatory and inhibitory signals depending on the acceleration or deceleration during the rotation. When the acceleration is zero, the cupula returns to its resting position.

The relative movement of the endolymph with respect to the semicircular canal walls converts the angular acceleration of the head into a proportional response in the velocity of the endolymph [35]. For this reason, the cupula, which is mechanically coupled with the endolymph, functions as a sensor for head rotation. Examining the example provided in Figure 1.4, the displacement of the initially resting cupula reveals oscillation in two directions: initially utriculipetal during acceleration (excitation) and then utriculifugal during deceleration (inhibition), before returning to its resting position. This behavior resembles that of a damped pendulum, similar to early mathematical models aimed at describing cupula displacements and the response of the semicircular canals to angular accelerations.

Understanding the function of semicircular canals dates back to 1933, when Steinhausen introduced the first mathematical model [5]. This model elucidates how the volumetric displacement $V(t)$ generated by the cupula obeys a second-order ordinary differential equation akin to that of a forced pendulum, assuming that the volumetric displacement of the cupula is proportional to the volumetric displacement of the endolymph [36]. As research progressed, efforts were made to refine this model by accounting for various factors. Subsequent

decades have witnessed advancements in determining the constants appearing in this model, incorporating an elastic model of the cupula, and leveraging the principles of fluid mechanics [37]. Later refinements considered the morphological intricacies of the canals and utricle [38], as well as the physical interaction within the endolymph and cupula [39] [11]. Despite these variations, the fundamental essence of these models remains rooted in an overdamped second-order differential equation with two characteristic time scales [40], given by

$$m\frac{\mathrm{d}^2V}{\mathrm{d}^2t}+r\frac{\mathrm{d}V}{\mathrm{d}t}+kV=F, \tag{1.1}$$

where m denotes the hydraulic mass of the endolymph in the semicircular canal, r denotes the hydraulic resistance of the semicircular canal, and k denotes the volumetric stiffness of the cupula. Based on this equation, the cupular displacement depends on these three parameters and the inertial forces generated during rotation, denoted here as F.

When solving Equation (1.1), two real eigenvalues are obtained because the hydraulic resistance is larger than the other parameters, indicating that the cupula behaves as an overdamped pendulum. These eigenvalues correspond to the lower-corner frequency f_L and upper-corner frequency f_U, which define the natural frequency range of the semicircular canals. The values of these corner frequencies can be determined using the time constants known as the cupula time constant τ_c and the viscosity time constant τ_v, which are inversely proportional to the eigenvalues, respectively defined as

$$f_L=\frac{1}{2\pi\tau_c}\approx\frac{k}{r}\quad\text{and}\quad f_U=\frac{1}{2\pi\tau_v}\approx\frac{r}{m}. \tag{1.2}$$

The cupula time constant τ_c represents the cupula relaxation time constant, indicating the time required for the cupula to return to its initial position after rotation, whereas the viscosity time constant τ_v represents the time necessary for the endolymph to come to a stop after rotation. These values depend on the parameters provided in Equation (1.1), which are affected by the physical properties and geometry of the vestibular system [12]. Experimental determination of these constants is challenging due to the variability between individuals, but estimates can be obtained based on the geometry and physical properties of the specific anatomy considered. For example, the values

$$\begin{aligned}\tau_c=2.9\text{ s}\quad&\rightarrow\quad f_L=0.055\text{ Hz}\\ \tau_v=0.005\text{ s}\quad&\rightarrow\quad f_U=31.8\text{ Hz},\end{aligned} \tag{1.3}$$

corresponds to the membranous labyrinth used in my research [9], providing insight into the natural frequency range for the semicircular canals of this specific anatomy. Because there are three semicircular canals, a system of three equations equivalent to Equation (1.1) is obtained, one for each cupula, resulting in a total of six time constants. The differences between them arise from the geometric characteristics of each canal and the elastic properties of their respective cupulae.

VOR can be characterized as a linear time-invariant (LTI) system that adheres to the principles of proportionality and superposition [41]. This implies that if the input exhibits a sinusoidal pattern, the output will also follow a sinusoidal pattern with the same frequency but differing amplitudes and phases. The amplitude and phase characteristics of the transfer function were illustrated using a Bode plot. This plot consists of two components: a gain diagram, which assesses whether there is attenuation or amplification in the system at different

frequencies, and a phase diagram, which indicates any phase difference between the input and output signals.

This mathematical property enables the examination of semicircular canal function behavior in the frequency domain, where the input signal is the angular acceleration of the head and the output signal is the cupula displacement. This is possible by applying the Laplace transform to the continuous-time function representing the volumetric displacement of the cupula, which allows the governing differential equation shown in Equation (1.1) to be transformed into an algebraic function. This transformation leads to a transfer function $H(s)$ [37], which relates the Laplace transform of the cupula volumetric displacement $\tilde{V}(s)$ to the Laplace transform of the angular velocity of the head $\tilde{\omega}(s)$ as

$$H(s) = \frac{\tilde{V}(s)}{\tilde{\omega}(s)} = \frac{-s}{(s+f_L)(s+f_U)} \quad \text{with} \quad s = i\omega. \tag{1.4}$$

Utilizing the frequency corners determined in Equation (1.2), the gain and phase diagram of the semicircular canal used for the numerical simulations can be represented, as shown in Figure 1.6. Within the frequency range bounded by the two corner frequencies ($f_L < f < f_U$), the viscosity of the endolymph flowing within the semicircular canals integrates the angular acceleration of the head, resulting in a cupular volume displacement proportional to the angular velocity of the head. Continuing with the assumption that the VOR functions as an LTI system, we can consider that eye movement is proportional to the head angular velocity. However, achieving this requires a combined transfer function that incorporates the relationship between the mechanical transfer function presented in Equation (1.4) and another representing the neurological pathways [41].

When operating at frequencies below the lower corner frequency ($f < f_L$), the influence of the endolymph viscosity becomes less significant, causing the semicircular canal to function more as an angular acceleration detector rather than a velocity sensor [40]. Additionally, at lower frequencies, hair cells become less sensitive to rotational stimuli, and a phenomenon known as mechanical adaptation arises [42]. Experimental measurements have shown that hair cells undergo movement to optimize stimulation effects and correct nonlinearities at low frequencies [43], complicating the establishment of a direct relationship between the VOR and biomechanics of semicircular canals during these types of rotations.

Above the upper corner frequency ($f > f_U$), the system experiences what is known as viscous blocking, where excessive shear stresses limit the velocity of the endolymph, breaking the correlation between the cupula displacement and the angular velocity of the head [44]. This phenomenon could also serve to separate the frequency domains between the vestibular and auditory systems, because higher-frequency sound waves do not affect the semicircular canal vestibular receptors [45].

However, this assumption, which considers the rigid walls of the membranous labyrinth, is valid only for low to middle frequencies. When frequency rotations of over 5 Hz are applied, the deformation of the walls in the semicircular canals becomes significant, affecting the displacement of the cupula owing to the effect of the perilymph [46]. This phenomenon leads to phase delays and damped resonance. While it is expected to enhance the high-frequency gain and extend the bandwidth owing to the shift of the high-corner frequency value, it also makes it more challenging to establish a direct correlation between the VOR and mechanical stimuli.

USC UNIVERSIDADE DE SANTIAGO DE COMPOSTELA

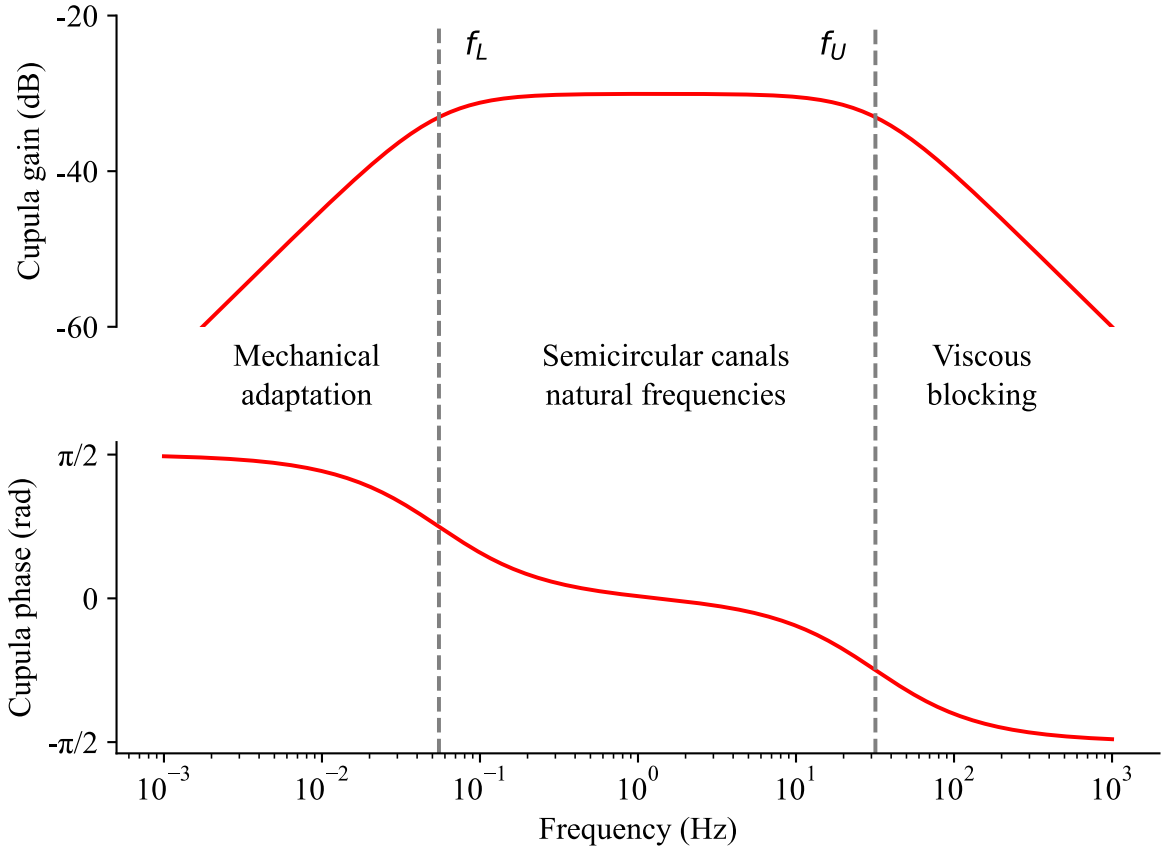

Figure 1.6: Bode plot showing the gain and phase diagrams of the cupula. The gain is in dB, and the phase is in radians relative to the frequency of the rotations measured in Hz using a logarithmic scale. The ranges for the semicircular canal natural frequencies, mechanical adaptation, and viscous blocking were defined based on the eigenvalues determined in Equation (1.3). The calculations of these frequency corners were based on the properties of the membranous labyrinth shown in Figure 1.1 [9], and implemented in the transfer function from Equation (1.4).

Returning to Equation (1.1), this seemingly simple equation provides a wealth of information regarding the function of the vestibular system. Various efforts have been made to solve this equation analytically. Notably, Obrist found an exact solution to this problem that could readily determine the volume displacement of the cupula in terms of the angular velocity of rotation [47]. However, as studies have delved into more complex geometries, including fluid flow in the entire membranous labyrinth, the limitations of considering independent semicircular canals have become more apparent [11]. Boselli et al. explained that endolymph vortices appear in different regions of the membranous labyrinth during rotation [33]. More recent models, such as those described by Goyens et al., suggest that the stimulation of the cupula is more complex due to asymmetries in the cupula walls caused by these vortices [34]. This introduces a more intricate behavior of the vestibular system that a simplified model, such as a toroid or ideal semicircular canal with its cupula modeled as a simple overdamped pendulum, could not accurately determine.

USC DE SANTIAGO DE COMPOSTELA

1.2.2 Numerical methods

In the preceding section, we have seen how the displacement of the cupula can be characterized by solving a second-order differential equation and how two characteristic time scales determine the frequency range over which semicircular canals respond appropriately. However, this analytical method has certain limitations that can be addressed using a different mathematical approach, known as numerical methods, used in the field of computational mechanics.

In the next chapter, the equations and methods employed for each developed mathematical model are described in detail. Prior to that, this section provides a brief overview of the theoretical and practical applications of these numerical methods. This will help identify important aspects to consider regarding numerical simulations and understand why certain decisions were made when designing the mathematical model.

Simplifying complex physical models while preserving the key features of the problem is fundamental for the efficient implementation of numerical methods. One important approach is the use of dimensionless numbers, which provide insight into the underlying physics governing the behavior of the system. They serve as a guide to identify the dominant mechanisms in the vestibular system and assess the validity of simplifying assumptions. In addition, defining the correct mathematical model requires the use of a set of equations that follow the fundamental laws that express conservation principles. For this purpose, the laws of conservation of mass, momentum, and energy must be preserved for both fluids and solids. Additionally, the fundamental laws that describe the electromagnetic behavior of a continuum are Maxwell's equations and the conservation of electric charge.

The principle of conservation of mass asserts that the overall mass of a closed system remains unchanged over time. This means that mass cannot be created or destroyed but can be rearranged in space or transformed into other forms of matter. The balance of mass through a control volume is expressed by

$$\frac{\partial \rho}{\partial t} + \nabla \cdot (\rho \mathbf{v}) = 0, \tag{1.5}$$

where ρ is the density, t is the time, ∇ is the vector differential operator, and $\mathbf{v}$ is the flow velocity field.

The conservation of momentum equation describes the motion of a fluid under the influence of various forces. The rate at which linear momentum changes over time is equal to the force acting on the continuum, represented by

$$\frac{\partial \rho \mathbf{v}}{\partial t} + (\mathbf{v} \cdot \nabla)\rho \mathbf{v} = \nabla \cdot \sigma + \mathbf{F}, \tag{1.6}$$

where $\mathbf{F}$ is the resultant volumetric force acting on the control volume, and σ is the stress tensor. In addition, the conservation of angular momentum requires the stress tensor to be symmetric,

$$\sigma = \sigma^T. \tag{1.7}$$

The conservation of energy equation is given by the first law of thermodynamics, which states that the rate of heat added plus the rate of work done on the system is equal to the total rate of change in the energy of the system. Mathematically, this can be expressed as

USC UNIVERSIDADE DE SANTIAGO DE COMPOSTELA

$$\frac{\partial(\rho E)}{\partial t} + \nabla \cdot (\rho E \mathbf{v}) = \nabla \cdot (\mathbf{v} \cdot \sigma) - \nabla \cdot \mathbf{q} + \mathbf{F} \cdot \mathbf{v} + S_E, \tag{1.8}$$

where E denotes the total energy per unit mass, $\mathbf{q}$ denotes the heat flux, and S_E denotes the energy source term per unit volume.

The behavior of fluid and solid continua in response to electromagnetic fields is described by Maxwell's equations, written as

$$\begin{aligned} \nabla \cdot \mathbf{E} &= \frac{\rho_q}{\varepsilon_0} \\ \nabla \cdot \mathbf{B} &= 0 \\ \nabla \times \mathbf{E} &= -\frac{\partial \mathbf{B}}{\partial t} \\ \nabla \times \mathbf{B} &= \mu_0 \left(\mathbf{J} + \varepsilon_0 \frac{\partial \mathbf{E}}{\partial t} \right) \end{aligned} \tag{1.9}$$

where ρ_q represents the electric charge density, ε_0 denotes the vacuum electric permittivity, μ_0 indicates the vacuum electric permeability, $\mathbf{E}$ denotes the electric field, $\mathbf{B}$ represents the magnetic flux density, and $\mathbf{J}$ stands for the electric current density.

Finally, the conservation of charge within a control volume is governed by the continuity equation, defined as

$$\nabla \cdot \mathbf{J} + \frac{\partial \rho_q}{\partial t} = 0. \tag{1.10}$$

All the equations utilized for the fluid, solid, and electromagnetic regions necessary for this research stem from these conservation laws. For example, the Navier-Stokes equations used for modeling the endolymphatic fluid can be derived from the principle of conservation of momentum shown in Equation (1.6). However, additional equations must be incorporated to ensure that the number of unknown quantities aligns with the number of equations. This depends on the variables we are interested in measuring. Alongside the boundary and initial conditions, which serve as inputs to the model, all of these features are crucial for solving the equations correctly and obtaining realistic results.

Once all these equations are defined, their discretization in space and time converts a continuous system of equations into discrete algebraic equations that can be solved using numerical techniques. One of the most widely employed numerical methods for solving fluid dynamics problems is the finite volume method (FVM). The FVM discretizes the computational domain into a finite number of control volumes, where the conservation equations governing the fluid flow are integrated over each control volume. Another significant numerical method is the finite element method (FEM), which is commonly used to calculate deformations, pressures, and stresses on solids. The coupling of these two methods is known as fluid-structure interaction (FSI) solvers, which enable the calculation of the bidirectional interaction between solids and fluids.

However, defining the equations correctly is not sufficient to ensure reliable predictions of real phenomena, and a detailed geometric model is also essential. The selection of three-dimensional models based on medical images, also known as digital twins, serves this aim. Nevertheless, as we aim to achieve higher precision, obtaining appropriate models becomes more challenging. The geometry used for the FVM and FEM discretizes the domain into

USC DE SANTIAGO

small cells, collectively forming a mesh. The quality of this mesh is essential for faithfully reproducing the geometry and ensuring that the model equations are appropriately solved. The density and quality of the mesh directly influence the computational resources required for the simulation. Although a finer mesh may offer increased accuracy, it also increases the number of equations to be solved, thereby necessitating a higher computational demand. A high-quality mesh optimally distributes elements, refining the mesh where necessary to capture important phenomena while keeping the overall number of elements manageable. In this regard, a strong effort was made to obtain an efficient mesh that balances the computational cost with the necessary accuracy for modeling the vestibular function, especially when implementing the FSI model. Modeling the interaction between the endolymph and cupulae is particularly sensitive and requires careful evaluation.

Additionally, evaluating vestibular stimulation over time or the displacement of the otoconia during the EM requires defining the problems as nonstationary. Here, the time interval is discretized into subintervals defined by time steps, and each time step is further divided into inner iterations, where the equations are solved. The aim of this discretization is to determine the correct value of the parameter of interest before moving to the next time step. This is crucial because the previous value serves as an input for the next time step, making its correct determination essential to avoid generating accumulated errors, known as residuals and numerical instabilities. Convergence, a fundamental concept in numerical methods, refers to the property of solutions to approach an exact solution. To ensure the convergence and stability of the solution, a specific time step is required for a mesh with a certain cell size. Normally, this is achieved by ensuring that the Courant–Friedrichs–Lewy (CFL) number,

$$\mathrm{CFL} = \frac{U\Delta t}{\Delta x}, \tag{1.11}$$

was lower than one throughout the entire computational domain. Where U represents the velocity within the specific cell, Δt is the time step used in the simulation, and Δx denotes the size of the cell.

One way to improve outcomes and facilitate the implementation of numerical methods is to use commercial software packages. These software packages offer a comprehensive suite of solvers and methods that have been rigorously validated and optimized. This provides robust and reliable solutions, alleviating the need for researchers to validate their own numerical methods and allowing them to focus on interpreting their results. In addition to the advantages of commercial software, the use of supercomputers significantly enhances the computational capabilities and performance of numerical simulations. Equipped with massive parallel processing capabilities and high-speed interconnects, supercomputers empower engineers and researchers to perform large-scale computationally intensive simulations, which are impractical for personal computers.

In the context of the vestibular system, the application of these numerical methods did not gain traction until this century, when high-performance computers became more prevalent in research. These advancements have enabled a broader set of simulations and facilitated the exploration of more complex studies using commercial software [34, 48, 49]. This technique allows the investigation of physical parameters closely related to those observed experimentally [50] and provides an innovative perspective for understanding different vestibular pathologies, such as the Tullio phenomenon [51] or Ménière's disease [52, 53]. These studies, among many others, underscore the significant potential of numerical simulations for understanding

USC DE COMPOSTELA

the physiology and pathophysiology of the vestibular system, opening up a field of research with previously untapped possibilities.

From the perspective of this research, these FSI models enable a comprehensive analysis of the behavior of the endolymphatic fluid using the Navier-Stokes equations and the equation of motion of an elastic solid that describes the behavior of the cupula. In addition to these FVM and FEM models, other methods allow the simulation of Lagrangian particles in the vestibular system to represent otoconia in BPPV and a magnetohydrodynamic (MHD) model for the study of MVS. To deploy this complex mix of methods and ensure appropriate results, one of the most widely used commercial software was utilized, Simcenter STAR CCM+ from Siemens (www.sw.siemens.com). Also, due to the high computational effort required to solve these methods in a coupled manner, numerical simulations were run on the supercomputer provided by the Galicia Supercomputing Center (CESGA) (www.cesga.es). Without the use of these tools, tackling complex simulations of the vestibular system would be computationally prohibitive.

Finally, validation is critical for ensuring that the simulation results are trustworthy and credible. Validation involves comparing the simulation results with experimental data or analytical solutions to assess the accuracy and reliability of the numerical model. From this perspective, the mathematical model used for the vestibular system has been compared with previous mathematical definitions in the literature, as well as with clinical data collected specifically during my years as a doctoral student.

Having laid out the anatomical and physiological foundations of the vestibular system as well as the clinical aspects of different vestibular conditions, this chapter also explains the use of numerical methods and how they could be an enhanced tool compared to previous mathematical descriptions that explain vestibular system behavior. By integrating these clinical and theoretical insights, a comprehensive framework for understanding and replicating vestibular functions can be elucidated. We are now ready to immerse in the subsequent chapter, which delves into the methodology employed for designing the numerical simulations directly supported by this background to answer the aim of this thesis: whether the use of these advanced numerical methods can increase our knowledge of the vestibular function and open the way to the future of personalized medicine for vestibular diseases.

USC UNIVERSIDADE DE SANTIAGO DE COMPOSTELA

Chapter 2

Methodology

Part of the text and figures for this chapter are reproduced from the following publications

(I) Arán-Tapia, I.[1,2,3], Soto-Varela, A.[4], Pérez-Muñuzuri, V.[1,3], Santos-Pérez, S.[4], Arán, I.[5], Muñuzuri, A. P.[1,2]. Numerical Simulations of the Epley Maneuver With Clinical Implications.*Ear & Hearing* **45**(4):1033-1044, July/August (2024). ISSN: 0196-0202. DOI: www.doi.org/10.1097/AUD.0000000000001493.

(II) Arán-Tapia, I.[1,2,3], Soto-Varela, A.[4], Pérez-Muñuzuri, V.[1,3], Santos-Pérez, S.[4], Arán, I.[5], Muñuzuri, A. P.[1,2]. Numerical simulations to determine the stimulation of the crista ampullaris during the Head Impulse Test. *Comput Biol Med.* **163**, 107225 (2023). ISSN: 0010-4825. DOI: https://doi.org/10.1016/j.compbiomed.2023.107225.

(III) Arán-Tapia, I.[1,2,3], Pérez-Muñuzuri, V.[1,3], Muñuzuri, A. P.[1,2], Soto-Varela, A.[4], Otero-Millan, J.[6,7], Roberts, D. C.[7], Ward, B. K[8]. The Biophysics of Magnetic Vestibular Stimulation: Clinical Insights from High-Field MRI. Under review in *Communications Medicine* (2024). ISSN: 2730-664X.

[1]Group of Nonlinear Physics, University of Santiago de Compostela, Spain
[2]Galician Center for Mathematical Research and Technology (CITMAga), Spain
[3]Cross-disciplinary Research in Environmental Technologies (CRETUS), Spain
[4]Department of Otorhinolaryngology, Hospital of Santiago de Compostela, Spain
[5]Department of Otorhinolaryngology, Hospital of Pontevedra, Spain
[6]Herbert Wertheim School of Optometry and Vision Science, University of California, USA
[7]Department of Neurology, Johns Hopkins University, USA
[8]Department of Otolaryngology-Head and Neck Surgery, Johns Hopkins University, USA

After exploring the context and aim of this research, the first chapter provided the necessary background to understand the concepts and terminology used throughout this thesis. Navigating through this information is essential for interpreting the following chapter, where the methodology employed to address the main hypothesis of the dissertation is explained. This includes defining the computational geometry and mesh, and identifying the most important dimensionless numbers, equations, boundary conditions, and other definitions necessary for the correct formulation of the mathematical models. Some sections of this chapter combine information about the three designed mathematical models because certain conditions implemented in the software are similar. Other sections are split into independent subsections

for each type of modeling, as there are significant differences that I consider necessary to mention separately for easier understanding.

Therefore, the aim of this chapter is to present all methodological processes for the different situations introduced in sections 1.1.3 Epley maneuver, 1.1.4 Head impulse test, and 1.1.5 Magnetic vestibular stimulation. This information serves as the groundwork for understanding the following chapters, in which the results, discussion, and conclusions of this thesis are described.

2.1 Computational geometry

The first step in conducting numerical simulations is to obtain a computational domain in which mathematical models can be implemented. Original dataset of the complete membranous labyrinth anatomy was obtained from the open-source Ariadne Toolbox software (www.earbank.org/ariadne.php), which offers inner ear data for different species [9]. In this case, a 3D reconstruction of the human left membranous labyrinth was selected. It was derived from a postmortem human specimen captured using high-resolution micro-computed tomography (μCT), enabling the precise definition of membranous labyrinth volumes and surfaces. The complete model is shown in Figure 1.1.

The portion of the membranous labyrinth consisting of the cochlea and saccule was excluded, simplifying the geometric model to focus on the utricle and three interconnected semicircular canals. To make these modifications, it was necessary to use various open-source software tools that enabled segmentation of the required parts, editing of the walls, and preparation of the model for appropriate importation into the Simcenter STAR CCM+ software. Some of these software tools are FreeCAD, Blender, MeshLab, and Meshmixer.

While the same membranous labyrinth anatomy was used throughout the entire research, there are variations in the regions considered depending on the mathematical model under study, as well as in the boundary regions. The reason for this is that unnecessary regions have a computational cost that is optimal to reduce in order to perform numerical simulations more efficiently.

Consequently, it is necessary to provide a more detailed description of the geometry, depending on the context in which it is utilized. A representation of these differences between the geometries used is shown in Figure 2.1, ordered by increasing complexity. The geometrical model for the Epley maneuver (EM) corresponds to the simplest model. Only the fluid region was considered, and the cupulae regions were discarded. This is because, for EM, we are interested in knowing the path of otoconia during the maneuver and not the stimuli they can cause. In addition to the fluid region, the geometry model for the head impulse test (HIT) includes the cupulae, color-coded depending on the semicircular canal considered. Finally, the most complex model designed is the geometry for the magnetic vestibular stimulation (MVS), which adds regions for the endolymph and cupulae, as well as the hair cell and dark cell surface regions corresponding to those observed in animals and humans [54, 55].

A symmetric geometry representing the right membranous labyrinth was designed and placed at an equivalent position using the sagittal plane as a reference. This permitted the analysis of vestibular stimulation generated during the HIT and MVS, which is composed of combined stimuli from the six cristae ampullares. Both labyrinths were located 40 mm away from the center of the head, as shown in Figure 2.2. The head position shown in this figure corresponds to the orientation of the head and labyrinth for the HIT study, with a 20° nose-down

USC DE COMPOSTELA

tilt to align the horizontal semicircular canals (LHRH plane) with the axial plane. See Figure 1.3.

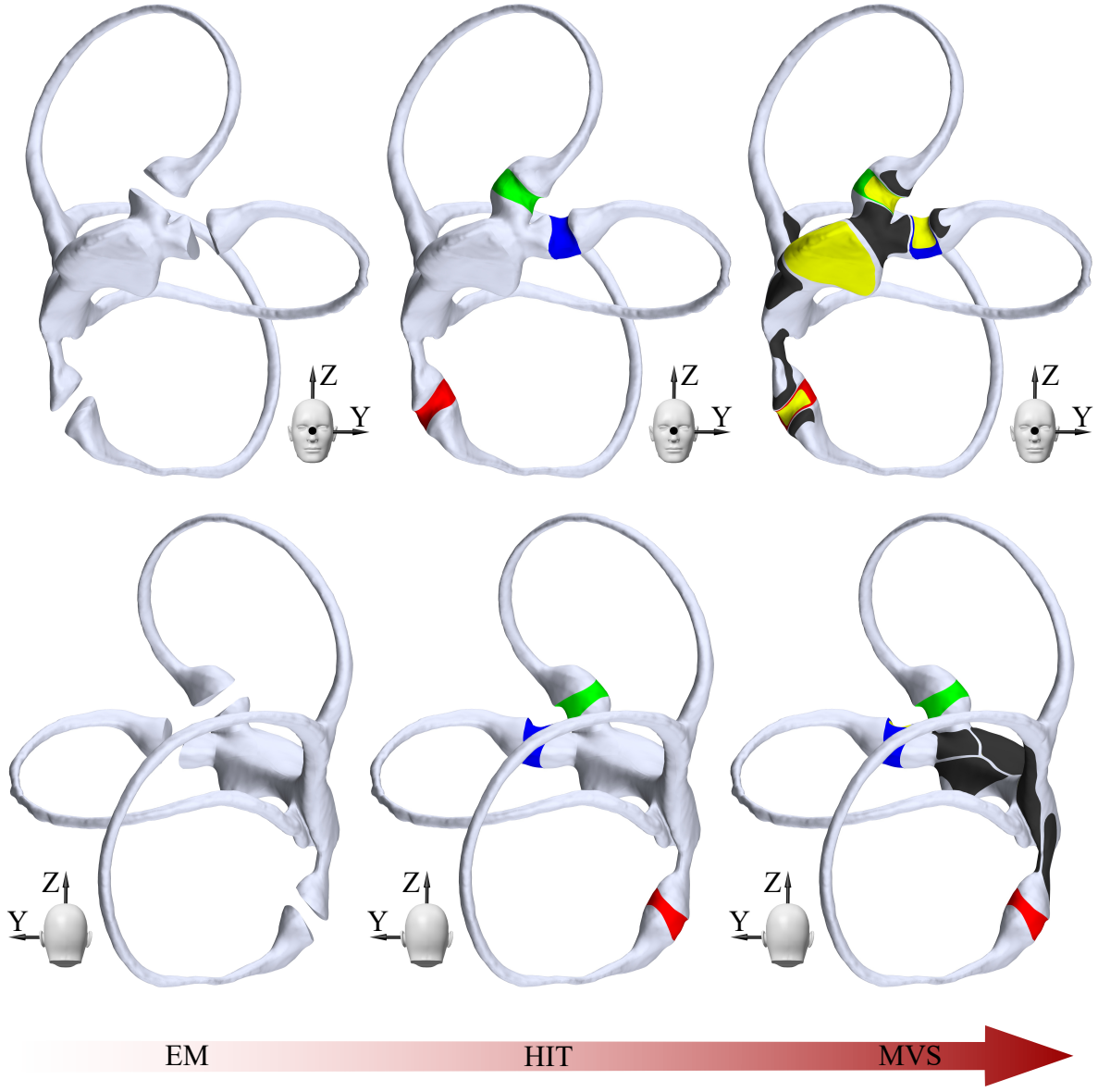

Figure 2.1: Human left membranous labyrinth anatomy model used for the numerical simulations. From left to right, the modeled regions for each study are presented in the order of increasing complexity. The geometry of the Epley maneuver (EM) only considers the endolymphatic region. The head impulse test (HIT) geometry includes the cupulae regions, colored blue for the horizontal cupula, green for the superior cupula, and red for the posterior cupula. In addition to the fluid and solid regions, the magnetic vestibular stimulation (MVS) geometry includes hair cell regions in yellow and dark cell regions in black. The orientation corresponds to the supine position of the head, with the upper row showing the front view perspective and the bottom row showing the back view.

USC
UNIVERSIDADE DE SANTIAGO DE COMPOSTELA

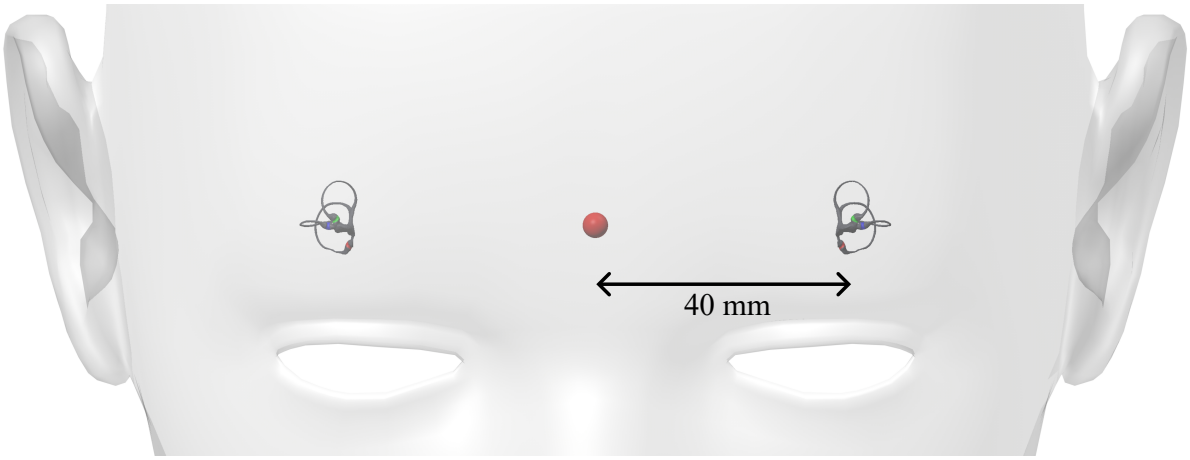

Figure 2.2: Location and orientation of both membranous labyrinths with respect to the head. Both geometries are located 40 mm away from the center of the head (red dot) and are mirrored with respect to the sagittal plane.

2.2 Meshing

After preparing the appropriate geometry, the corresponding membranous labyrinth was imported into the Simcenter STAR CCM+ software, and the different regions were characterized. This allowed the meshing study to begin with the aim of obtaining an optimal mesh that differs depending on the considered mathematical model. A thorough investigation was conducted with more than one hundred different meshes to achieve a high-quality mesh for the fluid, solid, and electromagnetic regions. As mentioned in the introduction section 1.2.2 Numerical methods, this process is fundamental for determining the simulation results in terms of accuracy, stability, and efficiency.

The final mesh was reevaluated during different software updates to ensure that satisfactory mesh quality and independence were achieved. The following sections outline the most important tools and parameters used to define the mesh and evaluate the conditions for each region separately. Both the left and right membranous labyrinths were meshed using the same criteria and simulated in independent files.

2.2.1 Fluid region

The fluid region encompassing the endolymph was utilized in all the studies, as shown in Figure 2.1. However, the mesh must be adapted to different necessities depending on the problem we want to solve, resulting in variations in the mesh size and properties depending on each study. Nevertheless, the fundamental definition of the mesh was similar in all cases.

The selected mesh type was a polyhedral mesh known for its adaptability to fluid media and its ability to combine the strengths of other mesh types while mitigating some of their weaknesses. Previous numerical studies [34, 48, 50] have also deemed a polyhedral mesh optimal for vestibular system modeling, thus enhancing support compared with other available mesh types in the software.

Furthermore, the surface remesher option available in the Simcenter STAR CCM+ software was chosen to enhance the mesh adaptability with the membranous labyrinth geometry [56]. Integrating this tool results in the geometry being reconstructed during the meshing process,

ensuring higher-quality cells near the boundaries. This option was deactivated for walls facing the cupulae to preserve their original shape.

Two cell prism layers were defined as optimal to accurately capture the flow behavior near the walls, generating a more gradual change in the cell volume when approaching the walls without unnecessarily increasing the total number of cells. An example of the final mesh shape in the horizontal semicircular canal is shown in Figure 2.3.

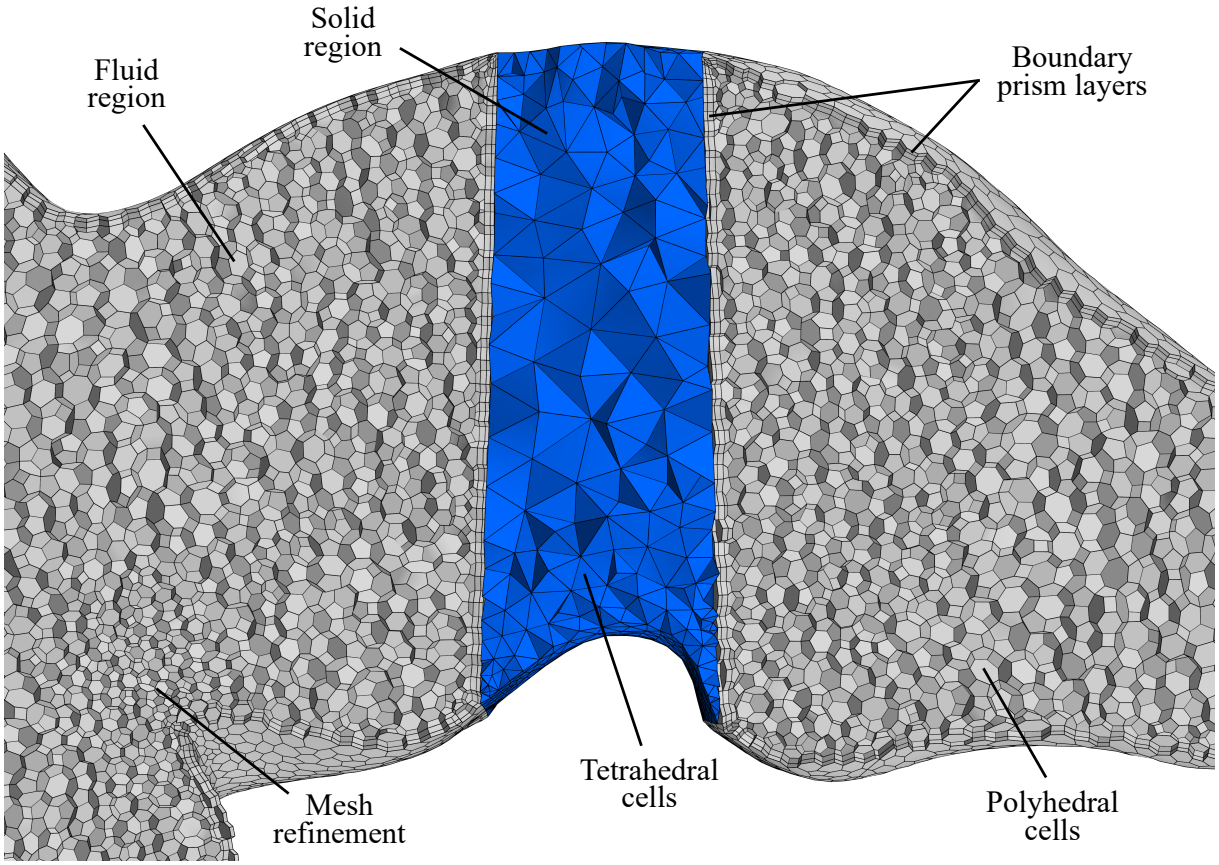

Figure 2.3: Visualization of the final mesh in the horizontal ampullary region for the head impulse test (HIT) and magnetic vestibular stimulation (MVS) models. Polyhedral cells surrounded by prism layer cells at the boundaries can be observed in the fluid region (gray). Mesh refinement with a higher cell density was observed at the entrance of the utricle. Tetrahedral cells form a mesh in the solid region of the horizontal cupula (blue). The cells that are in contact between the fluid and solid region generate the mapped interface where the fluid-structure interaction (FSI) solver exchanges information between the two regions.

Finally, Simcenter STAR CCM+ is renowned for its numerous options and capabilities for generating accurate meshes. Applying the maximum possible values for optimizing the meshing process, along with the boundary optimization option, enhances the quality of the final mesh despite the increasing meshing time. Additionally, it is possible to define different mesh sizes for specific regions, allowing for a denser mesh in areas with smaller diameters, such as the semicircular canals, and a coarser mesh in wider regions, such as the utricle. This significantly optimizes the mesh definition, thereby reducing the total number of cells without a loss of accuracy.

A total of five different mesh refinements were implemented, each evaluated individually

to ensure correct definition depending on the type of study. It is important to mention that cell mesh refinement for the EM study was necessary to achieve a higher accuracy of the geometry boundaries. This approach prevented solution instabilities and reduced the risk of otoconia disappearance; however, it significantly increased the number of cells compared to those used in the HIT and MVS studies.

In addition to the intensity of the mesh refinement and the number of prism layers, various mesh parameters were assessed, with the most significant being the cell skewness angle, neighborhood cell volume change, and cell quality [57]. Cells with very high aspect ratios, excessive skewness, or nonorthogonality can lead to numerical instabilities, which may result in a simulation failing to converge or producing erroneous results. After this in-depth analysis, the meshing process was concluded by determining that mesh independence was adequately achieved for all the final meshes used for the fluid regions. Table 2.1 lists the final number of cells depending on the study. A larger number of cells did not yield any significant differences in the otoconium path in the EM study, and the same was true for endolymphatic velocities in the HIT and MVS studies (error <1 %).

Table 2.1: Number of cells in the final meshes selected after the mesh independence analysis. The meshes were divided by region and study case: Epley maneuver (EM), head impulse test (HIT), and magnetic vestibular stimulation (MVS).

Study	Fluid (cells)	Solid (cells)	Electric (cells)	Total (cells)
EM	351716	-	-	351716
HIT	272209	53911	-	326120
MVS	275621	51818	216970	544409

Finally, to verify the convergence and stability of the solution, a specific time step is required for the mesh with a certain cell size, ensuring that the Courant–Friedrichs–Lewy (CFL) number defined in Equation (1.11) is smaller than one. Several variations of the limits for the number of iterations and residuals were investigated to determine the optimal time step that would significantly reduce the total time needed for running the simulations. For this reason, the time step that satisfied this criterion differed depending on the study requirements, as shown in Table 2.2. For the MVS study, a larger time step was optimal compared to that determined for the HIT and EM studies because of the lower endolymphatic velocities involved.

Table 2.2: Time steps that accomplish the Courant–Friedrichs–Lewy (CFL) number during the simulations for each study: Epley maneuver (EM), head impulse test (HIT), and magnetic vestibular stimulation (MVS).

Study	Time step (s)
EM	0.001
HIT	0.0005
MVS	0.002

USC UNIVERSIDADE DE SANTIAGO DE COMPOSTELA

2.2.2 Solid region

Because Simcenter STAR-CCM+ primarily focuses on fluid dynamics, the tools for meshing solids are more limited, and a mesh study could not be performed as thoroughly as for the fluid region. Similar to the polyhedral mesh in fluids, a tetrahedral mesh is typically employed to mesh solid regions, aligning with those selected in other mathematical model studies of the vestibular system that include cupulae [34, 48, 50].

An important consideration for the cupula is that some of the walls are in contact with the fluid region. Because the cells forming the interface between the fluid and solid meshes are distinct, nonconformal mapped interfaces are generated at the boundaries between both regions to facilitate data exchange at each inner iteration. In addition, the morpher mesh model included in the software package allows the fluid and solid regions to move with small deformations without the necessity of remeshing the regions at each time step. For this reason, prism layers on the boundaries of the solid regions were not used, and the size of the cells was significantly greater than those in the fluid region to avoid cell overlap during morphing, as shown in Figure 2.3.

The geometrical properties of the proposed meshes were determined by varying several mesh parameters, ensuring that the mesh elements were optimal, and following an optimization protocol similar to that for the fluid region. Subsequently, a mesh independence analysis was performed to determine the optimal configuration for the solid regions used in the HIT and MVS studies. The total number of cells are listed in Table 2.1. This final mesh was determined by comparing the shear strain XY, a parameter that will be described in more detail later in section 2.8 Measurement of the vestibular stimulation. The change in the shear strain XY for the left cristae ampullares was determined during HIT rotations with respect to the Z-axis, with an error of less than <1 %. The same meshing criteria were used for the MVS model.

The time step used for the HIT and MVS models in Table 2.2 ensures that the solid domain is correctly solved, and the information is effectively transferred between the fluid and solid regions at each iteration. This means that these simulations require much higher computational effort than those used for the EM model. Nevertheless, owing to the optimization of the mesh and time step, the total simulation time for the HIT model was reduced from several days to approximately 16 h. This was achieved by running on a supercomputer from the Galicia Supercomputing Center (CESGA) equipped with Intel Xeon Ice Lake 8352Y processors. In the case of the MVS model, a larger time step is selected, but the simulations take much longer because it is necessary to simulate for more seconds than those employed for rotations. Consequently, simulations can be run for weeks using the same supercomputer. On the other hand, simulations for the EM are faster, depending on the step of the maneuver studied, but usually vary between 2 and 4 h.

2.2.3 Electromagnetic region

For the MVS case, special treatment of the interfaces is necessary. As described in the previous section, the interfaces were modeled as nonconformal, meaning that the polyhedral and tetrahedral cell faces did not coincide at the interfaces. This resulted in an approximation of the final value averaged by the centroids of the cells in contact. However, calculating the electric potential in the domain is not possible when nonconformal cells are generating the interfaces. Therefore, it was necessary to replicate the geometry with both fluid and solid regions using a polyhedral mesh without defining the boundaries between them. This continuity in the mesh

domain enables the calculation of electromagnetic properties throughout the entire membranous labyrinth.

Similar to the mapped interfaces, data regarding the electromagnetic properties were mapped to the entire geometry, allowing this information to be later transferred to the cells defined for the fluid and solid regions. This requires duplicating the membranous labyrinth to share data at each iteration or time step, which is not an optimal solution. After contacting Simcenter STAR CCM+ developers, they could not provide another possibility. However, after making them aware of this necessity, they updated the software and corrected these limitations, possibly making it easier now to run the numerical simulation without the need to duplicate the geometry.

These data mappers were cautiously studied to evaluate the variables transferable bidirectionally and to determine whether transferring would be optimal at each iteration or time step. Fortunately, under static magnetic field conditions and constant current flow in the domain, the induced magnetohydrodynamic (MHD) forces are very small. Therefore, the electromagnetic model only needs to be run at the first time step of the numerical simulation to capture the static MHD effect of the Lorentz force. This is detailed in the subsequent sections related to the MVS problem. After this first time step, only the fluid-structure interaction (FSI) solver was employed, similar to the HIT model, but accounting for the constant mapped Lorentz forces throughout the simulation. The number of cells in the final mesh used for the duplicated membranous labyrinth is listed in Table 2.1.

2.3 Dimensionless numbers

Dimensionless numbers serve to delineate the range of physics of solids and fluids, enabling the selection of a model that accurately represents real conditions. These dimensionless numbers illustrate the ratios of different forces, thereby enabling the evaluation and prediction of fluid or solid behavior across different systems and scales. The calculation of these numbers is based on the approximate values in the equations that determine which force is dominant and at which scale. The dimensionless number can vary depending on the problem to be solved. Therefore, important dimensionless numbers for each case study are introduced in independent sections.

2.3.1 Epley maneuver

Two dimensionless numbers are critical for analyzing the behavior of the endolymph in a viscous Stokes flow, which is typically imposed in the low-mid frequency range for the considered angular rotations for the EM [58]. The first dimensionless number is the Reynolds number [59], which measures the ratio of viscous terms to inertial terms,

$$Re = \frac{\rho_e D v_e}{\mu_e} \approx 10^{-2}, \tag{2.1}$$

where ρ_e denotes the density of the endolymph ($\sim 10^3$ kg/m^3), D represents the characteristic diameter of the semicircular canal ($\sim 10^{-4}$ m), v_e is the maximum velocity of the endolymph for the EM ($\sim 10^{-4}$ m/s), and μ_e is the endolymph dynamic viscosity ($\sim 10^{-3}$ Pa.s). The Reynolds number is small, indicating that the nonlinear convective terms are negligible, which justifies

USC DE COMPOSTELA

the absence of turbulence.

The second number is the Womersley number [44], which represents the relationship between the frequency of a pulsating flow and the viscous effects,

$$Wo = \sqrt{\frac{\rho_e \omega D^2}{\mu_e}} \approx 10^{-1}, \tag{2.2}$$

where $\omega = 2\pi f$, with f representing the frequency of head rotation during the EM ($f \sim 10^{-1}$ Hz). A Womersley number smaller than 2π indicates that the inertial instability terms are not relevant, and viscous friction does not significantly change the endolymph movement, allowing for endolymphatic Poiseuille flow inside the semicircular canals.

In contrast, three dimensionless numbers are crucial for analyzing the behavior of otoconia within the endolymphatic fluid. The particle Reynolds number,

$$Re_p = \frac{\rho_e d_o |v_e - v_o|}{\mu_e} \approx 10^{-3}, \tag{2.3}$$

where d_o represents the characteristic diameter of the otoconium ($\sim 10^{-5}$ m) and v_o is the velocity of the otoconium ($\sim 10^{-4}$ m/s). The particle Reynolds number is even smaller than the endolymphatic Reynolds number, which makes the viscous forces associated with otoconia motion more dominant [60].

The Froude number serves to relate the inertial forces to the gravity forces acting on the system [47],

$$Fr = \sqrt{\frac{C}{\rho_e g \tau_v^4 \left(1 - \frac{\rho_e}{\rho_o}\right)}}, \approx 1 - 10 \tag{2.4}$$

where g represents the gravitational acceleration ($\sim 10\,\mathrm{m/s^2}$), τ_v is the viscous time scale ($\sim 10^{-2}$ s), and ρ_o is the density of otoconia ($\sim 10^{-2}\,\mathrm{kg/m^3}$). Considering C as the distance to the origin of rotation (head center $\sim 10^{-2}$ m and hip center ~ 1 m), we obtain two Froude numbers. For rotations relative to the head center, the Froude number is approximately equal to one, indicating that both inertial and gravity forces are equally important. However, for rotations relative to the hip center, the Froude number increases by an order of magnitude, indicating that inertial forces become dominant during rotation. When rotation is not applied, gravitational forces become dominant on the otoconia path. It is important to note that gravity is not relevant for the displacement of the endolymphatic fluid because it is completely confined within the membranous labyrinth walls.

Finally, the Stokes number is defined based on the relationship between the time scales for the slow particle mode and the cupula mode, given that the classical definition of the Stokes number is not useful for canalithiasis [47],

$$St = \frac{9\pi K D^4}{64 g \beta d_o^2 (\rho_o - \rho_e)} \approx 10^{-1} - 10, \tag{2.5}$$

where K represents the stiffness of the cupula ($\sim 10^{10}\,\mathrm{Pa/m^3}$) and β is the angle spanned by the posterior semicircular canal ($\sim 1.4\pi$ rad). Because this dimensionless number is highly sensitive to the size of the otoconia, two characteristic diameters of the otoconium d_o were selected (for large otoconia, $\sim 10^{-5}$ m and $\sim 10^{-6}$ m for small otoconia). For larger otoconia,

the Stokes number is lower than one, which means that the slow particle mode is dominant, and the velocities of the endolymph and otoconia point in opposite directions. For smaller otoconia, the Stokes number is greater than one, and the cupula mode becomes dominant, causing the velocities of the otoconia and endolymph to move in the same direction.

2.3.2 Head impulse test

In the case of the HIT, owing to the lack of otoconia, only the Reynolds number and Womersley number are important dimensionless numbers for analyzing the behavior of the endolymph. In this case, the maximum velocities v_e are much higher due to fast rotations needed for this test ($\sim 10^{-1}$ m/s), what serves to estimate the largest possible Reynolds number for the entire fluid region,

$$Re = \frac{\rho_e D v_e}{\mu_e} \approx 10. \tag{2.6}$$

Even in this disadvantageous extreme situation, the maximum Reynolds number is small, making the nonlinear convective terms insignificant, and justifying the lack of turbulence in the entire membranous labyrinth.

Similarly, the frequency of head rotation during the HIT ($f \sim 5$ Hz) results in a Womersley number,

$$Wo = \sqrt{\frac{\rho_e \omega D^2}{\mu_e}} \approx 1, \tag{2.7}$$

of the order of unity, which is also not sufficient to generate a change in viscous friction.

2.3.3 Magnetic vestibular stimulation

In the study of the MVS, the magnetic Reynolds number is a vital dimensionless parameter that gauges the significance of a magnetic field in a moving conductive fluid,

$$Re_m = \sigma_e \mu_0 v_e D \approx 10^{-14}. \tag{2.8}$$

In this equation, σ_e represents the conductivity of the endolymph ($\sim 1\,\mathrm{kg/m^3}$), which is assumed to be comparable to the conductivity of the cupulae σ_c. The constant μ_0 is the vacuum electric permeability ($\sim 10^{-6}\,\mathrm{kg/m^3}$), and v_e denotes the characteristic velocity of the endolymph fluid movement owing to the magnetic resonance imaging (MRI) magnetic fields ($\sim 10^{-4}$ m/s). The small magnetic Reynolds number suggests that the MHD forces generated by fluid movement within the inner ear are minor compared to the magnetic fields typically used in MRI machines. Consequently, the Lorentz force is the principal magnetic force that influences the motion of the endolymph and cupulae. This assumption simplifies the mathematical representation of the MVS, as explained in the next section.

2.4 Equations

USC UNIVERSIDADE DE SANTIAGO DE COMPOSTELA

This section presents the mathematical equations that form the foundation of the numerical models used during this research. These equations were solved in each cell of the mesh of the

previously defined computational domain, and their selection was based on the dimensionless number study explained in the previous section. The equations were defined in a specific order to highlight the increasing complexity of the model to meet the different needs of the studies.

Initially, the mathematical formulations that dictate the behavior of the endolymphatic fluid and otoconia in the context of the EM are introduced. Subsequently, equations that portray the dynamic response of the cupula during HIT were incorporated, disregarding the influence of otoconia. Ultimately, equations that delineate the interaction between the electromagnetic fields and vestibular variables responsible for the MVS are presented, together with the equations for the endolymph and cupula described previously.

By detailing these equations, the aim is to provide a comprehensive understanding of the theoretical framework underpinning the simulations and explain how the software solves them for each specific case.

2.4.1 Epley maneuver

The EM study can be considered the simplest set of equations, with some describing the movement of otoconia during benign paroxysmal positional vertigo (BPPV) and others detailing endolymphatic dynamics during rotations.

Regarding the first set, several forces determine the movement of otoconia during the EM. First, the inertial terms resulting from the rotation of the head or body, the Coriolis ($\mathbf{F}_o^{co}$), centrifugal ($\mathbf{F}_o^{c}$), and Euler ($\mathbf{F}_o^{e}$) volumetric forces are given by

$$\begin{aligned} \mathbf{F}_o^{co} &= -2\rho_o(\boldsymbol{\omega}\times\mathbf{v}_o) \\ \mathbf{F}_o^{c} &= -\rho_o\boldsymbol{\omega}\times(\boldsymbol{\omega}\times\mathbf{r}_o) \\ \mathbf{F}_o^{e} &= -\rho_o\frac{\partial\boldsymbol{\omega}}{\partial t}\times\mathbf{r}_o, \end{aligned} \tag{2.9}$$

where $\mathbf{r}_o$ is the position vector of the otoconia with respect to the head or body origin of rotation, and $\boldsymbol{\omega}$ is the angular velocity vector of the rotating reference frame.

The volumetric drag force exerted by otoconia ($\mathbf{F}_d$),

$$\mathbf{F}_d = \frac{3}{4}\frac{C_d}{d_o}\rho_e|\mathbf{v}_e-\mathbf{v}_o|(\mathbf{v}_e-\mathbf{v}_o), \tag{2.10}$$

which employs the Schiller-Naumann correlation (Schiller, 1933) for small particle Reynolds numbers, as shown in Equation (2.3). This allows to approximate the drag coefficient C_d by

$$C_d = \frac{24}{Re_p}(1+0.15{Re_p}^{0.687}). \tag{2.11}$$

The buoyancy ($\mathbf{F}_b$) and gravitational ($\mathbf{F}_g$) volumetric forces affecting the otoconia in opposed directions,

$$\begin{aligned} \mathbf{F}_b &= -\rho_e\mathbf{g} \\ \mathbf{F}_g &= \rho_o\mathbf{g}, \end{aligned} \tag{2.12}$$

where $\mathbf{g}$ is the gravitational acceleration.

The displacement of the otoconium immersed on the endolymphatic fluid can be determined by the sum of all these forces acting on the otoconium,

USC DE COMPOSTELA

$$\rho_o \frac{\mathrm{d}\mathbf{v}_o}{\mathrm{d}t} = \mathbf{F}_o^{co} + \mathbf{F}_o^{c} + \mathbf{F}_o^{e} + \mathbf{F}_d + \mathbf{F}_b + \mathbf{F}_g. \tag{2.13}$$

Equation (2.13) is solved using an implicit unsteady Lagrangian multiphase solver with a second-order tracking integration method. This method accurately determines the position and velocity of otoconia, which have been simplified to spherical particles. One hundred otoconia of varying sizes were simulated in this study, with diameters d_o ranging from 3 µm to 30 µm in increments of 3 µm, reflecting the range observed in humans [61]. This resulted in the creation of ten different groups, each consisting of ten otoconia of the same size. In addition, a two-way coupled solver was implemented to allow bidirectional interactions between the endolymph and otoconia. The interaction between the particles and walls was modeled as a perfect elastic collision, but collisions between particles were not simulated to reduce the computational costs. This assumption was made because of the small volume of otoconia compared to the endolymphatic volume, suggesting minimal interaction between otoconia during their movement [62].

The same forces that affect the otoconia also impact the endolymphatic flow, albeit with modifications to the inertial terms, which are now relative to the cell endolymph volume,

$$\begin{aligned} \mathbf{F}_e^{co} &= -2\rho_e(\boldsymbol{\omega} \times \mathbf{v}_e) \\ \mathbf{F}_e^{c} &= -\rho_e \boldsymbol{\omega} \times (\boldsymbol{\omega} \times \mathbf{r}_e) \\ \mathbf{F}_e^{e} &= -\rho_e \frac{\partial \boldsymbol{\omega}}{\partial t} \times \mathbf{r}_e. \end{aligned} \tag{2.14}$$

Here, $\mathbf{r}_e$ represents the position vector of the endolymph cell volume relative to the head or body origin of the rotation.

The solution for the endolymphatic flow is obtained by solving the Navier-Stokes equations,

$$\rho_e \frac{\partial \mathbf{v}_e}{\partial t} + \rho_e(\mathbf{v}_e \cdot \nabla)\mathbf{v}_e = -\nabla p + \mu_e \nabla^2 \mathbf{v}_e + \mathbf{F}_e^{co} + \mathbf{F}_e^{c} + \mathbf{F}_e^{e} - \mathbf{F}_d - \mathbf{F}_b - \mathbf{F}_g, \tag{2.15}$$

where p represents the pressure and μ_e represents the viscosity of the endolymph. In this equation, the terms defined for the drag, buoyancy, and gravitational volumetric forces, defined in Equations (2.10) and (2.12), are in opposite directions owing to Newton's third law.

The endolymphatic fluid was modeled as a laminar incompressible fluid. The model chosen to solve Equation (2.15) is a second-order segregated flow solver using second-order implicit unsteady temporal discretization in time. This solver iteratively solves the Navier-Stokes equation for the velocity and pressure, and then shares information with the Lagrangian multiphase solver at each inner iteration.

The values of all variables used for both otoconia and endolymph modeling are presented in Table 2.3. The viscosity and density of the endolymph were considered constant because the temperature did not vary during the simulations (37 ºC).

2.4.2 Head impulse test

USC UNIVERSIDADE DE SANTIAGO DE COMPOSTELA

In contrast to the EM study, the HIT study did not investigate the otoconia displacement. While the set of equations utilized to define the fluid dynamics remained unchanged, the

endolymphatic fluid was defined as a laminar, compressible fluid with one constant term and another term that depended on the pressure of the fluid and the speed of sound in the endolymph (c = 1500 m/s),

$$\rho_e' = \rho_e + \frac{p}{c^2}. \tag{2.16}$$

Table 2.3: Endolymph, otoconia and cupula parameters used to design the mathematical models.

Name	Variable	Value	Units	
Endolymph density	ρ_e	1000	kg/m^3	[9]
Endolymph dynamic viscosity	μ_e	8.15×10^{-4}	Pa·s	[9]
Endolymph electrical conductivity	σ_e	1.67	S/m	[63]
Otoconia density	ρ_o	1000	kg/m^3	[9]
Cupula density	ρ_c	1000	kg/m^3	[9]
Cupula Poisson ratio	ν	0.48		[9]
Cupula Young modulus	E	4.258	Pa	[9]
Cupula electrical conductivity	σ_c	1.67	S/m	[63]

This computational necessity allows for the modeling of the coupled behavior of fluids and elastic solids, which accounts for the increased complexity of this model. The change in density due to pressure variation was negligible during the entire rotation and only served as a parameter to ensure that the interactions between the endolymph and cupulae were accurately captured under varying conditions. For this reason the inertial forces are redefined as,

$$\begin{aligned} \mathbf{F}'^{co}_e &= -2\rho_e'(\boldsymbol{\omega} \times \mathbf{v}_e) \\ \mathbf{F}'^{c}_e &= -\rho_e'\boldsymbol{\omega} \times (\boldsymbol{\omega} \times \mathbf{r}_e) \\ \mathbf{F}'^{e}_e &= -\rho_e'\frac{\partial \boldsymbol{\omega}}{\partial t} \times \mathbf{r}_e, \end{aligned} \tag{2.17}$$

and the endolymphatic flow is solved using the same Navier-Stokes equation but without the force terms related to the otoconia, now only including the new inertial terms and the compressible density,

$$\rho_e'\frac{\partial \mathbf{v}_e}{\partial t} + \rho_e'(\mathbf{v}_e \cdot \nabla)\mathbf{v}_e = -\nabla p + \mu_e \nabla^2 \mathbf{v}_e + \mathbf{F}'^{co}_e + \mathbf{F}'^{c}_e + \mathbf{F}'^{e}_e. \tag{2.18}$$

Because the endolymph for Equation (2.18) was considered compressible instead of a segregated flow solver, a second-order coupled implicit solver was implemented for spatial integration. This means that the equations are solved together in a single-matrix system instead of iteratively. Due to the absence of otoconia, the time discretization is first-order implicit unsteady.

Similar to the endolymphatic fluid, the inertial forces affecting the cupulae are

USC UNIVERSIDADE DE SANTIAGO DE COMPOSTELA

$$\begin{aligned}\mathbf{F}_c^{co} &= -2\rho_c(\omega \times \mathbf{v}_c)\\ \mathbf{F}_c^{c} &= -\rho_c\omega \times (\omega \times \mathbf{r}_c)\\ \mathbf{F}_c^{e} &= -\rho_c\frac{\partial \omega}{\partial t} \times \mathbf{r}_c,\end{aligned} \tag{2.19}$$

where $\mathbf{r}_c$ and $\mathbf{v}_c$ represent the position vector and the velocity of the cupula cell volume, respectively. The displacement of the cupula $\mathbf{d}_c$ is governed by

$$\rho_c\frac{\partial^2 \mathbf{d}_c}{\partial t^2} = \nabla \cdot \sigma + \mathbf{F}_c^{co} + \mathbf{F}_c^{c} + \mathbf{F}_c^{e}, \tag{2.20}$$

and the Hooke's Law,

$$\varepsilon = \frac{(1+\nu)}{E}\sigma - \frac{\nu}{E}\mathrm{tr}(\sigma)\mathbf{I}. \tag{2.21}$$

The latter relates the stress tensor σ to the strain tensor ε using the cupula Young's modulus E and Poisson's ratio ν, the values of which are listed in Table 2.3. These two tensors can be described as matrices,

$$\begin{aligned}\sigma &= \begin{pmatrix}\sigma_{XX} & \sigma_{XY} & \sigma_{XZ}\\ \sigma_{XY} & \sigma_{YY} & \sigma_{YZ}\\ \sigma_{XZ} & \sigma_{YZ} & \sigma_{ZZ}\end{pmatrix}\\ \varepsilon &= \begin{pmatrix}\varepsilon_{XX} & \varepsilon_{XY} & \varepsilon_{XZ}\\ \varepsilon_{XY} & \varepsilon_{YY} & \varepsilon_{YZ}\\ \varepsilon_{XZ} & \varepsilon_{YZ} & \varepsilon_{ZZ}\end{pmatrix},\end{aligned} \tag{2.22}$$

each having nine components that provide a comprehensive characterization of the total stress or strain experienced at each point of the solid mesh.

The cupula regions are considered elastic, linear, and isotropic solids, exhibiting nearly incompressible material properties. For this reason, Equations (2.20) and (2.21) are solved using the solid stress solved with a backward Euler integration method, which is an unconditionally stable first-order method. Temporal discretization is first-order, similar to that applied to endolymphatic fluids. In addition, a two-way coupled FSI approach was included. This means that in addition to the different forces affecting the displacement of the endolymphatic fluid and cupulae, the pressures on the interfaces between the solid and fluid domains are reciprocally updated (fluid pressures influence solid deformation and vice versa) during each computational iteration to ensure an accurate FSI simulation. This approximation must be approached cautiously, as significant instabilities can occur during coupling between the fluid and solid boundaries. The main strategy for increasing the stability of the FSI model was to increase the number of inner iterations and reduce the under-relaxation factor to 0.5, thereby limiting the exchange of information on the interface to half of what occurs at each iteration. Higher under-relaxation factors resulted in numerical errors, preventing the completion of the numerical simulation regardless of the mesh or time step selected.

2.4.3 Magnetic vestibular stimulation

Finally, the most complex model designed is for the MVS study. This involves first addressing the electromagnetic equations and then solving the cupula and endolymph equations

in a manner similar to that described for the HIT study.

Operating within a quasi-static regime defined by a static magnetic field, a non-full-wave method based on Maxwell's equations can be used to solve the electromagnetic problem, as shown in Equation (1.9). Given the constant magnetic flux density **B** in MRI machines and the absence of free charges within the endolymph and cupulae, the electric field **E** is deduced by the gradient of the electric potential ϕ as

$$\mathbf{E} = -\nabla\phi. \tag{2.23}$$

Subsequently, the electric current density **J** within the endolymph and cupulae are described by Ohm's law as the product of the electric field and the respective electrical conductivity by

$$\mathbf{J} = \sigma\mathbf{E}. \tag{2.24}$$

Substituting Equation (2.23) in Equation (2.24), we derive the relationship for the current density in terms of the electric potential gradient, resulting in

$$\mathbf{J} = -\sigma\nabla\phi. \tag{2.25}$$

The boundary conditions specified for the dark and hair cell regions, as explained in the following section, allow the determination of the electric potential in the endolymph and cupulae domains. This electric potential can be used to solve Equation (2.25) and obtain the electric current density. As an initial condition, the electric potential was set to 0.01 V [40], and this value was maintained constant for the hair cell regions.

With the current density known, we can compute the Lorentz force $\mathbf{F}_l$ across a single mesh electromagnetic region for all endolymph and cupulae domains as

$$\mathbf{F}_l = \mathbf{J} \times \mathbf{B}. \tag{2.26}$$

Notably, the values of the Lorentz force remained unchanged during the simulation because they depended solely on the boundary conditions. In addition, the magnetic Reynolds number defined in Equation (2.8) is small. Therefore, there is no need to persistently execute the electrodynamic potential model with a hyperlinear solver to determine the electromagnetic variables. This solver was run only for the first time step using the mapped Lorentz force. For more information, refer to the definition of the electromagnetic region in the meshing section.

The endolymphatic flow is determined by solving the Navier-Stokes equations. The resulting velocity of the endolymph is influenced only by the Lorentz force, as established in Equation (2.26). The corresponding equation of motion for the endolymph is given by

$$\rho_e' \frac{\partial \mathbf{v}_e}{\partial t} + \rho_e'(\mathbf{v}_e \cdot \nabla)\mathbf{v}_e = -\nabla p + \mu_e \nabla^2 \mathbf{v}_e + \mathbf{F}_l. \tag{2.27}$$

In this model, the cupula regions were treated as described in the HIT study. This means that to calculate the displacement of the cupula, the Hooke Law from Equation (2.21) and the same dynamic equation but this time only affected by the Lorentz force are used,

$$\rho_c \frac{\partial^2 \mathbf{d}_c}{\partial t^2} = \nabla \cdot \sigma + \mathbf{F}_l. \tag{2.28}$$

USC DE COMPOSTELA

The solvers and procedures used to solve these fluid and solid equations were similar to

those used in the HIT study, including the FSI solver.

2.5 Boundary conditions

The software used for the numerical simulations, Simcenter Star CCM+, requires specific parameters as boundary conditions to ensure an accurate solution of the previous equations without leading to an overconstrained system. This avoids inconsistencies and provides a unique solution.

2.5.1 Fluid and solid regions

The walls of the membranous labyrinth enclosing the endolymphatic fluid are considered completely rigid because elasticity does not play a significant role in the frequencies employed in the EM, HIT, and MVS studies [40, 46, 64]. All of them are within the natural frequency range of the semicircular canal, as shown in Figure 1.6. The boundary conditions for the fluid consisted of a no-slip wall condition and a closed geometry without inlet or outlet walls.

In the case of the EM, the cupula walls are also assumed to be rigid because the endolymphatic flow generated by cupula displacement is not strong enough to move otoconia due to the differences in density between otoconia and the endolymphatic fluid [65]. However, in the case of HIT and MVS, the walls in contact with the cupula are considered to have elastic properties that allow them to undergo displacement. The remaining walls of the cupula were attached to the rest of the geometry, generating a fixed point that allowed for an appropriate boundary condition for solving the FSI problem.

2.5.2 Electromagnetic region

To effectively solve the electrodynamic potential model within the context of the MVS study, appropriate boundary conditions had to be established for the dark and hair cell regions in the membranous labyrinth. The model treated the other walls of the membranous labyrinth as insulating barriers, which effectively impede the flow of electric current out of the electromagnetic region domain.

Some parameters are unknown or have not been documented in the literature. To circumvent this issue, mathematical estimations were used to deduce these parameters from available experimental data. This involved calculating the electric potential and surface resistance for the regions with hair cells and the electric current and electric surface resistance for the regions with dark cells. These calculated values, along with the data used for the estimations, are shown in Table 2.4 for reference.

First, the hair cell density in each region was determined, denoted by ρ^h, using the number of hair cells per area, as reported in studies conducted on humans [66]. This reference provides a correlation between hair cell density and age. Therefore, regarding the model, the age of the membranous labyrinth anatomy is assumed to correspond to the age selected for the boundary conditions that determine the electrical currents. By applying the slopes and intercepts of the linear regressions from that study, the specific hair cell density for both cristae ampullares and the utricular macula was obtained for an age of 55 years. This age aligns with the average for adults in the USA and EU.

USC DE COMPOSTELA

The surface area of each hair cell region, referred to as A^h, and dark cell region, referred to as A^d, were defined manually in the Simcenter Star CCM+ software. The resulting surface areas matched those documented in animal [54] and human studies [55].

To calculate the total number of hair cells within each region n^h, the area of the region is multiplied by the density of hair cells,

$$n^h = \rho^h A^h. \tag{2.29}$$

Then, the total electric current for each hair cell region I^h can be estimated by multiplying the number of hair cells by the electric current produced by a single hair cell given as -100 pA from Roberts et al. [29], leading to

$$I^h = n^h i. \tag{2.30}$$

The negative sign of these values indicates that the current is exiting the membranous labyrinth, moving outward in a direction perpendicular to the surface. The aggregate of these currents gives a total outflow of -4.47 µA exiting from the membranous labyrinth. Considering the principle of conservation of electric currents within the membranous labyrinth, an equivalent total current with the opposite sign was assigned to the dark cell regions, which implies an inflow of current.

Subsequently, total electric current density in the dark cell regions J^d was deterined by summing all the electric currents from the hair cell regions and dividing by the total area of these regions as

$$J^d = \frac{\sum I^h}{\sum A^h}, \tag{2.31}$$

with the total current density (stated as J^d = 0.22 A/m^2), we can then determine the electric current for each dark cell region I^d by multiplying the current density by the area of the dark cell region,

$$I^d = J^d A^d. \tag{2.32}$$

This calculated current is assumed to be evenly distributed across the surface of the dark cell regions and is used as a boundary condition in the MVS simulations. Lastly, the surface resistance for both hair and dark cell regions was derived using Ohm's Law, incorporating the electric potential for endolymphatic fluid (set at V = 0.01 V from Rabbitt [40]), as part of the calculation, resulting in

$$\begin{aligned} R^h &= \frac{I^h A^h}{V} \\ R^d &= \frac{I^d A^d}{V}. \end{aligned} \tag{2.33}$$

USC UNIVERSIDADE DE SANTIAGO DE COMPOSTELA

Table 2.4: Parameters defining the electrodynamic potential model. These are denoted as $variable^{cell\ type}_{region}$, where the cell type is represented as h for hair cells and d for dark cells. The region specifies distinct anatomical locations within the vestibular system, designed as m for the macula, u for utricle, c for common crus, h for horizontal, p for posterior, and s for superior cell regions. Key parameters serving as boundary conditions within the model are identified by an asterisk ($*$). The values correspond to for a 55-year-old human based on measurements by Merchant et al. [66].

Name	Variable	Value	Units
Density of hair cells in the macula	ρ^h_m	5.94×10^9	units/m^2
Density of hair cells in the horizontal crista	ρ^h_h	5.81×10^9	units/m^2
Density of hair cells in the posterior crista	ρ^h_p	5.51×10^9	units/m^2
Density of hair cells in the superior crista	ρ^h_s	5.52×10^9	units/m^2
Area of macular hair cells	A^h_m	5.54×10^{-6}	m^2
Area of horizontal hair cells	A^h_h	7.90×10^{-7}	m^2
Area of posterior hair cells	A^h_p	4.74×10^{-7}	m^2
Area of superior hair cells	A^h_s	8.41×10^{-7}	m^2
Area of utricular dark cells	A^d_u	1.32×10^{-5}	m^2
Area of crus dark cells	A^d_c	6.15×10^{-6}	m^2
Area of horizontal dark cells	A^d_h	4.16×10^{-7}	m^2
Area of posterior dark cells	A^d_p	3.57×10^{-7}	m^2
Area of superior dark cells	A^d_s	4.76×10^{-7}	m^2
Number of hair cells in the macula	n^h_m	32884	units
Number of hair cells in the horizontal crista	n^h_h	4592	units
Number of hair cells in the posterior crista	n^h_p	2609	units
Number of hair cells in the superior crista	n^h_s	4639	units
Electric current of macular hair cells	I^h_m	-3.29×10^{-6}	A
Electric current of horizontal hair cells	I^h_h	-4.59×10^{-7}	A
Electric current of posterior hair cells	I^h_p	-2.61×10^{-7}	A
Electric current of superior hair cells	I^h_s	-4.64×10^{-7}	A
Electric current of utricular dark cells*	I^d_u	2.86×10^{-6}	A
Electric current of crus dark cells*	I^d_c	1.34×10^{-6}	A
Electric current of horizontal dark cells*	I^d_h	9.06×10^{-8}	A
Electric current of posterior dark cells*	I^d_p	7.77×10^{-8}	A
Electric current of superior dark cells*	I^d_s	1.04×10^{-7}	A
Electric potential in hair cells*	V	1×10^{-2}	V
Electric surface resistance of macular hair cells*	R^h_m	1.82×10^{-9}	Ωm^2
Electric surface resistance of horizontal hair cells*	R^h_h	3.63×10^{-11}	Ωm^2
Electric surface resistance of posterior hair cells*	R^h_p	1.24×10^{-11}	Ωm^2
Electric surface resistance of superior hair cells*	R^h_s	3.90×10^{-11}	Ωm^2
Electric surface resistance of utricular dark cells*	R^d_u	3.77×10^{-9}	Ωm^2
Electric surface resistance of crus dark cells*	R^d_c	8.23×10^{-10}	Ωm^2
Electric surface resistance of horizontal dark cells*	R^d_h	3.77×10^{-12}	Ωm^2
Electric surface resistance of posterior dark cells*	R^d_p	2.77×10^{-12}	Ωm^2
Electric surface resistance of superior dark cells*	R^d_s	4.93×10^{-12}	Ωm^2

USJ UNIVERSIDAD DE SAN JORGE

2.6 Coordinate systems

The use of coordinate systems is crucial for accurately modeling complex movements and interactions within the vestibular system. Each study required a unique reference framework to account for different initial head positions and rotational axes. These coordinate systems enable the correct application of forces and boundary conditions, thereby ensuring precise simulations. In this section, the various coordinate systems employed in this study are outlined, detailing their origins, orientations, and roles.

The membranous labyrinth was always located at the same position with respect to the head, as shown in Figure 2.2. However, the initial position of the head differs between studies. This creates a framework of coordinate systems with different origins and orientations necessary for each type of study, which is summarized in Table 2.5.

Table 2.5: Coordinate systems used for each study, including if their axes orientation is maintained or vary with the rotations.

Study	Head supine	Head nose-down	Hip	Canals	Cupulae
EM	Yes	No	Yes	Yes	No
HIT	No	Yes	No	Yes	Yes
MVS	Yes	No	No	No	Yes
Orientation	Fixed	Fixed	Fixed	Rotates	Rotates

There are two possible orientations of the head coordinate system. First, the supine position was used for the EM and MVS, in which the head was straight relative to the rest of the body. This orientation can be considered the standard position of the head at the start of the EM and when the subject lies inside the MRI bore. Regardless of whether the subject is sitting or lying down, the reference system of the head remains fixed, with the X-axis always pointing towards the nose, the Y-axis pointing to the left ear, and the Z-axis pointing to the top of the head. At this position, the membranous labyrinths have a specific orientation relative to these axes, as depicted in Figure 2.1. Second, the heat was oriented in a nose-down position in the HIT study. In this configuration, the head was tilted downward at an angle of 20º to align the horizontal semicircular canal approximately with the axial plane, as shown in Figure 2.2. The reference frame used in this case is known as the vestibular coordinate system, which is commonly employed in rotational vestibular diagnostic procedures [67].

For the EM study, another coordinate system was defined with the same orientation as the head, but with the origin located at the hip center. The distance between the head and hip origins is 75 cm, based on anthropometry and average human height [68]. When rotating relative to the hip origin, a more accurate representation of the forces during the maneuver is obtained. In this situation, the head coordinate system adjusts to ensure that the origin is always located at the center of the head. It is important to highlight that the orientations of the head and hip coordinate systems remain consistently aligned; therefore, the axis orientations do not vary during the rotations performed. Consequently, the rotational planes described in the next section always follow the same coordinate system criteria.

Six other coordinate systems were created, one for each semicircular canal, as listed in Table 2.6. These coordinate systems rotate with geometry, consistently maintaining their positions and axis orientations relative to the membranous labyrinth. This approach permitted

the comparison of the orientation of the semicircular canals with the maximum (MAX) and minimum (MIN) directions performed in the HIT study. Additionally, the posterior coordinate system was used for the EM study to calculate the position of each otoconium in relation to the center of the posterior semicircular canal. This enabled a comparison of the numerical simulation results based on the angular position of the otoconia along the posterior semicircular canal using polar coordinates.

Table 2.6: Location of the center of the semicircular canals and their orientation respect to the head nose-down coordinate system used for the head impulse test (HIT) study. The Z-axis vector is equivalent to the unitary normal vector of the plane of the semicircular canal.

Semicircular canal	Origin (cm)	Z-axis vector
Left horizontal	(-0.066, 4.253, -0.024)	(0.000, -0.093, 0.996)
Left posterior	(-0.422, 4.100, -0.048)	(-0.693, -0.713, -0.102)
Left superior	(0.018, 4.022, 0.342)	(-0.613, 0.782, -0.113)
Right horizontal	(-0.066, -4.253, -0.024)	(0.000, 0.093, 0.996)
Right posterior	(-0.422, -4.100, -0.048)	(-0.693, 0.713, -0.102)
Right superior	(0.018, -4.022, 0.342)	(-0.613, -0.782, -0.113)

Finally, six additional coordinate systems are shown in Table 2.7, each centered in the middle of a cupula, serving a singular purpose: to determine the stimulation for each crista ampullaris in the HIT and MVS studies. During rotations in the HIT study, the cupula coordinate systems rotated similarly to the canal coordinate systems. Rotations were not applied in the MVS study; instead, different positions of the head were defined, as depicted in Figure 2.4, which also altered the orientation of the canal coordinate systems with respect to the head coordinate system used as a reference.

Table 2.7: Location of the center of the cupula and the vector corresponding with the unitary normal vector to the cupula walls in contact with the endolymph, defined as X-axis vector. See Figure 2.7 for visual aid.

Cupula	Origin (cm)	X-axis vector
Left horizontal	(0.224, 4.205, -0.007)	(-0.1133, -0.9806, -0.1597)
Left posterior	(-0.214, 3.862, -0.3200)	(-0.3563, 0.7821, -0.5112)
Left superior	(0.2820, 4.0860, 0.0960)	(0.3047, 0.5762, 0.7584)
Right horizontal	(0.2240, -4.2050, -0.0070)	(-0.1133, 0.9806, -0.1597)
Right posterior	(-0.2140, -3.8620, -0.3200)	(-0.3563, -0.7821, -0.5112)
Right superior	(0.2820, -4.0860, 0.0960)	(0.3047, -0.5762, 0.7584)

USC UNIVERSIDADE DE SANTIAGO DE COMPOSTELA

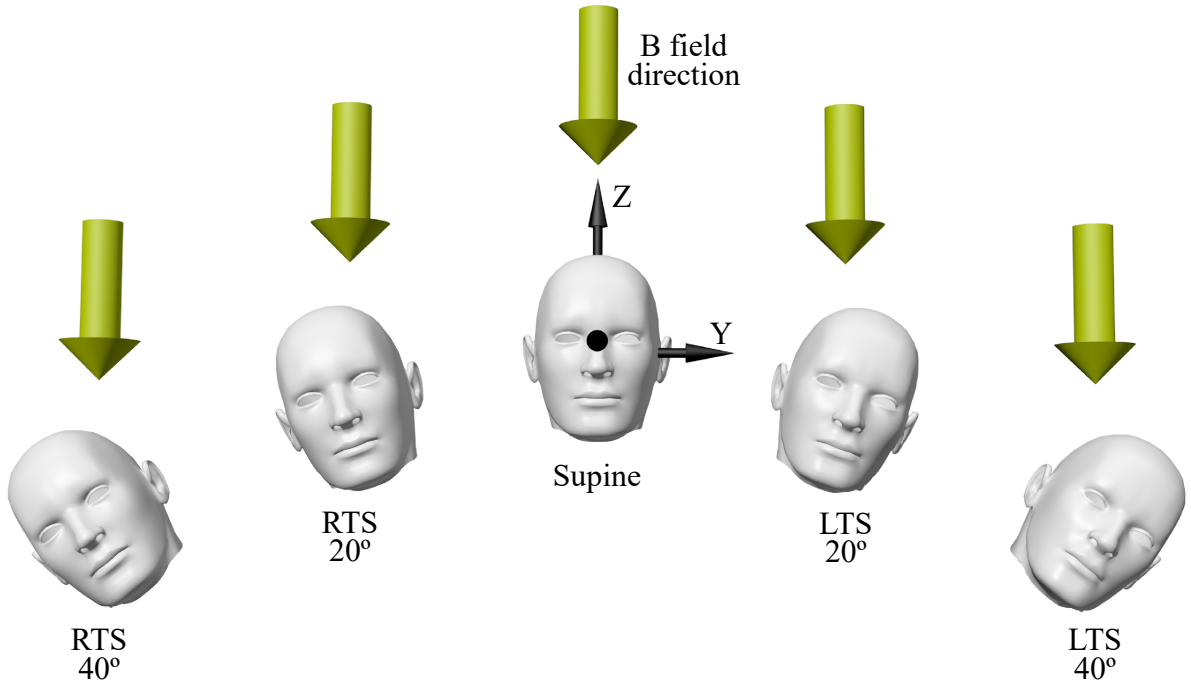

Figure 2.4: Head positions used to compare experimental and numerical results in the magnetic vestibular stimulation (MVS) study. The supine position corresponds to the standard position inside the MRI machine, and different ear-to-shoulder (ETS) positions were tested to study the changes in the vestibular response.

2.7 Definition of the rotations

As explained previously, the EM and HIT studies involve mechanical rotations to evaluate the displacement of the otoconia and the stimulation of the cristae ampullares, respectively. This section explains how these rotations were defined, and the criteria followed to understand the results and discussion of these two studies. Their definitions are based on the coordinate systems defined in the previous section.

2.7.1 Rotation for the Epley maneuver

The EM considered for the numerical simulation was based on the original EM [18]. The only modification to the original maneuver is that it concludes with the patient sitting at the bedside. Instead of returning to the same initial position, the body was rotated 90º on the Z-axis, looking towards the side of the unaffected canal (right side), as described in Table 2.8. This variation is typically applied to facilitate the transition of the patient to the sitting position during step 4 of the maneuver [69]. It is expected that this will not have a significant effect on the otoconia path because the Z-axis of rotation is aligned with the direction of gravity.

USC
UNIVERSIDADE DE SANTIAGO DE COMPOSTELA

Table 2.8: Steps and substeps of the standard Epley maneuver (EM) considered for the numerical simulations. A positive ϑ indicates an anticlockwise rotation, whereas a negative value indicates a clockwise rotation. Normal vectors of rotation $\hat{\mathbf{n}}$ are defined based on the directions of the static coordinate system, but the origin of rotation varies depending on the substep being studied.

Step	Substep	$\hat{\mathbf{n}}$	Origin	ϑ (º)
1	A	(0.000, 0.000, 1.000)	Head	45
1	B	(0.000, 1.000, 0.000)	Hip	-90
1	C	(0.000, 1.000, 0.000)	Head	-30
2	A	(0.866, 0.000, 0.500)	Head	90
3	A	(1.000, 0.000, 0.000)	Hip	90
4	A	(0.000, 1.000, 0.000)	Hip	90
4	B	(1.000, 0.000, 0.000)	Head	30
5	A	(0.000, 0.000, 1.000)	Head	45
5	B	(1.000, 0.000, 0.000)	Head	20
6	A	(1.000, 0.000, 0.000)	Head	-20

To investigate the potential causes of treatment failure, several modifications were made to the substeps identified as challenging during the execution of clinical procedures. For this purpose, variations of 5º on the specific substep under study were made. Step 4 used a different perspective, considering that otoconia started at three different locations. Additionally, a variation that combines steps 4 and 5 was implemented, named step 4-5. This modification was considered because the original EM indicated that these two steps should be performed separately [18], but currently, these two steps are often performed together (without resting time between them), and the final step 5 of a 20º nose-down is not always incorporated [69]. All variations with respect to the standard EM are summarized in Table 2.9.

Table 2.9: Variations in the rotation angles $\Delta\vartheta$ considered to assess the effectiveness of the Epley maneuver (EM). For a more comprehensive view of these variations, refer to the head orientations depicted in Figure 3.5.

Step	Substep	$\hat{\mathbf{n}}$	Origin	$\Delta\vartheta$ (º)
1	A	(0.000, 0.000, 1.000)	Head	30<45<60
1	C	(0.000, 1.000, 0.000)	Head	-15<-30<-45
2	A	(0.866, 0.000, 0.500)	Head	75<90<105
3	A	(1.000, 0.000, 0.000)	Hip	75<90<105
4		Initial position in the superior semicircular canal		
4		Initial position in the backside of the utricle		
4		Initial position in the frontside of the utricle		
4-5		No resting time between steps		
4-5	B	(1.000, 0.000, 0.000)	Head	0<20<90

USC UNIVERSIDADE DE SANTIAGO DE COMPOSTELA

The same rotational function was applied independently of the maneuver step. The selected function was proposed by Obrist [70],

$$\dot{\alpha} = \frac{-\vartheta}{2187}\left(140(t-t_0)^6 + 1260(t-t_0)^5 + 3780(t-t_0)^4 + 3780(t-t_0)^3\right), \tag{2.34}$$

where ϑ represents the degrees of rotation and t_0 is the initial time, which depends on the specific step of the maneuver under consideration. The duration of this function was set to a total of 3 s. By multiplying Equation (2.34) by the different normal vectors of rotation depicted in Table 2.8 and Table 2.9, we obtain the angular velocity ω as

$$\omega = \dot{\alpha}\hat{\mathbf{n}}, \tag{2.35}$$

which can be used to determine the inertial forces in Equations (2.9) and (2.14).

Despite the curved geometry of the semicircular canals, the time necessary for the otoconium to achieve the final position during a step of the maneuver can be estimated by the settling time, using the Stokes formulae [65],

$$t = t_0 + a d_o^{-2}. \tag{2.36}$$

This theoretical equation indicates that larger otoconia settle faster than smaller ones, inversely proportional to the square of the otoconium diameter d_o. Parameter a depends on the viscosity of the endolymph and the difference between the endolymph and otoconia densities, as shown in Table 2.3. The optimal rotation for each step is the one that displaces the otoconia at the largest distance in an indefinite resting time to determine, permitting all otoconia to reach their final position regardless of its size. It is important to note that the definition of resting time does not include the time taken during the rotation used for the Obrist function (3 s for each substep), and that there are no resting times between substeps within a given step.

Finally, treatment failure was defined as otoconia not reaching the frontside region of the utricle at the end of the complete maneuver, where the utricular macula is located. Considering this region as having a low probability of treatment failure (PTF), other regions, such as the common crus or the backside of the utricle, were considered medium PTF. When the otoconia reached the semicircular canals, including the posterior ampulla, it was considered a high PTF. This criterion was also used for the numerical assessment of the maneuver steps.

2.7.2 Rotation for the head impulse test

Although it is possible to stimulate the cristae ampullares using any rotational direction, it is expected that a specific direction of rotation will maximize or minimize the effect of stimulation in a particular semicircular canal because of their specific orientation in space. By varying the direction of rotation, it is possible to create an interpolated 3D map that records the response of each crista ampullaris to identify the MAX and MIN response directions. To simplify the visualization, the results were presented by projecting two hemispheres onto the axial plane. This projection yields a 2D polar map, where the radial coordinate corresponds to the θ ($0^\circ < \theta < 90^\circ$) spherical coordinate, with 0° representing the poles and 90° representing the equator. The angular coordinate corresponds to the ϕ ($0^\circ < \phi < 360^\circ$) spherical coordinate, where the line connecting the front 90° and chin 270° represents the sagittal plane, and the line connecting the left ear 180° and right ear 0° represents the coronal plane. To facilitate the comprehension of these definitions, please compare the planes from Figure 1.3a with the head and hemisphere

representations in Figure 2.5.

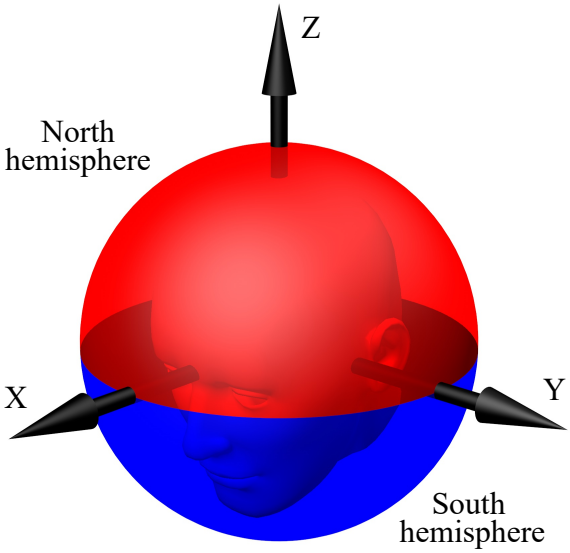

Figure 2.5: Head hemispheres used to generate the vestibular stimulation map in the head impulse test (HIT) study. The head orientation corresponds to the initial orientation of the head nose-down position employed for rotational vestibular testing.

As outlined in the introduction section 1.2.1 Vestibular mathematical modeling, the vestibular system behaves as a linear time-invariant (LTI) system, which means that the response to stimulation is equivalent to the function of rotation [41]. Therefore, the stimulation results were compared with the rotational function defined in this study. Similar to the EM, the same rotational function was applied independently of the rotational direction selected, but this time, the function comprises a Gaussian function that represents the commonly employed rotations during HIT [23],

$$\dot{\alpha} = Ae^{-(t-0.1)^2/0.001}, \tag{2.37}$$

where A denotes the peak velocity of the Gaussian function (A = 150 °/s). This function can be multiplied by the normal vector $\hat{\mathbf{n}}$ of the considered direction of rotation using Equation (2.35), resulting in the angular velocities used for the inertial force terms in Equations (2.17) and (2.19). Taking the derivative of this function, we obtain the corresponding angular acceleration,

$$\ddot{\alpha} = -2000(t-0.1)Ae^{-(t-0.1)^2/0.001}, \tag{2.38}$$

which reached peaks exceeding 4000 °/s^2. Additionally, integrating Equation (2.37) yields the head angular displacement,

$$\alpha = -0.028A\text{erf}\left(\frac{0.1-t}{\sqrt{0.001}}\right) + 0.073, \tag{2.39}$$

where erf is the Gaussian error function, resulting in a total displacement of approximately 8°.

This fast rotation, with a total duration of 0.2 s, is shown in Figure 2.6, where the velocity, acceleration, and displacement are colored in red, blue, and green, respectively. Depending on whether the rotation is counterclockwise or clockwise, the head moves towards the left or right

ear, respectively. The rotational origin is the center of the head, as shown in Figure 2.2. Based on previous studies [71], selecting the center of the head as the rotational origin constitutes a more realistic representation of the testing conditions.

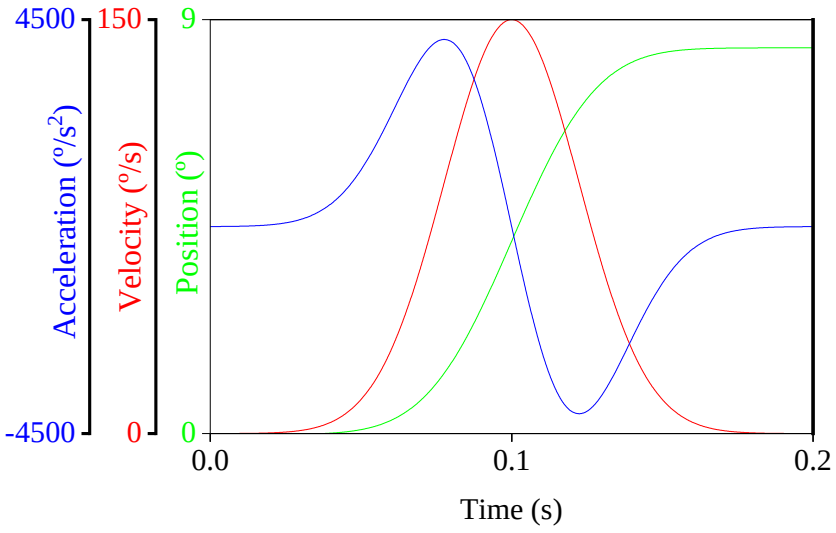

Figure 2.6: Gaussian function employed as a rotation function in the head impulse test (HIT) study. Angular acceleration is represented in blue, angular velocity in red, and angular position in green.

2.8 Measurement of the vestibular stimulation

In this section, we delve into the methodologies used to measure vestibular stimulation in the HIT and MVS studies. Understanding these measurements is crucial for accurately interpreting the simulation results and comparing them with the experimental data. We focus on two primary metrics: the shear strain XY and slow-phase velocity (SPV), with the latter being explained both numerically and experimentally.

2.8.1 Shear strain XY

As previously mentioned, the EM model focuses solely on the otoconia path and does not include solid regions that represent the cupulae. In contrast, the HIT and MVS models incorporate an FSI solver. This approach provides a more accurate response of the cupula by modeling it as an elastic body, addressing the limitations found in nonelastic models where only transcupular pressure could be measured [34, 52]. Although recent elastic models have assessed cupula stimulation through displacement and expansion [72], they often fail to accurately determine the local hair cell deflection based on the average cupula wall displacement [39]. This suggests that relying solely on physical measurements of cupula walls may not provide an accurate representation of hair cell stimulation. Other numerical simulations have demonstrated a nonsymmetric displacement of the cupula walls owing to the presence of an endolymph vortex within the ampullary regions [34]. The impact of this asymmetry can be minimized

by measuring the response exactly in the crista ampullaris regions, where the hair cells are located. Some studies have measured the maximum equivalent strain [50, 73]. However, this physical parameter encompasses all the components of the strain tensor from Equation (2.22), determining the overall deformation experienced by the cupula and does not distinguish between positive and negative values. Previous investigations have suggested that the most suitable parameter for representing crista ampullaris stimulation is the shear strain in the plane perpendicular to the direction of displacement, as this is the preferred disposition of hair cells attached to the crista ampullaris [74, 75].

Considering these two assumptions, the designed mathematical model measures ε_{XY}, the shear strain component in the XY plane shown in Equation (2.22), within the volume encompassing the crista ampullaris where the hair cells are embedded. This approach obtains a response at six cristae that closely reflects the reality of complete vestibular system stimulation. To achieve this, several independent coordinate systems were established, with one for each cupula. An example of the location of the horizontal crista ampullaris and its cupula coordinate system is shown in Figure 2.7. One advantage of using this parameter is its ability to differentiate between excitation and inhibition. The sign of the shear strain XY allows us to determine whether hair cells deflect in the direction of excitation (positive shear strain XY) or inhibition (negative shear strain XY), which means that the firing rate of the afferent nerve fibers is above or below their resting value, respectively. The X-axis for each crista was aligned with the excitatory response based on the orientation of the kinociliums (utriculipetal for the horizontal crista and utriculifugal for the posterior and superior crista). The volumetric regions representing the cristae ampullares were designed based on the geometrical shape of the catenoid [76], the area occupied by the original geometry, and the height of the hair cells, which was approximately 90 µm [9].

2.8.2 Numerical slow-phase velocity

For the final analysis of the stimulation, the averaged shear strain XY was determined for each crista ampullaris. This means that positive values in one cell mesh from the crista ampullaris cancel out, with similar values of the opposite sign in another cell. Although this is a good approximation, it has several limitations. First, it considers the same role for hair cells, independent of their type or location in the crista ampullaris. In addition, this description does not consider the distribution of afferents in the cristae and the role of the neurological pathways. This implies that a direct relationship may not always be obtained between the cristae ampullares stimuli and eye components. This is evident in the HIT study, where the high frequencies associated with this test may imply that inhibitory signals are less influential than excitatory signals [77], resulting in an average total stimulation that cannot be directly used to measure nystagmus eye components. However, for the MVS study, the lower frequencies involved allowed us to predict an equilibrium between the impact of the excitation and inhibition of hair cells, enabling us to assume a linear summation of stimuli. This facilitates the determination of eye components of nystagmus based on numerical results, allowing for a direct comparison with experimental results. This model also assumes that the vestibulo-ocular reflex (VOR) response is perfectly calibrated, the canals are perfectly perpendicular to each other, and the shear at each crista has the same relationship with the head movements.

The shear strain XY reached a plateau 30 s after starting to be under the influence of a magnetic field. This was determined by a convergence criterion in which subsequent stimulus

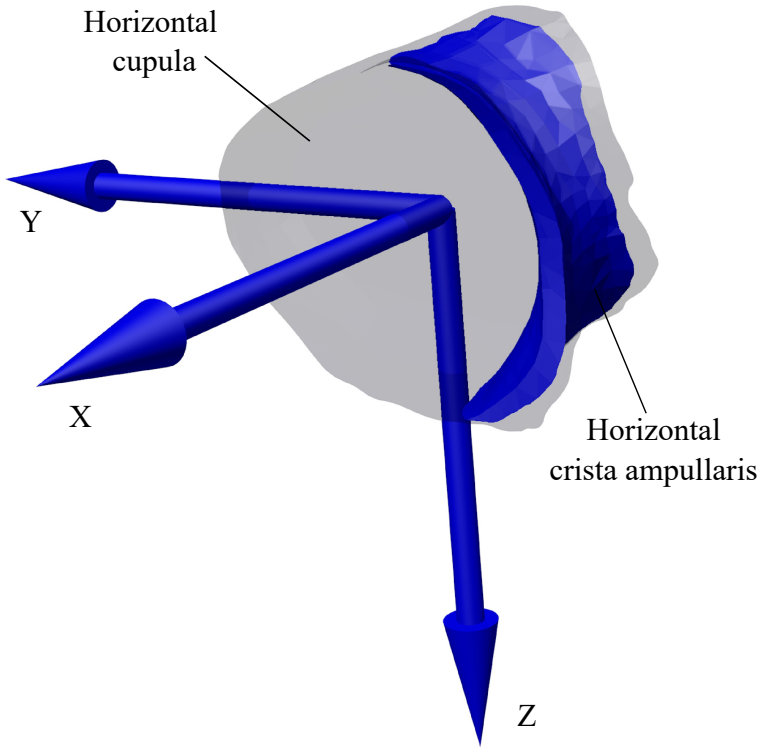

Figure 2.7: Horizontal cupula with the respective crista ampullaris and the cupula coordinate system. The origin of the coordinate system was located in the middle of the cupula. The X-axis points to the utricle, indicating the excitatory direction. The same criteria were followed for the rest of the cupulae, but with the X-axis pointing to their respective excitatory direction. The X-axis direction of all cupula coordinate systems can be seen in Table 2.7.

increments did not exceed 1 µPa within a 2 s interval. At this steady-state level, the computed averaged shear strain XY in the cristae ampullares was used to derive the SPV. The SPV for each directional component—horizontal, vertical, and torsional—was calculated using the following relationships,

$$\begin{aligned} \mathrm{SPV}_{hor} &= \mathrm{LH}^{ex} + \mathrm{RH}^{in} - \mathrm{LH}^{in} - \mathrm{RH}^{ex} \\ \mathrm{SPV}_{ver} &= \mathrm{LS}^{ex} + \mathrm{RS}^{ex} + \mathrm{LP}^{in} + \mathrm{RP}^{in} - \mathrm{LS}^{in} - \mathrm{RS}^{in} - \mathrm{LP}^{ex} - \mathrm{RP}^{ex} \\ \mathrm{SPV}_{tor} &= \mathrm{LS}^{ex} + \mathrm{RS}^{in} + \mathrm{LP}^{ex} + \mathrm{RP}^{in} - \mathrm{LS}^{in} - \mathrm{RS}^{ex} - \mathrm{LP}^{in} - \mathrm{RP}^{ex}. \end{aligned} \tag{2.40}$$

Each variable corresponds to the magnitude of the absolute response from a specific crista, with L denoting the left and R the right membranous labyrinth and H, P, and S the horizontal, posterior, and superior cristae, respectively. The superscripts *ex* and *in* denote excitation and inhibition, respectively. The sum of these signals, informed by the known neurological pathways of the vestibulo-ocular reflex, yields the SPV [78]. Positive SPV values indicate movement to the right, upward, and counterclockwise (top pole of the eye to the person's right side), whereas negative values suggest movement to the left, downward, and clockwise for each corresponding eye movement component.

The normalized SPV results at different head positions were adjusted to a normalized

sinusoidal function to determine the adjusted R-squared, which provides an assessment of the goodness of fit of the regression model.

2.8.3 Experimental slow-phase velocity

Using custom software, it was possible to identify the start and end of each nystagmus slow phase and apply automatic least-squares fitting to the intervening data points. This process yielded a series of SPV data points. Ocular torsion was quantified according to the methodology described by Otero-Millan et al. [79]. Upon MRI entry, an initial surge in nystagmus velocity was observed, culminating in a peak before partial central adaptation [80]. To focus on the maximal response and avoid adaptive effects, the code refines the raw eye movement data by removing artifacts from saccades, quick phases, and blinks. Then, the data corresponding to the temporal window encompassing the peak nystagmus were isolated, and the ten highest SPV values for each eye and movement component were selected. These values were averaged to ascertain the mean peak SPV for each nystagmus component per trial, assessing the fidelity of the experimental findings to the simulations at different B-field intensities and head positions. To do this, the difference between the normalized SPV data points was calculated, and the average value of these differences was determined as a percentage.

To isolate the MVS effect, the SPV values were adjusted by subtracting the mean baseline SPV recorded in Earth's magnetic field in the supine position. This correction ensured that the findings reflected the MVS response, uncontaminated by any inherent nystagmus in darkness. The average peak SPV for all subjects and trials within the same MRI scanner was calculated. Using the 20 highest and lowest peak SPV values, a range of peak ocular velocities characteristic of the study population was determined, which were used as error bars in the analysis.

Regarding the orientation of The magnetic field vector in the MRI machines was oriented cephalocaudally in the 7T and 3T machines, with subjects entering the MRI in a supine, head-first position. In contrast, the 1.5T MRI magnetic field was directed caudocephalically, as expected in accordance with the manufacturer's standard installation practice. This inversion is associated with nystagmus occurring in the reverse direction. To maintain consistency in comparing results across different MRI field strengths and considering simulations indicating that the results should be mirror images, the sign of the SPV data collected from the 1.5T MRI was inverted.

Finally, to compare the experimental data with the simulation outputs, the peak SPV experimental and numerical values were normalized relative to the maximum value of each eye movement component. Vertical nystagmus was minimal when the subjects lay in a head-neutral position; hence, normalization of the vertical SPV was based on the maximum horizontal SPV. We assessed the fidelity of the experimental findings to the simulations by calculating the discrepancies between the averaged normalized SPV and the simulated values for each type of eye movement.

2.9 Clinical study

In the MVS study, clinical data were collected in collaboration with researchers from Johns Hopkins Hospital to compare the numerical and experimental SPV explained in the previous section.

USC DE COMPOSTELA

Five healthy volunteers (aged 24 to 41 years, four males) were studied to capture three-dimensional binocular eye movements. These individuals were positioned supine in a darkened environment, and eye movements were recorded using infrared video goggles. Collected data were in the Earth's magnetic field and within the bore of MRI scanners at different field strengths: 7T (Achieva, Philips, Hamburg, Germany), 3T (dStream Achieva, Philips), and 1.5T (Espree, Siemens, Munich, Germany). This study received ethical approval from the Johns Hopkins Institutional Review Board, and all participants provided informed consent before their inclusion in the study.

Participants were positioned supine on the MRI table, with their heads aligned to a standardized pitch angle of approximately 100º relative to Earth's horizontal plane. This alignment ensured that the lateral semicircular canals were elevated by approximately 30º, which was consistent across trials. The head pitch angles were monitored throughout each trial. Before the ear-to-shoulder (ETS) tilt trials, a nonmetallic protractor was employed for precise positioning. Visual stimuli were occluded using a double-layered black felt cloth, and eye movement baselines were established outside the magnetic field of the MRI. The field strength near the participants' ears was 0.7T in the 7T environment and below 0.5T in both 3T and 1.5T settings.

The trials commenced with the subjects gazing directly ahead, and their gaze continuity was confirmed by the experimenter. Eye movement data were recorded throughout the entire experiment. After initial data collection from the MRI bore, the subjects were moved into the MRI bore for a 3 min exposure to the scan static magnetic field, followed by a 2 min rest period outside the MRI bore to mitigate any residual effects. Each participant underwent three trials in a single session to ensure response stability. In the 7T MRI, additional eye movement data were recorded at 20º and 40º lateral head tilts to both sides, as shown in Figure 2.4. Control experiments were conducted in an offsite lab, recording eye movements in the Earth's magnetic field with similar head tilts. Subjective vestibular sensations were documented post-experiment. Reports included transient rotational perceptions at 1.5T in one subject, mild turning sensations at 3T in two subjects, and rotational sensations at 7T in all subjects, often described as the head rotating leftward and feet rightward. With the ETS head tilts, the participants described a perceived tilt in the rotation axis corresponding to the direction of the tilt.

Using MRI-compatible infrared videooculography goggles (RealEyes xDVR, Micromedical Technologies Inc.), we recorded the eye movements of subjects at rest in a dark environment at a capture rate of 100 frames/s. The goggles, equipped with two Firefly MV cameras (PointGrey Research Inc., Richmond, BC, Canada), allowed dual capture of the infrared imagery of each eye. We monitored the real-time binocular eye position at a sampling rate of 100 Hz, assessing horizontal and vertical movements via pupillary tracking and torsional movements through iris pattern recognition. Ocular torsion angles were computed using a template-matching algorithm that compared iris patterns against a baseline image taken with the subject's head upright at the start of the recording session. The methodologies employed for these measurements have been elaborated in a prior publication by researchers at this hospital [81].

The goggles were outfitted with an accelerometer (MPU-92/65 sensor, InvenSense) and a high-field magnetometer (MV2, MagVector, with a range of up to 10T) to concurrently track head tilt angles and magnetic field strength. These instruments were interfaced with an Arduino (Teensy 3.2), which fed the data directly into the camera system. The accelerometer was calibrated to gauge the participant's head pitch relative to gravity, whereas the magnetometer

measured the magnetic field intensity adjacent to the participant's right temple. The accelerometer continuously monitored the pitch angle, ensuring real-time consistency of the head pitch angle during scans. Owing to the supine position of the participants, rendering the accelerometer unable to detect ETS head tilts, we employed a nonmetallic protractor for tilt measurements. The pitch and lateral tilts were synchronized with the centerline of the MRI table, extending from the chin through the midpoint of the nose. We selected lateral tilt angles of 20º and 40º, the latter being the maximum permissible within the spatial constraints of the 7T MRI bore.

USC
UNIVERSIDADE DE SANTIAGO DE COMPOSTELA

Chapter 3

Results and discussion

Part of the text and figures for this chapter are reproduced from the following publications

(I) Arán-Tapia, I.[1,2,3], Soto-Varela, A.[4], Pérez-Muñuzuri, V.[1,3], Santos-Pérez, S.[4], Arán, I.[5], Muñuzuri, A. P.[1,2]. Numerical Simulations of the Epley Maneuver With Clinical Implications.*Ear & Hearing* **45**(4):1033-1044, July/August (2024). ISSN: 0196-0202. DOI: www.doi.org/10.1097/AUD.0000000000001493.

(II) Arán-Tapia, I.[1,2,3], Soto-Varela, A.[4], Pérez-Muñuzuri, V.[1,3], Santos-Pérez, S.[4], Arán, I.[5], Muñuzuri, A. P.[1,2]. Numerical simulations to determine the stimulation of the crista ampullaris during the Head Impulse Test. *Comput Biol Med.* **163**, 107225 (2023). ISSN: 0010-4825. DOI: https://doi.org/10.1016/j.compbiomed.2023.107225.

(III) Arán-Tapia, I.[1,2,3], Pérez-Muñuzuri, V.[1,3], Muñuzuri, A. P.[1,2], Soto-Varela, A.[4], Otero-Millan, J.[6,7], Roberts, D. C.[7], Ward, B. K[8]. The Biophysics of Magnetic Vestibular Stimulation: Clinical Insights from High-Field MRI. Under review in *Communications Medicine* (2024). ISSN: 2730-664X.

[1]Group of Nonlinear Physics, University of Santiago de Compostela, Spain
[2]Galician Center for Mathematical Research and Technology (CITMAga), Spain
[3]Cross-disciplinary Research in Environmental Technologies (CRETUS), Spain
[4]Department of Otorhinolaryngology, Hospital of Santiago de Compostela, Spain
[5]Department of Otorhinolaryngology, Hospital of Pontevedra, Spain
[6]Herbert Wertheim School of Optometry and Vision Science, University of California, USA
[7]Department of Neurology, Johns Hopkins University, USA
[8]Department of Otolaryngology-Head and Neck Surgery, Johns Hopkins University, USA

Based on the motivation and aim outlined in this thesis, this chapter presents the findings of three studies conducted as part of this research. Similar to the clinical and methodological information provided in the previous chapters, this chapter describes and discusses the results in order of increasing complexity of the mathematical models employed. This increased detail in the models allows us to address the challenges presented by each of the problems to be solved in this thesis.

This chapter begins with a fluid model of the endolymph with rigid membranous labyrinth walls combined with a Lagrangian particle model. The primary objective of this initial model is to forecast the paths of otoconia during the Epley maneuver (EM), which is used to treat

benign paroxysmal positional vertigo (BPPV). Additionally, the simulations conducted allow for an examination of how various head movements affect the repositioning of otoconia and the amount of time required at each step of the maneuver, thereby enabling personalization of treatment for patients with BPPV. The discussion encompasses the biophysical mechanisms of the maneuver, the role of different forces, and the potential for personalized modifications based on individual anatomy to enhance the treatment outcomes of BPPV. Future work, such as investigating other treatment maneuvers and clinically evaluating the simulation results, is suggested.

Next, the results of the head impulse test (HIT) are presented, which necessitate a complex model that incorporates a fluid-structure interaction (FSI) model, accounting for the elasticity of the cupulae and their interaction with the endolymph. The simulations offer both qualitative and quantitative results for endolymph fluid dynamics and stimulation in the cristae ampullares during head rotations. Consequently, a three-dimensional stimulation map was created to identify the planes of rotation that elicited the maximum and minimum stimulation in each crista ampullaris. The discussion challenges prior hypotheses, demonstrating that the vestibular response is more aligned with the angular acceleration of the head rather than the angular velocity. Furthermore, it underscores the significance of considering the orientation of the cupulae for precise and individualized diagnosis and recommends future research to improve the diagnostic accuracy of rotational tests and to develop more precise mathematical models.

Finally, this chapter examines the modeling of magnetic vestibular stimulation (MVS) caused by magnetic resonance imaging (MRI) machines. To accomplish this, a combination of the FSI model used for the HIT and the magnetohydrodynamic (MHD) model is utilized. The findings of this analysis reveal the biophysical variables that influence magnetic vestibular stimulation, and the numerical predictions are validated through the use of experimental data. The discussion section of this chapter explores the robustness of the model and the impact of variables, such as patient age, on stimulation results. Additionally, it delves into the Lorentz force hypothesis, which explains how the slow-phase velocity of nystagmus varies with head orientation. Finally, this section suggests potential avenues for future research, such as refining the models and exploring new clinical applications of MVS, giving the idea of how personalized medicine could be applied using this novel type of vestibular stimulation.

Each study begins with a brief introduction, followed by the results and discussion. This structure allows for a clear presentation of how the models address specific issues in the vestibular system, culminating in a summary and suggestions for future research in each specific area. The intention of this chapter is to highlight how these models contribute to the understanding of vestibular function and their potential applications in personalized medicine, a topic that will be further concluded in the final chapter of this thesis.

3.1 Epley maneuver

A plausible explanation for the ineffectiveness of treatment maneuvers in some patients diagnosed with benign paroxysmal positional vertigo (BPPV) could stem from individual variations in the anatomical properties of the affected membranous labyrinth. Canalith repositioning maneuvers (CRP) are designed with the assumption that the membranous labyrinth has an ideal shape, where the angular relationships between the semicircular canals are orthogonal, as depicted in Figure 1.3, and the utricle and common crus maintain consistent orientations in relation to these canals. However, it is known that there are differences in the

USC DE COMPOSTELA

amplitudes of these semicircular canal angles between individuals [82] and that there is also variability in other regions of the labyrinth [83]. Based on this assumption, the hypothesis of this study is that the standard definition of CRPs might not be optimal for a specific patient, and a personalized maneuver that considers the specific vestibular system anatomy of the patient could be necessary to enhance treatment outcomes. Although some CRPs, such as the Epley maneuver (EM), already have a high success rate, a significant number of patients are refractory to treatment, as explained in the introduction section 1.1.3 Epley maneuver. These patients could potentially benefit from personalized modifications provided by numerical studies.

As discussed in the introduction section 1.2.2 Numerical methods, numerical simulations serve as a noninvasive analytical tool that has proven to be useful for studying the human vestibular system. In the context of BPPV, various mathematical models have been developed to investigate the behavior of otoconia within the semicircular canals [65, 84, 85, 86], shedding light on the mechanisms underlying fatigability [62], and proposing modified maneuvers [87]. In addition, in vitro studies on the Sémont maneuver have shown its potential for enhancing its effectiveness by incorporating small variations in the maneuver [88].

This study examines the effectiveness of the EM and potential modifications based on the unique anatomical features of a computational human membranous labyrinth, as depicted in Figure 2.1. For detailed insights into the study design, refer to chapter 2 Methodology. The primary goal of this study was to conduct a numerical assessment to determine whether modifications in timing and head positioning during the EM can improve treatment outcomes for BPPV compared to the standard EM. Initially, the findings are presented, followed by a comprehensive discussion integrating all pertinent information from this study. Finally, the study results are summarized and future work that is currently being pursued or planned for the future is outlined.

3.1.1 Results

Three types of analyses were performed in this study. First, a study of the standard EM, leaving an indefinite time for rotation, was conducted to understand the total time required for the otoconia to achieve the final position at each step and to determine if the standard head positions provide successful treatment. Second, a study about the standard EM applying two different clinically recommended resting times to evaluate if otoconia can leave the posterior semicircular canal. Third, the degrees of rotation were modified during all steps to evaluate whether the outcomes of the maneuver could benefit from a potential personalized treatment.

3.1.1.1 Analysis of the standard Epley maneuver

This section provides an analysis of the standard EM for treating BPPV in the posterior semicircular canal. The analysis focused on biophysical aspects, studying the trajectory and resting times of otoconia particles. The aim was to determine if the maneuver is satisfactory for the specific membranous labyrinth anatomy studied and, if not, to identify the reasons for its failure.

The path followed by otoconia was similar regardless of their diameter; however, the time needed to reach the same final position in each maneuver step was different. An example is shown in Figure 3.1, which illustrates the situation after 30 s of resting time for step 1. Under this consideration, larger otoconia, represented by red spherical particles, reached their final

USC DE COMPOSTELA

position owing to the effect of gravity, whereas smaller otoconia did not have enough time to reach a similar final position. For this reason, a proper analysis of the success of the standard EM requires studying the complete path for otoconia. This means leaving enough resting time for all otoconia, regardless of their size, to achieve the final position for each step presented in Table 2.8.

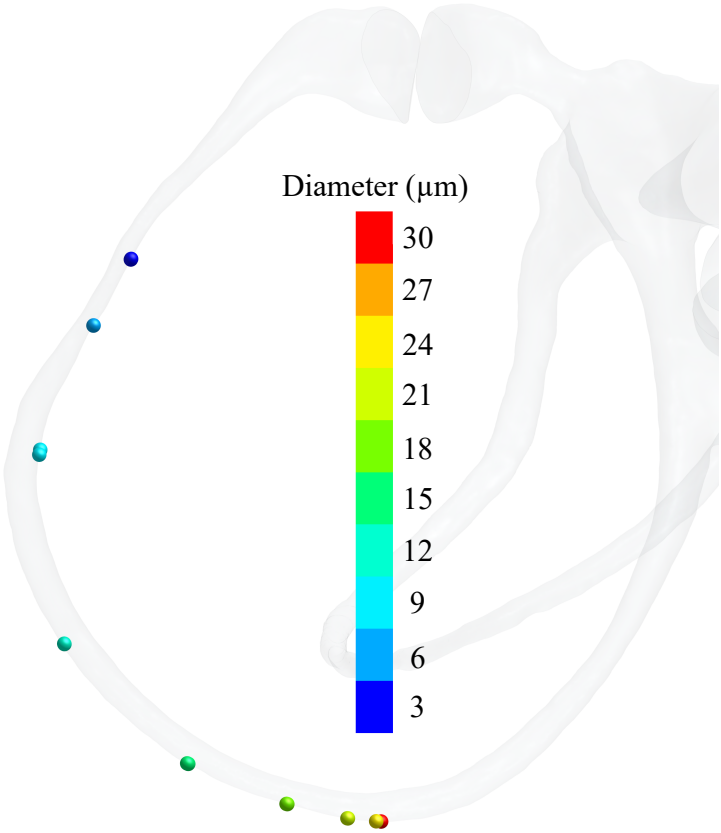

Figure 3.1: Position of otoconia after 30 s of resting time in the step 1. Enlarged spherical particles representing the otoconia are color-coded depending on their diameter.

Figure 3.2 illustrates the trajectory of all otoconia during the standard EM when provided with infinite time. Initially, otoconia were assumed to be positioned at the bottom of the canal, where gravity would naturally lead them over time when the head was in a supine position. This starting position can be inferred from Figure 2.1, which shows the initial orientation of the membranous labyrinth.

USC UNIVERSIDADE DE SANTIAGO DE COMPOSTELA

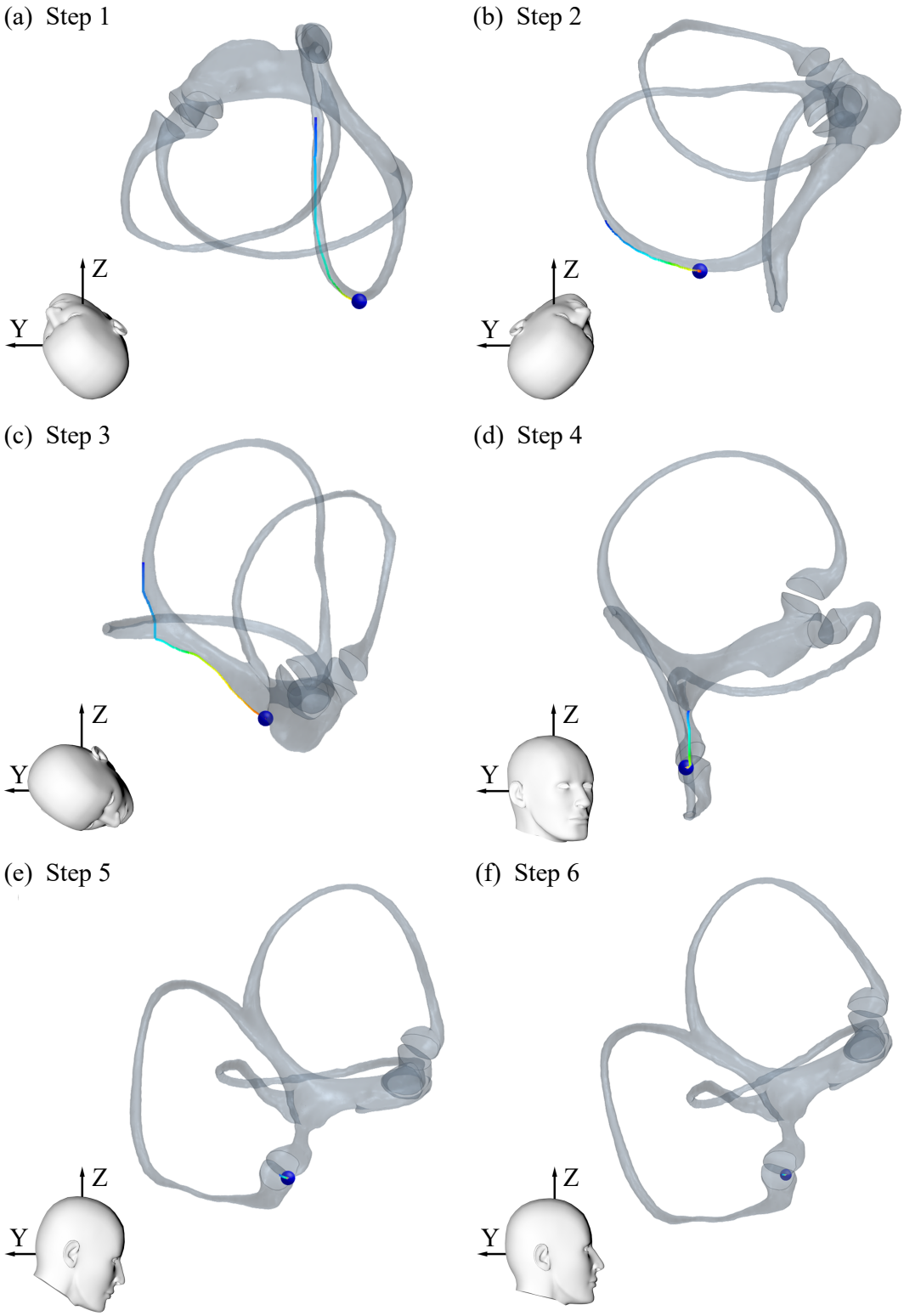

Figure 3.2: Displacement of the otoconia during the standard Epley maneuver (EM). Each image corresponds to different positions of the left membranous labyrinth and head orientation for each step of the EM. The paths of the otoconia are illustrated, and their final positions are represented by an enlarged blue sphere. The steps shown include (a) step 1, (b) step 2, (c) step 3, (d) step 4, (e) step 5, and (f) step 6, marking the end of the maneuver.

The first three steps of the maneuver effectively displaced the otoconia out of the posterior semicircular canal, as shown in Figures 3.2a, 3.2b, and 3.2c. During these steps, the otoconia moved 125.5º, 51.2º, and 34.6º, respectively, resulting in a total displacement of 211.3º, which was required to exit the posterior semicircular canal region and enter the common crus. Approximately 82 % of this displacement occurred when the membranous labyrinth model was at rest and the remaining 18 % occurred during rotation.

Upon completing step 3, as shown in Figure 3.2c, the otoconia were positioned at the backside of the utricle. Subsequently, during step 4, all otoconia, regardless of size, moved into the posterior ampullary region from the utricular side, as shown in Figure 3.2d. Once the otoconia enter this region, successive steps 5 and 6 fail to resolve the situation, leaving the otoconia in the posterior ampulla at the conclusion of the maneuver, as depicted in Figures 3.2e and 3.2f. According to the criteria outlined in the definition of the maneuver in the methodology section 2.7.1 Rotation for the Epley maneuver, the standard EM for this anatomical geometry cannot be considered successful, as the otoconia do not ultimately reach the front side of the utricle, where the utricular macula is located.

The time required for all otoconia to reach their final positions for each step simulated in the standard EM is presented in Table 3.1. Please note that the resting times for steps 5 and 6 are not displayed because the otoconia were already trapped within the posterior ampulla, as shown in Figure 3.2. By determining the resting time for each otoconia diameter, it was possible to calculate the total resting time needed to exit the posterior semicircular canal, as shown in Figure 3.3a, and the total required resting time to reach the posterior ampulla by the end of step 4, as illustrated in Figure 3.3b. The bars are divided according to the time required for each step.

Table 3.1: The resting times for all the steps required for otoconia to reach the posterior ampullary region. The calculations are performed for different otoconia diameters, as shown in Figure 3.3a.

Otoconia diameter (μm)	Resting time (s)			
	Step 1	Step 2	Step 3	Step 4
3	2193.9	1402.9	1312.3	361.3
6	551.8	367.7	327.4	88.4
9	240.0	154.4	144.5	49.2
12	135.6	85.9	82.0	22.0
15	86.6	47.1	51.0	11.7
18	59.0	38.3	35.1	10.2
21	42.3	28.2	25.5	7.5
24	31.6	21.9	20.2	5.6
27	23.9	17.4	14.9	4.3
30	18.7	14.0	11.6	3.5

USC UNIVERSIDADE DE SANTIAGO DE COMPOSTELA

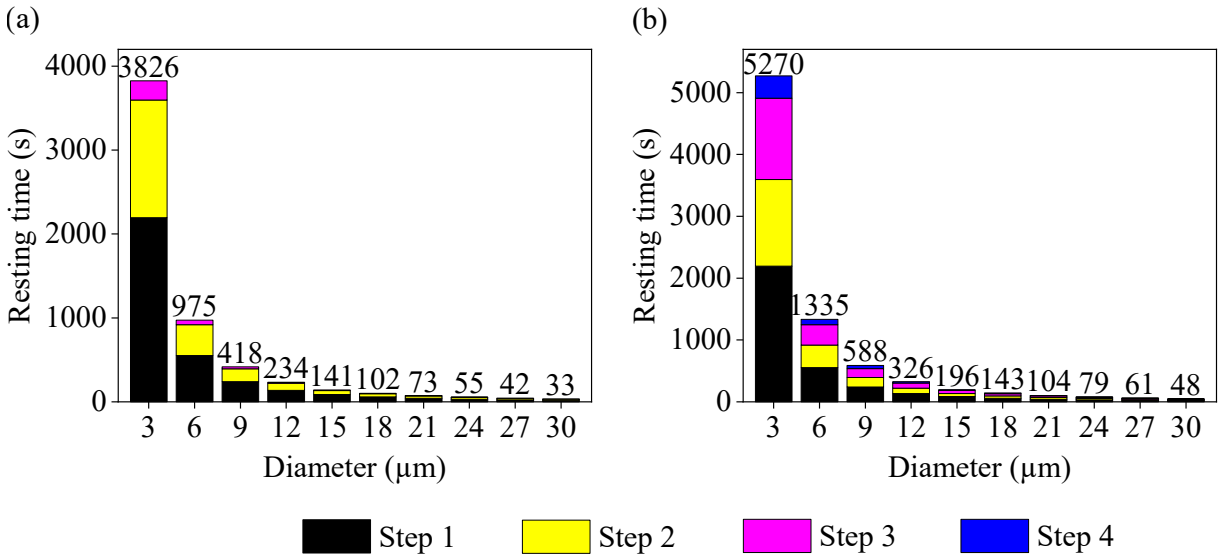

Figure 3.3: Resting times required for the otoconia to reach the final position at each step for each otoconium diameter. A) Resting times were recorded until otoconia left the posterior semicircular canal. B) Resting times recorded including all necessary steps for the otoconia to fall into the interior of the posterior ampulla.

Since these results summarize what happens during an indefinite time for the maneuver, to get closer to reality, it is also important to study what happens during the usually employed resting times. Therefore, two different resting time conditions were studied to evaluate the position attained for otoconia. In Figure 3.4a, when the resting time is limited to 30 s, otoconia greater than 15 µm exit the posterior semicircular canal during step 3, but otoconia smaller than 15 µm do not have sufficient time to achieve the exit. In step 4, they finally become trapped in the posterior semicircular canal. In the case of the resting time limited to 60 s, as depicted in Figure 3.4b, a similar outcome occurs, but this time otoconia of 12 and 9 µm exited the posterior semicircular canal during steps 3 and 4, respectively. This indicated that only smaller otoconia remained inside the posterior semicircular canal.

USC
UNIVERSIDADE DE SANTIAGO DE COMPOSTELA

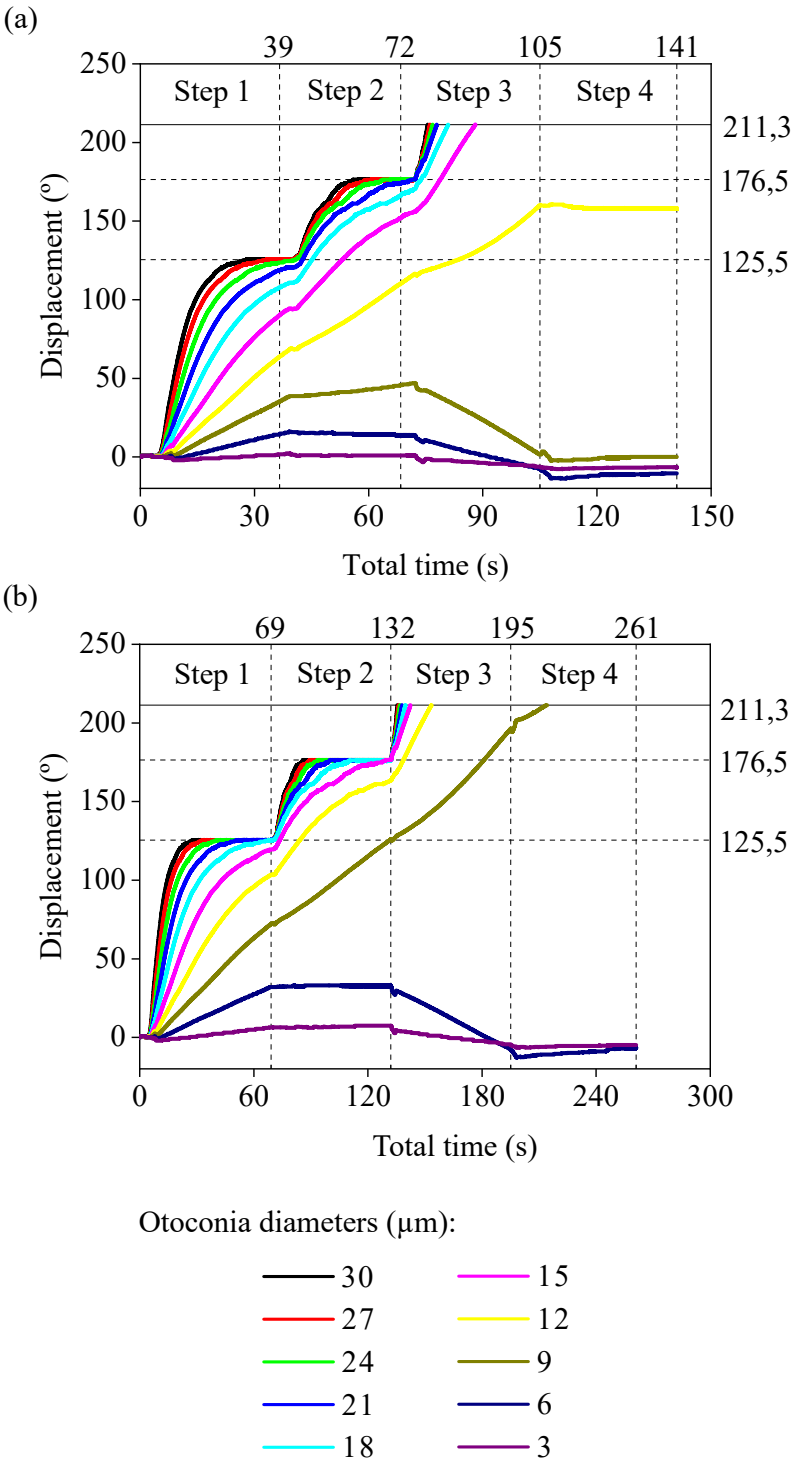

Figure 3.4: Displacement of otoconia and total time needed to exit the posterior semicircular canal (resting time + rotation time). Dashed lines indicate the final angular position for each step and the time block period required for (a) 30 s, and (b) 60 s resting time conditions.

3.1.1.2 Personalization of the Epley maneuver

In the previous section, an analysis of otoconia for the standard EM under different resting time conditions was provided, highlighting potential causes of failure that may hinder the

success of the procedure. In this section, we consider the modifications to the maneuver presented in Table 2.9 to potentially provide a solution to these causes. A summary of the results for each substep is provided in Figure 3.5, where comparisons can be made to determine which head orientation provides better outcomes.

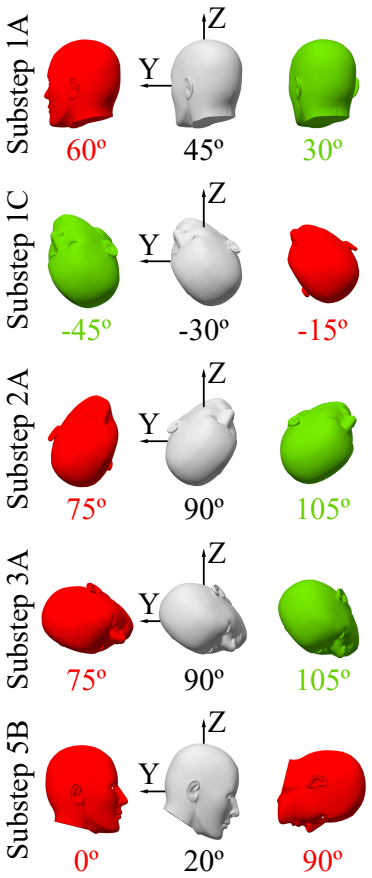

Figure 3.5: Head orientations representing the range of angle variations for each substep, as outlined in Table 2.9. The standard position is denoted in gray, while red indicates poorer performance, and green signifies better performance. For the optimal position for substep 5B, refer to Figure 3.7.

For the initial position of the EM, different initial locations of the otoconia were studied, and it was found that even in the most unfavorable position, such as being close to the posterior cupula, otoconia can advance along the semicircular canal during the next steps.

For personalized rotations of the first three steps, Table 3.2 can be consulted. In substep 1A, rotating an angle ϑ lower than the standard 45º provides a greater angular displacement δ for the otoconia. The displacement increased as the orientation moved away from the standard position. The resting time remained practically constant, indicating that otoconia can be displaced by a larger number of degrees without necessarily requiring longer resting times. Conversely, angles larger than 45º yield a smaller displacement. In substep 1C, the angular displacement of the otoconia increases when the angles of rotation are above the standard 30º and decreases when below 30º. In step 2, a rotation angle over 90º leads to a larger angular displacement of the otoconia, while angles under 90º result in worse outcomes. This effect becomes more pronounced as the angle deviates further from 90º.

Table 3.2: Displacement of otoconia δ for different angle of rotation ϑ in the substep 1A, 1C, 2A and 3A. In the substep 3A, otoconia achieve different positions once they are out of the posterior semicircular canal.

Substep 1A		Substep 1C		Substep 2A		Substep 3A	
ϑ (º)	δ (º)	ϑ (º)	δ (º)	ϑ (º)	δ (º)	ϑ (º)	δ (º)
30	128.9	-15	106.7	75	29.9	75	Superior canal
35	128.4	-20	111.8	80	31.7	80	Superior canal
40	127.3	-25	122.5	85	35.9	85	Superior canal
45	125.5	-30	125.5	90	51.2	90	Utricle backside
50	120.5	-35	127.7	95	61.5	95	Utricle frontside
55	112.3	-40	132.4	100	63.0	100	Utricle frontside
60	112.4	-45	133.6	105	63.3	105	Utricle frontside

The analysis of step 3 indicates that an angular rotation below 90º can cause otoconia to fall inside the superior semicircular canal, potentially transforming a simple posterior BPPV into a superior or multi-canal BPPV, as elucidated in Figure 3.6a. On the other hand, the standard position of 90º leaves the otoconia on the backside of the utricle, as shown in Figure 3.6b, which may result in otoconia falling into the ampullary region during the next step, as mentioned in the previous section. Positions above 90º move otoconia to the frontside of the utricle, practically placing them over the macula, as seen in Figure 3.6c. Despite this, all positions effectively displaced the otoconia out of the posterior semicircular canal, and the time required for the otoconia to exit the canal was nearly identical. However, the resting times needed to complete step 3 differed depending on whether the otoconia passed through the common crus or entered the superior semicircular canal.

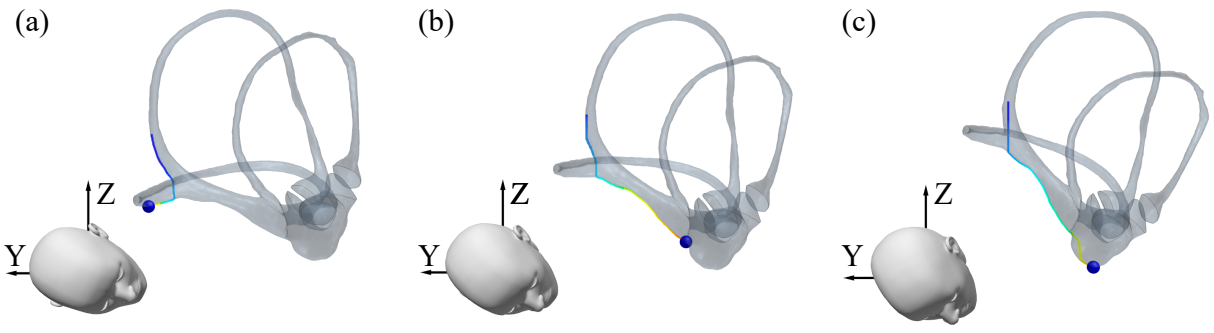

Figure 3.6: Different positions reached by otoconia when it is applied the step 3 with a rotation angle of A) 75º, B) 90º, and C) 105º.

USC
DE SANTIAGO
DE COMPOSTELA

For step 4, three different initial positions corresponding to the possible final positions observed during step 3 were evaluated. Refer to Table 2.9 for further information. All otoconia that start at the backside of the utricle or in the superior semicircular canal fall into the posterior ampullary region from the utricular side. When they start at the frontside of the utricle, smaller otoconia fall into the posterior ampulla, but larger ones do not.

In the analysis of the combined steps 4 and 5, when avoiding resting time between them, the majority of otoconia fell inside the posterior ampullary region or finished at the backside of the utricle, regardless of the initial position chosen for step 4. However, different degrees of rotation for substep 5B yielded different results. These different situations were analyzed to determine the final success of the maneuver based on the probability of treatment failure (PTF), as shown in Figure 3.7a. When otoconia start on the backside of the utricle, they all fall into the ampullary region. This indicates that combining steps 4 and 5 produces similar results to implementing them separately. But when the starting position of the otoconia is on the frontside of the utricle, larger particles are displaced towards the backside of the utricle or the posterior ampulla, while the smaller ones remain on the frontside of the utricle. Figure 3.7b shows a map of the final positions depending on the otoconium diameter and angle of rotation for this scenario. Performing the standard 20º nose-down rotation causes some otoconia to fall into the ampullary region. However, if no rotation is applied in substep 5B, all otoconia remain on the backside of the utricle, which is not desirable. A large angle of rotation (larger than 75º) is needed to maintain all otoconia on the frontside of the utricle, leading to a successful outcome.

Another possibility is that otoconia start in the superior semicircular canal. In this case, most of them moved toward the common crus after substep 5A, with only the smaller ones remaining in the canal. If the standard 20º nose-down movement or no rotation during substep 5B is performed, all otoconia still fall inside the posterior ampulla. However, larger rotations (around 75º) force otoconia to move toward the frontside of the utricle. In this case, angular displacements exceeding 80º might cause maneuver failure, as the smaller particles are unable to leave the superior semicircular canal. Figure 3.7c provides an equivalent map as presented in Figure 3.7b, but for this scenario.

Combining these results, a nose-down movement ranging between 75º and 80º during substep 5B ensures a successful step 4-5, independently of the initial position of the otoconia. Figure 3.7d shows a combined map of the scenarios shown in Figures 3.7b and 3.7c.

USC
UNIVERSIDADE DE SANTIAGO DE COMPOSTELA

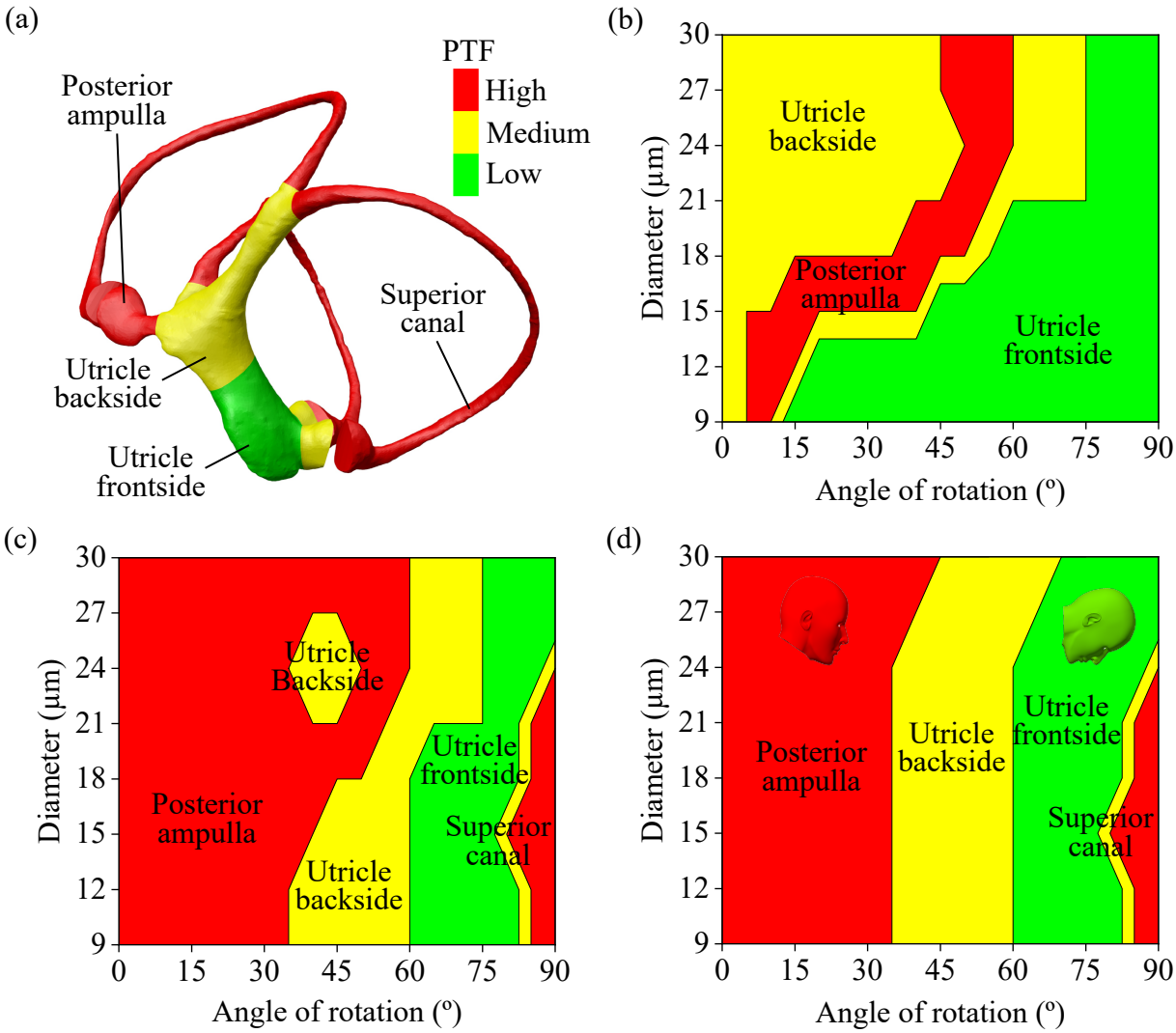

Figure 3.7: Final position of the otoconia depending on their diameter and the angle of nose-down rotation in the substep 5B. A) Regions of the membranous labyrinth were classified according to different probabilities of treatment failure (PTF). The yellow region positioned between the frontside of the utricle (green), the posterior ampulla (red), and the common crus (yellow region that connects the posterior and superior semicircular canals) can be identified as the backside of the utricle. Results are depicted for otoconia starting in B) the frontside of the utricle, C) the superior semicircular canal, and D) the combination of both. In Figure 5A, the orientation of the membranous labyrinth corresponds to 75º nose-down, aligning with the green head orientation depicted in Figure 5D. The standard 20º nose-down orientation is represented by the red head.

3.1.2 Discussion

This study focuses on applying theoretical knowledge regarding the forces affecting BPPV to facilitate the understanding of otoconia displacements during the EM. This could provide helpful insights and answers for clinicians, potentially leading to an improved success rate of the EM. For this reason, the discussion section is divided into three parts. First, we delve into the role of these forces and how they can be interpreted in conjunction with other studies and

theoretical behaviors. Second, a detailed discussion of the numerical analysis conducted is provided for both the standard and personalized EM. Third, a clinical overview highlighting the most important findings that could be clinically useful for implementation in future EM procedures is provided.

3.1.2.1 Biophysics behind the Epley maneuver

The movement of otoconia inside the semicircular canal, as shown in Figure 3.1, is consistent with previous results based on one-dimensional, two-dimensional, and three-dimensional models [65, 85, 87] or particle models using the lattice Boltzmann method [89]. To properly understand the role of the forces acting on the otoconia, this discussion section is divided into two parts: the situation during rotation and after rotation. Finally, some of the limitations of this mathematical model are discussed.

During rotation, the transport of otoconia is primarily determined by inertial forces, which become more significant for rotations with respect to the hip center owing to the larger distance from the origin of rotation. Conversely, rotations with respect to the head center lead to a decrease in inertial forces, which become approximately equal to gravitational forces. Therefore, all the forces presented in Equation (2.13) are relevant; see the methodology section 2.3 Dimensionless numbers for further information. Additionally, faster rotations result in increased inertial forces because they are linearly proportional to the angular velocity. This strategy is also employed in other CRPs, such as the Sémont maneuver, which relies on a high angular velocity for its success [90, 91]. In contrast, the EM results indicate that the displacement of otoconia during rotation is relatively small compared to that after rotation. This observation aligns with the established understanding that the EM is a CRP based on gravitational forces rather than inertial forces [18].

After rotation, the otoconia movement is primarily determined by the forces presented in Equation (2.13) without the influence of the inertial terms. Hence, only the combined effects of drag, buoyancy, and gravitational forces exerted on the otoconia act on the endolymph, generating a change in velocity, as expressed in Equation (2.15). Consequently, endolymph displacement generates vestibular stimulation that evokes the positional nystagmus observed during BPPV. Among these three forces, the gravitational force is always dominant, causing otoconia to move along the direction of gravity. As a result, otoconia can be observed rolling down along the walls of the labyrinth and detaching from them at specific points, which depends on the anatomical properties of the membranous labyrinth and its orientation with respect to the gravitational force; see Figure 3.2. As the size of the otoconium decreases, the dominance of the gravitational force is reduced, making the buoyancy force more relevant. Because the buoyancy force always acts in the opposite direction to gravity, smaller otoconia move at a lower velocity compared to larger otoconia, and thus require more time to reach their final position [92]. This phenomenon also explains why otoconia move in a single file along the bottom inside the surface of the canal, as observed in Figure 3.1, and has been predicted theoretically and observed experimentally in animals with glass microbeads inserted into their canals [62, 93]. The resting time analysis from Table 3.1 and Figure 3.3 agrees with this description, showing that the resting time increases approximately in proportion to the square of the diameter. This behavior closely aligns with the Stokes formula in Equation (2.36) and with other studies that compared resting time with nystagmus onset latency [87].

Incorporating a more complex model, such as one with elastic walls or sticky properties

USC DE COMPOSTELA

for otoconia due to the presence of remains of the otolithic membrane attached to them [94] or accounting for their collision, would likely increase resting times. Resting times can also differ if accumulative otoconia are considered in certain portions of the geometry, as in the canalith jam [95]. However, this is not expected to occur in this model because the number of particles selected for the study is low, and clumps of otoconia typically disperse during their motion along the semicircular canal [62]. Finally, these resting times were obtained with idealized spherical otoconia. When the shape factor is considered, otoconia with less spherical shapes (closer to the actual geometry of the otoconium) require longer resting times to achieve successful EM [96].

3.1.2.2 Numerical analysis

The initial position of the otoconia at the start of the EM depends on the anatomy of the posterior canal in each patient, as the otoconia are positioned at locations of minimum potential energy when the head is at rest. All initial positions studied in this human membranous labyrinth resulted in positive outcomes because otoconia can advance along the semicircular canal during subsequent steps. This advancement is facilitated by the inertial force generated by rotation, which helps expel otoconia away from the ampulla, preventing them from becoming trapped after step 1 of the EM.

Furthermore, the initial position may vary if a Dix-Hallpike test is performed before the EM. Numerical simulations indicate that performing a Dix-Hallpike test before the EM would not significantly affect the outcome of the maneuver, and a lower nystagmus intensity during the EM may not necessarily indicate better or worse performance, but simply that otoconia may have started with the advantage of being displaced away from the ampulla, which could explain fatigue [62]. For instance, a clinical study observed an increase in the duration of nystagmus and severity of symptoms during the loaded Dix-Hallpike test [97]. Based on my analysis, rotating the head downward before initiating the maneuver, as in this clinical experiment, moves the otoconia closer to the ampullary region and results in a longer path during step 1. This could be the reason for the duration and severity of nystagmus, which could enhance the diagnosis. However, regarding appropriate treatment, it may be beneficial to maintain the head in the supine position for several minutes to ensure that otoconia move away from the ampullary region and settle before initiating the maneuver.

There were no significant complications involved in the first and second steps of the EM, as all head positions studied were effective in achieving the displacement of the otoconia away from the ampullary region. The standard movements defined for these steps were based on an idealized orthogonal configuration of the semicircular canals. However, the orientation of the planes that create the semicircular canals can vary among individuals [82], suggesting that an optimal position that is dependent on this orientation can be expected. This study did not include an extensive analysis comparing the behavior of otoconia in terms of anatomical properties, such as the bent toroidal shape of the posterior semicircular canal or the range of angular variation in its normative plane. Despite this, we can observe that in certain instances, otoconia may descend freely, achieving larger velocities. In other instances, depending on the local orientation of the canal in relation to gravity, otoconia may roll along the wall, thus requiring more time to reach the same final position. Therefore, minimizing the contact between the otoconia and the wall allows them to travel larger distances without necessarily requiring longer resting times, as shown in Table 3.2. Based on these observations, we can infer that the orientation and

USC UNIVERSIDADE DE COMPOSTELA

anatomical peculiarities of specific sections of the semicircular canal, where the otoconia are set to move, are more important than the averaged plane commonly used to determine the angular relationships between the semicircular canals.

A discussion has arisen regarding the possibility of placing the head of the patient on a pillow to alleviate anxiety [14] or moving the head by less than 30º during step 1, particularly when the patient has limitations on their neck movement. Clinical studies have reported minor differences in their effectiveness. However, the numerical analysis presented here indicates that the greater the rotation angle below the bed plane for step 1, the larger the displacement of otoconia, potentially resulting in better effectiveness. This optimization with respect to the excursion angle was also observed in in vitro models for the Sémont maneuver [88] and in clinical trials [98], where deviations larger than those studied here could result in undesired outcomes during the equivalent step or reduced efficacy.

The displacement of the otoconia during step 2 was lower than that achieved during the previous step, as shown in Table 3.2. This is because the local orientation of the posterior canal is less vertical than that in the first step, leading to irregularities and perturbations in the canal walls having a more significant impact. In this case, if the rotation of the head is much lower than the standard position, there is a possibility of otoconia falling toward the ampulla due to the change in the slope of the posterior semicircular canal. To avoid this, it is important to maintain the position of the head below the bed plane during this step.

Step 3 is considered the most critical phase of the maneuver, and various modifications have been proposed to facilitate the entrance of otoconia into the common crus [87]. This study revealed that even a minor deviation in the final position of the head can result in unsatisfactory outcomes. For instance, the downbeating nystagmus that occurs when a patient returns to an upright head position [99] can be elucidated by the results presented in Figure 3.6a. When the rotation angle is lower than 90º during step 3, the otoconia may move inside the superior semicircular canal, potentially evoking downbeating nystagmus in step 4. This observation was also reported in a vector analysis of BPPV [100]. It is also worth noting that this step alone can position the otoconia close to the macula if a rotation exceeding 90º is achieved, as illustrated in Figure 3.6c. However, such neck excursions may be challenging, and the use of repositioning chairs may be beneficial for achieving the required positioning, particularly in patients with limited mobility [101].

Regardless of the initial position studied in step 4, the majority of otoconia fell into the posterior ampullary region. This confirms that when otoconia are at the backside of the utricle, there is a higher probability of them descending into the posterior ampulla, as observed in the standard EM in Figure 3.2d. This occurs because the utricular floor has a relative slope related to the axial plane, with the backside of the utricle positioned beneath the frontside. Figure 1.3 compares the axial plane orientation with respect to the utricular plane, which can be considered approximately similar to the left horizontal-right horizontal (LHRH) plane.

Considering this, merging steps 4 and 5 into a single step, referred to as step 4-5, and concluding with an orientation of the membranous labyrinth that keeps otoconia far from the ampullary entrance is important for the success of the maneuver. Although there is controversy regarding the effectiveness of this last substep 5B, and it is typically discarded [69, 102], the numerical results for this anatomy indicate that not only is it essential, but it is also required to have an angle of rotation larger than the 20º originally proposed by Epley [18]. The reason behind this is that a larger angle of rotation allows otoconia to move along the utricular floor due to gravity in the direction of the frontside of the utricle, something that does not occur during the

standard step, as shown in Figure 3.2e. Furthermore, clinical studies have suggested that there are fewer residual symptoms when the head is inclined forward [103], which likely indicates that a greater number of otoconia have reached the frontside of the utricle, as suggested by the 75º nose-down positions in the simulations shown in Figure 3.7d.

Note that the otoconia finish at different locations despite starting at the same position during step 4-5, as can be seen in the graphs in Figure 3.7. This variation is due to the specific locations they reach during rotation, as they experience slightly different inertial forces. Consequently, the gravitational forces acting afterward displaced them to different regions of the membranous labyrinth.

Finally, step 6, which involves placing the head of the patient in an upright position, results in the movement of the otoconia to the posterior ampulla or the backside of the utricle. These findings imply that it is essential to maintain the previous position (75º nose-down at substep 5B) for as long as possible, establishing a new stable position in the utricle, with the aim of placing otoconia over the utricular macula. Previous research conducted on bullfrogs indicated that the expected time for otoconia refixation to the utricular macula ranges from 1 to 5 min [104]. Furthermore, maintaining otoconia in the utricle helps their dissolution because they are in contact with a larger volume of endolymphatic fluid [105]. Clinical trials have demonstrated that postural restrictions following the application of the EM lead to increased effectiveness [106]. Therefore, postural restrictions utilized to prevent vertical orientation of the utricle floor would impede the movement of otoconia into undesired regions and facilitate refixation or dissolution of the otoconia.

3.1.2.3 Clinical overview

During the results section, it was explained that the EM could not be successful for two reasons: the position of the labyrinth relative to the direction of gravity and the resting time employed. Both factors are interrelated, meaning that if we do not employ sufficient resting time, we may not achieve the correct solution, even if we have correctly oriented the head of the patient.

This complex situation of both time-position problems is something in which the use of numerical simulations of the EM might result in a very useful tool. However, it is important to note that the findings presented in this study were obtained for a specific human membranous labyrinth, and clinical validation of these results in a larger set of cases should be performed. Nevertheless, some general recommendations can still be applied by clinicians to prevent potential failures during the EM. Table 3.3 summarizes the potential errors encountered and how they could be solved. Steps 1 and 2 were useful for displacing the otoconia further away from the posterior ampulla and rotating them more degrees than the standard position. Step 3 allows the otoconia to exit the posterior semicircular canal and slight deviations can move them into undesired regions. Steps 4 and 5, performed together, were more effective than applying them independently. Additionally, in substep 5B, rotating the head further down than the standard position could allow otoconia to reach the utricular macula, and maintaining this position for a few minutes would facilitate refixation to the utricular macula.

The range of angular deviation studied in Table 3.2 falls within the range of errors observed during the EM with and without guidance devices [107]. In fact, a lack of precision was more frequently observed in the steps of the maneuver where there was a higher susceptibility to failure. The findings presented here suggest that success or failure may sometimes be

USC UNIVERSIDADE DE COMPOSTELA

determined by errors of only a few degrees, underscoring the importance of accurately positioning the head of the patient (a task that is not always accomplished). The use of nystagmography goggles with integrated gyroscopes is recommended, as they provide support for tracking nystagmus and degrees of rotation during the maneuver. In addition, chairs can assist in aligning the membranous labyrinth at various angles, as determined by numerical simulations [108, 109], which could be potentially useful for personalized CRP.

Table 3.3: Summary of the Epley maneuver (EM), including the probability of treatment failure (PTF), potential errors, and possible solutions for each step.

Step	PTF	Potential error	Solution
0	Low	Otoconia start close to the cupula wall.	Wait some minutes before starting the EM with the patient upright.
1	Low	Otoconia delayed.	In substep 1A, rotate by less than 45º. In substep 1C rotate more than 30º.
2	Medium	Otoconia delayed or move backward.	Rotate more than 90º. Maintain the head below the bed plane.
3	High	Otoconia enter the superior semicircular canal or the backside of the utricle.	Rotate more than 95º for otoconia remain on the frontside of the utricle.
4	High	Otoconia fall in the posterior ampulla.	Perform both step 4 and step 5, without resting time.
4-5	High	Otoconia fall in the posterior ampulla.	Place the head in the step 5B around 75º to leave otoconia in the frontside of the utricle.
6	Medium	Otoconia fall in the posterior ampulla or in the backside of the utricle.	Wait some minutes before starting step 6 to allow otoconia to refixate on the utricular macula.

Based on the physical description of the EM, the resting times obtained in Table 3.1 should be considered as a reference for the minimum resting time needed for otoconia to achieve their final position during each step. However, to understand the combined effect of successive steps, it is necessary to refer to Figure 3.4, where the total displacement of otoconia is compared for two different resting time conditions. When the resting time is increased, smaller otoconia can continue to advance, facilitating expulsion from the posterior semicircular canal. This is significant when considering the average size of otoconia in humans, which is approximately 10 µm. Simulations indicate that they can only be expelled when steps are performed for 60 s, rather than the 30 s typically applied during the EM [69, 102]. If residual symptoms persist after completing the maneuver [110, 111], this probably means that the orientation of the labyrinth was correct, but the time was insufficient. In this case, repeating the maneuver with longer resting times would be recommended. In fact, personalizing the EM by adapting the resting time of the maneuver depending on the size of the otoconium evoking positional nystagmus for a certain patient would be the optimal approach. However, it is currently not possible to

determine with certainty the mixture of otoconia responsible for nystagmus. Furthermore, the resting time required for the smallest otoconia size is of the order of tens of minutes for each step, whereas the time allotted for clinicians with each patient is usually limited to several minutes for the entire maneuver.

3.1.3 Summary

This study evaluated the effectiveness of the EM for treating BPPV in the posterior semicircular canal, exploring potential modifications through numerical simulations of a specific human membranous labyrinth obtained via micro-computed tomography (μCT). The analysis demonstrates that the standard EM is not uniformly effective, suggesting that slight variations in head position could significantly impact its success in ensuring otoconia reach the utricular macula. Additionally, the recommended resting times are likely insufficient, as smaller otoconia require more time owing to the smaller gravitational force they experience.

This study suggests that personalized modifications to the EM, based on numerical simulations considering individual anatomical variations, could improve treatment outcomes. These techniques can help predict the optimal head position and resting time for each patient during the entire treatment maneuver, offering valuable insights to clinicians that cannot be obtained from clinical or imaging observations alone. This approach could alleviate functional disability associated with persistent vertigo and potentially reduce healthcare costs.

3.1.4 Future work

Based on the findings from this study, it seems reasonable to anticipate that a personalized approach, tailored to the specific anatomy of an individual's membranous labyrinth, could improve the success rate of the EM, especially in patients who are refractory to standard treatment. Although this study demonstrated that numerical simulations are likely to be useful, clinical validation by applying these personalized maneuvers to real patients is necessary.

This effort is currently underway, involving collaboration with several hospitals in the Galician region (Complexo Hospitalario Universitario de Santiago, Pontevedra, and Lugo), together with the Nonlinear Physics Group, where I developed my dissertation. This national project is financed by grants from the Acción Estratégica en Salud 2023 of the Instituto de Salud Carlos III (2024-2026), with appropriate approval by the Bioethics Committee. Additionally, we received direct financial support through the Acelerador de Transferencia program from the University of Santiago de Compostela and contributions from international companies interested in our work. Notably, Interacoustics, a leading company in the vestibular medical devices sector, provided us with equipment valued at 90000 € for this study. Other companies have also shown interest in the development of our project, demonstrating the need to address these types of pathologies.

This clinical study will include 54 refractory patients who do not respond to the standard EM after three attempts. The standard protocol includes magnetic resonance imaging (MRI) of patients to rule out neurological disorders, which will be used to reconstruct their bony labyrinths and analyze their vestibular anatomy. The membranous labyrinth of the refractory patient was then obtained based on the centerlines computed from a μCT dataset and the centerlines of the bony labyrinth in question, using a custom code that we plan to intellectually protect soon. Numerical simulations to determine the optimal EM were then performed for the

predicted membranous labyrinth of the patient, similar to the study presented here. Finally, the results were compiled into a report shared with clinicians. These clinicians will then compare the outcomes of patients treated in the TRV chair using the standard EM versus the personalized EM. This TRV chair allowed for accurate rotations, ensuring that the maneuver was performed optimally, as suggested by the simulations.

The preliminary results of the study indicate that the anatomy of the vestibular system may explain why some patients are refractory to conventional repositioning maneuvers. As hypothesized, these standardized maneuvers do not consider the variability in canal orientation, preventing otoconia from being expelled from the canal once the maneuver is completed. However, the inclusion of more patients in the coming years is necessary to statistically confirm this finding and to share it in scientific publications.

Similar to the EM, other maneuvers for the treatment of BPPV could be studied. Despite the Epley Maneuver being the most commonly used, there are dozens of other maneuvers referenced in the literature, some of which have discrepancies regarding their effectiveness. The use of this mathematical model could help to accept or reject maneuvers employed today, such as the Yacovino maneuver for the treatment of superior semicircular canal BPPV, which I am currently testing.

3.2 Head impulse test

In the previous section, mathematical models were discussed as a means of treating common vestibular disorders, such as BPPV. In this section, the implementation of a higher complexity model, including the elastic cupulae solid regions and the endolymphatic fluid region in a fluid-structure interaction model, is presented. This model permits to determine the vestibular stimulation during one of the most widely used diagnostic tools, the head impulse test (HIT). For further information on the methodology followed for this research topic, refer to the sections discussing the HIT study in chapter 2 Methodology.

As outlined in the introduction section 1.1.4 Head impulse test, the HIT involves performing rapid head rotations in different planes corresponding to the orientations of the semicircular canals [23], as depicted in Figure 1.3. Similar to the EM, it was hypothesized that personalizing the HIT could be achieved by adjusting the direction of rotation based on the patient's unique membranous labyrinth morphology. This is particularly useful for the HIT, as it independently assesses vestibular function in each semicircular canal.

Previous research suggests that rotating the head in a direction orthogonal to the plane of a semicircular canal maximizes the stimulus in that canal, whereas rotations within the plane of the canal generate minimal stimulation. However, these optimal directions also affect other semicircular canals because their arrangement is not perfectly orthogonal [82, 112]. Therefore, identifying the prime direction that maximizes stimulation in one canal while minimizing it in others is crucial for personalized diagnosis [11, 113]. This optimal rotation plane induces a vestibulo-ocular reflex (VOR), predominantly from the stimulation of a specific canal, thereby facilitating accurate vestibular function evaluation.

As discussed in the introduction section 1.2.1 Vestibular mathematical modeling, various mathematical models have been developed to replicate the complex behavior of the vestibular system [11, 33, 50, 72, 73, 114, 115]. These models have advanced our understanding of endolymphatic fluid and cupula dynamics during rotation. However, some of these models fail to provide a comprehensive view of vestibular stimuli or the effects of interconnected

semicircular canals. For instance, recent studies have indicated that inertial effects produce different vestibular stimulation patterns depending on the origin of the rotation [71]. To achieve realistic vestibular responses, accurate numerical simulations must consider the center of the head as the origin of rotation, an aspect that has often been overlooked in previous studies.

This study aims to overcome these limitations by evaluating the response of all six cupulae by varying the rotation direction relative to the head center using a typical HIT rotation, as illustrated in Figure 2.6. By measuring the shear strain over the crista ampullaris region, we expect to obtain more accurate results than those of previous models, potentially uncovering new insights. Ultimately, this enhanced mathematical model seeks to deepen our understanding of vestibular system responses and illustrates that the development of personalized diagnostic techniques relies on advanced numerical methods.

3.2.1 Results

To provide a comprehensive description of the results obtained from the HIT numerical simulations, the results section is divided into several segments. First, a biophysical description of the most important parameters related to the vestibular system and stimulation for a specific scenario is presented. Subsequently, the results of the stimulation for all possible head positions are explained, creating a 3D map of stimuli that allows for the determination of the maximum (MAX) and minimum (MIN) stimulation directions for each crista ampullaris. This allows an analysis of the angular relationships between these extremes of stimulus and with respect to the vestibular anatomy, such as the planes of the semicircular canals and cupulae. Finally, a brief explanation of the impact of the origin of rotation and its possible role in the stimulation of vestibular receptors is provided.

3.2.1.1 Qualitative analysis of effect of rotations

Qualitative analysis of the effect of rotations is critical for understanding vestibular system behavior during the HIT. This section focuses on the dynamics of the endolymphatic fluid and its impact on cupulae during rotational movements. This analysis provides a foundation for how rotations influence the endolymph flow and the resulting shear strain XY on the cristae ampullares, which will be determined next to determine the MAX and MIN directions of stimulation.

During rotation, the endolymphatic fluid moves, generating a complex structure of fluid dynamics that varies depending on the membranous labyrinth region. Figure 3.8 shows the results for the left membranous labyrinth during the deceleration phase of the counterclockwise rotation with respect to the Z-axis. The maximum endolymphatic velocity was obtained in the utricle, where a centered counterclockwise vortex was generated. Additionally, ampullofugal Poiseuille flow occurs in the horizontal semicircular canal, whereas the velocity in the other canals remains practically null. When rotations are performed in other directions, the endolymphatic fluid in the other semicircular canals starts to increase or decrease, depending on their relative orientation with respect to the plane of rotation. A vortex in the utricle is always present regardless of the direction of rotation considered.

USC UNIVERSIDADE DE SANTIAGO DE COMPOSTELA

Figure 3.8: Quantitative variables used to determine the vestibular stimulation during numerical simulations of the head impulse test (HIT). Two different views allow for better visualization of the effects of counterclockwise rotation with respect to the Z-axis (corresponding to stimulation on the plane of the horizontal semicircular canal) during the deceleration stage. Three different physical parameters can be observed: endolymphatic velocity in all fluid regions plotted by plane sections, cupula wall displacements at the horizontal, posterior, and superior cupulae, and shear strain XY on the crista ampullaris for each cupula.

USC
UNIVERSIDADE DE SANTIAGO DE COMPOSTELA

This endolymphatic flow generates a displacement in the three cupulae, which is greater in the wall facing the utricular region in all cases, probably caused by the stronger pressures generated by the vortex in the utricle. This displacement was greater in the middle of the cupula walls than at the borders because these borders were attached to the membranous labyrinth walls, as illustrated in Figure 3.8.

This displacement occurs in the entire domain of the cupula, including the location of the hair cells, which are located in the crista ampullaris. In Figure 3.8, it can be seen that the shear strain XY is maximum and of opposite sign (blue and red) at both sides of each crista ampullaris. This shows simultaneous excitation and inhibition of hair cells that will depend on their location in the crista ampullaris.

Another parameter useful for understanding the interconnection of semicircular canals is the endolymphatic velocity streamline generated during rotation. In a similar scenario of counterclockwise rotation in the Z-axis direction, the endolymphatic fluid starts in a specific semicircular canal, exits this region, and enters other locations of the membranous labyrinth. For instance, in Figure 3.9, the velocity streamlines exiting the horizontal semicircular canal (blue) are divided, with some flowing to the common crus and others to the utricle, entering the vortex, and finally distributing into the three semicircular canals.

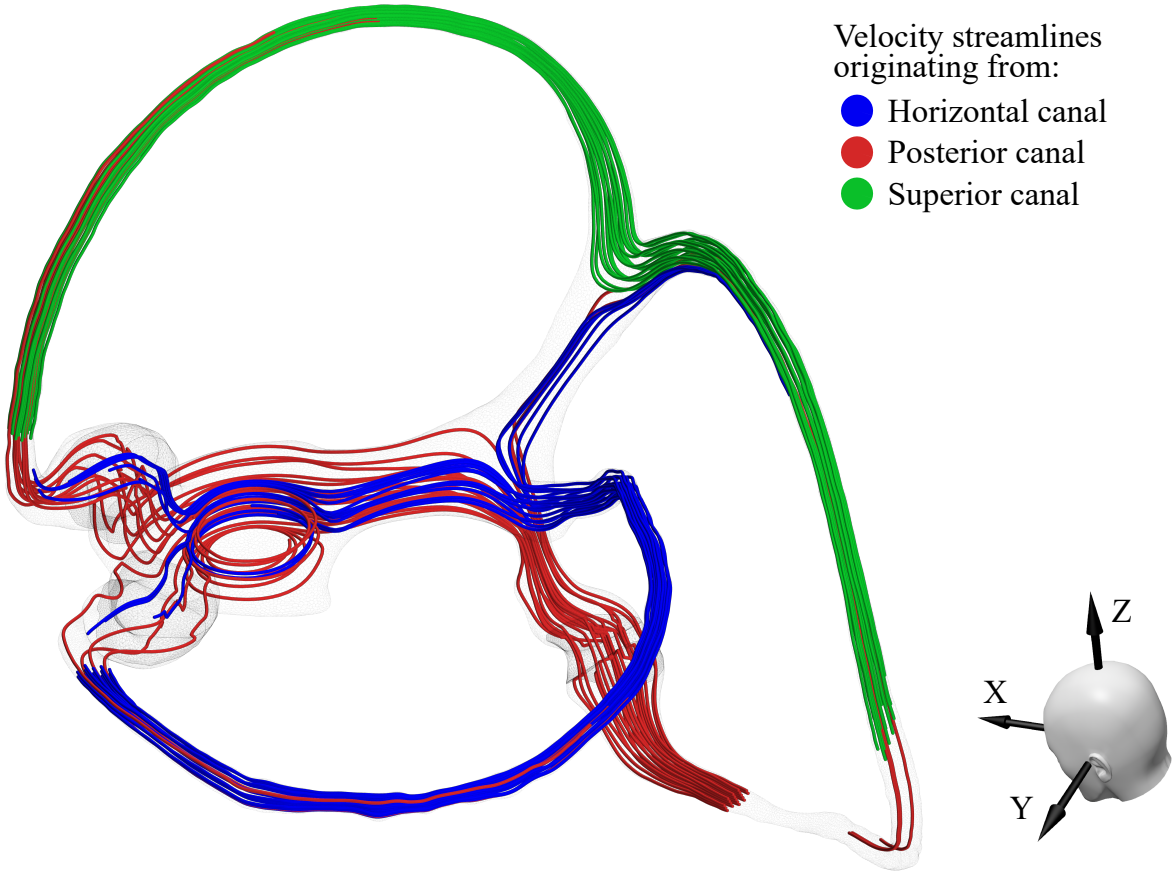

Figure 3.9: Endolymphatic velocity streamlines for the left membranous labyrinth during the head impulse test (HIT). The streamlines are color-coded based on their origin, with each streamline commencing from a different semicircular canal.

USC UNIVERSIDADE DE SANTIAGO DE COMPOSTELA

3.2.1.2 Stimulation response of cristae ampullares

In the previous section, a qualitative analysis of the effects of rotations during the HIT was discussed. We now focus on the specific responses of the cristae ampullares to these rotations. This measurement will be performed based on the analysis of shear strain XY, which is the best parameter for assessing the stimulation of the crista ampullaris during rotations, as discussed in section 2.8 Measurement of the vestibular stimulation.

As an example of the measured results conducted for all simulations in this study, Figure 3.10 shows the averaged shear strain XY response in all cristae of the left and right membranous labyrinths. Specifically, it shows the effect of applying a counterclockwise rotation in the Z-axis direction, corresponding to the stimulation results shown in Figure 3.8. Note that the coordinate system used for the HIT is the head nose-down, as explained in section 2.6 Coordinate systems, with the horizontal canal plane coinciding with the axial plane of the head.

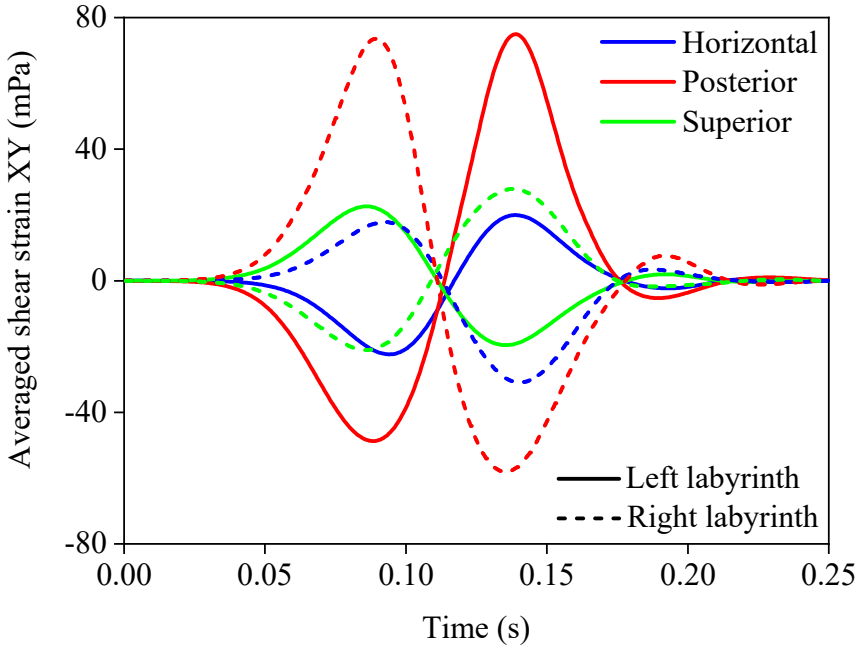

Figure 3.10: Averaged shear strain XY on all cristae ampullares for the left and right membranous labyrinths during a counterclockwise rotation in the Z-axis direction corresponding to the standardized head impulse test (HIT) for the horizontal semicircular canal. Positive values indicate excitation, and negative values indicate inhibition. The left and right cupulae are differentiated by solid and dashed lines, respectively (using the same color code as cupulae in Figure 2.1).

The averaged shear strain XY measured in the cristae responds to the acceleration function of the HIT showed in Figure 2.6. A brief delay (0.01-0.02 s) was observed between the head acceleration and cristae response. Furthermore, when the head stopped at 0.2 s, the shear strain over the cristae continued for approximately 0.05 s. Considering the positive and negative values, when the average shear strain XY on a specific crista from the left labyrinth is positive, the response for the same crista on the right labyrinth is negative, and vice versa. This implies that when one crista is excited at the same instant, the equivalent crista in the other labyrinth is inhibited.

By calculating the area under the curve for the averaged shear strain XY responses, it is

possible to quantify the overall stimulation of each cupula and determine the percentage of excitation and inhibition. This percentage was determined based on the location of the area: if it is located in the region of positive averaged shear strain XY, it is considered excitatory; if it is located in the region of negative values, it is considered inhibitory. In the specific case of the Z-axis direction shown in Figure 3.10, the stimulation was larger for the right cristae than for the left cristae. Among the different crista pairs, the posterior cristae experienced the highest level of stimulation, followed by the superior and horizontal cristae. For detailed values and percentages of excitatory stimulation, refer to Table 3.4.

Table 3.4: Stimulation results obtained by integrating the averaged shear strain XY for each crista during rotation in the Z-axis direction shown in Figure 3.10. Values in parentheses represent percentages of excitatory stimulation.

	Cristae ampullares stimulus (mPa.s)		
Labyrinth	Horizontal	Posterior	Superior
Left	1.56 (43.3%)	4.63 (53.4%)	1.67 (55.9%)
Right	1.86 (38.8%)	5.06 (55.0%)	1.95 (55.4%)

Analyzing the results for excitation and inhibition percentages along all directions, the asymmetry between excitation and inhibition increases as the stimulation value decreases. The regions where this asymmetry is most pronounced are in the directions along the coronal plane (φ = 0º and φ = 180º) and directions along the axial plane (θ = 90º), reaching a maximum at the intersection of both planes, corresponding to the direction of the ±Y-axis. Refer to Figure 1.3a for a visual aid.

3.2.1.3 Mapping the stimuli

After explaining how to determine the average shear strain XY in the previous section, this section focuses on mapping the stimuli responses for all possible directions of rotation. This comprehensive analysis will provide a deeper understanding of how different rotation angles impact the vestibular system and help identify the directions for maximum and minimum stimulation based on the averaged shear strain measured in each crista ampullaris.

Figures 3.11, 3.12, 3.13, and 3.14 show a color-coded stimulation 2D map for each crista ampullaris projected onto the north and south hemispheres, as illustrated in Figure 2.7, based on spherical coordinates θ and φ. The colors in these figures represent the intensity of the crista ampullaris response obtained from simulations of the mathematical model for different rotation directions, as described in section 2.7.2 Rotation for the head impulse test. The red color indicates the direction of maximum stimulation, whereas the dark blue regions represent the directions of the lowest stimuli. These diagrams are shown for the left and right membranous labyrinths considering a counterclockwise rotation maneuver in Figures 3.11 and 3.12, and the equivalent results for clockwise rotation are presented in Figures 3.13 and 3.14. The largest stimulation recorded corresponded to the posterior crista, followed by the superior and horizontal crista (6.19 mPa.s, 2.66 mPa.s, and 2.14 mPa.s, respectively).

USC UNIVERSIDADE DE SANTIAGO DE COMPOSTELA

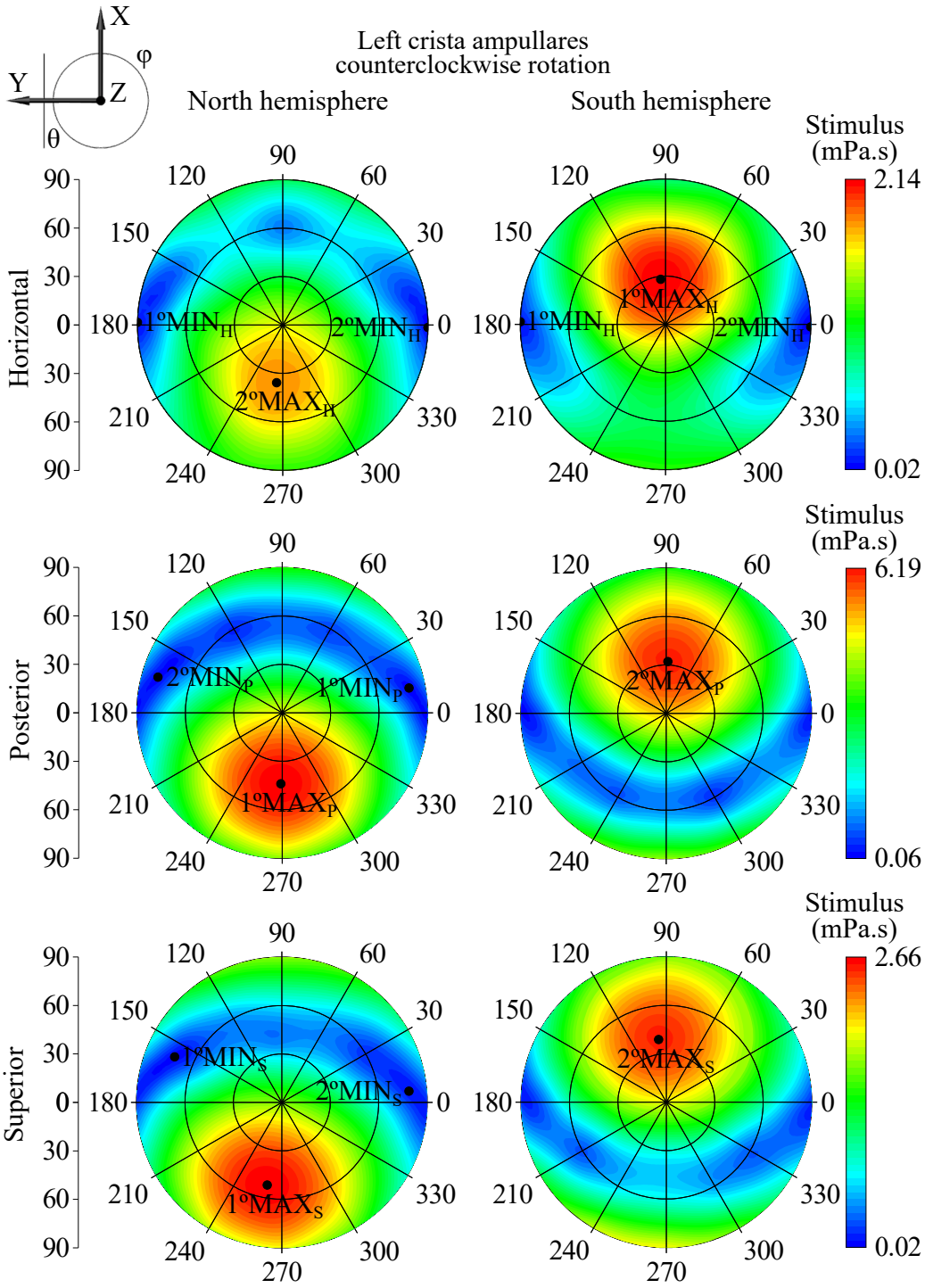

Figure 3.11: Map of stimulation response on each left crista for counterclockwise rotation measured as the averaged shear strain XY results in each direction. The angular axis indicates the φ coordinates, and the radial axis indicates the θ coordinates in spherical coordinates. The hemispheres were projected over a 2D plane corresponding to the axial plane of the head (XY) from the Z-axis perspective. In this projection, the X-axis corresponds to $\varphi = 90º$ and the Y-axis corresponds to $\varphi = 180º$. The maximum (MAX) and minimum (MIN) directions are plotted as dot points, considering that the 1ºMAX represents the extreme with the highest stimulation and 1ºMIN represents the extreme with the minimum stimulation.

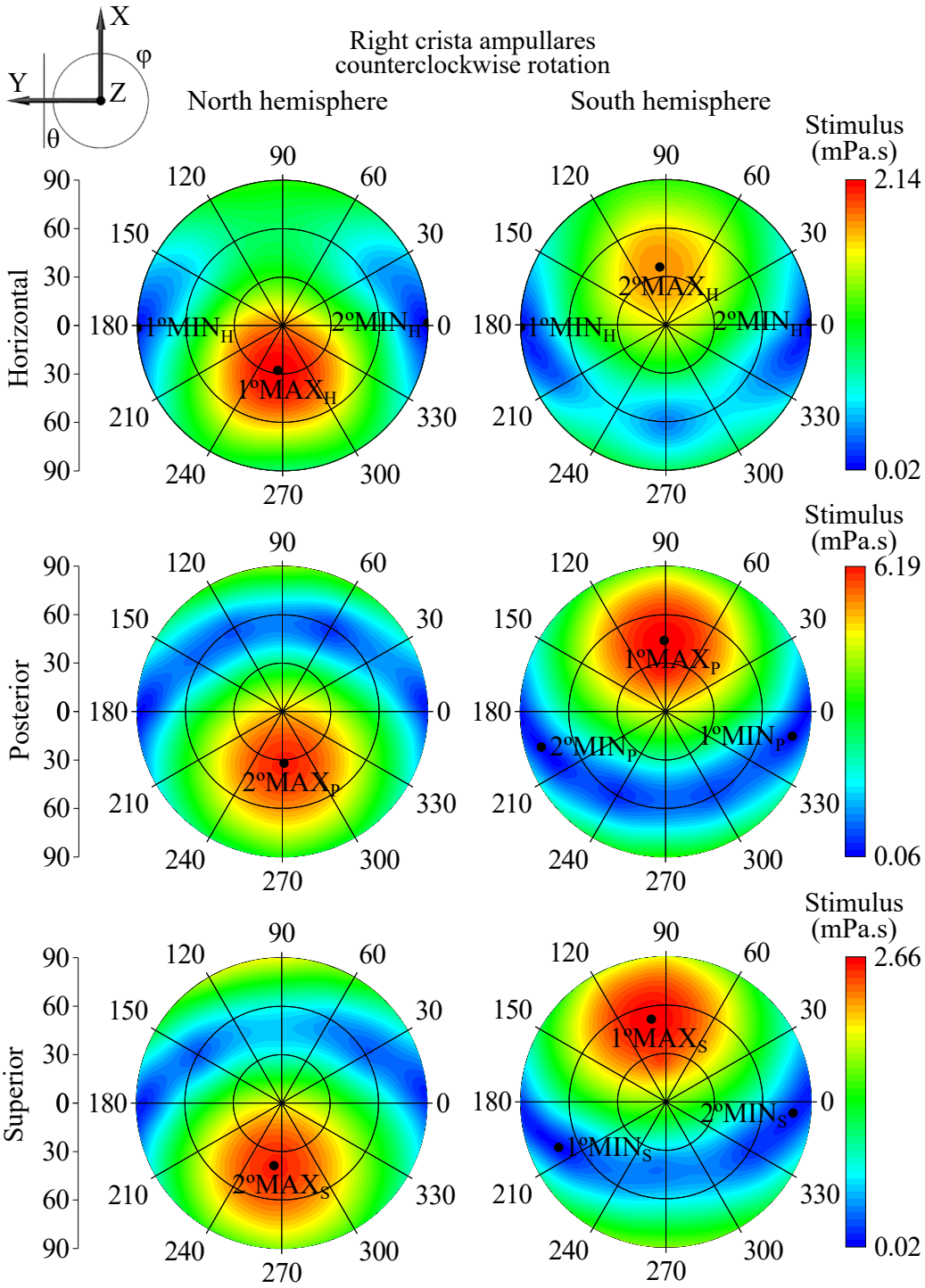

Figure 3.12: Map of stimulation response on each right crista for counterclockwise rotation measured as the averaged shear strain XY results in each direction. Similar considerations to those in Figure 3.11.

USC
UNIVERSIDADE DE SANTIAGO DE COMPOSTELA

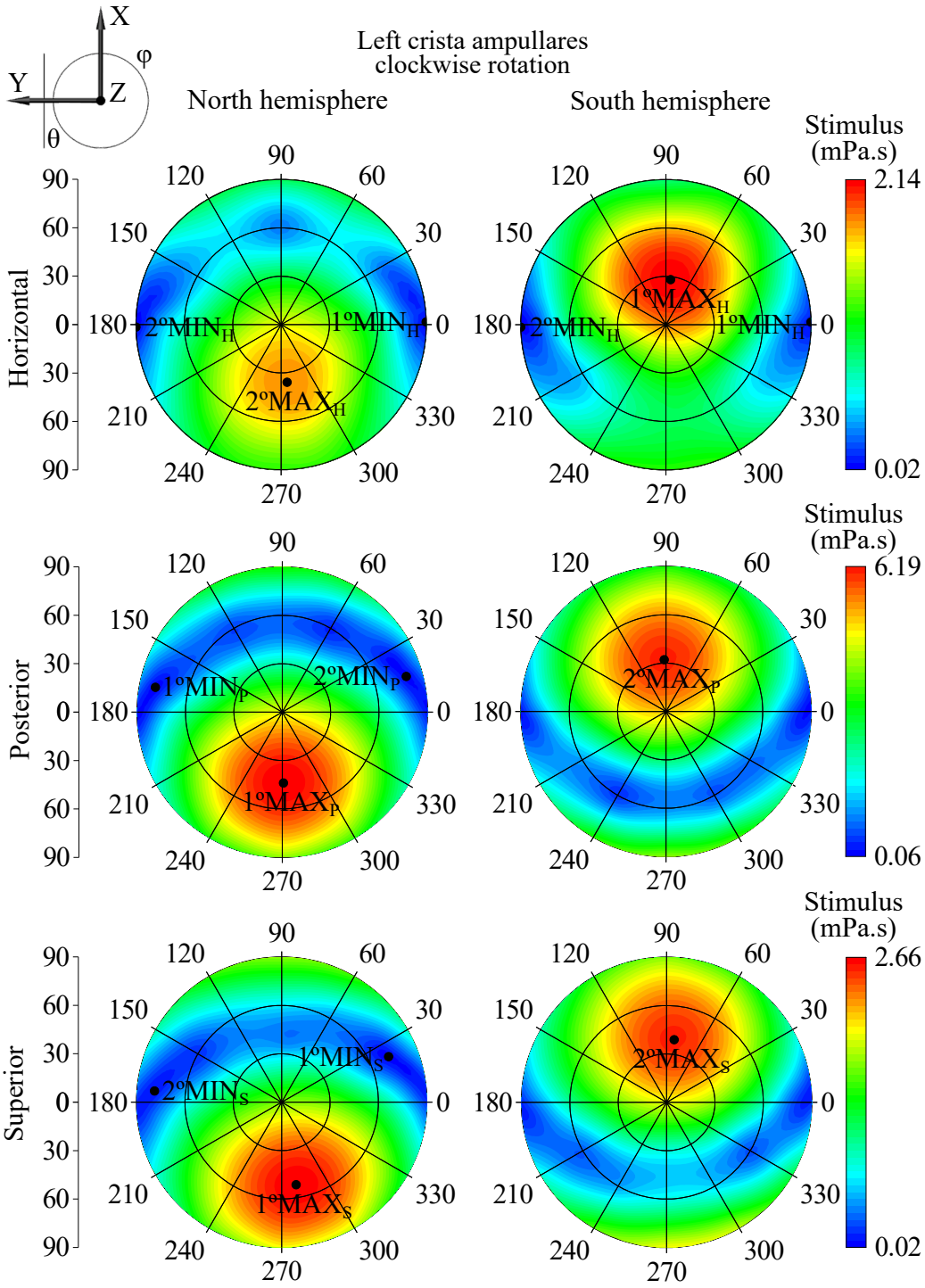

Figure 3.13: Map of stimulation response on each left crista for clockwise rotation measured as the averaged shear strain XY results in each direction. Similar considerations to those in Figure 3.11.

USC
UNIVERSIDADE DE SANTIAGO DE COMPOSTELA

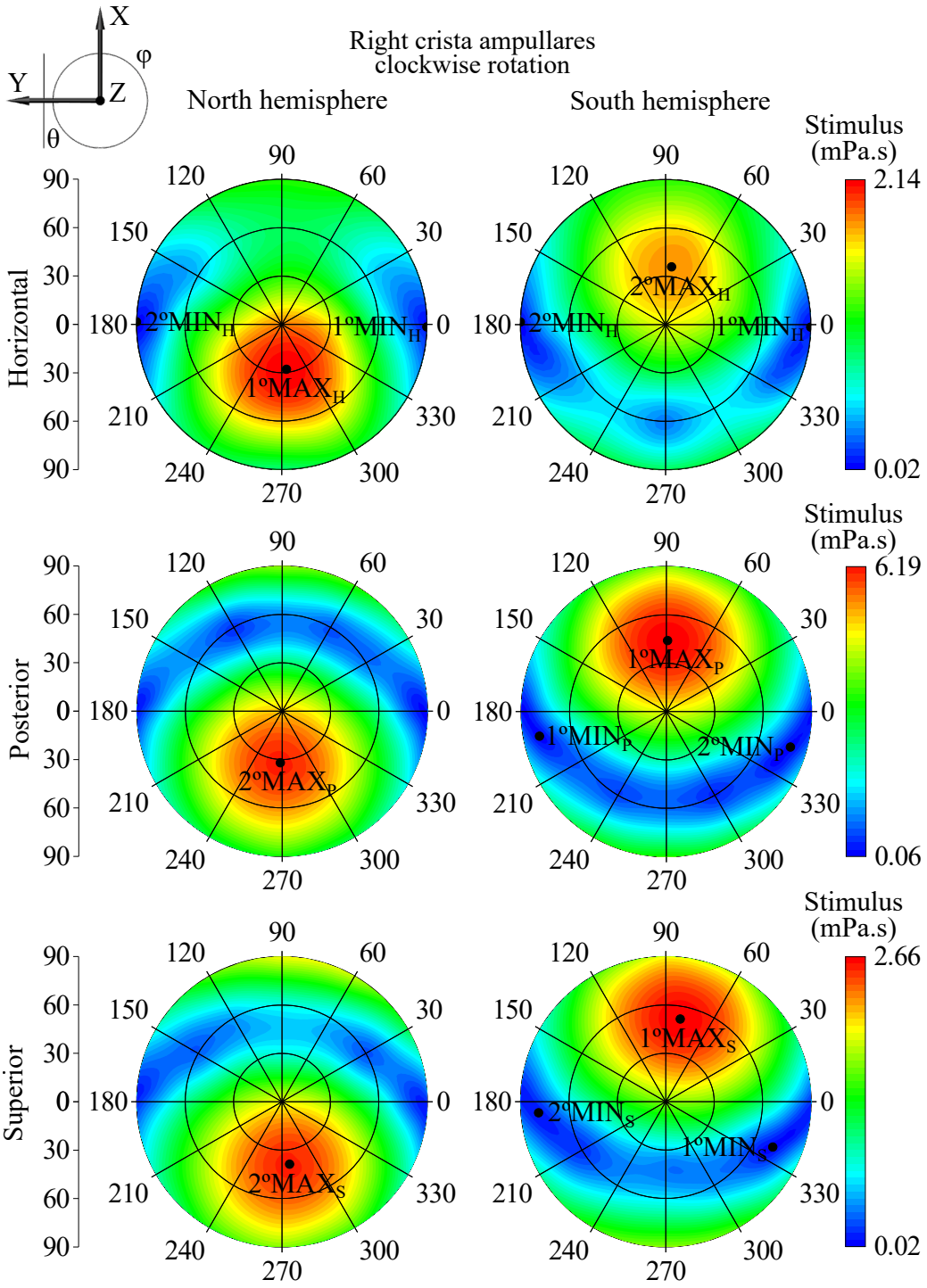

Figure 3.14: Map of stimulation response on each right crista for clockwise rotation measured as the averaged shear strain XY results in each direction. Similar considerations to those in Figure 3.11.

In all cases, the regions with maximum stimulation (red regions) are surrounded by a ring (blue region) at approximately $\theta = 90°$ with respect to the maximum region. This ring represents the direction of the minimum stimulation. Regardless of the crista being studied, there is always one maximum region located in the north hemisphere and another in the south hemisphere. Note that for the left labyrinth, independent of a clockwise or counterclockwise rotation, the MAX

direction for the horizontal crista is larger in the south hemisphere of the head, while for the posterior and superior cristae, it is in the north hemisphere (black dots in Figures 3.11 and 3.13). This pattern was reversed when the right labyrinth cristae were considered (black dots in Figures 3.12 and 3.14). For the MIN directions, we found that both were present in the same hemisphere, except for the horizontal minima, which coincided exactly with the equator (the axial plane formed by the XY plane in Figure 2.7). The spherical coordinates of these extremes are listed in Table 3.5.

Table 3.5: Maximum (MAX) and minimum (MIN) directions for the left and right cristae ampullares during the counterclockwise and clockwise rotations. Spherical coordinates for each extreme equivalent to the plotted dots in Figures 3.11, 3.12, 3.13 and 3.14.

	Left cristae counterclockwise rotation			Right cristae counterclockwise rotation		
Extreme	Direction vector	φ (º)	θ (º)	Direction vector	φ (º)	θ (º)
1ºMAX$_H$	(0.467, 0.049, -0.883)	96	152	(-0.467, 0.049, 0.883)	264	28
2ºMAX$_H$	(-0.585, 0.061, 0.809)	264	36	(0.585, 0.061, -0.809)	96	144
1ºMIN$_H$	(0.018, 0.999, 0.000)	179	90	(-0.018, 0.999, 0.000)	181	90
2ºMIN$_H$	(-0.018, -0.999, 0.000)	359	90	(0.018, -0.999, 0.000)	1	90
1ºMAX$_P$	(-0.695, 0.012, 0.719)	269	44	(0.695, 0.012, -0.719)	91	136
2ºMAX$_P$	(0.530, -0.019, -0.848)	88	148	(-0.530, -0.019, 0.848)	272	32
1ºMIN$_P$	(0.188, -0.967, 0.174)	11	80	(-0.188, -0.967, -0.174)	349	100
2ºMIN$_P$	(0.271, 0.947, 0.174)	164	80	(-0.271, 0.947, -0.174)	196	100
1ºMAX$_S$	(-0.776, 0.137, 0.616)	260	52	(0.776, 0.137, -0.616)	100	128
2ºMAX$_S$	(0.625, 0.077, -0.777)	97	141	(-0.625, 0.077, 0.777)	263	39
1ºMIN$_S$	(0.372, 0.875, 0.309)	157	72	(-0.372, 0.875, -0.309)	203	108
2ºMIN$_S$	(0.087, -0.978, 0.191)	5	79	(-0.086, -0.978, -0.191)	355	101
	Left cristae clockwise rotation			Right cristae clockwise rotation		
Extreme	Direction vector	φ (º)	θ (º)	Direction vector	φ (º)	θ (º)
1ºMAX	(0.467, -0.049, -0.883)	84	152	(-0.467, -0.049, 0.883)	276	28
2ºMAX	(-0.585, -0.061, 0.809)	276	36	(0.585, -0.061, -0.809)	84	144
1ºMIN	(0.018, -0.999, 0.000)	1	90	(-0.018, -0.999, 0.000)	359	90
2ºMIN	(-0.018, 0.999, 0.000)	181	90	(0.018, 0.999, 0.000)	179	90
1ºMAX	(-0.695, -0.012, 0.719)	271	44	(0.695, -0.012, -0.719)	89	136
2ºMAX	(0.530, 0.019, -0.848)	92	148	(-0.530, 0.019, 0.848)	268	32
1ºMIN	(0.188, 0.967, 0.174)	169	80	(-0.188, 0.967, -0.174)	191	100
2ºMIN	(0.271, -0.947, 0.174)	16	80	(-0.271, -0.947, -0.174)	344	100
1ºMAX	(-0.776, -0.137, 0.616)	280	52	(0.776, -0.137, -0.616)	80	128
2ºMAX	(0.625, -0.077, -0.777)	83	141	(-0.625, -0.077, 0.777)	277	39
1ºMIN	(0.372, -0.875, 0.309)	23	72	(-0.372, -0.875, -0.309)	337	108
2ºMIN	(0.086, 0.978, 0.191)	175	79	(-0.086, 0.978, -0.191)	185	101

USC

The observed behaviors display symmetry in the coronal plane (YZ plane) and axial plane (XY plane) when comparing the left and right labyrinths. For instance, the maximum

stimulation region of the left horizontal crista is found in the south hemisphere towards the front of the head, whereas the equivalent region for the right horizontal crista is found in the north hemisphere towards the chin. Comparing the counterclockwise and clockwise maps, symmetry exists in the sagittal plane (XZ plane).

3.2.1.4 Maximum and minimum directions

Considering the stimulation maps shown in the previous section, we can now study the orientation of these extremes of stimuli in relation to each other and to the head and vestibular anatomies. This will help to identify any symmetries or correlations in the responses.

By analyzing the stimuli maps, we observed that there are two MAX and two MIN directions for each crista. The directions of these maxima and minima vary depending on whether we consider a counterclockwise or clockwise rotation for the left/right labyrinth, as shown in Table 3.5. However, the degree of stimulation in these directions was similar in all cases because of the symmetries found in the stimulation maps. Table 3.6 lists the values of the stimulation in each crista for the MAX and MIN directions. As an example, Figure 3.15 shows the MAX and MIN directions for all left cristae ampullares during counterclockwise rotation, where it is possible to observe their orientation with respect to the head and the left membranous labyrinth.

Table 3.6: Stimulation of cristae ampullares for maximum (MAX) and minimum (MIN) directions from Table 3.5. These results are similar and independent of the left/right labyrinth or clockwise/counterclockwise rotation. The cursive results are the stimulations for the cristae that correspond to the MAX and MIN directions. The values between parenthesis indicate what percentage of that stimulation is excitatory.

	Cristae ampullares stimulation (mPa.s)		
Extreme	Horizontal	Posterior	Superior
1ºMAX$_H$	*2.14 (39.9%)*	6.06 (57.8%)	2.51 (55.0%)
2ºMAX$_H$	*1.83 (42.3%)*	6.27 (57.8%)	2.55 (56.6%)
1ºMIN$_H$	*0.02 (29.1%)*	0.13 (3.5%)	0.12 (90.3%)
2ºMIN$_H$	*0.02 (78.7%)*	0.15 (96.6%)	0.11 (1.7%)
1ºMAX$_P$	1.81 (42.4%)	*6.34 (58.3%)*	2.61 (56.4%)
2ºMAX$_P$	2.13 (40.1%)	*6.10 (58.2%)*	2.53 (54.4%)
1ºMIN$_P$	0.11 (48.0%)	*0.07 (67.8%)*	0.16 (18.8%)
2ºMIN$_P$	0.11 (61.4%)	*0.10 (10.0%)*	0.06 (81.0%)
1ºMAX$_S$	1.77 (42.4%)	6.22 (58.3%)	*2.66 (56.0%)*
2ºMAX$_S$	2.10 (40.4%)	6.03 (58.3%)	*2.56 (54.5%)*
1ºMIN$_S$	0.23 (57.4%)	0.26 (34.2%)	*0.02 (57.7%)*
2ºMIN$_S$	0.22 (51.0%)	0.46 (57.4%)	*0.09 (4.7%)*

USC UNIVERSIDADE DE SANTIAGO DE COMPOSTELA

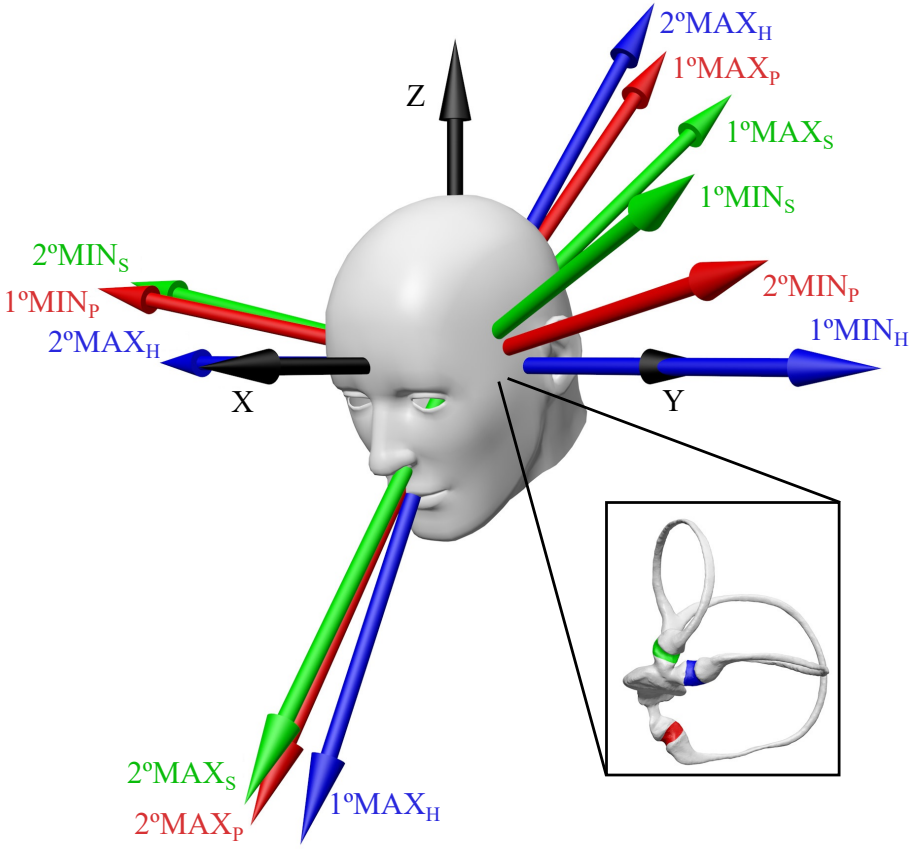

Figure 3.15: Maximum (MAX) and minimum (MIN) directions for cristae ampullares from the left labyrinth during counterclockwise rotation, represented by black dots in Figure 3.11 and their stimulation values in Table 3.6. The left membranous labyrinth representation helps visualize the relationship between the orientation of the semicircular canals and vectors. The color codes of the vectors are defined depending on each crista: blue for the horizontal crista, red for the posterior crista, and green for the superior crista.

The MAX direction produced a stimulation that was approximately 100 times larger than the MIN direction. Stimulation in the two MAX directions for each crista was similar (4 %), except for the horizontal crista, where the difference between the maxima was 17 %. Larger differences were observed between the MIN directions, with the superior direction exhibiting the largest difference (77 %). Regardless of the crista being studied, the posterior crista is always the most stimulated, even when attempting to maximize stimulation in cristae other than the posterior crista.

The angular relationships among all maxima, minima, and maxima-minima are presented in Table 3.7. Ideally, the angular relationships between the same extremes (MAX-MAX and MIN-MIN) should form opposite vectors of 180º, while the relationship between different extremes (MAX-MIN) should be 90º. A deviation from these ideal conditions can be observed in Table 3.8, where the superior crista exhibits the largest discrepancy from the ideal conditions. However, it can be considered that the maxima are approximately orthogonal to the MIN direction, and that the MAX directions are opposite to each other. This holds true for the MIN directions only in the case of horizontal stimulation, but not for the posterior (33.5º) and superior (40.1º) ones.

Table 3.7: Angular relationships between extremes measured in degrees (º). Results are similar for left/right cristae and counterclock/clockwise rotations.

Extreme	1ºMAX$_H$	2ºMAX$_H$	1ºMIN$_H$	2ºMIN$_H$	1ºMAX$_P$	2ºMAX$_P$	1ºMIN$_P$	2ºMIN$_P$	1ºMAX$_S$	2ºMAX$_S$	1ºMIN$_S$	2ºMIN$_S$
1ºMAX$_H$	-	169.8	86.7	93.3	163.5	5.7	96.5	88.9	154.1	11.0	93.2	100.2
2ºMAX$_H$	169.8	-	87.1	92.9	8.7	175.4	91.6	87.7	16.2	171.5	85.0	87.5
1ºMIN$_H$	86.7	87.1	-	179.2	90.0	90.5	164.4	18.0	82.9	85.0	28.1	167.5
2ºMIN$_H$	93.3	92.9	179.2	-	90.0	89.5	15.6	162.0	97.1	95.0	151.9	12.5
1ºMAX$_P$	163.5	8.7	90.0	90.0	-	168.0	91.0	93.0	10.4	172.7	91.4	86.2
2ºMAX$_P$	5.7	175.4	90.5	89.5	168.0	-	91.7	91.2	159.3	8.8	94.7	95.6
1ºMIN$_P$	96.5	91.6	164.4	15.6	91.0	91.7	-	146.5	99.9	95.3	136.3	6.0
2ºMIN$_P$	88.9	87.7	18.0	162.0	93.0	91.2	146.5	-	88.5	83.8	10.5	150.4
1ºMAX$_S$	154.1	16.2	82.9	97.1	10.4	159.3	99.9	88.5	-	162.3	88.8	94.7
2ºMAX$_S$	11.0	171.5	85.0	95.0	172.7	8.8	95.3	83.8	162.3	-	86.6	99.8
1ºMIN$_S$	93.2	85.0	28.1	151.9	91.4	94.7	136.3	10.5	88.8	86.6	-	139.9
2ºMIN$_S$	100.2	87.5	167.5	12.5	86.2	95.6	6.0	150.4	94.7	99.8	139.9	-

Table 3.8: Average deviations from orthogonality (MAX-MIN) and opposition (MAX-MAX and MIN-MIN) of the maximum (MAX) and minimum (MIN) directions of stimulation.

	MAX-MIN (º)	MAX-MAX (º)	MIN-MIN (º)
Horizontal	3.1	10.2	0.8
Posterior	1.7	12.0	33.5
Superior	4.8	17.7	40.1

The angular relationships between the MAX and MIN directions with respect to the orientation of the semicircular canals and cupulae are presented in Tables 2.6 and 2.7. These relationships are summarized in Table 3.9, focusing on the left cristae during the counterclockwise rotation case.

USC
UNIVERSIDADE DE SANTIAGO DE COMPOSTELA

Table 3.9: Angular relationships for left cristae extremes during counterclockwise rotation respect to the normal vector of the semicircular canal planes and the X-axis direction of the cupula planes. Angles are measured in degrees (º). HSC means horizontal semicircular canal, and HC horizontal cupula.

Extreme	$1ºMAX_H$	$2ºMAX_H$	$1ºMIN_H$	$2ºMIN_H$	$1ºMAX_P$	$2ºMAX_P$	$1ºMIN_P$	$2ºMIN_P$	$1ºMAX_S$	$2ºMAX_S$	$1ºMIN_S$	$2ºMIN_S$
Left HSC	152.1	36.9	95.3	84.7	44.4	147.4	74.8	85.1	53.1	141.3	76.9	73.7
Left PSC	105.6	73.8	136.5	43.5	66.5	105.5	57.2	151.8	67.8	114.1	156.0	51.8
Left SSC	98.5	71.6	39.6	140.4	69.3	104.1	152.9	56.4	59.1	103.6	65.1	147.0
Right HSC	151.0	35.8	84.7	95.3	44.2	147.8	85.2	74.9	51.3	140.1	67.1	84.3
Right PSC	101.5	68.5	45.5	134.5	65.4	107.1	146.9	62.0	55.1	107.4	70.4	140.9
Right SSC	103.0	77.4	142.4	37.6	70.4	102.4	51.6	157.8	72.6	110.8	161.3	46.3
Left HC	87.7	97.1	169.2	10.8	92.8	84.6	26.0	170.7	98.3	91.3	161.8	23.3
Left PC	71.1	99.0	39.1	140.9	96.4	76.7	155.7	56.3	86.1	76.4	66.8	153.2
Left SC	119.9	61.9	54.4	125.6	70.1	119.5	111.6	40.5	72.0	110.8	31.6	113.1
Right HC	82.2	90.2	11.9	168.1	91.4	86.7	175.5	29.6	82.9	82.6	39.9	177.6
Right PC	75.7	104.7	142.0	38.0	97.5	75.0	53.1	157.8	98.4	83.4	167.2	50.4
Right SC	123.8	66.4	124.8	55.2	70.9	118.1	41.8	109.3	81.3	116.3	99.0	42.8

Ideally, the MAX direction should align with the normal vector of the canal plane, whereas the MIN direction should lie within the canal plane. Analysis of the deviation for the MAX directions in relation to the normal vector of the canal planes and for the MIN directions in relation to the surface of the canal plane indicated that the MAX and MIN directions were not aligned with the planes of the semicircular canals. As an example, the left cristae during counterclockwise rotation results are shown in Table 3.10, where the horizontal MAX and MIN directions showed a relatively higher alignment with the horizontal canal plane, albeit with significant discrepancies of 32.4º and 5.3º, respectively.

Table 3.10: Average deviation for the maximum (MAX) directions from the normal vector of the canal planes, and for the minimum (MIN) directions from the surface of the canal plane. Results for the extremes obtained for the left cristae during counterclockwise rotation.

	MAX(º)	MIN (º)
Horizontal	32.4	5.3
Posterior	70.5	47.3
Superior	67.8	41.0

Finally, the angular relationships between the normal vectors of the cupula walls with respect to the MAX and MIN directions were examined. In Table 3.11, the results show the deviation for the MAX directions with respect to the plane formed by the cupula walls in contact with the endolymph (YZ plane of each cupula) and the deviation of the MIN directions from the normal vector of the cupula walls in contact with the endolymph (X-axis of each cupula). These findings indicate that there is better agreement when compared with calculations based on canal planes, at least for the MAX directions. However, the superior directions still exhibited a larger discrepancy. Figure 3.16 illustrates the case of the horizontal maximum, where the angular relationships between the horizontal MAX direction with respect to the normal vector of the horizontal canal plane and the YZ plane of the horizontal cupula are shown. The MAX direction aligns approximately with the YZ plane of the cupula (4.7º), whereas it is 32.4º with the normal vector of the canal plane. Equivalent visual representations can be inferred from Tables 3.10 and 3.11 for the MAX and MIN directions with respect to the other canal and cupula planes.

Table 3.11: The average deviation of the maximum (MAX) directions with respect to the averaged plane formed by the cupula walls in contact with the endolymph (YZ plane of the horizontal cupula) and the average deviation of the minimum (MIN) directions with respect to the averaged normal vector of the cupula walls in contact with the endolymph (X-axis of the horizontal cupula). The results consist on the case for the left cristae during a counterclockwise rotation.

	MAX(º)	MIN (º)
Horizontal	4.7	10.8
Posterior	9.8	40.3
Superior	19.4	49.2

USC UNIVERSIDADE DE SANTIAGO DE COMPOSTELA

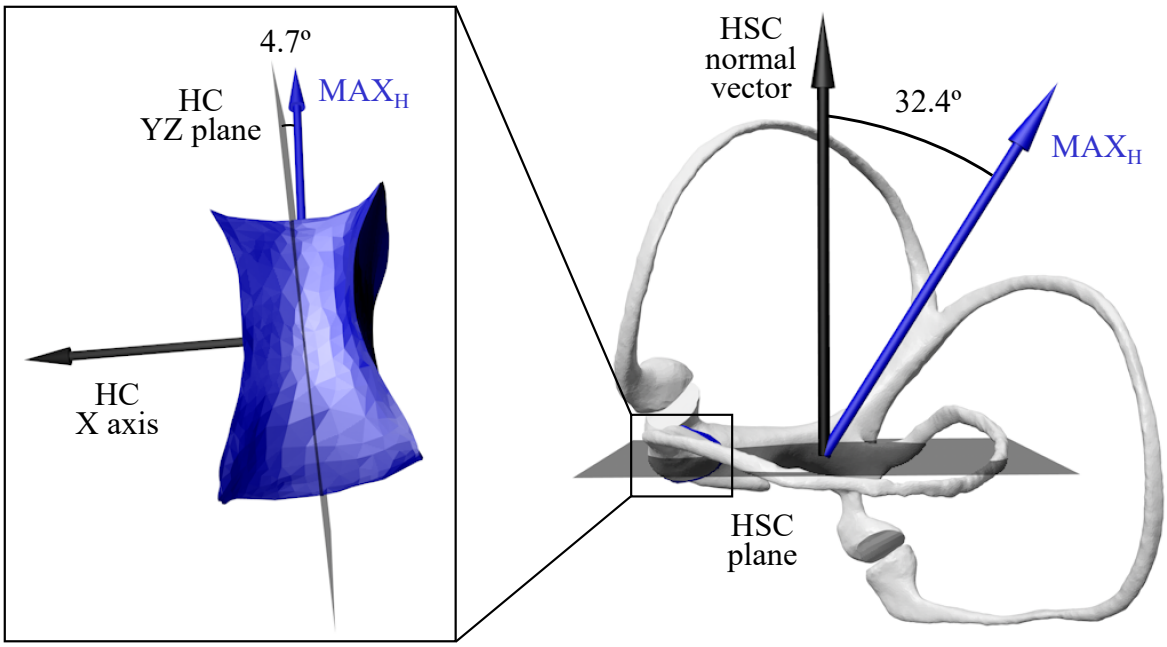

Figure 3.16: Sketch illustrating the angular relationship of the averaged horizontal maximum (MAX) direction with respect to the normal vector of the horizontal canal plane (32.4º) and YZ plane of the horizontal cupula (4.7º). HSC means horizontal semicircular canal, and HC horizontal cupula.

3.2.1.5 Origin of rotation

To determine whether the origin of rotation affects vestibular stimulation, the simulation shown in Figure 3.8 (performed with respect to the center of the head) was repeated with the rotation origin at the center of the horizontal semicircular canal. The results of the averaged shear strain XY for the left cristae ampullares are shown in Figure 3.17. The stimulus was significantly smaller for all cristae when the rotation was centered on the semicircular canal than when it was centered on the head. In addition, the patterns of excitation and inhibition were reversed.

USC
UNIVERSIDADE DE SANTIAGO DE COMPOSTELA

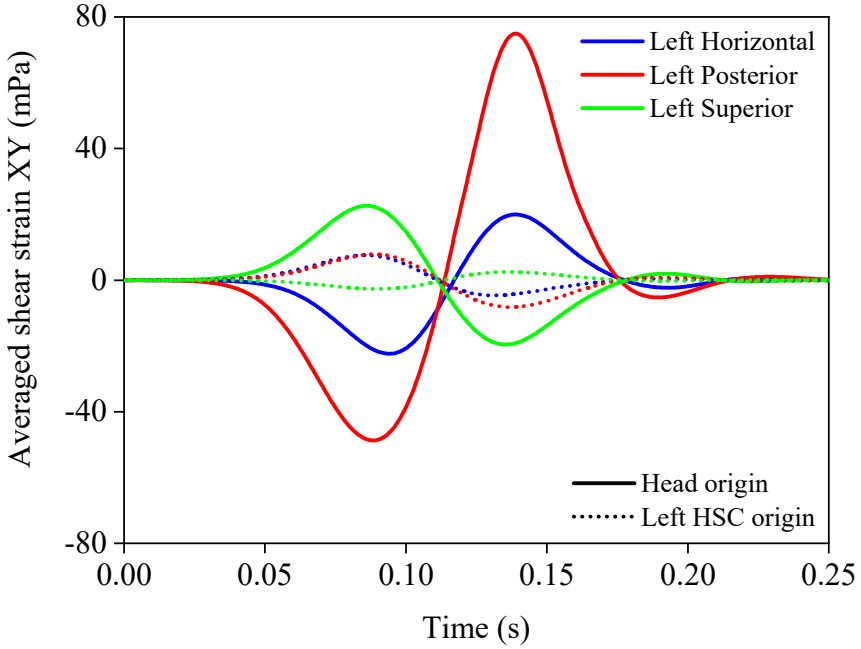

Figure 3.17: Averaged shear strain XY measured at the three left cristae ampullares during a counterclockwise rotation in the Z-axis direction when rotation was performed with respect to the center of the head or the center of the horizontal semicircular canal (HSC), indicated by the straight and dotted lines respectively. Positive values indicate excitation, and negative values indicate inhibition. The color-code criteria are similar to those in Figure 3.10.

3.2.2 Discussion

This study provides novel insights into vestibular stimulation and its potential applications in rotational testing. The discussion section is divided into three subsections, each of which addresses different aspects of the numerical simulation results. The first subsection examines the discrepancies between the expected vestibular stimulation based on the angular velocity and the observed response aligned with the angular acceleration. The second subsection delves into the interpretation of vestibular responses and their relationship to anatomical variations. The third subsection explores how inertial forces and the origin of rotation affect vestibular stimulation, which could possibly explain the differences between these results and previous literature.

3.2.2.1 Biophysical process during the head impulse test

As outlined in the introduction section 1.2.1 Vestibular mathematical modeling, vestibular stimulation is expected to correspond to the velocity of rotation, following a Gaussian function approximately similar to that shown in Figure 2.6. This phenomenon arises because of the integration effect caused by the endolymph within the semicircular canals. However, the numerical simulations revealed a response that was more aligned with the angular acceleration rather than the angular velocity of rotation. This discrepancy is evident when comparing the acceleration function in Figure 2.6 with the stimuli responses in Figure 3.10, which is consistent with previous findings [50, 72]. An initial positive (negative) response followed by a negative (positive) response occurs, which changes sign approximately after the maximum velocity of

the head is attained. The delay and final damping observed in the responses of the cristae can be attributed to the elasticity and restoring properties of the cupula [36].

One possible explanation for this deviation in behavior compared to the prior literature could be attributed to the vortex found within the utricle, as depicted in Figure 3.8. This vortex generates the highest endolymphatic velocities, surpassing those in the semicircular canals, which are anticipated to contribute to response integration. Consequently, a greater cupula displacement occurred from the walls facing the utricle, resulting in a shear strain XY response proportional to the angular acceleration. In addition, Figure 3.9 underscores the importance of a 3D model of the entire membranous labyrinth, because all interconnected regions allow for endolymphatic fluid displacement across all semicircular canals. It is anticipated that the stimuli generated by the rotational effect arise from this complex behavior rather than simply being attributed to the effects of stimulation on three individual semicircular canals.

Finally, the relationship between hair cells and subsequent neural processes was not explored in this study. This is important to mention because although shear strain XY is considered the most reliable physical parameter for determining hair cell stimulation [74], it should not be regarded as the sole factor determining vestibular function. The vestibular response is also influenced by afferent responses, which depend on mechanoelectrical transduction, mechanical adaptation [116], and other factors, such as amplification [43]. In animal studies, the inhibitory signal was found to be lower than the excitatory signal [77], indicating that the simple addition of both labyrinth signals does not accurately correlate with eye displacement during rotation. However, the MAX and MIN directions for each crista ampullaris are independent of neurological processes [40]. Therefore, numerical results are relevant for clinical rotational testing.

3.2.2.2 Interpretation of the stimuli

The responses of the left and right cristae during rotation were in opposite phases, indicating that when one crista was excited, the corresponding crista in the other labyrinth was inhibited. This phenomenon results in symmetry in the responses, which has also been observed in cupula deflection simulations [72]. However, certain directions exhibit higher asymmetry, in which either excitation or inhibition is dominant. This asymmetry was more evident for the MIN directions shown in Table 3.6, which were aligned with the ± Y-axis, as depicted in Table 3.5. In contrast, the example provided along the Z-axis in Table 3.4 exhibits greater symmetry between the excitation and inhibition areas because this direction of rotation is orthogonal to the Y-axis. The increased asymmetry between excitation and inhibition is directly associated with the nonlinearity of the response, as the averaged shear strain XY stops responding to the acceleration function of the head in these directions. According to these results, this nonlinearity is more pronounced in directions with lower stimulation, a finding that has also been experimentally observed [43].

Additionally, the left and right membranous labyrinths were mirrored with respect to the sagittal plane. This mirroring explains the observed symmetries in the stimulation maps for the left/right cristae and counterclockwise/clockwise rotations (Figures 3.11, 3.12, 3.13, and 3.14). However, it is expected that the left and right labyrinths of the same patient will exhibit different anatomical properties [82, 83, 112], leading to a loss of symmetry in the axial, coronal, and sagittal planes. Instead, new symmetry planes adapted to each individual are likely to emerge.

The stimulation results from all these directions were combined to generate a 3D map,

USC UNIVERSIDADE DE SANTIAGO DE COMPOSTELA

which can be explained using the three-dimensional cosine rule [113]. This cosine response explains why two maxima of approximately the same intensity were found for each crista ampullaris, positioned in opposite directions and orthogonal to the MIN direction, as shown in Table 3.8 and Figure 3.15. The area formed by the minimum stimulation in all maps in Figures 3.11, 3.12, 3.13, and 3.14 resembles a ring-like structure, similar to the null plane predicted by the cosine rule [113].

However, upon comparing the orientation of these cosines in space, they do not align with the previous results from the literature, which indicated that the maxima are roughly aligned with the normal vector of the semicircular canal planes, and the plane of minima coincides with the plane of the semicircular canal. In the stimulation maps shown here, the regions of maximum stimulation were almost identical for all three cristae. In Table 3.7, it can be observed that these MAX directions are far from orthogonal to each other, as expected from the approximate orthogonal orientation of the semicircular canals in the studied membranous labyrinth anatomy [9]. Consequently, the prediction of the prime direction in other studies [11, 113] is not consistent with the findings of the numerical analysis presented herein.

3.2.2.3 Inertial forces and origin of rotation

Based on the findings presented in Tables 3.10 and 3.11, the MAX and MIN directions exhibit a stronger alignment with the orientation of the cupulae rather than the semicircular canals. The reason that the maxima appear to respond better to the orientation of the cupula can be attributed to the inertial forces created during rotation, which directly affect the elastic cupula walls, as expressed in Equation (2.20). When the resultant forces over the crista act in the same direction as the deflection of the cupula walls, the shear strain XY over the crista ampullaris reaches its maximum value. Figure 3.16 suggests that this occurs when the MAX direction aligns with the YZ plane of the cupula, as the inertial forces point in the orthogonal direction, coinciding with the X-axis of the cupula. This finding aligns with previous research that determined the dominance of the centrifugal and Euler terms for vestibular stimulation, making the orientation of the semicircular canals and endolymphatic velocity less relevant [71]. However, the vortex in the utricle could also play a significant role, as evidenced by the asymmetrical response generated on the cupula walls [34] and previously described in the discussion.

When rotations are performed with respect to the center of the head, the directions of rotation with respect to the Z-axis tend to maximize the inertial forces, whereas rotations with respect to the Y-axis tend to minimize them. The numerical results confirm that close to these Y-directions, stimulation ceases to respond to acceleration, resulting in a higher nonlinearity of the response. The role of these inertial forces could explain the lower stimulation of the three cupulae simultaneously and the appearance of a higher nonlinearity in the response.

This also explains why the three-dimensional cosines, one for each crista, tend to align in the same direction and not orthogonally, as previously described in a study that used the same membranous labyrinth [9]. This difference could be attributed to the fact that in my simulations, the head rotates around its own center, whereas in their model, the rotation is with respect to the center of the semicircular canals, where the inertial forces are expected to be smaller. The results in Figure 3.17 highlight this differing response when the origin of rotation was varied, with the stimulation being smaller for all cristae when performed with respect to the center of the semicircular canal. The most significant change occurred for the posterior crista, which

USC DE COMPOSTELA

consistently exhibited greater stimulation across most angular directions when rotating with respect to the center of the head. This phenomenon does not occur when rotations from the center of the semicircular canals are considered [113, 117], which can be attributed to changes in the pressure distribution caused by inertial forces and the anatomical location of the posterior semicircular canal [72]. Therefore, performing center-of-the-head rotations is necessary for accurate numerical simulations to provide a reliable response for HIT or other rotational tests.

3.2.3 Summary

The findings of this study highlight several important insights into the biophysics of the HIT and its clinical implications. First, the study revealed that the vestibular stimulation response, as determined by shear strain XY on the cristae ampullares, aligns more closely with angular acceleration rather than the velocity of rotation, as previously described in the literature. This divergence may be attributed to the presence of a vortex within the utricle, where higher endolymphatic velocities could play a significant role compared to the flow within the semicircular canals, which was employed by previous simplified models.

Second, the response patterns observed in the stimulation maps indicate a consistent alignment with a three-dimensional cosine rule, with two opposing maxima orthogonal to a plane of minima. Interestingly, these cosine responses do not align with the orientation of the semicircular canals but appear to correspond better with the orientation of the cupulae. This suggests that inertial forces during rotation acting on both the endolymph and cupula domains may influence this preferred alignment. Furthermore, variations in the origin of rotation affected the final stimulus, highlighting the importance of performing numerical simulations with respect to the center of the head rather than the center of the semicircular canals.

Third, this study advances the understanding of vestibular system function and serves as a valuable tool for enhancing the accuracy and reliability of rotational testing in clinical practice. By focusing on the shear strain XY measured in the cristae ampullares and incorporating a comprehensive 3D model, this study contrasts previous research and offers novel insights into vestibular stimulation. Based on these findings, the identification of new optimal prime directions for rotational testing could provide personalized diagnostic techniques for vestibular disorders.

3.2.4 Future work

Our understanding of the role of the vestibular receptors remains limited. An intriguing question arises regarding how the sensors in the utricular macula distinguish between linear accelerations due to translations and those resulting from rotations, which are often combined in everyday activities. Traditional descriptions of peripheral receptors suggest that the crista ampullaris in the semicircular canals exclusively detects angular velocities, whereas the maculae detect angular accelerations from inertial forces, which can be considered linear accelerations. However, the results of the HIT model challenged these assumptions. Because the cupula experiences inertial forces similar to those of the endolymphatic fluid, it may also function as a sensor of angular accelerations resulting from rotations, enabling the distinction between different types of acceleration during combined translations and rotations. For this reason, the cupula may play a previously unexplored role in this process, something that the model presented here is capable of describing, and I am currently investigating to gain more

insight.

However, a notable limitation of this model is that it only considers the average value of the shear strain XY over the crista ampullaris as a parameter for measuring vestibular stimulation. Based on the observed results of the shear strain XY distribution along cristae ampullares in Figure 3.8, it is conceivable that the precise location of hair cells and afferents within the crista ampullaris plays a significant role, a facet not yet fully understood. To advance the study of vestibular function, the next crucial step would likely involve simulating a comprehensive model that combines this biophysical mathematical model with a neurological model representing a realistic distribution of hair cells over the crista and their connections to different vestibular afferents. Future studies could benefit from interdisciplinary collaboration, particularly by integrating knowledge from biomedical engineering, neuroscience, and otoneurology.

Furthermore, when it comes to personalizing the HIT or any rotational test, the model suggests that considering the orientation of the cupula along with that of the semicircular canals could provide valuable insights. However, implementing these models to determine the optimal directions for clinical practice has several limitations. The most significant limitation is that medical imaging techniques currently lack the precision required to accurately determine cupular regions, which is a crucial aspect highlighted by this study. Although these results were based on a µCT scan of a postmortem patient, obtaining similar high-resolution images in living humans remains challenging. Nevertheless, I am confident that future advancements in image acquisition techniques could provide the resolution required to implement the necessary geometric models for accurate simulations of patients. This aspect is currently being explored based on the in vivo membranous labyrinth prediction code utilized in the BPPV clinical study. These types of tools could provide an accurate description of membranous anatomy, paving the way for personalized medicine in vestibular diagnosis.

3.3 Magnetic vestibular stimulation

In the first part of this chapter, the mathematical model for EM offers guidance for future personalized treatment strategies for vestibular diseases, such as BPPV. Going a step further in the second section, the model included a higher complex simulation based on an FSI model that provided valuable insights into the function of the vestibular system during rotations. This paves the way for future personalized diagnosis, such as the HIT. In this section, the model is enhanced again by implementing the MHD model over the previous FSI model, permitting the measurement of vestibular stimulation based on the magnetic vestibular stimulation (MVS), a field in its early stages that holds the potential for developing diagnostics and treatments based on the effects of magnetic fields.

The underlying mechanisms of dizziness reported on MRI machines are only partially understood. As explained in introduction section 1.1.5 Magnetic vestibular stimulation, ionic currents flowing from dark cells to hair cells couple with the MRI magnetic field. See Figure 2.1 for the visualization of these cells in the membranous labyrinth. This coupling causes a Lorentz force that perturbs the endolymphatic fluid, thereby generating vestibular stimulation [29, 30, 31]. However, this theory does not account for all observed phenomena, including the full physical consequences of these forces on the endolymph or clinical observations, such as vertical nystagmus in healthy adults [29, 118].

This MVS study aims to address these knowledge gaps and provide a comprehensive understanding of the intricate network of biomechanical interactions that occur within the

vestibular system during MRI scans. For details on model coupling, equations, boundary conditions, clinical study, and measurements, refer to the sections of chapter 2 Methodology related to the MVS study. The model was validated against quantitative analyses of three-dimensional eye movements in subjects exposed to MRI magnetic fields. This approach substantiates the role of Lorentz forces in MVS and elucidates the fluid-mechanical pathways that lead to horizontal, vertical, and torsional nystagmus.

3.3.1 Results

This section presents the findings of the MVS study to assess the ability of the model to predict magnetic field effects on the vestibular system. This section examines the sensitivity of the model to various boundary conditions and the associated biophysical variables of the MVS. Moreover, the results of the numerical simulations were experimentally validated for different magnetic field intensities and head orientations, followed by a thorough analysis of the simulated eye movement responses to different head orientations, which contributes to a better understanding of nystagmus caused by the MVS.

3.3.1.1 Sensitivity to the boundary conditions

First, various boundary conditions were tested to understand their impact on the variables responsible for MVS and to assess the robustness of the model. The three modified parameters were age, electric potential (V), and electrical conductivity (σ) to evaluate how these parameters influenced the slow-phase velocity (SPV) of the horizontal and torsional eye components computed from the shear strain XY. The vertical component was always null in the supine condition. Additionally, it was studied how these parameters affected the average electric current density ($\bar{J}$), average Lorentz force ($\bar{f}_l$), and maximum endolymph velocity (v_{max}) in the utricle plane shown in Figure 3.18.

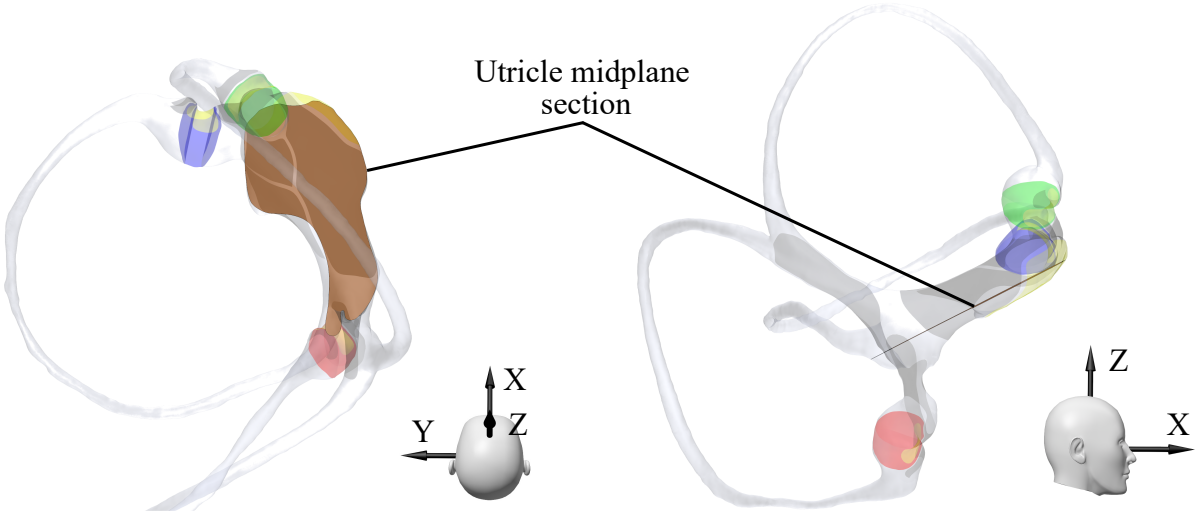

Figure 3.18: The transverse section of the mid-region of the utricle is presented relative to the membranous labyrinth from two different perspectives. This plane was employed to determine the average electric current density, average Lorentz force, and maximum velocity for determining the sensitivity of the electrodynamic potential model to the boundary conditions. Additionally, it served to illustrate the Lorentz forces and velocities in Figure 3.21.

The results are presented in Table 3.12, expressing the relative percentage variation for each tested parameter compared to the standard conditions chosen for the model: 55 years of age, with 0.01 V of electric potential, and conductivities of 1.67 S/m for both endolymph and cupulae.

Table 3.12: Effect of boundary condition on variables defining the magnetic vestibular stimulation (MVS). Relative variation for different ages, electric potential V, and electrical conductivity σ conditions compared to the standard boundary conditions from Table 2.4. Values are presented as percentages. The average electric current density $\bar{J}$, average Lorentz force $\bar{F}_l$, and maximum endolymph velocity v_e^{max} were measured in the section plane of the utricle, as shown in Figure 3.18. Conductivity results are divided depending on the relation between the electrical conductivity of the endolymph σ_e and the cupulae σ_c.

Variable (% per)	Δ age (year)	Δ V (V)	$\Delta\sigma$ when $\sigma_e = \sigma_c$ (S/m)	$\Delta\sigma$ when $\sigma_e < \sigma_c$ ($\sigma_e/\sigma_c = k$ times)	$\Delta\sigma$ when $\sigma_e > \sigma_c$ ($\sigma_e/\sigma_c = k$ times)
$\Delta\bar{J}$	-0.4	0.0	0.0	2.3	1.0
$\Delta\bar{F}_l$	-0.4	0.0	0.0	2.0	0.9
Δv_e^{max}	-0.4	0.0	0.0	1.4	0.7
$\Delta \mathrm{SPV}_{hor}$	-0.4	0.0	0.0	17.1	5.6
$\Delta \mathrm{SPV}_{ver}$	-	-	-	-	-
$\Delta \mathrm{SPV}_{tor}$	-0.4	0.0	0.0	14.6	0.4

First, the model was tested for different ages, ranging from 20 to 90 years. All variables, including the resulting SPV, decreased by 0.4 % per year. This implies that young adults aged 20 years are expected to have an approximately 13 % stronger SPV relative to 55-year-olds, whereas elderly adults aged 90 years have a 13 % lower SPV relative to 55-year-olds. Figure 3.19a shows how the normalized SPV diminishes with age.

Second, the electric potential boundary condition was varied for all hair cell regions simultaneously in the range from 0.001 to 0.1 V. These changes in the electric potential did not affect any of the studied variables.

Third, the electrical conductivity of both the endolymph and cupulae was varied between 0.167 and 16.7 S/m, yielding different results depending on the considered scenario. When both the endolymph and cupula electrical conductivities were equally varied, there was no change in the variables, similar to the effect caused by the electric potential. However, when the relative change between the endolymph and cupulae conductivities was compared, all variables followed a single-exponential growth function, as shown in Figure 3.19b for the normalized SPV. This indicates that when the ratio σ_e/σ_c is smaller than unity, the variables are affected more significantly, as shown in the relative percentages in the $\sigma_e < \sigma_c$ column in Table 3.12. In the case of $\sigma_e > \sigma_c$, there were still changes, but they were smaller because of the characteristics of the exponential function.

USC UNIVERSIDADE DE SANTIAGO DE COMPOSTELA

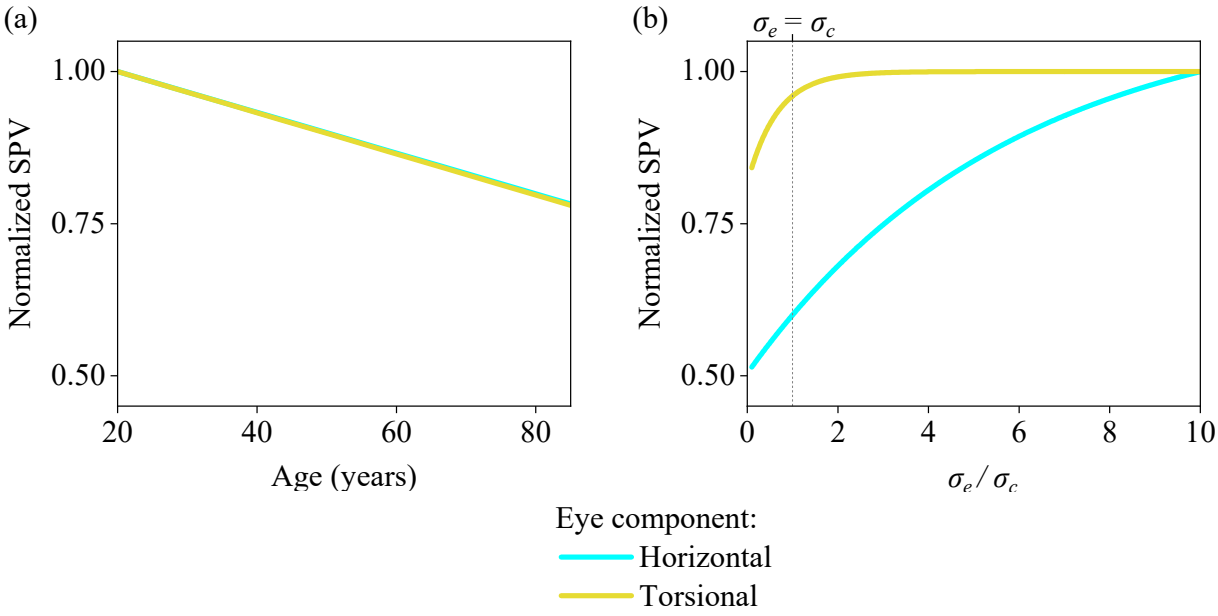

Figure 3.19: Effect of boundary conditions on vestibular parameters used to determine the magnetic vestibular stimulation (MVS). The results are presented for the normalized slow-phase velocity (SPV) for (a) the effect of age and (b) the relative change in electrical conductivity for the horizontal and torsional components. The vertical component was always null.

3.3.1.2 Biophysical variables in magnetic vestibular stimulation

The previous analysis confirmed how changes in the input model parameters affect vestibular stimulation. This relative error seems acceptable, and the model conditions defined in Table 2.4 are useful for interpreting vestibular stimulation. In this section, a more detailed explanation of these evaluated variables is provided to understand the biophysics behind the MVS.

The streamlines of the electrical current depicted in Figure 3.20 indicate the direction of the current flow throughout the membranous labyrinth, entering the endolymph from the dark cells lining the labyrinth, and flowing to regions of sensory hair cells. The hair cells of the cristae ampullares within the semicircular canals receive an electric current from the dark cell regions near their respective cristae. Additionally, dark cell regions in the common crus and back of the utricle also contribute to the current, which flows through the entire semicircular canal. The currents flowing to the utricular macula primarily originate from the dark cell regions in the utricle. The currents originating from the back of the utricle and common crus terminate in the posterior part of the macula, whereas the remaining currents coming from other dark cell regions are distributed throughout the macula. As a result, the highest electric current density occurred in the center of the utricle, where most of the current was directed toward the front of the utricle.

When the head is exposed to a magnetic field, the complex current distribution interacts with the magnetic field (i.e., the B field), generating a Lorentz force. Based on Equation (2.26), the direction of the Lorentz force is orthogonal to both the B field and electric current directions, with the latter varying depending on the specific region of the membranous labyrinth. For instance, the B field can be aligned along the Z-axis from the head to the feet, and the electric current direction in the utricle is mostly along the X-axis from the posterior to the anterior region

of the utricle, as shown in Figure 3.20. This coupling generates a resultant Lorentz force that points approximately along the Y-axis from the right ear toward the left ear in both membranous labyrinths, reaching its maximum at the center of the utricle, where a higher electric current density occurs. The Lorentz force distribution on the utricular midplane is shown in Figure 3.21a.

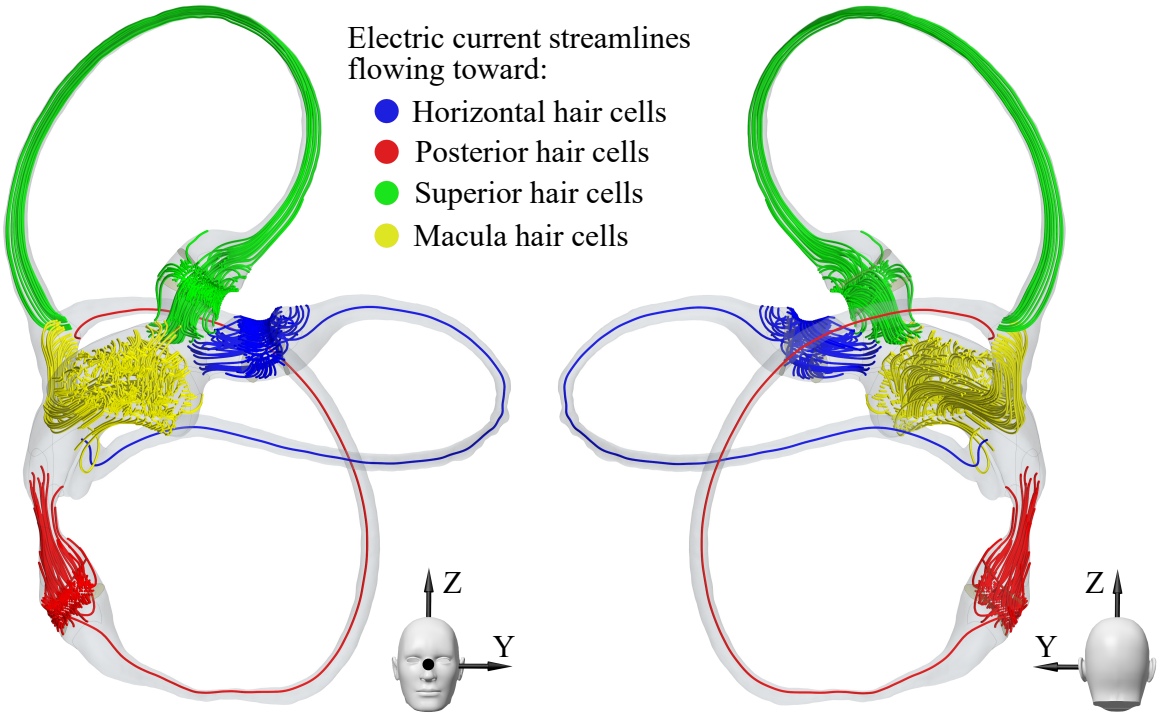

Figure 3.20: Electric current streamlines within the left membranous labyrinth. Streamlines are projected from dark cells to sensory hair cells, viewed from anterior and posterior perspectives. The streamlines are color-coded according to the associated vestibular receptor containing the targeted hair cells, with distinct colors for each crista ampullaris and the utricular macula.

The endolymph, initially at rest to simulate the head in a resting position, begins to flow because of the Lorentz force acting within it. This interaction is maintained when the magnetic field is present, similar to the conditions inside an MRI bore. The combination of Lorentz forces in the utricle generates higher fluid velocities in the midplane, resulting in two vortices, which can be observed in Figure 3.21b. The larger vortex was in front of the utricle (maximum velocity of 134 µm/s in a 7T MRI). A smaller one with lower velocities (maximum of 55 µm/s) was found at the back. In both labyrinths, the rotation direction was clockwise for the larger vortex and counterclockwise for the smaller vortex. While the axis of rotation of the larger vortex is approximately along the Z-axis, the axis of rotation of the posterior vortex is more longitudinally oriented along the utricle, extending into the common crus. Because there is an electrical current throughout the membranous labyrinth, Lorentz forces appear in the entire anatomy, but with lower intensity. For instance, fluid displacements occur within semicircular canals and ampullae with velocities three and two orders of magnitude smaller than those in the utricle, respectively (the average maximum velocity for all canals was 0.3 µm/s, and for all ampullae, it was 2 µm/s).

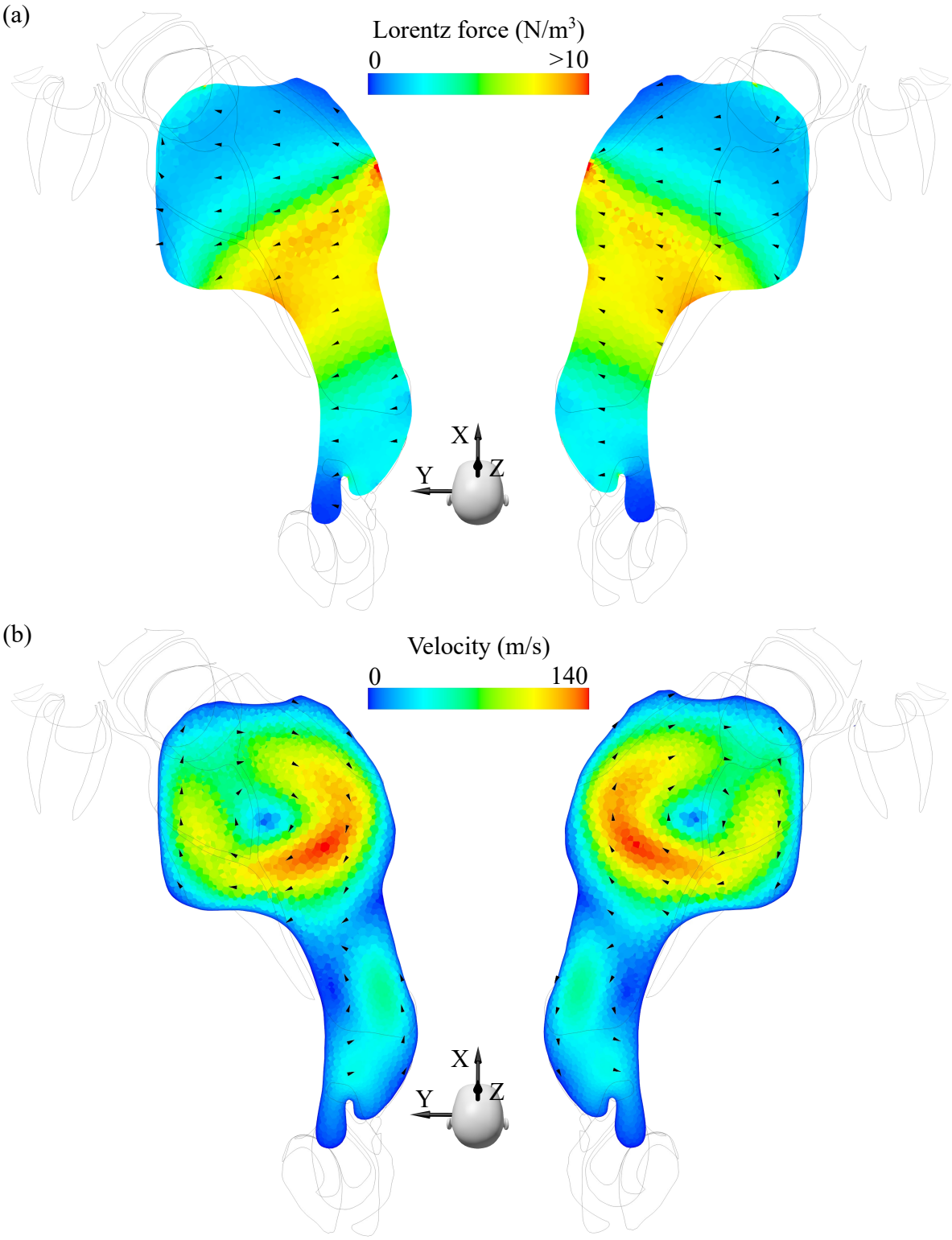

Figure 3.21: Illustration of two important variables in magnetic vestibular stimulation (MVS). The representation of both scalar and vector components of (a) Lorentz forces and (b) endolymphatic fluid velocities within the transverse section of the utricle is depicted in Figure 3.18. The flow pattern is characterized by two vortices generated by the Lorentz force effect: a stronger clockwise vortex at the anterior part of the utricle, and a smaller counterclockwise vortex at the posterior part of the utricle.

Endolymphatic flow displaced the cupulae of all six semicircular canals. Although the fluid velocity quickly stabilizes within one second, a steady state of deformation occurs after approximately 30 s owing to the viscoelastic properties of the cupula. The stimulus of the cupula can be measured as shear strain XY in the cristae ampullares regions illustrated in Figure 3.22. All cristae ampullares exhibited the same shear strain pattern, with excitation/inhibition in the central zones and an opposite stimulus pattern in the periphery. The average of this shear strain XY pattern was the variable used to determine the overall excitation/inhibition for each crista. The shear strain XY results of the cristae ampullares were opposite when comparing the right and left labyrinths, as shown in the bottom panel of Figure 3.22. The net result is the deflection of all cupulae of the right labyrinth toward the utricle (i.e., utriculipetal direction) and the left labyrinth away from the utricle (i.e., utriculifugal direction) when the head is in the supine position, as shown in Figure 2.4.

Reversing the direction of the magnetic field, so that it aligns along the Z-axis from the feet to the head, inversely affects the Lorentz forces, now oriented in the negative Y-direction in the utricle midplane. Consequently, this reversal alters the rotational direction of the fluid vortices and changes the direction of deflection of the cupulae. Despite this change in direction, the magnitude of the resultant stimuli remained unchanged. This observation indicates that reversing the magnetic field direction inhibits any cristae ampullares previously excited by the original field orientation and excites any cristae ampullares previously inhibited.

USC
UNIVERSIDADE DE SANTIAGO DE COMPOSTELA

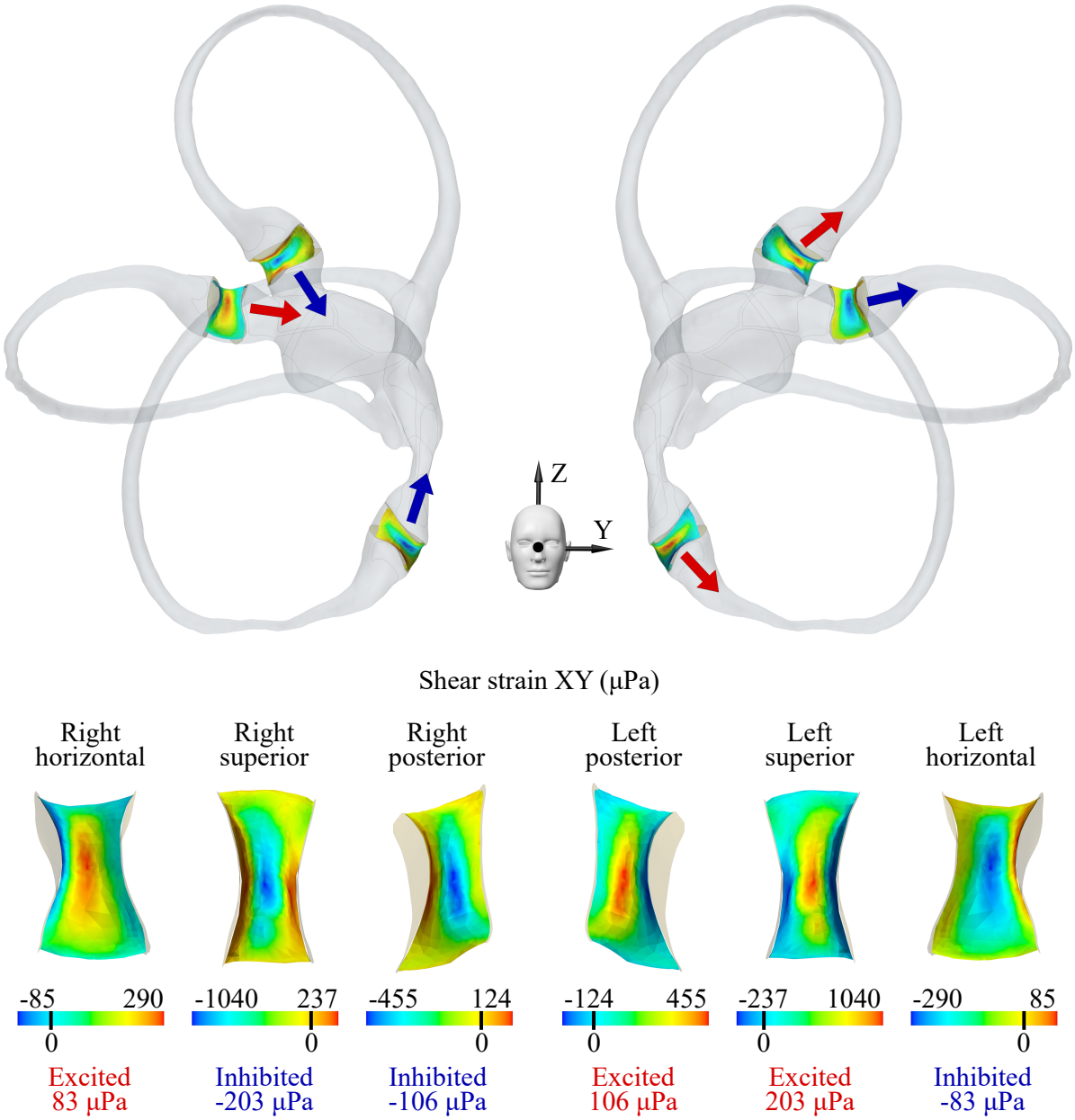

Figure 3.22: Mapping of shear strain XY across cristae ampullares. Positive shear strain XY values indicate excitation (red), whereas negative values indicate inhibition (blue). Excitatory flow in horizontal semicircular canals is characterized by movement toward the utricle. In contrast, excitatory flow in the superior and posterior canals occurs in the opposite direction. The colored arrows represent the overall direction of cupula displacement in this regard. The state of the cupula, whether excited or inhibited, is determined by the average shear strain XY across the entire crista.

3.3.1.3 Experimental validation of numerical results

In the previous section, the entire biophysical process leading to the determination of the SPV from numerical simulations was explained. This section compares these results with the three-dimensional eye movements observed experimentally to assess the effects of varying

magnetic field strengths and head positions.

Figure 3.23a presents a typical example of normalized SPV values for nystagmus in one participant, reflecting the consistent pattern found across all participants. The initial 20 s period represents the time required for the participant to enter the bore of the 7T MRI scanner in a supine position. The observed slow phase was predominantly leftward and counterclockwise (top pole of the eye to the person's right side) with negligible vertical movement, consistent with a null vertical SPV. Numerical simulations estimated the average shear strain XY across the cristae ampullares, and these computational results corroborate the directionality of the eye movements observed experimentally, as shown in Figure 3.23a. Following a peak at approximately 30 s, the simulation values plateaued, whereas the experimental SPV measurements gradually decreased, thereby reflecting neurological adaptation.

Analysis across three different magnetic field (B-field) strengths revealed a proportional response in the horizontal and torsional eye movement components, with all subjects maintaining leftward and counterclockwise SPVs, regardless of the strength of the magnetic field (top pole of the eye to the person's right side for the torsional component). In contrast, the vertical SPV did not exhibit an increase at higher B-field strengths. Figure 3.23b summarizes the averaged SPV values for all participants and compares them with the numerical SPV.

Different head orientations, specifically varying ear-to-shoulder (ETS) positions, as shown in Figure 2.4, were analyzed to ascertain their effects on eye movement components. Figure 3.23c shows that both the horizontal and torsional SPVs decreased as the head moved away from the supine position. In contrast, the vertical SPV exhibited directionally dependent behavior: upward SPV was recorded with the left ETS positions and downward SPV with the right ETS positions, with the transition through zero occurring in the supine position. These observations suggest that the vertical eye component behaves differently than the horizontal and torsional components.

The computational and experimental data demonstrated good agreement, as indicated by the average percentage deviation between the simulated and clinical SPV results in Table 3.13. For different B-field strengths, the average percentage deviation was 1.6 % for the horizontal component, 6.5 % for the vertical component, and 7.7 % for the torsional component. Similarly, for different ETS positions, the average percentage deviation was 10.3 % for the horizontal eye component, 9.7 % for the vertical component, and 8.8 % for the torsional component.

Table 3.13: The average percentage deviation between numerical and experimental normalized slow-phase velocities (SPV) at different magnetic field intensities (ΔB) and ear-to-shoulder (ΔETS) positions. The data points used are those depicted in Figures 3.23b and 3.23c.

	ΔB (%)	ΔETS (%)
ΔSPV_{hor}	1.6	10.3
ΔSPV_{ver}	6.5	9.7
ΔSPV_{tor}	7.7	8.8

USC UNIVERSIDADE DE SANTIAGO DE COMPOSTELA

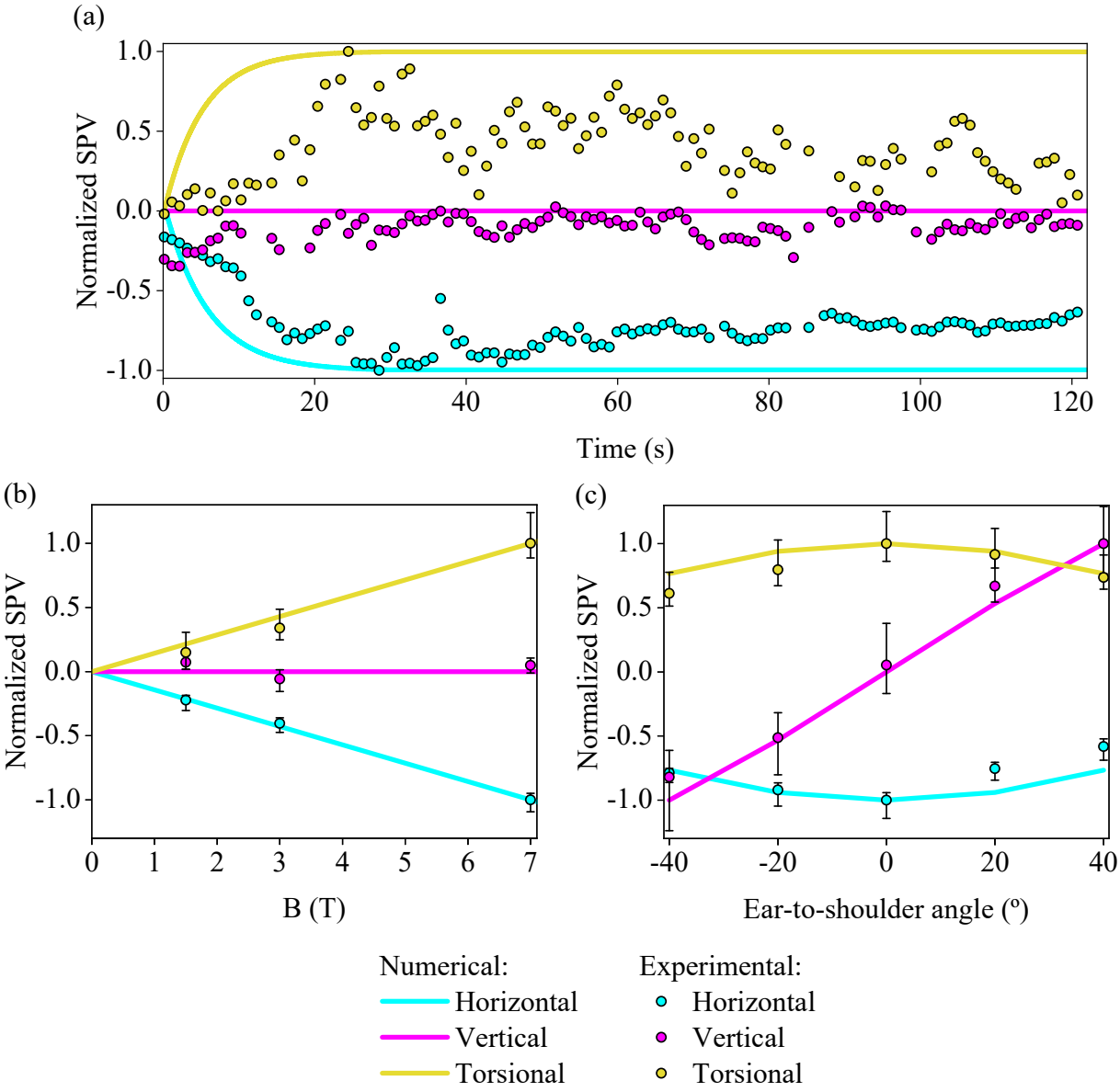

Figure 3.23: Comparative normalized slow-phase velocity (SPV) from numerical and experimental data. Negative SPV values represent leftward, downward, and clockwise (top pole of the eye to the left ear) movements. In contrast, positive values represent rightward, upward, and counterclockwise movements of the horizontal, vertical, and torsional components of eye movement, respectively. (a) Comparison of normalized SPVs from computational analysis with experimental measurements from a representative participant inside the 7T MRI scanner. (b) Aggregated normalized SPVs from computational and experimental data across varying magnetic field strengths while supine, with experimental values reflecting the average peak SPV for all participants. (c) Normalized computational and experimental SPV peak data for different ear-to-shoulder (ETS) head positions; negative angles denote the right ETS, and positive angles denote the left ETS, as shown in Figure 2.4. The vertical component SPVs in graphs (a) and (b) were normalized against the peak horizontal component values, whereas the other components were normalized to their own peak values. The error bars represent the inter-subject variability in peak nystagmus recorded after entering the bore for the five subjects under study.

USC UNIVERSIDADE DE SANTIAGO DE COMPOSTELA

3.3.1.4 Simulated eye movement responses to head orientations

The previous section demonstrated good agreement between the numerical and experimental results. However, the head positions in the MRI scanner are limited owing to space constraints, whereas numerical simulations do not have this limitation. Therefore, this section explains the eye movement responses for a complete range of different theoretical head positions based on the numerical SPV.

Simulations aligned with the Z-axis, coincident with the magnetic field direction, revealed uniform responses across all cristae, mirroring the eye movement patterns observed in the supine position, as illustrated in Figure 3.23c at a 0º angle.

Head rotation about the X-axis, simulating ETS tilts, was modeled to assess its effect on eye movements. The simulations predicted a sinusoidal pattern with a 180º wavelength ($R^2 = 1$) for all simulated eye movement components, providing a comprehensive representation of the normalized SPV over a 360º range of head positions along the X-axis observed in Figure 3.24a. The simulated horizontal and torsional components displayed antiphase behavior, neutralizing at -90º and 90º, while the vertical component showed a 90º phase lag, resulting in zero values at 0º and 180º. These null points for the nystagmus eye components are summarized in Table 3.14 and were obtained based on the shear strain XY values for each crista with their respective phase shifts, as detailed in Figure 3.24c and Table 3.15.

Additionally, simulations of head rotations along the Y-axis, representing flexion-extension (FE) movements, suggested that horizontal and torsional normalized SPV also fit a sinusoid with a 180º wavelength ($R^2 = 1$), but the vertical component remained null (Figure 3.24b). The horizontal SPV reaches a null point at approximately 27º of flexion and 153º of extension, whereas the torsional SPV reaches a null point at approximately 50º of flexion and 130º of extension, see Table 3.14. These patterns were obtained from the shear strain XY measured in the cristae, which differed in phase and amplitude from those associated with the ETS positions. In this case, the responses from Figure 3.24d and their respective null points in Table 3.15 lead to the null eye components for the FE shown in Table 3.14.

Table 3.14: Null points for nystagmus eye components for ear-to-shoulder (ETS) and flexion-extension (FE) head positions. The head orientation measured in degrees corresponds to null points in the sinusoidal eye components shown in Figures 3.24a and 3.24b.

Eye component	ETS angle (º)		FE angle (º)	
	1º null	2º null	1º null	2º null
Horizontal	-90	90	-27	153
Vertical	0	180	-	-
Torsional	-90	90	-50	130

USC UNIVERSIDADE DE SANTIAGO DE COMPOSTELA

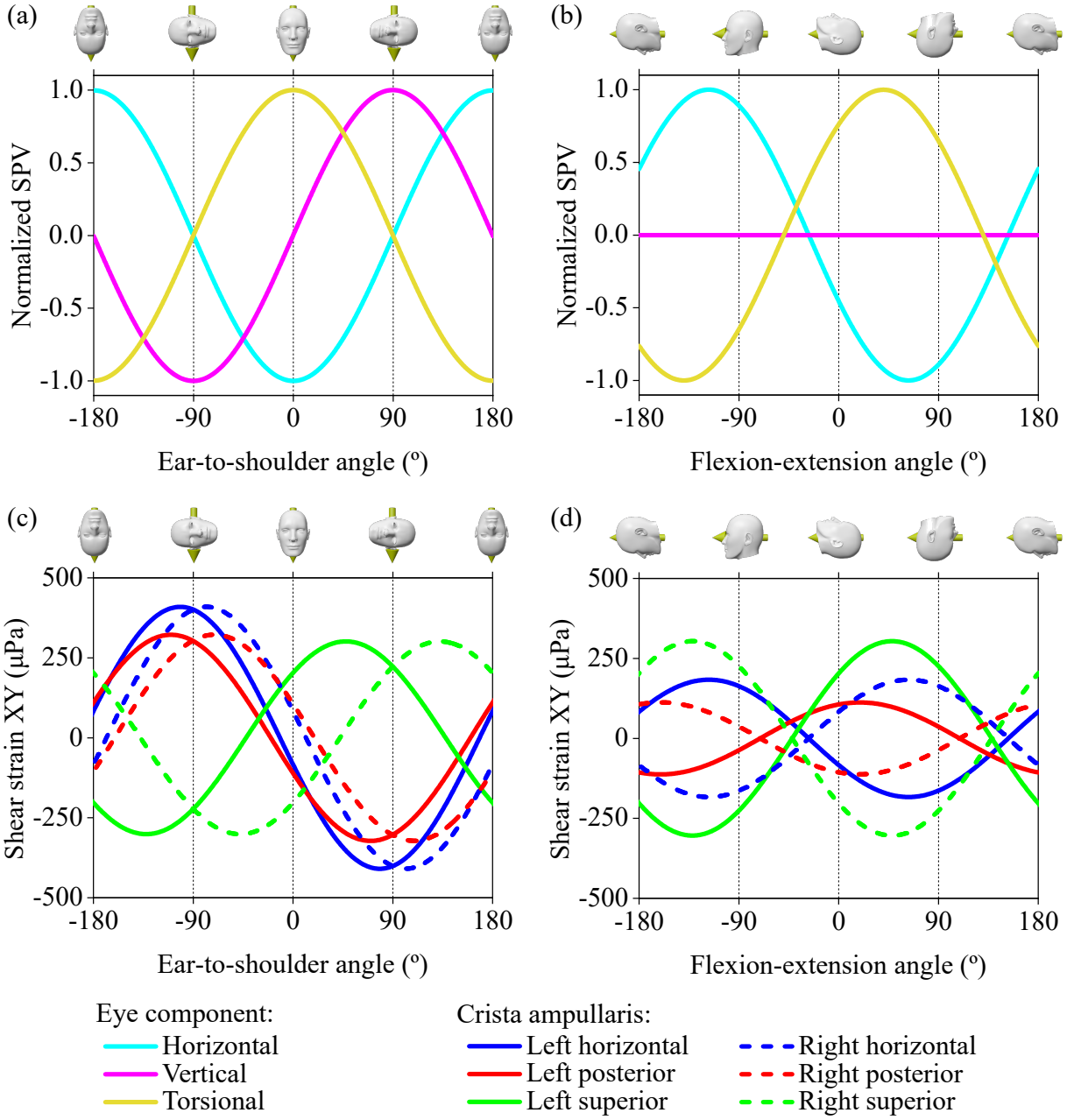

Figure 3.24: Computationally derived normalized slow-phase velocity (SPV) of eye movements across various head orientations and the respective cristae ampullares stimuli. (a) SPV profiles for head tilts simulating ear-to-shoulder (ETS) movements, where negative values indicate head-oriented right ETS and positive values indicate left ETS. (b) SPV profiles for head movements in flexion-extension (FE), where negative values indicate head flexion and positive values indicate head extension. (c) Cristae ampullares stimulus profiles for ETS positions. (d) Cristae ampullares stimuli profiles for FE positions. Positions for the null stimulus for each eye component and in each crista can be found in Tables 3.14 and 3.15 for all head orientations.

USC UNIVERSIDADE DE SANTIAGO DE COMPOSTELA

Table 3.15: Null points for the cristae ampullares stimuli for ear-to-shoulder (ETS) and flexion-extension (FE) head positions. The head orientation measured in degrees corresponds to null points in the sinusoidal shear strain XY responses shown in Figures 3.24c and 3.24d.

ETS angle (º)				
Crista	Left ear		Right ear	
ampullaris	1º null	2º null	1º null	2º null
Horizontal	-12	168	12	192
Posterior	-19	161	19	199
Superior	-42	138	42	222

FE angle (º)				
Crista	Left ear		Right ear	
ampullaris	1º null	2º null	1º null	2º null
Horizontal	-27	153	-27	153
Posterior	-71	109	-71	109
Superior	-42	138	-42	138

3.3.2 Discussion

This section discusses the findings of the MVS study. First, a brief discussion of the robustness of the MVS model is provided to evaluate its applicability. Then, the biophysical mechanisms behind the MVS and the findings from the numerical simulations were compared with the experimental data to validate the accuracy of the model. Finally, the insights provided by the model based on the SPV components determined by the vestibular responses induced by the MVS in the numerical simulations are discussed.

3.3.2.1 Model robustness

The model robustness analysis demonstrates that the magnitude and distribution of the variables explaining the MVS in this mathematical model are governed by factors such as the age of the subject and the relative electrical conductivity between the cupulae and endolymph. Changing the electric potential did not affect the electric currents, and the Lorentz force remained similar, resulting in no differences in the endolymph displacement or the cristae ampullares stimuli. It is noteworthy that this variation was applied simultaneously under all boundary regions. When the relative electric potential between the macula and cupulae changed, electric currents flowed from some hair cell regions to another, which does not have a physical basis based on the function of the hair cells as a sink of electric currents.

However, a decline in hair cell numbers associated with aging could diminish the overall electric current [66], thereby reducing susceptibility to MVS in older populations. After the analysis in Figure 3.19a, the MVS was reduced proportionally to the total electric current determined by the age change. It is important to note that age can affect other neurological factors, potentially modifying the resulting MVS. However, this model only collects information from the mechanical stimulation of the crista ampullaris.

USC DE SANTIAGO DE COMPOSTELA

Similarly, variations in the ratio between cupulae and endolymph conductivity in the simulations correlated with alterations in electric current and, consequently, the vestibular stimulus experienced. Based on other inner ear tissue measurements [63], the electrical conductivity in the cupula is expected to be of the same order of magnitude as the endolymph, or even slightly smaller, owing to the minor concentration of water compared to the endolymphatic fluid. Considering this, we are in the range $\sigma_e > \sigma_c$ shown in Figure 3.19b, which does not show a significant variation in the numerical SPV results. In the future, it would be useful to experimentally determine the electrical conductivity of the vestibular system structures and model these conditions to understand more precisely how they may affect the MVS.

As a conclusion of the model robustness study, the constant boundary conditions selected for the model accurately reflected the quantitative responses observed across different individuals. This indicates that the boundary conditions listed in Table 2.4 can be used to explain MVS based on the normalized SPV described in this study. However, more precise measurements of these parameters in humans could further refine the model accuracy. For instance, using the same boundary conditions for different head orientations may not accurately capture the slight variations in current flow through the utricular macula caused by different deflections of hair cells due to gravity [10, 119].

3.3.2.2 Biophysics behind magnetic vestibular stimulation

Assuming that the model is capable of predicting the biophysics behind the MVS based on the selected boundary conditions, the numerical and experimental results are now explained to demonstrate their correlation and elucidate the biophysical behavior of the vestibular system when affected by the MVS.

The electric current density within the membranous labyrinth is unaffected by the duration or strength of the magnetic field exposure, always showing a distribution as shown in Figure 3.20. Despite this, these currents, when coupled with the magnetic field oriented differently, generate changes in Lorentz forces that do not uniformly correspond to heightened vestibular stimuli across different head positions. Instead, the anatomical nuances of the utricle, along with the specific origin points and terminations of the electrical currents, play a pivotal role in determining the fluid movement and formation of vortices. The observed fluid dynamics within the utricle vortices often defy the primary orientation of the Lorentz forces, showing movements in various directions, including counter to the force. Refer to the vectors in Figures 3.21a and 3.21b. Previous models, such as that by Antunes et al. [120] have not accounted for this intricate behavior, likely due to a less detailed representation of the inner ear's geometry than what is achieved here with µCT [9]. This approach, which integrates the electrodynamic potential model with an FSI solver, captures the complex interactions leading to the stimuli experienced by all six cristae ampullares, as shown in Figure 3.22. Although the model also considers the MHD electromotive forces arising from endolymph movement, their impact is minimal relative to the magnetic field of the MRI machine, as indicated by the low magnetic Reynolds number outlined in 2.3.3 Magnetic vestibular stimulation. Interestingly, the vortex locations identified in the stimulations correspond to artifacts recently observed in 3T MRI scans, which have been hypothesized to stem from the movement of protons in these vortices [121].

The endolymphatic velocity within the vortices quickly reached equilibrium in less than a second. However, cupulae exhibit a delayed response, achieving a stable deformation after

USC DE COMPOSTELA

approximately 30 s owing to their intrinsic elasticity and restoring force[36]. This value is consistent with predictions of constant acceleration based on the dynamics of the endolymph in semicircular canals [122]. This response, where the cupulae retain this displaced state until the magnetic field is discontinued, causes constant nystagmus and simulates constant acceleration [80]. Although such a response is detectable experimentally, neural adaptation causes a slow reduction in nystagmus over time, resulting in a small divergence between the numerical and experimental results, as shown in Figure 3.23a. It is also crucial to recognize that simulations presuppose a consistently applied magnetic field, disregarding the transient effects experienced by subjects as they transition into the magnetic field of the MRI. This entry process involves the movement of the bed into the bore and through a gradient magnetic field, typically lasting approximately 20 s, which likely moderates the slope of the stimulus observed experimentally compared to the results from the computational model, as observed in Figure 3.23a.

In Figure 3.23b, a linear response of the horizontal and torsional eye movement components to the magnetic field strength was observed across all subjects, whereas the vertical component typically approached a null value. This phenomenon is explained by the computational simulation outcomes for each crista, as shown in Figure 3.22, and by the differential responses of the eye components based on Equation (2.40). Specifically, the left horizontal cupula was inhibited while the right cupula was excited, amplifying the leftward horizontal eye movement in proportion to the magnetic field strength. In contrast, the vertical eye movement component was neutralized due to opposing responses from the right superior and posterior cristae and left superior and posterior cristae. The net torsional eye movement component results in counterclockwise movement. Notably, the strong concordance between the simulations and experimental data, shown in Table 3.13, with an average deviation of just 5.3 % for all eye components, validates the capacity of the model to predict the vestibular response to varying B-field intensities. These findings are consistent with the predictions of the Lorentz force theory and corroborate the patterns observed in previous clinical research and the current study [29] [120]. Although this study focused on the peak values of nystagmus obtained inside the scanner, all data collected (before, during, and after the effect of the B field) for all participants were consistent with those of previous studies. They all showed a reversal of nystagmus [32], and the peak response was delayed because of the time taken for entry and exit from the MRI bore [123].

Outside the MRI bore, the magnetic field (B-field) strength is typically less than 1T for 1.5T and 3T MRI machines but can approximate 1T near 7T machines [124]. It might be presumed that such exposure could lead to an adaptive response, potentially obscuring a more pronounced stimulus upon entering the 7T field. However, the experimental data did not show a significant adaptation effect that would alter the peak nystagmus measurements inside the bore. A more influential factor was the baseline nystagmus data collected while lying in the dark away from the MRI scanner. Subtracting this baseline nystagmus was particularly relevant when the stimulus was small, as it markedly affected the determination of the null point of the vertical component across various B-field strengths. This decision also allows for a comparison of the peak response upon entering the bore using normalized values referenced to the same baseline.

The left and right membranous labyrinth models are symmetrical along the sagittal plane, leading to mirrored responses in the left and right cristae, as shown in Figure 3.22, and when simulating head-first versus feet-first entry (i.e., reversing the B-field direction). Anatomical variations between the actual left and right labyrinths in individuals [82, 83] may account for the lack of symmetry in some participant responses. Such interindividual variability is likely

responsible for the range of responses observed across subjects, as reflected in the error bars in Figure 3.23, which represent the intersubject variability in the peak nystagmus recorded after entering the bore. Refer to the methodology section 2.8.3 Experimental slow-phase velocity for further details.

Unlike in the supine position, asymmetries arise in ETS orientations owing to the different alignments of the left and right membranous labyrinths relative to the magnetic field. This causes Lorentz forces to change their direction at the equivalent points of one labyrinth relative to the other. These asymmetries likely caused the observed decrease in horizontal and torsional eye movement components when the head was positioned away from the supine position, as shown in Figure 3.23c. In contrast, the vertical eye component increased with upward movements in the left ETS and downward movements in the right ETS. The computational model results closely matched these experimental observations, as shown in Table 3.13, with an average deviation of 9.6 % for all eye movement components, supporting its predictive capability for SPV eye movements across various head orientations. A detailed analysis of the average stimulus of each crista ampullaris, as shown in Figure 3.24c, clarifies these effects. The horizontal and posterior cristae responses were more excitatory in the right ETS positions, whereas the superior cristae were more inhibitory, with inverse effects noted in the left ETS orientations. This pattern accounts for the vertical eye movement component behaving inversely to the torsional one, since the superior and posterior cristae contribute differently to the vertical response but similarly to the torsional response within the neurological pathways.

3.3.2.3 Numerical prediction of the magnetic vestibular stimulation

The results discussed in the previous section demonstrate that the numerical results accurately predict the real behavior of the vestibular system due to the MVS in different subjects. This provides an opportunity to theoretically study MVS for other head orientations, increasing the understanding of the role of Lorentz forces in the membranous labyrinth, and determining possible head positions that minimize reports of nystagmus and dizziness in subjects exposed to high-field MRI machines.

The most important finding is that numerical simulations reveal that the stimulus to each crista ampullaris for different head positions relative to the magnetic field is characterized by a sinusoidal pattern with a 180º wavelength. This consistent pattern across all cupulae allowed the creation of a predictive model for SPV eye movement responses to ETS and FE head positions, as depicted in Figure 3.24. The neurological integration of these stimuli, involving the simple addition or subtraction of the outputs from each crista, results in SPV eye movements that also exhibit a 180º sinusoidal wavelength. These findings are consistent with the experimental observations for various ETS orientations reported by Mian et al. [118]. However, the results presented here diverge from their suggestion that FE movements follow a sinusoid of a different wavelength. Corroborating this experimentally requires data that are not currently obtainable, given the physical geometrical constraints of the human body and MRI machines.

The simulations provided a method for identifying the null points of the eye movement components by summing the sinusoidal outputs from each crista. This approach elucidates the observed phenomena, wherein the null points of eye movements during ETS and FE positions occur at different head angles. For ETS movements, the responses of each pair of cristae follow a sinusoid dephased at an equal distance with respect to 0º, but diverge in direction, see Figure 3.24c and Table 3.15. This results in null points for eye movement components at 90º intervals,

USC DE COMPOSTELA

as shown in Figure 3.24a. Conversely, in FE movements, the sinusoids of the corresponding pairs of cristae in both ears are in opposed phases, leading to specific null points for each crista pair at the same head position, see Figure 3.24d and Table 3.15. Notably, the computed eye components in Figure 3.24b exhibit different behaviors during FE. The horizontal SPV component reaches a null point at approximately 27º of flexion, which may correlate with the alignment of the utricular macula relative to the magnetic field (see the supplementary material from Roberts et al. [29]). However, the torsional SPV null point occurs at 50º of flexion, suggesting that it is not possible to achieve a complete null response to the MVS at a specific head position.

3.3.3 Summary

This study supports the Lorentz force hypothesis as being responsible for MVS. Interactions between the MRI magnetic field and ionic currents in the inner ear generate a Lorentz force, resulting in endolymphatic flow that produces a vestibular response similar to rotation with constant angular acceleration. These vestibular responses increase proportionally to the B-field intensity and exhibit different stimuli at varying head orientations relative to the B-field direction, which follows the expected behavior of this type of magnetic force.

The numerical results were aligned with eye movements in individuals exposed to different MRI magnetic fields and head positions, and the model demonstrated robustness under varying boundary conditions. This reliability indicates that normalized SPV variation accurately reflects MVS biophysical behavior, despite the use of anatomical data from a single individual. The model can predict eye component responses to various head positions in ETS and FE, identifying specific positions that evoke null eye component stimuli caused by the sinusoidal response of a 180º wavelength crista ampullaris stimulus.

This numerical model is a significant advancement that provides novel insights into MVS and its effects on vestibular function, which can lead to personalized medicine. It holds promise for future diagnostic and treatment applications based on magnetic field effects on the vestibular system and can serve as a basis for safety guidelines and future MRI technology design.

3.3.4 Future work

As explained previously, this study aimed to clarify the biophysical mechanisms underlying MVS and connect fragmented theoretical and experimental studies on the effects of magnetic fields on the vestibular system. It is important to acknowledge that, similar to HIT studies, the requisite image quality for precise MVS modeling currently precludes in vivo validation. This limits the potential of personalized medicine in this context today.

MVS is viewed as a novel method for generating vestibular stimulation, albeit with no current clinical application. However, future diagnostic testing or rehabilitation based on this stimulus may lead to more accurate and innovative diagnostic and treatment methods. The model presented here could facilitate this task, providing the necessary physical fundamentals to design applications regarding MVS. For instance, investigating vestibular adaptation lasting hours inside the MRI bore could yield valuable insights, as well as modifying boundary conditions to mimic the effects of vestibular hydrops. Additionally, MVS could play a crucial role in the future development and safe commercialization of high-field MRI machines.

Currently, I intend to apply this novel mathematical approach to demonstrate how

nystagmus can be reduced when the head of the patient is oriented in a certain position relative to the magnetic field. The model designed during these years can predict these orientations for the anatomical geometry studied, and it is anticipated that other subjects will experience a null point around this head orientation based on the results of the clinical study we performed. This null point, in addition to mitigating minor dizziness, could prove valuable in fMRI research aimed at identifying brain regions activated with or without the effects of MVS. Future research will focus on this direction, collaborating with colleagues from Johns Hopkins Hospital, who can test subjects in these high-field MRI machines and corroborate the numerical results from specific simulations.

USC
UNIVERSIDADE DE SANTIAGO DE COMPOSTELA

Chapter 4

Conclusions

This dissertation aims to develop and validate advanced mathematical models of the vestibular system to facilitate personalized medicine, thereby improving the diagnosis, treatment, and understanding of vestibular disorders. Through the creation and application of numerical simulations, this research sought to provide a low-cost and noninvasive method for individualized studies on patients. Studies conducted as part of this thesis have demonstrated significant advancements in this field, highlighting the potential of mathematical modeling in personalized vestibular healthcare.

The research was organized in increasing order of complexity, beginning with a rigid anatomical model of the membranous labyrinth, which contains a fluid model for the dynamics of the endolymph and a Lagrangian particle model for the dynamics of otoconia. This initial model evaluated the effectiveness of the Epley maneuver (EM) in treating benign paroxysmal positional vertigo (BPPV) and explored potential modifications based on numerical simulations of a specific human membranous labyrinth. The findings revealed that the standard EM is not uniformly effective and that slight variations in head position could significantly impact its success. Personalized modifications to the EM, tailored to individual anatomical variations, have been suggested to improve treatment outcomes. This approach has the potential to reduce functional disability associated with refractory vertigo and decrease healthcare costs. Ongoing clinical validation involving refractory patients will further assess the effectiveness of personalized maneuvers.

Subsequently, the focus shifts to the vestibular receptors located in the ampullae, incorporating a fluid-structure interaction (FSI) model that reflects the elastic nature of this region and its interaction with the endolymph. This study provides insights into the biophysics of the vestibular system during the head impulse test (HIT), determining vestibular stimulation and its clinical implications. It was found that the vestibular stimulation response aligns more closely with angular acceleration than with velocity, thus challenging the previous assumptions. This study also highlights the importance of considering the orientation of the cupulae alongside the semicircular canals for more accurate rotational testing. Future work involves developing a comprehensive model that integrates biophysical and neurological aspects to enhance the understanding of vestibular function. In addition, advancements in medical imaging are necessary to achieve the precision required for accurate simulations in clinical practice, which can lead to the application of personalized medicine.

Finally, this thesis delves into the modeling of the magnetic vestibular stimulation (MVS) induced by the magnetic fields produced by magnetic resonance imaging (MRI) machines.

USC
UNIVERSIDADE DE SANTIAGO DE COMPOSTELA

Based on a magnetohydrodynamic (MHD) model coupled with the FSI model, this study supports the Lorentz force hypothesis and provides a robust numerical model that aligns with the observed eye movements at different MRI magnetic field intensities and head positions. This model offers novel insights into the effects of magnetic fields on vestibular function, which may lead to future diagnostic and therapeutic applications. While current imaging limitations prevent in vivo validation, the model holds promise for future research on diagnostic testing and rehabilitation based on MVS. Collaborations with institutions that use high-field MRI machines will further explore the potential of this approach.

These three studies exemplify the potential of numerical simulations to advance personalized medicine for the vestibular system. Despite the EM, HIT, and MVS studies having different clinical applications, they follow a similar research pattern: understanding vestibular function and the effects of various physical stimuli that elicit vestibular responses. The mathematical models designed in this dissertation provide a deeper understanding than previous studies, addressing the lack of personalized diagnostic and therapeutic approaches for vestibular disorders. This progressive integration of complexity underscores the potential of mathematical models in personalized vestibular medicine, suggesting promising, cost-effective, and noninvasive approaches for future clinical applications.

However, this study had certain limitations. One of the primary challenges is accurately obtaining the geometry of the membranous labyrinth using noninvasive techniques that do not cause secondary effects on the patient. Despite advancements in medical imaging technologies, achieving an acceptable resolution of the membranous structures of the inner ear in living patients remains difficult. Techniques such as the use of gadolinium in magnetic resonance imaging, though promising, require invasive procedures that are not always feasible due to potential adverse effects and limitations in their applications. Additionally, the rapid decomposition of the labyrinth postmortem further hampers the acquisition of precise data.

Furthermore, additional resources and time are necessary to investigate these research topics in depth. Although certain findings have been confirmed through clinical trials, thereby validating the accuracy of mathematical models, other aspects continue to undergo clinical validation.

Future research should focus on overcoming these limitations. Interdisciplinary collaboration is crucial for advancing our understanding of vestibular physiology and for enhancing the application of personalized medicine in this field. This is proven by the anticipated outcomes of this study, which have the potential to significantly impact individual health and the healthcare system, thereby shaping the future of vestibular medicine.

In conclusion, this thesis successfully bridges the gap between theoretical and clinical research, constructing a multidisciplinary path towards personalized medicine through advanced mathematical modeling. The insights gained from numerical simulations provide a foundation for more accurate and individualized approaches to diagnose and treat vestibular disorders, ultimately contributing to improved patient outcomes and healthcare efficiency. Despite these advancements, further research is needed to fully integrate these mathematical tools into clinical practice.

USC
UNIVERSIDADE DE SANTIAGO DE COMPOSTELA

Abbreviations

List of abbreviations.

Abbreviation	Description
BPPV	Benign paroxysmal positional vertigo
CESGA	Galicia Supercomputing Center
CFL	Courant–Friedrichs–Lewy
CRP	Canalith repositioning procedures
EM	Epley maneuver
ETS	Ear-to-shoulder
FE	Flexion-extension
FEM	Finite element method
FSI	Fluid-structure interaction
FVM	Finite volume method
HC	Horizontal cupula
HIT	Head impulse test
HSC	Horizontal semicircular canal
LARP	Left anterior-right posterior
LHRH	Left horizontal-right horizontal
LTI	Linear time-invariant
MAX	Maximum
MIN	Minimum
MRI	Magnetic resonance imaging
MVS	Magnetic vestibular stimulation
MHD	Magnetohydrodynamic
PTF	Probability of treatment failure
RALP	Right anterior-left posterior
SPV	Slow-phase velocity
VOR	Vestibulo-ocular reflex
μCT	Micro-computed tomography

USC
UNIVERSIDADE DE SANTIAGO DE COMPOSTELA

List of figures

1.1 An illustration depicting the anatomy of the inner ear in a human specimen. The membranous labyrinth filled with endolymph is depicted in red, whereas the bony labyrinth is shown in gray. The vestibular receptor locations used in this study are highlighted in yellow. (a) Front view. (b) Back view. The three-dimensional model was generated using a high-resolution medical image obtained from the Ariadne Toolbox [9]. 27
1.2 Illustrations of the vestibular receptors. (a) Structure of the utricular and saccular macula, including otoconia, and detailed representation of hair cells. (b) Structure of the crista ampullaris and its location in the ampulla. The hair cell types are similar for both types of vestibular receptors. Created with www.biorender.com. 28
1.3 Reference orthogonal planes for the head and the orientation of the semicircular canals. (a) The axial, coronal, and sagittal planes were used as references for the orientation of the head. (b) The planes of the left horizontal-right horizontal (LHRH), left anterior-right posterior (LARP), and right anterior-left posterior (RALP) canal pairs encompass the orientations of the six semicircular canals. The LHRH plane is inclined at 20º to the axial plane, while the LARP and RALP planes maintain orthogonality with each other and with the LHRH plane, and are oriented at 45º relative to the coronal and sagittal planes. 30
1.4 Vestibular stimulation scheme for horizontal semicircular canals during a counterclockwise rotation over the left horizontal-right horizontal (LHRH) plane. The endolymphatic fluid moves in the opposite direction of rotation, generating utriculipetal and utriculifugal flows in the left and right horizontal semicircular canals, respectively. This generates excitation in the hair cells located in the left crista ampullaris (red) and inhibition in the hair cells located in the right crista ampullaris (blue). Both of these electric currents are transmitted to the brain, which interprets these signals and generates a response in the extraocular muscles, providing a displacement of the eyes that counteracts the head rotation, known as the vestibulo-ocular reflex (VOR). Brain image collected from www.pixabay.com. 31
1.5 Schematic representation of the endolymph and cupula displacements during a counterclockwise rotation. The cupula (red) behaves like an overdamped pendulum, generating both excitatory and inhibitory signals depending on the acceleration or deceleration during the rotation. When the acceleration is zero, the cupula returns to its resting position. 34

USC UNIVERSIDADE DE SANTIAGO DE COMPOSTELA

1.6 Bode plot showing the gain and phase diagrams of the cupula. The gain is in dB, and the phase is in radians relative to the frequency of the rotations measured in Hz using a logarithmic scale. The ranges for the semicircular canal natural frequencies, mechanical adaptation, and viscous blocking were defined based on the eigenvalues determined in Equation (1.3). The calculations of these frequency corners were based on the properties of the membranous labyrinth shown in Figure 1.1 [9], and implemented in the transfer function from Equation (1.4). 37

2.1 Human left membranous labyrinth anatomy model used for the numerical simulations. From left to right, the modeled regions for each study are presented in the order of increasing complexity. The geometry of the Epley maneuver (EM) only considers the endolymphatic region. The head impulse test (HIT) geometry includes the cupulae regions, colored blue for the horizontal cupula, green for the superior cupula, and red for the posterior cupula. In addition to the fluid and solid regions, the magnetic vestibular stimulation (MVS) geometry includes hair cell regions in yellow and dark cell regions in black. The orientation corresponds to the supine position of the head, with the upper row showing the front view perspective and the bottom row showing the back view. 44

2.2 Location and orientation of both membranous labyrinths with respect to the head. Both geometries are located 40 mm away from the center of the head (red dot) and are mirrored with respect to the sagittal plane. 45

2.3 Visualization of the final mesh in the horizontal ampullary region for the head impulse test (HIT) and magnetic vestibular stimulation (MVS) models. Polyhedral cells surrounded by prism layer cells at the boundaries can be observed in the fluid region (gray). Mesh refinement with a higher cell density was observed at the entrance of the utricle. Tetrahedral cells form a mesh in the solid region of the horizontal cupula (blue). The cells that are in contact between the fluid and solid region generate the mapped interface where the fluid-structure interaction (FSI) solver exchanges information between the two regions. 46

2.4 Head positions used to compare experimental and numerical results in the magnetic vestibular stimulation (MVS) study. The supine position corresponds to the standard position inside the MRI machine, and different ear-to-shoulder (ETS) positions were tested to study the changes in the vestibular response. . . 62

2.5 Head hemispheres used to generate the vestibular stimulation map in the head impulse test (HIT) study. The head orientation corresponds to the initial orientation of the head nose-down position employed for rotational vestibular testing. 65

2.6 Gaussian function employed as a rotation function in the head impulse test (HIT) study. Angular acceleration is represented in blue, angular velocity in red, and angular position in green. 66

USC UNIVERSIDADE DE SANTIAGO DE COMPOSTELA

2.7 Horizontal cupula with the respective crista ampullaris and the cupula coordinate system. The origin of the coordinate system was located in the middle of the cupula. The X-axis points to the utricle, indicating the excitatory direction. The same criteria were followed for the rest of the cupulae, but with the X-axis pointing to their respective excitatory direction. The X-axis direction of all cupula coordinate systems can be seen in Table 2.7. 68

3.1 Position of otoconia after 30 s of resting time in the step 1. Enlarged spherical particles representing the otoconia are color-coded depending on their diameter. 75
3.2 Displacement of the otoconia during the standard Epley maneuver (EM). Each image corresponds to different positions of the left membranous labyrinth and head orientation for each step of the EM. The paths of the otoconia are illustrated, and their final positions are represented by an enlarged blue sphere. The steps shown include (a) step 1, (b) step 2, (c) step 3, (d) step 4, (e) step 5, and (f) step 6, marking the end of the maneuver. 76
3.3 Resting times required for the otoconia to reach the final position at each step for each otoconium diameter. A) Resting times were recorded until otoconia left the posterior semicircular canal. B) Resting times recorded including all necessary steps for the otoconia to fall into the interior of the posterior ampulla. 78
3.4 Displacement of otoconia and total time needed to exit the posterior semicircular canal (resting time + rotation time). Dashed lines indicate the final angular position for each step and the time block period required for (a) 30 s, and (b) 60 s resting time conditions. 79
3.5 Head orientations representing the range of angle variations for each substep, as outlined in Table 2.9. The standard position is denoted in gray, while red indicates poorer performance, and green signifies better performance. For the optimal position for substep 5B, refer to Figure 3.7. 80
3.6 Different positions reached by otoconia when it is applied the step 3 with a rotation angle of A) 75º, B) 90º, and C) 105º. 81
3.7 Final position of the otoconia depending on their diameter and the angle of nose-down rotation in the substep 5B. A) Regions of the membranous labyrinth were classified according to different probabilities of treatment failure (PTF). The yellow region positioned between the frontside of the utricle (green), the posterior ampulla (red), and the common crus (yellow region that connects the posterior and superior semicircular canals) can be identified as the backside of the utricle. Results are depicted for otoconia starting in B) the frontside of the utricle, C) the superior semicircular canal, and D) the combination of both. In Figure 5A, the orientation of the membranous labyrinth corresponds to 75º nose-down, aligning with the green head orientation depicted in Figure 5D. The standard 20º nose-down orientation is represented by the red head. 83

USC UNIVERSIDADE DE SANTIAGO DE COMPOSTELA

3.8 Quantitative variables used to determine the vestibular stimulation during numerical simulations of the head impulse test (HIT). Two different views allow for better visualization of the effects of counterclockwise rotation with respect to the Z-axis (corresponding to stimulation on the plane of the horizontal semicircular canal) during the deceleration stage. Three different physical parameters can be observed: endolymphatic velocity in all fluid regions plotted by plane sections, cupula wall displacements at the horizontal, posterior, and superior cupulae, and shear strain XY on the crista ampullaris for each cupula. . 92
3.9 Endolymphatic velocity streamlines for the left membranous labyrinth during the head impulse test (HIT). The streamlines are color-coded based on their origin, with each streamline commencing from a different semicircular canal. . 93
3.10 Averaged shear strain XY on all cristae ampullares for the left and right membranous labyrinths during a counterclockwise rotation in the Z-axis direction corresponding to the standardized head impulse test (HIT) for the horizontal semicircular canal. Positive values indicate excitation, and negative values indicate inhibition. The left and right cupulae are differentiated by solid and dashed lines, respectively (using the same color code as cupulae in Figure 2.1). 94
3.11 Map of stimulation response on each left crista for counterclockwise rotation measured as the averaged shear strain XY results in each direction. The angular axis indicates the φ coordinates, and the radial axis indicates the θ coordinates in spherical coordinates. The hemispheres were projected over a 2D plane corresponding to the axial plane of the head (XY) from the Z-axis perspective. In this projection, the X-axis corresponds to $\varphi = 90^{\circ}$ and the Y-axis corresponds to $\varphi = 180^{\circ}$. The maximum (MAX) and minimum (MIN) directions are plotted as dot points, considering that the 1ºMAX represents the extreme with the highest stimulation and 1ºMIN represents the extreme with the minimum stimulation. 96
3.12 Map of stimulation response on each right crista for counterclockwise rotation measured as the averaged shear strain XY results in each direction. Similar considerations to those in Figure 3.11. 97
3.13 Map of stimulation response on each left crista for clockwise rotation measured as the averaged shear strain XY results in each direction. Similar considerations to those in Figure 3.11. 98
3.14 Map of stimulation response on each right crista for clockwise rotation measured as the averaged shear strain XY results in each direction. Similar considerations to those in Figure 3.11. 99
3.15 Maximum (MAX) and minimum (MIN) directions for cristae ampullares from the left labyrinth during counterclockwise rotation, represented by black dots in Figure 3.11 and their stimulation values in Table 3.6. The left membranous labyrinth representation helps visualize the relationship between the orientation of the semicircular canals and vectors. The color codes of the vectors are defined depending on each crista: blue for the horizontal crista, red for the posterior crista, and green for the superior crista. 102

USC UNIVERSIDADE DE SANTIAGO DE COMPOSTELA

3.16 Sketch illustrating the angular relationship of the averaged horizontal maximum (MAX) direction with respect to the normal vector of the horizontal canal plane (32.4º) and YZ plane of the horizontal cupula (4.7º). HSC means horizontal semicircular canal, and HC horizontal cupula. 107
3.17 Averaged shear strain XY measured at the three left cristae ampullares during a counterclockwise rotation in the Z-axis direction when rotation was performed with respect to the center of the head or the center of the horizontal semicircular canal (HSC), indicated by the straight and dotted lines respectively. Positive values indicate excitation, and negative values indicate inhibition. The color-code criteria are similar to those in Figure 3.10. 108
3.18 The transverse section of the mid-region of the utricle is presented relative to the membranous labyrinth from two different perspectives. This plane was employed to determine the average electric current density, average Lorentz force, and maximum velocity for determining the sensitivity of the electrodynamic potential model to the boundary conditions. Additionally, it served to illustrate the Lorentz forces and velocities in Figure 3.21. 113
3.19 Effect of boundary conditions on vestibular parameters used to determine the magnetic vestibular stimulation (MVS). The results are presented for the normalized slow-phase velocity (SPV) for (a) the effect of age and (b) the relative change in electrical conductivity for the horizontal and torsional components. The vertical component was always null. 115
3.20 Electric current streamlines within the left membranous labyrinth. Streamlines are projected from dark cells to sensory hair cells, viewed from anterior and posterior perspectives. The streamlines are color-coded according to the associated vestibular receptor containing the targeted hair cells, with distinct colors for each crista ampullaris and the utricular macula. 116
3.21 Illustration of two important variables in magnetic vestibular stimulation (MVS). The representation of both scalar and vector components of (a) Lorentz forces and (b) endolymphatic fluid velocities within the transverse section of the utricle is depicted in Figure 3.18. The flow pattern is characterized by two vortices generated by the Lorentz force effect: a stronger clockwise vortex at the anterior part of the utricle, and a smaller counterclockwise vortex at the posterior part of the utricle. 117
3.22 Mapping of shear strain XY across cristae ampullares. Positive shear strain XY values indicate excitation (red), whereas negative values indicate inhibition (blue). Excitatory flow in horizontal semicircular canals is characterized by movement toward the utricle. In contrast, excitatory flow in the superior and posterior canals occurs in the opposite direction. The colored arrows represent the overall direction of cupula displacement in this regard. The state of the cupula, whether excited or inhibited, is determined by the average shear strain XY across the entire crista. 119

USC UNIVERSIDADE DE SANTIAGO DE COMPOSTELA

3.23 Comparative normalized slow-phase velocity (SPV) from numerical and experimental data. Negative SPV values represent leftward, downward, and clockwise (top pole of the eye to the left ear) movements. In contrast, positive values represent rightward, upward, and counterclockwise movements of the horizontal, vertical, and torsional components of eye movement, respectively. (a) Comparison of normalized SPVs from computational analysis with experimental measurements from a representative participant inside the 7T MRI scanner. (b) Aggregated normalized SPVs from computational and experimental data across varying magnetic field strengths while supine, with experimental values reflecting the average peak SPV for all participants. (c) Normalized computational and experimental SPV peak data for different ear-to-shoulder (ETS) head positions; negative angles denote the right ETS, and positive angles denote the left ETS, as shown in Figure 2.4. The vertical component SPVs in graphs (a) and (b) were normalized against the peak horizontal component values, whereas the other components were normalized to their own peak values. The error bars represent the inter-subject variability in peak nystagmus recorded after entering the bore for the five subjects under study. 121

3.24 Computationally derived normalized slow-phase velocity (SPV) of eye movements across various head orientations and the respective cristae ampullares stimuli. (a) SPV profiles for head tilts simulating ear-to-shoulder (ETS) movements, where negative values indicate head-oriented right ETS and positive values indicate left ETS. (b) SPV profiles for head movements in flexion-extension (FE), where negative values indicate head flexion and positive values indicate head extension. (c) Cristae ampullares stimulus profiles for ETS positions. (d) Cristae ampullares stimuli profiles for FE positions. Positions for the null stimulus for each eye component and in each crista can be found in Tables 3.14 and 3.15 for all head orientations. 123

USC
UNIVERSIDADE DE SANTIAGO DE COMPOSTELA

List of tables

2.1 Number of cells in the final meshes selected after the mesh independence analysis. The meshes were divided by region and study case: Epley maneuver (EM), head impulse test (HIT), and magnetic vestibular stimulation (MVS). . . 47

2.2 Time steps that accomplish the Courant–Friedrichs–Lewy (CFL) number during the simulations for each study: Epley maneuver (EM), head impulse test (HIT), and magnetic vestibular stimulation (MVS). 47

2.3 Endolymph, otoconia and cupula parameters used to design the mathematical models. 54

2.4 Parameters defining the electrodynamic potential model. These are denoted as $variable^{cell\ type}_{region}$, where the cell type is represented as h for hair cells and d for dark cells. The region specifies distinct anatomical locations within the vestibular system, designed as m for the macula, u for utricle, c for common crus, h for horizontal, p for posterior, and s for superior cell regions. Key parameters serving as boundary conditions within the model are identified by an asterisk ($*$). The values correspond to for a 55-year-old human based on measurements by Merchant et al. [66]. 59

2.5 Coordinate systems used for each study, including if their axes orientation is maintained or vary with the rotations. 60

2.6 Location of the center of the semicircular canals and their orientation respect to the head nose-down coordinate system used for the head impulse test (HIT) study. The Z-axis vector is equivalent to the unitary normal vector of the plane of the semicircular canal. 61

2.7 Location of the center of the cupula and the vector corresponding with the unitary normal vector to the cupula walls in contact with the endolymph, defined as X-axis vector. See Figure 2.7 for visual aid. 61

2.8 Steps and substeps of the standard Epley maneuver (EM) considered for the numerical simulations. A positive ϑ indicates an anticlockwise rotation, whereas a negative value indicates a clockwise rotation. Normal vectors of rotation $\hat{\mathbf{n}}$ are defined based on the directions of the static coordinate system, but the origin of rotation varies depending on the substep being studied. 63

2.9 Variations in the rotation angles $\Delta\vartheta$ considered to assess the effectiveness of the Epley maneuver (EM). For a more comprehensive view of these variations, refer to the head orientations depicted in Figure 3.5. 63

3.1 The resting times for all the steps required for otoconia to reach the posterior ampullary region. The calculations are performed for different otoconia diameters, as shown in Figure 3.3a. 77

USC UNIVERSIDADE DE SANTIAGO DE COMPOSTELA

3.2 Displacement of otoconia δ for different angle of rotation ϑ in the substep 1A, 1C, 2A and 3A. In the substep 3A, otoconia achieve different positions once they are out of the posterior semicircular canal. 81
3.3 Summary of the Epley maneuver (EM), including the probability of treatment failure (PTF), potential errors, and possible solutions for each step. 88
3.4 Stimulation results obtained by integrating the averaged shear strain XY for each crista during rotation in the Z-axis direction shown in Figure 3.10. Values in parentheses represent percentages of excitatory stimulation. 95
3.5 Maximum (MAX) and minimum (MIN) directions for the left and right cristae ampullares during the counterclockwise and clockwise rotations. Spherical coordinates for each extreme equivalent to the plotted dots in Figures 3.11, 3.12, 3.13 and 3.14. 100
3.6 Stimulation of cristae ampullares for maximum (MAX) and minimum (MIN) directions from Table 3.5. These results are similar and independent of the left/right labyrinth or clockwise/counterclockwise rotation. The cursive results are the stimulations for the cristae that correspond to the MAX and MIN directions. The values between parenthesis indicate what percentage of that stimulation is excitatory. 101
3.7 Angular relationships between extremes measured in degrees (º). Results are similar for left/right cristae and counterclock/clockwise rotations. 103
3.8 Average deviations from orthogonality (MAX-MIN) and opposition (MAX-MAX and MIN-MIN) of the maximum (MAX) and minimum (MIN) directions of stimulation. 104
3.9 Angular relationships for left cristae extremes during counterclockwise rotation respect to the normal vector of the semicircular canal planes and the X-axis direction of the cupula planes. Angles are measured in degrees (º). HSC means horizontal semicircular canal, and HC horizontal cupula. 105
3.10 Average deviation for the maximum (MAX) directions from the normal vector of the canal planes, and for the minimum (MIN) directions from the surface of the canal plane. Results for the extremes obtained for the left cristae during counterclockwise rotation. 106
3.11 The average deviation of the maximum (MAX) directions with respect to the averaged plane formed by the cupula walls in contact with the endolymph (YZ plane of the horizontal cupula) and the average deviation of the minimum (MIN) directions with respect to the averaged normal vector of the cupula walls in contact with the endolymph (X-axis of the horizontal cupula). The results consist on the case for the left cristae during a counterclockwise rotation. 106
3.12 Effect of boundary condition on variables defining the magnetic vestibular stimulation (MVS). Relative variation for different ages, electric potential V, and electrical conductivity σ conditions compared to the standard boundary conditions from Table 2.4. Values are presented as percentages. The average electric current density $\bar{J}$, average Lorentz force $\bar{F}_l$, and maximum endolymph velocity v_e^{max} were measured in the section plane of the utricle, as shown in Figure 3.18. Conductivity results are divided depending on the relation between the electrical conductivity of the endolymph σ_e and the cupulae σ_c. 114

USC UNIVERSIDADE DE SANTIAGO DE COMPOSTELA

3.13 The average percentage deviation between numerical and experimental normalized slow-phase velocities (SPV) at different magnetic field intensities (ΔB) and ear-to-shoulder (ΔETS) positions. The data points used are those depicted in Figures 3.23b and 3.23c. 120
3.14 Null points for nystagmus eye components for ear-to-shoulder (ETS) and flexion-extension (FE) head positions. The head orientation measured in degrees corresponds to null points in the sinusoidal eye components shown in Figures 3.24a and 3.24b. 122
3.15 Null points for the cristae ampullares stimuli for ear-to-shoulder (ETS) and flexion-extension (FE) head positions. The head orientation measured in degrees corresponds to null points in the sinusoidal shear strain XY responses shown in Figures 3.24c and 3.24d. 124

USC UNIVERSIDADE DE SANTIAGO DE COMPOSTELA

List of publications

(I) Arán-Tapia, I., Soto-Varela, A., Pérez-Muñuzuri, V., Santos-Pérez, S., Arán, I., Muñuzuri, A. P. Numerical Simulations of the Epley Maneuver With Clinical Implications. Ear & Hearing **45**(4):1033-1044, July/August (2024). ISSN: 0196-0202. DOI: www.doi.org/10.1097/AUD.0000000000001493.

Specific contribution in the publication

Designing the models, performing the simulations, analyzing the results, creating figures and writing the original manuscript.

Quality indexes 2022

Impact factor: 3.7
CiteScore: 5.7
Quartile: Q1 (1/35 in AUDIOLOGY)

(II) Arán-Tapia, I., Soto-Varela, A., Pérez-Muñuzuri, V., Santos-Pérez, S., Arán, I., Muñuzuri, A. P. Numerical simulations to determine the stimulation of the crista ampullaris during the Head Impulse Test. *Comput Biol Med.* **163**, 107225 (2023). ISSN: 0010-4825. DOI: www.doi.org/10.1016/j.compbiomed.2023.107225.

Specific contribution in the publication

Designing the models, performing the simulations, analyzing the results, creating figures and writing the original manuscript.

Quality indexes 2022

Impact factor: 7.7
CiteScore: 9.2
Quartile: Q1 (4/55 in MATHEMATICAL & COMPUTATIONAL BIOLOGY)

(III) Arán-Tapia, I., Pérez-Muñuzuri, V., Muñuzuri, A. P., Soto-Varela, A., Otero-Millan, J., Roberts, D. C., Ward, B. K. The Biophysics of Magnetic Vestibular Stimulation: Clinical Insights from High-Field MRI. Under review in *Communications Medicine* (2024). ISSN: 2730-664X.

Specific contribution in the publication

Designing the models, performing the simulations, collecting data in the clinical trial, analyzing the results, creating figures and writing the original manuscript.

Quality indexes 2022

Impact factor: N/A
CiteScore: N/A
Quartile: N/A

USC
UNIVERSIDADE
DE SANTIAGO
DE COMPOSTELA

Copyright permissions

Article 1. Arán-Tapia, I., Soto-Varela, A., Pérez-Muñuzuri, V., Santos-Pérez, S., Arán, I., Muñuzuri, A. P. Numerical Simulations of the Epley Maneuver With Clinical Implications. Ear & Hearing **45**(4):1033-1044, July/August (2024). ISSN: 0196-0202. DOI: www.doi.org/10.1097/AUD.0000000000001493.

This article was published by Wolters Kluwer under the Creative Commons Attribution 4.0 license (www.creativecommons.org/licenses/by/4.0) in the Ear & Hearing journal. Therefore, no permission is required, but an embargo of 12 months is requested. For further information, please refer to www.wolterskluwer.com/en/solutions/lippincott-journals/lippincott-open-access.

Article 2. Arán-Tapia, I., Soto-Varela, A., Pérez-Muñuzuri, V., Santos-Pérez, S., Arán, I., Muñuzuri, A. P. Numerical simulations to determine the stimulation of the crista ampullaris during the Head Impulse Test. *Comput Biol Med.* **163**, 107225 (2023). ISSN: 0010-4825. DOI: www.doi.org/10.1016/j.compbiomed.2023.107225.

This article was published by Elsevier under the Creative Commons Attribution 4.0 license (www.creativecommons.org/licenses/by/4.0) in the Computers in Biology and Medicine journal. No permission is therefore required. For further information, please refer to www.sciencedirect.com/journal/computers-in-biology-and-medicine/publish/open-access-options.

USC
UNIVERSIDADE DE SANTIAGO DE COMPOSTELA

Article 3. Arán-Tapia, I., Pérez-Muñuzuri, V., Muñuzuri, A. P., Soto-Varela, A., Otero-Millan, J., Roberts, D. C., Ward, B. K. The Biophysics of Magnetic Vestibular Stimulation: Clinical Insights from High-Field MRI. Under review in *Communications Medicine* (2024). ISSN: 2730-664X.

This article is under review by Springer Nature under the Creative Commons Attribution 4.0 license (www.creativecommons.org/licenses/by/4.0) in the Communications Medicine journal. No permission is therefore required. For further information, please refer to www.nature.com/commsmed/open-access.

Figure 1.2. The design elements in this figure were taken from BioRender (www.biorender.com) and then adapted to create the final figure. The BioRender license permits this use for doctoral theses published in repositories that are not considered commercial or for-profit publications. For more information, please refer to www.biorender.com/basic-license.

Figure 1.4. The brain image showed was collected from GDJ artist in Pixabay (www.pixabay.com) and included as a part of the final figure. The Creative Commons Zero (CC0) license (www.creativecommons.org/publicdomain/zero/1.0) applicabe for this image in Pixabay permits the use for all personal and commercial purposes. For more information, please refer to www.pixabay.com/pt/service/terms.

I declare that the rest of the figures shown in this thesis were either of my own making or reproduced from the publications stated above.

USC UNIVERSIDADE DE SANTIAGO DE COMPOSTELA

Dissemination of reseach

International oral communication. Arán-Tapia, I., Soto-Varela, A., Pérez-Muñuzuri, V., Arán, I., Muñuzuri, A. P. Personalized Medicine for Optimal Stimulation of the Semicircular Canals. *XXXI Bárány Society Meeting*. May 9-11, 2022, Madrid, Spain.

National poster presentation. Arán-Tapia, I., Soto-Varela, A., Pérez-Muñuzuri, V., Arán, I., Muñuzuri, A. P. Mathematical Model for the Vestibular System. *XXIII Congreso de Fïsica Estadística*. May 12-14, 2022, Zaragoza, Spain.

National oral communication. Arán-Tapia, I., Soto-Varela, A., Pérez-Muñuzuri, V., Arán, I., Muñuzuri, A. P. El Papel de la Física No Lineal en el Sistema Vestibular. *Patología Vestibular: desde la Investigación Básica hasta la Aplicación Clínica*. June 2, 2022, A Coruña, Spain.

International oral communication. Arán-Tapia, I., Soto-Varela, A., Pérez-Muñuzuri, V., Santos-Pérez, S., Arán, I., Muñuzuri, A. P, Otero-Millan, J., Roberts, D. C., Ward, B. K. Mahtematical Modeling of the Vestibular System: BPPV, vHIT and MVS. *Johns Hopkins Hospital Division of Neuro-Visual and Vestibular Disorders Seminar Series*. Novemeber 16, 2023, Baltimore, USA.

National oral communication. Arán-Tapia, I., Soto-Varela, A., Pérez-Muñuzuri, V., Santos-Pérez, S., Arán, I., Muñuzuri, A. P. Personalización de la Maniobra de Epley a partir de simulaciones numéricas. *4º Reunión de Invierno de Otoneurología*. February 23-24, 2024, Madrid, Spain.

National oral communication. Arán-Tapia, I., Soto-Varela, A., Pérez-Muñuzuri, V., Santos-Pérez, S., Arán, I., Muñuzuri, A. P. Simulaciones numéricas del Sistema Vestibular: VPPB, VHIT y Estimulación Vestibular Magnética. *Programa de mentorización a la investigación de la Sociedad Española de Otorrinolaringología y Cirugía de Cabeza y Cuello*. April 11, 2024, Online.

International oral communication. Arán-Tapia, I., Soto-Varela, A., Pérez-Muñuzuri, V., Santos-Pérez, S., Arán, I., Muñuzuri, A. P. Personalizing the Epley Maneuver through Computational Modeling of Vestibular Anatomy. *XXXII Bárány Society Meeting*. Scheduled for August 25-28, 2024, Uppsala, Sweden.

International poster presentation. Arán-Tapia, I., Pérez-Muñuzuri, V., Muñuzuri, A. P., Soto-Varela, A., Otero-Millan, J., Roberts, D. C., Ward, B. K. The Biophysics of Magnetic Vestibular Stimulation. *XXXII Bárány Society Meeting*. Scheduled for August 25-28, 2024, Uppsala, Sweden.

USC
UNIVERSIDADE DE SANTIAGO DE COMPOSTELA

Funding information

This research was supported by the Spanish Ministerio de Economía y Competitividad and the European Regional Development Fund, research grant RTI2018-097063-B-I00 AEI/FEDER, UE; Xunta de Galicia, research grant No. 2021-PG036 (both programs are co-funded by FEDER EU); the Spanish Instituto de Salud Carlos III, research grant PI23/00248; and the United States National Institutes of Health, research grant K23DC018302.

Several other small grants, enterprises, and awards supported this research and facilitated its dissemination. Computation took place at Centro de Supercomputación de Galicia (CESGA).

USC
UNIVERSIDADE
DE SANTIAGO
DE COMPOSTELA

Bibliography

[1] Graf, W. M. Evolution of the Vestibular System. In Binder, M. D., Hirokawa, N. & Windhorst, U. (eds.) *Encyclopedia of Neuroscience*, 1440–1448 (Springer, Berlin, Heidelberg, 2009).

[2] Jamon, M. The development of vestibular system and related functions in mammals: Impact of gravity. *Frontiers in Integrative Neuroscience* **8**, 11 (2014).

[3] Hawkins, J. E. Sketches of otohistory. Part 1: Otoprehistory: How it all began. *Audiology & Neuro-Otology* **9**, 66–71 (2004).

[4] Desai, S. S. & Dua, A. History of Research in the Vestibular System: A 400-Year-Old Story. *Anatomy & Physiology* **04** (2014).

[5] Steinhausen, W. Über die Beobachtung der Cupula in den Bogengangsampullen des Labyrinths des lebenden Hechts. *Pflüger's Archiv für die gesamte Physiologie des Menschen und der Tiere* **232**, 500–512 (1933).

[6] Goldberg, J. M. *et al. The Vestibular System: A Sixth Sense* (Oxford University Press, 2012).

[7] Walker, M. Vestibular System. In Aminoff, M. J. & Daroff, R. B. (eds.) *Encyclopedia of the Neurological Sciences (Second Edition)*, 647–656 (Academic Press, Oxford, 2014).

[8] Hibino, H. & Kurachi, Y. Molecular and physiological bases of the K+ circulation in the mammalian inner ear. *Physiology (Bethesda, Md.)* **21**, 336–345 (2006).

[9] David, R., Stoessel, A., Berthoz, A., Spoor, F. & Bennequin, D. Assessing morphology and function of the semicircular duct system: Introducing new in-situ visualization and software toolbox. *Scientific Reports* **6**, 32772 (2016).

[10] Jaeger, R. & Haslwanter, T. Otolith responses to dynamical stimuli: Results of a numerical investigation. *Biological Cybernetics* **90**, 165–175 (2004).

[11] Rabbitt, R. D. Directional coding of three-dimensional movements by the vestibular semicircular canals. *Biological Cybernetics* **80**, 417–431 (1999).

[12] Highstein, S. M., Fay, R. R., Popper, A. N., Fay, R. R. & Popper, A. N. (eds.) *The Vestibular System*, vol. 19 of *Springer Handbook of Auditory Research* (Springer, New York, NY, 2004).

USC UNIVERSIDADE DE SANTIAGO DE COMPOSTELA

[13] Lopez-Escamez, J. A., Gamiz, M. J., Fernandez-Perez, A. & Gomez-Fiñana, M. Long-term outcome and health-related quality of life in benign paroxysmal positional vertigo. *European archives of oto-rhino-laryngology: official journal of the European Federation of Oto-Rhino-Laryngological Societies (EUFOS): affiliated with the German Society for Oto-Rhino-Laryngology - Head and Neck Surgery* **262**, 507–511 (2005).

[14] Lee, S.-H. & Kim, J. S. Benign paroxysmal positional vertigo. *Journal of Clinical Neurology (Seoul, Korea)* **6**, 51–63 (2010).

[15] von Brevern, M. *et al.* Epidemiology of benign paroxysmal positional vertigo: A population based study. *Journal of Neurology, Neurosurgery, and Psychiatry* **78**, 710–715 (2007).

[16] van der Zaag-Loonen, H. J., van Leeuwen, R. B., Bruintjes, T. D. & van Munster, B. C. Prevalence of unrecognized benign paroxysmal positional vertigo in older patients. *European archives of oto-rhino-laryngology: official journal of the European Federation of Oto-Rhino-Laryngological Societies (EUFOS): affiliated with the German Society for Oto-Rhino-Laryngology - Head and Neck Surgery* **272**, 1521–1524 (2015).

[17] Kalmanson, O. & Foster, C. A. Cupulolithiasis: A Critical Reappraisal. *OTO Open* **7**, e38 (2023).

[18] Epley, J. M. The canalith repositioning procedure: For treatment of benign paroxysmal positional vertigo. *Otolaryngology–Head and Neck Surgery: Official Journal of American Academy of Otolaryngology-Head and Neck Surgery* **107**, 399–404 (1992).

[19] Hilton, M. P. & Pinder, D. K. The Epley (canalith repositioning) manoeuvre for benign paroxysmal positional vertigo. *The Cochrane Database of Systematic Reviews* CD003162 (2014).

[20] Choi, S. J. *et al.* Clinical features of recurrent or persistent benign paroxysmal positional vertigo. *Otolaryngology–Head and Neck Surgery: Official Journal of American Academy of Otolaryngology-Head and Neck Surgery* **147**, 919–924 (2012).

[21] Baloh, R. W. Robert Bárány and the controversy surrounding his discovery of the caloric reaction. *Neurology* **58**, 1094–1099 (2002).

[22] Sanz Fernández, R. & Martín Sanz, E. *Exploración otoneurólogica: interpretación de las pruebas vestibulares : abordaje práctico del paciente con vértigo y alteraciones del equilibrio* (Indica, 2016).

[23] Halmagyi, G. M. *et al.* The Video Head Impulse Test. *Frontiers in Neurology* **8** (2017).

[24] Stevens, M. N., Garrison, D. B. & Kaylie, D. M. What is the potential clinical utility of vHIT when assessing adult patients with dizziness? *The Laryngoscope* **127**, 2689–2690 (2017).

[25] Theysohn, J. M. *et al.* Subjective acceptance of 7 Tesla MRI for human imaging. *Magma (New York, N.Y.)* **21**, 63–72 (2008).

USC UNIVERSIDADE DE SANTIAGO DE COMPOSTELA

[26] Theysohn, J. M. *et al.* Vestibular effects of a 7 Tesla MRI examination compared to 1.5 T and 0 T in healthy volunteers. *PloS One* **9**, e92104 (2014).

[27] Schaap, K. *et al.* Occupational exposure of healthcare and research staff to static magnetic stray fields from 1.5-7 Tesla MRI scanners is associated with reporting of transient symptoms. *Occupational and Environmental Medicine* **71**, 423–429 (2014).

[28] Marcelli, V. *et al.* Spatio-temporal pattern of vestibular information processing after brief caloric stimulation. *European Journal of Radiology* **70**, 312–316 (2009).

[29] Roberts, D. C. *et al.* MRI magnetic field stimulates rotational sensors of the brain. *Current biology: CB* **21**, 1635–1640 (2011).

[30] Houpt, T. A., Kwon, B., Houpt, C. E., Neth, B. & Smith, J. C. Orientation within a high magnetic field determines swimming direction and laterality of c-Fos induction in mice. *American Journal of Physiology - Regulatory, Integrative and Comparative Physiology* **305**, R793–R803 (2013).

[31] Mian, O. S., Li, Y., Antunes, A., Glover, P. M. & Day, B. L. On the vertigo due to static magnetic fields. *PloS One* **8**, e78748 (2013).

[32] Ward, B. K., Roberts, D. C., Otero-Millan, J. & Zee, D. S. A decade of magnetic vestibular stimulation: From serendipity to physics to the clinic. *Journal of Neurophysiology* **121**, 2013–2019 (2019).

[33] Boselli, F., Obrist, D. & Kleiser, L. Vortical flow in the utricle and the ampulla: A computational study on the fluid dynamics of the vestibular system. *Biomechanics and Modeling in Mechanobiology* **12**, 335–348 (2013).

[34] Goyens, J., Pourquie, M. J. B. M., Poelma, C. & Westerweel, J. Asymmetric cupula displacement due to endolymph vortex in the human semicircular canal. *Biomechanics and Modeling in Mechanobiology* **18**, 1577–1590 (2019).

[35] Angelaki, D. E. & Cullen, K. E. Vestibular system: The many facets of a multimodal sense. *Annual Review of Neuroscience* **31**, 125–150 (2008).

[36] Rabbitt, R. D. *et al.* Dynamic displacement of normal and detached semicircular canal cupula. *Journal of the Association for Research in Otolaryngology: JARO* **10**, 497–509 (2009).

[37] Van Buskirk, W. C., Watts, R. G. & Liu, Y. K. The fluid mechanics of the semicircular canals. *Journal of Fluid Mechanics* **78**, 87–98 (1976).

[38] Oman, C. M., Marcus, E. N. & Curthoys, I. S. The influence of semicircular canal morphology on endolymph flow dynamics. An anatomically descriptive mathematical model. *Acta Oto-Laryngologica* **103**, 1–13 (1987).

[39] Damiano, E. R. & Rabbitt, R. D. A singular perturbation model of fluid dynamics in the vestibular semicircular canal and ampulla. *Journal of Fluid Mechanics* **307**, 333–372 (1996).

[40] Rabbitt, R. D. Semicircular canal biomechanics in health and disease. *Journal of Neurophysiology* **121**, 732–755 (2019).

[41] Ramat, S. Understanding the rotational vestibular ocular reflex: From differential equations to Laplace transforms. *Progress in Brain Research* **248**, 29–44 (2019).

[42] Martin, P. & Hudspeth, A. J. Compressive nonlinearity in the hair bundle's active response to mechanical stimulation. *Proceedings of the National Academy of Sciences of the United States of America* **98**, 14386–14391 (2001).

[43] Rabbitt, R. D., Boyle, R. & Highstein, S. M. Mechanical amplification by hair cells in the semicircular canals. *Proceedings of the National Academy of Sciences of the United States of America* **107**, 3864–3869 (2010).

[44] Obrist, D. Flow Phenomena in the Inner Ear. *Annual Review of Fluid Mechanics* **51**, 487–510 (2019).

[45] Curthoys, I. S., Grant, J. W., Pastras, C. J., Fröhlich, L. & Brown, D. J. Similarities and Differences Between Vestibular and Cochlear Systems - A Review of Clinical and Physiological Evidence. *Frontiers in Neuroscience* **15**, 695179 (2021).

[46] Iversen, M. M. & Rabbitt, R. D. Wave Mechanics of the Vestibular Semicircular Canals. *Biophysical Journal* **113**, 1133–1149 (2017).

[47] Obrist, D. Fluidmechanics of semicircular canals – revisited. *Zeitschrift für angewandte Mathematik und Physik* **59**, 475–497 (2008).

[48] Wu, X., Yu, S., Shen, S. & Liu, W. Quantitative analysis of the biomechanical response of semicircular canals and nystagmus under different head positions. *Hearing Research* **407**, 108282 (2021).

[49] Wu, X., Yu, S., Shen, S. & Liu, W. Exploring the biomechanical responses of human cupula by numerical analysis of temperature experiments. *Scientific Reports* **11**, 8208 (2021).

[50] Wu, X., Yu, S., Liu, W. & Shen, S. Numerical modeling and verification by nystagmus slow-phase velocity of the function of semicircular canals. *Biomechanics and Modeling in Mechanobiology* **19**, 2343–2356 (2020).

[51] Grieser, B. J., Kleiser, L. & Obrist, D. Identifying Mechanisms Behind the Tullio Phenomenon: A Computational Study Based on First Principles. *Journal of the Association for Research in Otolaryngology: JARO* **17**, 103–118 (2016).

[52] Rey-Martinez, J., Altuna, X., Cheng, K., Burgess, A. M. & Curthoys, I. S. Computing Endolymph Hydrodynamics During Head Impulse Test on Normal and Hydropic Vestibular Labyrinth Models. *Frontiers in Neurology* **11**, 289 (2020).

[53] Senofsky, N., Faber, J. & Bozovic, D. Vestibular Drop Attacks and Meniere's Disease as Results of Otolithic Membrane Damage-A Numerical Model. *Journal of the Association for Research in Otolaryngology: JARO* **24**, 107–115 (2023).

USC UNIVERSIDADE DE SANTIAGO DE COMPOSTELA

[54] Kimura, R. S. Distribution, structure, and function of dark cells in the vestibular labyrinth. *The Annals of Otology, Rhinology, and Laryngology* **78**, 542–561 (1969).

[55] Watanuki, K. & Schuknecht, H. F. A morphological study of human vestibular sensory epithelia. *Archives of Otolaryngology (Chicago, Ill.: 1960)* **102**, 853–858 (1976).

[56] Johannessen, S. R. *Use of CFD to Study Hydrodynamic Loads on Free-Fall Lifeboats in the Impact Phase: A Verification and Validation Study.* Master's thesis, Institutt for marin teknikk (2012).

[57] Profir, M. M. Automated moving mesh techniques and re-meshing strategies in CFD applications using morphing and rigid motions. Technical Report (2012).

[58] Obrist, D. Numerical simulation of the endolymph flow in a semicircular canal. *PAMM* **7**, 4100029–4100030 (2007).

[59] Brody, J. P., Yager, P., Goldstein, R. E. & Austin, R. H. Biotechnology at low Reynolds numbers. *Biophysical Journal* **71**, 3430–3441 (1996).

[60] Hain, T. C., Squires, T. M. & Stone, H. A. Clinical implications of a mathematical model of benign paroxysmal positional vertigo. *Annals of the New York Academy of Sciences* **1039**, 384–394 (2005).

[61] Jang, Y. S., Hwang, C. H., Shin, J. Y., Bae, W. Y. & Kim, L. S. Age-related changes on the morphology of the otoconia. *The Laryngoscope* **116**, 996–1001 (2006).

[62] Boselli, F., Kleiser, L., Bockisch, C. J., Hegemann, S. C. A. & Obrist, D. Quantitative analysis of benign paroxysmal positional vertigo fatigue under canalithiasis conditions. *Journal of Biomechanics* **47**, 1853–1860 (2014).

[63] Finley, C. C., Wilson, B. S. & White, M. W. Models of Neural Responsiveness to Electrical Stimulation. In Miller, J. M. & Spelman, F. A. (eds.) *Cochlear Implants: Models of the Electrically Stimulated Ear*, 55–96 (Springer, New York, NY, 1990).

[64] Breneman, K. D. & Rabbitt, R. D. Piezo- and Flexoelectric Membrane Materials Underlie Fast Biological Motors in the Ear. *Materials Research Society Symposia Proceedings. Materials Research Society* **1186E**, 1186–JJ06–04 (2009).

[65] Squires, T. M., Weidman, M. S., Hain, T. C. & Stone, H. A. A mathematical model for top-shelf vertigo: The role of sedimenting otoconia in BPPV. *Journal of Biomechanics* **37**, 1137–1146 (2004).

[66] Merchant, S. N. *et al.* Temporal bone studies of the human peripheral vestibular system. Normative vestibular hair cell data. *The Annals of Otology, Rhinology & Laryngology. Supplement* **181**, 3–13 (2000).

[67] Schubert, M. C., Tusa, R. J., Grine, L. E. & Herdman, S. J. Optimizing the Sensitivity of the Head Thrust Test for Identifying Vestibular Hypofunction. *Physical Therapy* **84**, 151–158 (2004).

[68] Roser, M., Appel, C. & Ritchie, H. Human Height. *Our World in Data* (2013).

USC UNIVERSIDADE DE SANTIAGO DE COMPOSTELA

[69] Pérez-Vázquez, P. *et al.* Practice Guidelines for the Diagnosis and Management of Benign Paroxysmal Positional Vertigo Otoneurology Committee of Spanish Otorhinolaryngology and Head and Neck Surgery Consensus Document. *Acta Otorrinolaringologica Espanola* **69**, 345–366 (2018).

[70] Obrist, D., Hegemann, S., Kronenberg, D., Häuselmann, O. & Rösgen, T. In vitro model of a semicircular canal: Design and validation of the model and its use for the study of canalithiasis. *Journal of Biomechanics* **43**, 1208–1214 (2010).

[71] Goyens, J. Modelling shows that stimulation of the semicircular canals depends on the rotation centre. *Hearing Research* **396**, 108071 (2020).

[72] Shen, S. *et al.* Biomechanical Analysis of Angular Motion in Association with Bilateral Semicircular Canal Function. *Biophysical Journal* **118**, 729–741 (2020).

[73] Goyens, J. & Aerts, P. Why the semicircular canals are not stimulated by linear accelerations. *Bioinspiration & Biomimetics* **14**, 056004 (2019).

[74] Yamauchi, A., Rabbitt, R. D., Boyle, R. & Highstein, S. M. Relationship between inner-ear fluid pressure and semicircular canal afferent nerve discharge. *Journal of the Association for Research in Otolaryngology: JARO* **3**, 26–44 (2002).

[75] Wu, C.-q. *et al.* Dynamic analysis of fluid-structure interaction of endolymph and cupula in the lateral semicircular canal of inner ear. *Journal of Hydrodynamics, Ser. B* **23**, 777–783 (2011).

[76] Marianelli, P., Berthoz, A. & Bennequin, D. Crista egregia: A geometrical model of the crista ampullaris, a sensory surface that detects head rotations. *Biological Cybernetics* **109**, 5–32 (2015).

[77] Rabbitt, R. D., Boyle, R., Holstein, G. R. & Highstein, S. M. Hair-cell versus afferent adaptation in the semicircular canals. *Journal of Neurophysiology* **93**, 424–436 (2005).

[78] Cohen, B., Suzuki, J. I. & Bender, M. B. Eye movements from semicircular canal nerve stimulation in the cat. *The Annals of Otology, Rhinology, and Laryngology* **73**, 153–169 (1964).

[79] Otero-Millan, J., Zee, D. S., Schubert, M. C., Roberts, D. C. & Ward, B. K. Three-dimensional eye movement recordings during magnetic vestibular stimulation. *Journal of Neurology* **264**, 7–12 (2017).

[80] Jareonsettasin, P. *et al.* Multiple Time Courses of Vestibular Set-Point Adaptation Revealed by Sustained Magnetic Field Stimulation of the Labyrinth. *Current biology: CB* **26**, 1359–1366 (2016).

[81] Otero-Millan, J., Roberts, D. C., Lasker, A., Zee, D. S. & Kheradmand, A. Knowing what the brain is seeing in three dimensions: A novel, noninvasive, sensitive, accurate, and low-noise technique for measuring ocular torsion. *Journal of Vision* **15**, 11 (2015).

USC UNIVERSIDADE DE SANTIAGO DE COMPOSTELA

[82] Della Santina, C. C., Potyagaylo, V., Migliaccio, A. A., Minor, L. B. & Carey, J. P. Orientation of human semicircular canals measured by three-dimensional multiplanar CT reconstruction. *Journal of the Association for Research in Otolaryngology: JARO* **6**, 191–206 (2005).

[83] Johnson Chacko, L. *et al.* Analysis of Vestibular Labyrinthine Geometry and Variation in the Human Temporal Bone. *Frontiers in Neuroscience* **12**, 107 (2018).

[84] House, M. G. & Honrubia, V. Theoretical models for the mechanisms of benign paroxysmal positional vertigo. *Audiology & Neuro-Otology* **8**, 91–99 (2003).

[85] Obrist, D. & Hegemann, S. Fluid-particle dynamics in canalithiasis. *Journal of the Royal Society, Interface* **5**, 1215–1229 (2008).

[86] Rajguru, S. M., Ifediba, M. A. & Rabbitt, R. D. Biomechanics of horizontal canal benign paroxysmal positional vertigo. *Journal of Vestibular Research: Equilibrium & Orientation* **15**, 203–214 (2005).

[87] Rajguru, S. M., Ifediba, M. A. & Rabbitt, R. D. Three-dimensional biomechanical model of benign paroxysmal positional vertigo. *Annals of Biomedical Engineering* **32**, 831–846 (2004).

[88] Gebhart, I. *et al.* Sémont Maneuver for Benign Paroxysmal Positional Vertigo Treatment: Moving in the Correct Plane Matters. *Otology & Neurotology* **42**, e341–e347 (2021).

[89] Djukic, T. & Filipovic, N. Numerical modeling of the cupular displacement and motion of otoconia particles in a semicircular canal. *Biomechanics and Modeling in Mechanobiology* **16**, 1669–1680 (2017).

[90] Bhandari, A., Kingma, H. & Bhandari, R. BPPV Simulation: A Powerful Tool to Understand and Optimize the Diagnostics and Treatment of all Possible Variants of BPPV. *Frontiers in Neurology* **12**, 632286 (2021).

[91] Faldon, M. E. & Bronstein, A. M. Head accelerations during particle repositioning manoeuvres. *Audiology & Neuro-Otology* **13**, 345–356 (2008).

[92] Yu, S., Wang, J., Guo, Y., Sun, X. & Shen, S. A Numerical Investigation of the Effects of Benign Paroxysmal Positional Vertigo on the Balance Function of the Inner Ear. *Computer Modeling in Engineering & Sciences* **116**, 315–322 (2018).

[93] Rajguru, S. M. & Rabbitt, R. D. Afferent responses during experimentally induced semicircular canalithiasis. *Journal of Neurophysiology* **97**, 2355–2363 (2007).

[94] Kao, W. T. K., Parnes, L. S. & Chole, R. A. Otoconia and otolithic membrane fragments within the posterior semicircular canal in benign paroxysmal positional vertigo. *The Laryngoscope* **127**, 709–714 (2017).

[95] Castellucci, A. *et al.* Isolated horizontal canal hypofunction differentiating a canalith jam from an acute peripheral vestibular loss. *American Journal of Otolaryngology* **40**, 319–322 (2019).

[96] Yu, S. *et al.* Study of the biomechanical mechanisms of benign paroxysmal positional vertigo. *Journal of Vestibular Research: Equilibrium & Orientation* **31**, 163–172 (2021).

[97] Andera, L., Azeredo, W. J., Greene, J. S., Sun, H. & Walter, J. Optimizing Testing for BPPV – The Loaded Dix-Hallpike. *The Journal of International Advanced Otology* **16**, 171–175 (2020).

[98] Strupp, M. *et al.* BPPV: Comparison of the SémontPLUS With the Sémont Maneuver: A Prospective Randomized Trial. *Frontiers in Neurology* **12** (2021).

[99] Oh, H. J., Kim, J. S., Han, B. I. & Lim, J. G. Predicting a successful treatment in posterior canal benign paroxysmal positional vertigo. *Neurology* **68**, 1219–1222 (2007).

[100] Aw, S. T., Todd, M. J., Aw, G. E., McGarvie, L. A. & Halmagyi, G. M. Benign positional nystagmus: A study of its three-dimensional spatio-temporal characteristics. *Neurology* **64**, 1897–1905 (2005).

[101] Luryi, A. L. *et al.* Treatment of Patients With Benign Paroxysmal Positional Vertigo and Severe Immobility Using the Particle Repositioning Chair: A Retrospective Cohort Study. *The Annals of Otology, Rhinology, and Laryngology* **127**, 390–394 (2018).

[102] Mandalà, M., Salerni, L. & Nuti, D. Benign Positional Paroxysmal Vertigo Treatment: A Practical Update. *Current Treatment Options in Neurology* **21**, 66 (2019).

[103] Gan, Z. *et al.* Self-Treatment of Posterior Canal Benign Paroxysmal Positional Vertigo: A Preliminary Study. *Frontiers in Medicine* **8**, 654637 (2021).

[104] Otsuka, K. *et al.* Model experiments of otoconia stability after canalith repositioning procedure of BPPV. *Acta Oto-Laryngologica* **130**, 804–809 (2010).

[105] Zucca, G., Valli, S., Valli, P., Perin, P. & Mira, E. Why do benign paroxysmal positional vertigo episodes recover spontaneously? *Journal of Vestibular Research: Equilibrium & Orientation* **8**, 325–329 (1998).

[106] Hunt, W. T., Zimmermann, E. F. & Hilton, M. P. Modifications of the Epley (canalith repositioning) manoeuvre for posterior canal benign paroxysmal positional vertigo (BPPV). *The Cochrane Database of Systematic Reviews* **2012**, CD008675 (2012).

[107] Moroz, M. *et al.* Evaluating the Epley Canalolith Repositioning Procedure With and Without a Visual Assistive Device. *Otology & Neurotology: Official Publication of the American Otological Society, American Neurotology Society [and] European Academy of Otology and Neurotology* **42**, 765–773 (2021).

[108] Tan, J. *et al.* Comparative study of the efficacy of the canalith repositioning procedure versus the vertigo treatment and rehabilitation chair. *Acta Oto-Laryngologica* **134**, 704–708 (2014).

[109] West, N., Bloch, S. L., Møller, M. N., Hansen, S. & Klokker, M. Reposition Chair Treatment Improves Subjective Outcomes in Refractory Benign Paroxysmal Positional Vertigo. *The Journal of International Advanced Otology* **15**, 146–150 (2019).

USC UNIVERSIDADE DE SANTIAGO DE COMPOSTELA

[110] Martellucci, S. *et al.* Features of Residual Dizziness after Canalith Repositioning Procedures for Benign Paroxysmal Positional Vertigo. *Otolaryngology–Head and Neck Surgery: Official Journal of American Academy of Otolaryngology-Head and Neck Surgery* **154**, 693–701 (2016).

[111] Richard-Vitton, T. & Viirre, E. Unsteadiness and drunkenness sensations as a new sub-type of BPPV. *Revue De Laryngologie - Otologie - Rhinologie* **132**, 75–80 (2011).

[112] Blanks, R. H. I., Curthoys, I. S. & Markham, C. H. Planar Relationships Of The Semicircular Canals In Man. *Acta Oto-Laryngologica* **80**, 185–196 (1975).

[113] Ifediba, M. A., Rajguru, S. M., Hullar, T. E. & Rabbitt, R. D. The Role of 3-Canal Biomechanics in Angular Motion Transduction by the Human Vestibular Labyrinth. *Annals of Biomedical Engineering* **35**, 1247–1263 (2007).

[114] Selva, P., Morlier, J. & Gourinat, Y. Toward a three-dimensional finite-element model of the human inner ear angular accelerometers sensors. *International Journal for Computational Vision and Biomechanics (IJCV & B)* **3**, 149 (2010).

[115] Shen, S. *et al.* Numerical simulation of the role of the utriculo-endolymphatic valve in the rotation-sensing capabilities of semicircular canals. *Journal of Biomechanics* **49**, 1532–1539 (2016).

[116] Rabbitt, R. D., Highstein, S. M. & Boyle, R. Determinants of Semicircular Canal Afferent Response Dynamics in Fish. *Annals of the New York Academy of Sciences* **781**, 213–243 (1996).

[117] Wang, Z. *et al.* Development of Bionic Semicircular Canals and the Sensation of Angular Acceleration. *Bioengineering* **9**, 180 (2022).

[118] Mian, O. S., Li, Y., Antunes, A., Glover, P. M. & Day, B. L. Effect of head pitch and roll orientations on magnetically induced vertigo. *The Journal of Physiology* **594**, 1051–1067 (2016).

[119] Jaeger, R., Takagi, A. & Haslwanter, T. Modeling the relation between head orientations and otolith responses in humans. *Hearing Research* **173**, 29–42 (2002).

[120] Antunes, A., Glover, P. M., Li, Y., Mian, O. S. & Day, B. L. Magnetic field effects on the vestibular system: Calculation of the pressure on the cupula due to ionic current-induced Lorentz force. *Physics in Medicine and Biology* **57**, 4477–4487 (2012).

[121] Ward, B. K., Mair, A., Nagururu, N., Bauer, M. & Büki, B. Correlation between Histopathology and Signal Loss on Spin-Echo T2-Weighted MR Images of the Inner Ear: Distinguishing Artifacts from Anatomy. *AJNR. American journal of neuroradiology* **43**, 1464–1469 (2022).

[122] Wilson, V. J. & Jones, G. M. *Mammalian Vestibular Physiology* (Springer US, Boston, MA, 1979).

[123] Pogson, J. M. *et al.* Longer duration entry mitigates nystagmus and vertigo in 7-Tesla MRI. *Frontiers in Neurology* **14** (2023).

[124] Hoff, M. N. *et al.* Safety Considerations of 7-T MRI in Clinical Practice. *Radiology* **292**, 509–518 (2019).

USC
UNIVERSIDADE DE SANTIAGO DE COMPOSTELA

The objective of this doctoral thesis is to develop and validate mathematical models of the vestibular system in order to deepen our understanding of its physiology and pave the way for personalized medicine in diagnosis and treatment within the field of otorhinolaryngology. This thesis presents the outcomes of multidisciplinary research that utilized high-performance computing and advanced numerical methods to perform numerical simulations of various studies. Initially, a rigid model of the membranous labyrinth combined with a Lagrangian particle model to simulate the Epley maneuver. Subsequently, a fluid-structure interaction model to simulate the head impulse test. Finally, a fluid-structure interaction model was coupled with a magnetohydrodynamic model to simulate the magnetic vestibular stimulation.